Photonic wiring of enzymatic reactions to photoactive entities for the construction of biohybrid electrodes

Dissertation (kumulativ)

zur Erlangung des akademischen Grades
"doctor rerum naturalium"
(Dr. rer. nat.)
in der Wissenschaftsdisziplin "Analytische Biochemie"

eingereicht an der
Mathematisch-Naturwissenschaftlichen Fakultät
Institut für Biochemie und Biologie
der Universität Potsdam

von

Marc Riedel

Potsdam, März 2018

Gutachter: Prof. Dr. Fred Lisdat
Prof. Dr. Frieder Scheller
Dr. Till Bachmann

Published online at the
Institutional Repository of the University of Potsdam:
URN urn:nbn:de:kobv:517-opus4-417280
http://nbn-resolving.de/urn:nbn:de:kobv:517-opus4-417280

Abstract

In this work, different strategies for the construction of biohybrid photoelectrodes are investigated and have been evaluated according to their intrinsic catalytic activity for the oxidation of the cofactor NADH or for the connection with the enzymes PQQ glucose dehydrogenase (PQQ-GDH), FAD-dependent glucose dehydrogenase (FAD-GDH) and fructose dehydrogenase (FDH). The light-controlled oxidation of NADH has been analyzed with InGaN/GaN nanowire-modified electrodes. Upon illumination with visible light the InGaN/GaN nanowires generate an anodic photocurrent, which increases in a concentration-dependent manner in the presence of NADH, thus allowing determination of the cofactor. Furthermore, different approaches for the connection of enzymes to quantum dot (QD)-modified electrodes via small redox molecules or redox polymers have been analyzed and discussed. First, interaction studies with diffusible redox mediators such as hexacyanoferrate(II) and ferrocenecarboxylic acid have been performed with CdSe/ZnS QD-modified gold electrodes to build up photoelectrochemical signal chains between QDs and the enzymes FDH and PQQ-GDH. In the presence of substrate and under illumination of the electrode, electrons are transferred from the enzyme via the redox mediators to the QDs. The resulting photocurrent is dependent on the substrate concentration and allows a quantification of the fructose and glucose content in solution. A first attempt with immobilized redox mediator, i.e. ferrocenecarboxylic acid chemically coupled to PQQ-GDH and attached to QD-modified gold electrodes, reveal the potential to build up photoelectrochemical signal chains even without diffusible redox mediators in solution. However, this approach results in a significant deteriorated photocurrent response compared to the situation with diffusing mediators. In order to improve the photoelectrochemical performance of such redox mediator-based, light-switchable signal chains, an osmium complex-containing redox polymer has been evaluated as electron relay for the electronic linkage between QDs and enzymes. The redox polymer allows the stable immobilization of the enzyme and the efficient wiring with the QD-modified electrode. In addition, a 3D inverse opal TiO_2 (IO-TiO_2) electrode has been used for the integration of PbS QDs, redox polymer and FAD-GDH in order to increase the electrode surface. This results in a significantly improved photocurrent response, a quite low onset potential for the substrate oxidation and a broader glucose detection range as compared to the approach with ferrocenecarboxylic acid and PQQ-GDH immobilized on CdSe/ZnS QD-modified gold electrodes. Furthermore, IO-TiO_2 electrodes are used to integrate sulfonated polyanilines (PMSA1) and PQQ-GDH, and to investigate the direct interaction between the polymer and the enzyme for the light-switchable detection of glucose. While PMSA1 provides visible light excitation and ensures the efficient connection between the IO-TiO_2 electrode and the biocatalytic entity, PQQ-GDH enables the oxidation of glucose. Here, the IO-TiO_2 electrodes with pores of approximately 650 nm provide a

suitable interface and morphology, which is required for a stable and functional assembly of the polymer and enzyme. The successful integration of the polymer and the enzyme can be confirmed by the formation of a glucose-dependent anodic photocurrent. In conclusion, this work provides insights into the design of photoelectrodes and presents different strategies for the efficient coupling of redox enzymes to photoactive entities, which allows for light-directed sensing and provides the basis for the generation of power from sun light and energy-rich compounds.

Zusammenfassung

In dieser Arbeit werden verschiedene Strategien für den Aufbau biohybrider Photoelektroden untersucht und hinsichtlich ihrer intrinsischen katalytischen Aktivität für die Oxidation des Kofaktors NADH oder für die Kontaktierung mit den Enzymen PQQ Glukosedehydrogenase (PQQ-GDH), FAD-abhängige Glukosedehydrogenase (FAD-GDH) und Fruktosedehydrogenase (FDH) evaluiert. Der Licht-gesteuerten Nachweis von NADH wurde mittels InGaN/GaN Nanodraht-modifizierten Elektroden untersucht. Bei Beleuchtung mit sichtbarem Licht generieren die InGaN/GaN Nanodrähte einen anodischen Photostrom, welcher in der Anwesenheit von NADH konzentrationsabhängig ansteigt und somit eine Bestimmung des Kofaktors erlaubt. Des Weiteren werden verschiedene Ansätze für die Kontaktierung von Enzymen mit Quantum Dot (QD)-modifizierten Elektroden unter Verwendung von kleinen Redoxmolekülen oder Redoxpolymeren analysiert und diskutiert. Zunächst wurden Interaktionsstudien mit den Redoxmediatoren Kaliumhexacyanoferrat(II) und Ferrocencarbonsäure in Lösung an CdSe/ZnS QD-modifizierten Goldelektroden durchgeführt um darauf aufbauend photoelektrochemische Signalketten zwischen QDs und den Enzymen FDH und PQQ-GDH aufzubauen und für den Nachweis von Fruktose und Glukose zu nutzen. In Anwesenheit von Substrat und unter Beleuchtung der Elektrode werden Elektronen von dem Enzym über die Redoxmediatoren zu den QDs übertragen. Der daraus resultierende Photostrom ist abhängig von der Substratkonzentration und erlaubt eine Bestimmung des Fruktose- und Glukosegehalts in Lösung. Ein erster Ansatz mit immobilisierten Redoxmediatoren, d.h. Ferrocencarbonsäure kovalent an PQQ-GDH gebunden und auf QD-modifizierten Goldelektroden immobilisiert, zeigt das Potential photoelektrochemische Signalketten auch ohne Redoxmediatoren in Lösung aufzubauen. Jedoch resultierte dieser Ansatz in einer deutlichen Verschlechterung der Photostromantwort im Vergleich zum Ansatz mit Mediatoren in Lösung. Um die photoelektrochemische Leistungsfähigkeit Redoxmediator-basierter, Licht-schaltbarer Signalketten zu verbessern, wurde ein Osmiumkomplex-Redoxpolymer für die elektronische Kontaktierung zwischen QDs und Enzymen untersucht. Das Redoxpolymer erlaubt eine stabile Immobilisierung des Enzymes und eine effiziente Kontaktierung mit der QD-modifizierten Elektrode. Zusätzlich wurde eine 3D „inverse opale“ TiO_2 (IO-TiO_2) Elektrode für die Integration der PbS QDs, des Redoxpolymers und der FAD-GDH verwendet um die Elektrodenoberfläche zu vergrößern. Dies führt zu einer deutlich verbesserten Leistungsfähigkeit hinsichtlich der Photostromantwort, des Startpotentials für die Substratoxidation und des Nachweisbereiches für Glukose im Vergleich zu dem Ansatz mit Ferrocencarbonsäure und PQQ-GDH immobilisiert auf CdSe/ZnS QD-modifizierten Goldelektroden. Des Weiteren wurden IO-TiO_2 Elektroden verwendet um sulfonierte Polyaniline (PMSA1) und PQQ-GDH zu integrieren und die direkte

Interaktion zwischen dem Polymer und dem Enzym für den Licht-schaltbaren Nachweis von Glukose zu untersuchen. Während PMSA1 eine Anregung mit sichtbaren Licht ermöglicht und die effiziente Verbindung zwischen der IO-TiO_2-Elektrode und der biokatalytischen Einheit sicherstellt, ermöglicht die PQQ-GDH die Oxidation von Glukose. Hierbei bieten die IO-TiO_2-Elektroden mit Poren von ca. 650 nm eine geeignete Schnittstelle und Morphologie, welche für eine stabile und funktionelle Assemblierung des Polymers und Enzyms benötigt wird. Die erfolgreiche Integration des Polymers und des Enzyms kann durch die Ausbildung eines Glukose-abhängigen anodischen Photostroms bestätigt werden. Zusammenfassend gibt diese Arbeit Einblicke in den Aufbau von Photoelektroden und präsentiert verschiedene, effiziente Kopplungsstrategien zwischen Redoxenzymen und photoaktiven Komponenten, welche einen Licht-gesteuerten Nachweis von Analyten ermöglichen und die Grundlage für die Energieerzeugung aus Licht und energiereichen Verbindungen bilden.

Table of Contents

List of Abbreviations

0D	Zero-dimensional
1D	One-dimensional
2D	Two-dimensional
3D	Three-dimensional
ALP	Alkaline phosphatase
AMP	Adenosine monophosphate
BDT	Benzenedithiol
BRC	Bacteria reaction center
CB	Conduction band
CNT	Carbon nanotube
cyt *c*	Cytochrome c
DCPIP	2,6-dichlorophenolindophenol
DET	Direct electron transfer
DNA	Deoxyribonucleic acid
EB	Emeraldine base
EDC	N-(3-dimethylaminopropyl)-N′-ethylcarbodiimide hydrochloride
EIS	Electrochemical impedance spectroscopy
Eg	Band gap energy
EQE	External quantum efficiency
ES	Emeraldine salt
FAD	Flavin adenine dinucleotide
FAD-GDH	FAD-dependent glucose dehydrogenase
Fc-COOH	Ferrocenecarboxylic acid
FDH	Fructose dehydrogenase
FMN	Flavin mononucleotide
FRET	Förster resonance energy transfer
FTO	Fluorine doped tin oxide
GDH	NAD-dependent glucose dehydrogenase
GMP	Guanosine monophosphate
GOx	Glucose oxidase
HCF	Hexacyanoferrate
HEPES	4-(2-hydroxyethyl)-1-piperazineethanesulfonic acid
HOMO	Highest occupied molecular orbital
HRP	Horseradish peroxidase
HRXRD	High Resolution X-ray Diffraction
I_{max}	Maximum current
IO-TiO_2	Inverse opal titanium dioxide
IQE	Internal quantum efficiency
ITO	Indium tin oxide
K_M	Michaelis-Menten constant

$K_{M,app}$	Apparent Michaelis-Menten constant
LB	Polystyrene latex beads
LE	Leucoemeraldine
LED	Light emitting diodes
LUMO	Lowest unoccupied molecular orbital
MES	2-(N-morpholino)ethanesulfonic acid
MV	Methylviologen
MWCNT	Multi-walled carbon nanotubes
NAD^+	Oxidized nicotinamide adenine dinucleotide
NADH	Reduced nicotinamide adenine dinucleotide
$NADP^+$	Oxidized nicotinamide adenine dinucleotide phosphate
NADPH	Reduced nicotinamide adenine dinucleotide phosphate
NP	Nanoparticle
NW	Nanowire
OCP	Open circuit potential
PAA	Poly(allylaminehydrochloride)
PAMBE	Plasma-assisted molecular beam epitaxy
PANI	Polyaniline
PEC	Photoelectrochemical
PEG4000	Poly(ethylene glycol) (4000 g mol^{-1})
PG	Pernigraniline
pI	Isoelectric point
PMSA1	Poly(2- methoxyaniline-5-sulfonic acid)-co-aniline polymer
P_{Os}	Poly(1-vinylimidazole-co-allylamine)-Os(bipy)$_2$Cl-redox polymer
PQQ	Pyrroloquinoline quinone
PQQ-GDH	PQQ glucose dehydrogenase
PSI	Photosystem 1
PSII	Photosystem 2
PSS	Poly(styrenesulfonic acid)
QCM	Quartz Crystal Microbalance
QD	Quantum dot
Rpm	Rounds per minute
Rps	Rounds per second
RSM	Reciprocal space map
SEM	Scanning electron microscopy
SHE	Standard hydrogen electrode
SILAR	Successive ionic layer adsorption and reaction
SOx	Sulfite oxidase
TEM	Transmission electron microscopy
TOP	Trioctylphosphine
TOPO	Trioctylphosphine oxide
TTIP	Titaniumtetraisopropoxide
VB	Valence band

1 Introduction

The sun provides us with light as the most abundant energy source in the world and represents the basic requirement for life on our planet. Over billions of year's nature evolved light-converting organisms such as photosynthetic bacteria, algae and plants, which exploit solar radiation for the transformation in chemical energy. This well-known process is called photosynthesis and enables the utilization of low energy CO_2 via harnessing light energy for the production of energy-rich sugars. In photosynthetic organisms this reaction is initialized via absorption of photons by protein-pigment complexes, inducing an excited electronic state and triggers a multistep energy/electron transfer cascade resulting in a transformation of chemicals. Inspired by this, scientists tried to mimic natural photosynthetic reactions. For the utilization of sun's power natural dyes have been in the focus of light-induced energy and electron transfer studies and served as inspiration for the modification and development of new artificial dyes.[1] Further efforts have been made to not only use dyes as individual building blocks but also to imitate the whole light-harvesting antenna system by integration of chromophores in 3D structures.[2–4] Besides organic dyes also inorganic semiconducting materials play a major role for the construction of light-converting systems. This area strongly benefits from the great progress in the design and synthesis of nanostructures. Particularly, semiconductor nanocrystals called quantum dots have revolutionized the field of light-harvesting nanostructures due to their unique photophysical properties giving access to various optoelectronic applications.[5,6]

Using the sun as an inexhaustible and sustainable energy source has gained much attention for the conversion of solar into electrical energy, providing by far enough energy to completely supply the humanity with power.[7] Silicon-based photovoltaics are well established devices that already operate in large solar cell parks representing the benchmark for other light-to-current converting systems. However, silicon-based solar cells lack to achieve efficiencies above 20%, and thus much work is dedicated to the design and construction of new nanostructured systems as they promise a further boost of the solar-to-current conversion efficiency and at the same time reducing the costs for their production. Another direction of research is more oriented towards the utilization of light-sensitive entities as catalysts, which overcome the energetic reaction barrier for chemical transformations with light. Here, the light-sensitive element itself can either be both, light-harvester and catalyst, or the catalytic activity is introduced by a combination with second catalytic material. The field of applications is rather widespread and includes the production of fuels such as H_2, the fixation of CO_2, the remediation of hazardous wastes, the synthesis of medical substances and the utilization as sensors.[8] Even if the amount of available catalysts is constantly increasing by new developments in the fields of materials, surface modifications or morphologies, these catalysts stay often behind the effectivity

and specificity of biocatalysts found in nature.[9] Furthermore, some chemicals can up to date only be transformed with biocatalysts or under energy-intensive harsh conditions. This has increased the interest in using biocatalysts commercially, but also to understand the reasons leading to their outstanding properties for the construction of bioinspired artificial catalysts.

Redox enzymes represent one of the most widely studied groups of biocatalysts. This can be attributed to their ability to transfer electrons not only with natural interaction partners, but also to communicate with electrodes.[10,11] In this case the electrode acts as a transducer, which converts the biological signal of the enzyme in an electrical measureable signal, making enzyme electrodes interesting for bioelectronics, biosensors and biofuel cells.

Recently, the combination of both, light-sensitive entities with redox enzymes, has initiated a new research field. Such biohybrid systems unit the ability to harvest light energy and offer biocatalytic activity and specificity simultaneously in one integrated system, providing the potential to create new approaches for sensing and bioenergetics, which cannot be realized by the light-sensitive entity or the enzyme alone. For example, photoelectrochemical sensors can be designed, which allow to control electrode reactions not only by the applied potential, but also by modulation of a light source. Thus, the background signal (dark current) can be separated from the analytical signal (photocurrent), this can also help to improve the sensitivity. Furthermore, the construction of self-sufficient sensors relying only on sunlight becomes feasible. The light-harvesting functionality can also help to improve the power-output of biofuel cells for the transformation of biomass by exploiting additional energy gained by solar radiation. However, practical prospects cannot be foreseen and therefore several aspects have to be considered. Particularly, the realization of an efficient connection between the electrode and the light-sensitive entity on the one hand, and between the enzyme and the light-sensitive entity on the other hand remains challenging. Currently, the communication between photoactive materials and enzymes is mostly realized via soluble enzymatic cofactors, substrates or products, which often limits the application. Moreover, also the reaction mechanism is often not well studied in detail. Therefore, a detailed investigation of photoelectrodes and the electronic linkage of biocatalysts to photoactive entities via mediators or direct electron transfer could help to overcome these limitations. This may push forward the utilization of light-converting biohybrids in advanced sensorial and energetic applications.

2 Aim of this work

The aim of this thesis is to design and analyze biohybrid photoelectrochemical electrodes, which combine the photophysical properties of light-sensitive entities with the biocatalytic features of enzymes. Therefore, new strategies for the construction of photoanodes using semiconductor nanostructures such as quantum dots and InGaN/GaN nanowires or conductive polymers as photoactive entity shall be explored. The constructed photoanodes should either be exploited regarding its intrinsic photocatalytic activity for the light-directed detection of NADH or for establishing light-triggered signal chains with biocatalysts including PQQ glucose dehydrogenase, FAD glucose dehydrogenase and fructose dehydrogenase. The electrical linkage of the enzyme to the photoactive entity shall be achieved via mediated or direct electron transfer. Here, the focus is placed on the optimization of the performance of the biohybrid photoanodes in terms of the signal stability, the usable wavelength range for the photoexcitation, the photocurrent amplitude, the onset potential for the analyte oxidation, and the detection range.

3 Theoretical Background

3.1 Light-converting materials

Materials capable of converting solar radiation in electrical or chemical energy have gained much attention for solving energetic human demands with photovoltaic and photocatalytic devices, but have also found application for the construction of sensorial systems. So far, a barely manageable number of different photoactive materials and material combinations have been studied for their light-harvesting capabilities and/or catalytic features. Roughly, photoactive materials can be classified according to the chemical composition into inorganic and organic semiconductors. This chapter will give an overview about light-induced processes in semiconductor materials in order to understand this work, highlighting the most important facts about light-sensitive entities used in this thesis, i.e. quantum dots, nanowires, and polyanilines. More detailed informations about the properties of photoactive materials used in sensors, and light-to-current and light-to-chemical converting systems can be found in ref. [5,12–17].

3.1.1 Electronic and optical properties of semiconductors

The ability of semiconductors to convert light energy can be attributed to their fascinating (photo)-electrical properties. While semiconductors act at the temperature of absolute zero as nonconductors, by supply of energy e.g. heat or light the material can become conductive. This effect can be understand with the band model depicted in Figure 1. A band is a broad electronic energy level that arises from the overlapping of many individual molecular orbitals in a macroscopic solid. The molecular orbitals within semiconductor solids leads to a formation of an upper occupied band, i.e. the valence band (VB), and a lower unoccupied band, i.e. the conduction band (CB). The CB and VB are separated by a band gap, which describes the energetic states that are according to quantum mechanics not allowed and cannot be occupied by electrons. In the unexcited state the valence band is filled with electrons and the conduction band is empty. If sufficient energy is applied to overcome the band gap, electrons can be transferred from the VB to the CB leaving behind a hole in the VB (figure 1). This state is called electron-hole pair or exciton and represents free charge carriers, which contribute to the electrical conductivity of the material. The exciton is not stable and can undergo recombination, charge carrier separation or energy transfer. The recombination can be divided in radiative and nonradiative reactions, which are accompanied by a return of the excited electron from the CB to its initial state in the VB. While the radiative recombination results in an emission of a photon with a wavelength corresponding to the band gap energy, for the nonradiative recombination the energy is converted into a lattice vibration in the crystal,

also known as phonon.[18] Charge carrier separation involves the transfer of excited electrons from the semiconductor to a second reaction partner (reduction) or the fill up of holes of the semiconductor with electrons of a second reaction partner (oxidation). The efficiency of the electron transfer between two reactants can be described with the model of the Marcus theory and depends on several factors such as the solvent, the size, the distance of the reactants and the free enthalpy of the redox reaction.[19] By contrast, the energy transfer is based on the radiation-free transfer of energy from a donor to a acceptor. The Förster resonance energy transfer (FRET) represents the most important energy transfer process. The efficiency of a FRET strongly depends on the distance between the donor and acceptor, which should not exceed 10 nm.[20] A further requirement for a FRET is that the emission spectrum of the donor overlap with the absorbance spectrum of the acceptor.

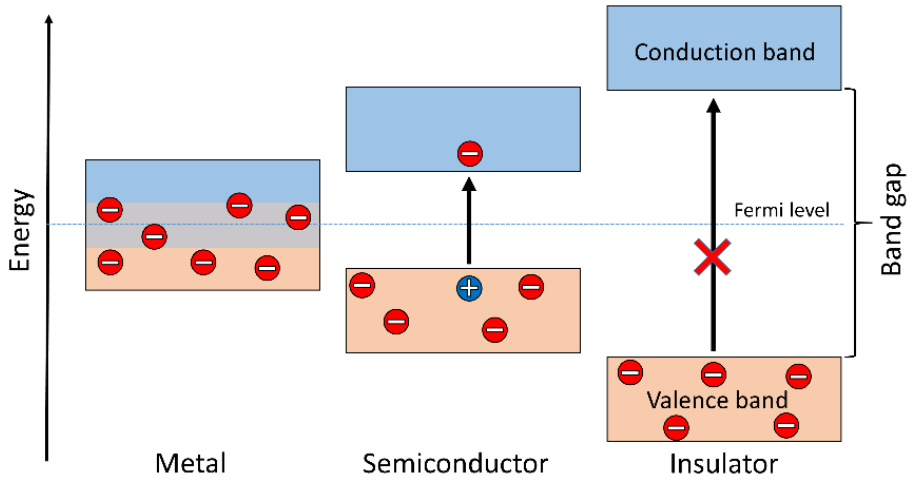

Figure 1. Schematic illustration of the band model for metals, semiconductors and insulators. While for metals the valence and conduction band overlap providing the material conductivity, in semiconductors and insulators both states are separated by a band gap. The difference between semiconductors and insulators is that electrons in semiconductors can overcome the band gap with additional energy e.g. heat or light. This is not possible for insulators.

For intrinsic semiconductors the number of free charge carriers in the CB and VB determines the electrical properties.[21] However, the conductivity of semiconductor materials can be amplified via doping with impurities in order to introduce charge carriers. The foreign atoms introduce either an additional electron (n-type) or have one electron less (p-type) than atoms of the raw semiconductor crystal. A typical example for doping is the modification of silicon with boron or phosphorus for the construction of p-type or n-type semiconductors, respectively.

Inorganic semiconductors can be divided in elementary and compound semiconductors. While elementary semiconductors are composed of only one element such as silicon or germanium, compound semiconductors are formed by at least two elements from two different groups in the periodic system. Examples are material compositions from the III and V group e.g. GaP, GaN and InGaN, the II and VI group e.g. CdS, CdSe, ZnS and

ZnO, and from the IV and VI group e.g. PbS and PbSe. These materials have different capabilities to absorb sun light and generate electron-hole pairs, which is determined by the band gap of the respective semiconductor material. In figure 2, the band gap energy (Eg) of some often used semiconductors is illustrated and has been arranged within the solar spectrum according to the light energy (wavelength) needed to generate electron-hole pairs and overcome the band gap.

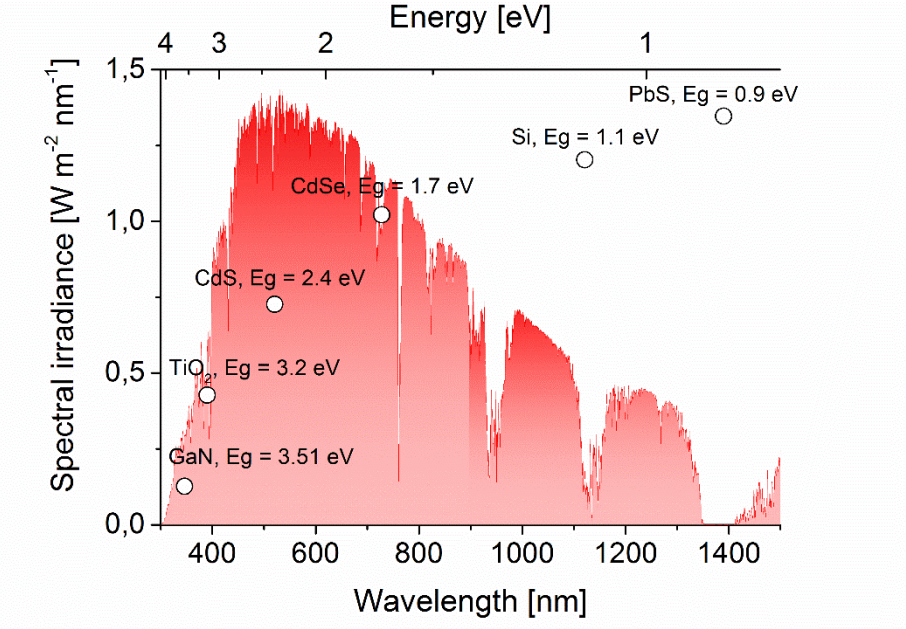

Figure 2. Wavelength-dependent intensity spectrum of the terrestrial solar radiation between 300 nm and 1500 nm.[22] Additionally, the band gaps (Eg) of several macroscopic semiconductors are illustrated by a circle, corresponding to the minimum energy in eV needed to generate electron-hole pairs.[23,24]

It is obvious that for example GaN (Eg = 3.51 eV)[24] cannot be excited with visible light due to its large band gap and is thus less suitable for the efficient conversion of sun light as the sole material. However, a modification of pure GaN can shift the excitation range to longer wavelength.[25] For instance, the insertion of indium within GaN results in $In_xGa_{1-x}N$ alloys with changed optical and electrical properties.[26–28] A indium proportion of 20% results in a decrease of the band gap by about 0.7 eV and allows a excitation up to wavelength of about 440 nm, while pure GaN allows only the use of UV light.[28] Similar to GaN, also TiO_2 (Eg = 3.2 eV) is only able to exploit the UV part of the sun spectrum. However, the beneficial properties such as non-toxicity, photochemical stability and the location of the electronic states (i.e. CB and VB), and the great availability on earth makes TiO_2 to an interesting material for (photo-)electronic applications.[29] Besides doping TiO_2 for shifting the excitation in the visible range, particularly the combination with a second small band gap semiconductor such as CdSe and PbS, or dyes has been shown to be promising for an improved utilization of sun light.[30] The latter approach is often applied for the construction of solar cells. Here, TiO_2 serves as electrode material for the assembly of the sensitizer, but is also able to accept eletrons from the sensitizer. In detail, after

photoexcitation of the sensitizer, excited electrons are injected into the CB of TiO_2, which facilitates the charge carrier separation and allows the exploitation of visible light with a TiO_2 electrodes.

Besides a wide excitation range the semiconductor should also meet the following requirements: (1) suitable energetic states for the catalysis of a redox reaction, i.e. more positive valence band than the redox potential of the donor and more negative conduction band than the redox potential of the acceptor, (2) strong catalytic activity, (3) high charge carrier mobility, life time and long diffusion length in order to reduce recombination processes, (4) sufficient stability, and (5) sustainability and low costs.[8]

3.1.2 Inorganic semiconductor nanostructures

Nanostructures describe materials with at least one dimension (x-, y-and z-direction) in the nanometer scale and behave physical different as compared to macroscopic systems. They can be distinguished by the number of dimensions existing in the nanometer range in zero-dimensional (0D), one-dimensional (1D) and two-dimensional (2D) materials. While for 0D nanomaterials all dimensions are in the nanometer range, 1D structures have two dimensions in the nanometer range and one in the macroscopic range, and 2D materials provide only one dimension in the nanoscale and two macroscopic dimensions. Prominent examples for 0D, 1D and 2D nanostructures are nanoparticles such as quantum dots, nanowires and nanosheets, respectively.

Nanostructuring has strong implications on the properties of the material. Due to the restriction of the material to the nanometer scale, the amount of atoms exposed to the solution is drastically increased and thus offers an enlarged surface area for the catalytic reaction. This implies that despite an identical volume, nanostructured materials can possess a higher reactivity than their macroscopic counterparts. Furthermore, also the energetic properties of the material are influenced as a result of nanostructuring. If only single atoms and molecules are considered in the energetic model, only sharp separated energy level are formed, which can be occupied with electrons. Continuous bands are only formed within macroscopic materials due to the dense arrangement of atoms, resulting in an overlapping of the molecular orbitals. Nanostructures, however, represent an intermediate state between the molecular and the macroscopic world. Thus, the continuous bands of the bulk are reduced to discrete energetic levels for materials with at least one dimension in the nanoscale. This is also accompanied by an increase of the band gap energy and can be explained by the quantum confinement of charge carriers in nanoscaled architectures.[31] This effect is particularly pronounced in 0D nanostructures such as quantum dots,[5,32] but has also been observed in 1D nanostructures such as nanowires.[33]

3.1.2.1 Quantum dots

Quantum dots (QDs) are 0D nanoparticles with a size of only a few nanometers that have revolutionized the application of semiconductors in the field of photodetectors, light-emitting devices and photovoltaics.[34] Monodisperse colloidal QDs are typically synthesized in solution in the presence of ligands such as trioctylphosphine oxide (TOPO) and trioctylphosphine (TOP), and organometallic precursors on the basis of a nucleation process and a diffusion-controlled growth.[12] Alternatively, QDs have also been synthesized via molecular beam epitaxy, lithographic techniques and successive ionic layer adsorption and reaction (SILAR).[5,12] Typically, QDs consist of binary compounds such as CdS, CdSe, CdTe, InP, PbS and PbSe, but also ternary material compositions such as $CdSe_xS_{1-x}$ and $CdSe_xTe_{1-x}$ have been reported.[12]

The great interest in using QDs can be mainly attributed to the pronounced quantum confinement effect found in these nanoparticle, which enables the tuning of the optical and electrical properties by the size and shape of the nanocrystal.[35,12] As illustrated in figure 3, the quantum confinement within QDs is reflected in the absorbance and fluorescence spectra. A decreasing particle size leads to an enhanced confinement of the charge carriers and causes a further separation of the conduction and valence band with the concomitant increase of the band gap.[36,37] Thus, the energy needed to generate electron-hole pairs increases as the particle size decreases and shifts the absorbance to lower (energy-rich) wavelength. Moreover, the absorbance spectra of the QDs shows one prominent peak that is attributable to the lowest discrete energy optical transition. After excitation the life time of electron-hole pairs within QDs is limited to time scales in the range of several nanoseconds.[38,39] The discrete energy level within QDs are also responsible for the formation of an emission spectrum with a rather sharp peak. Similar to the absorbance spectra also the maximum of the photoluminescence spectra is influenced by the QD size and shifts to smaller wavelength with decreasing particle diameter. This allows to tune the photoluminescence properties of QDs by changing their size and has increased the interest in using QDs as optical label in bioanalytical applications.[15]

The tunable band gap of QDs has also found reasonable attention in studies on recombination and electron transfer dynamics with other materials.[12,34] Normally, a multiexponential decay of the photoluminescence is found for QDs, which demonstrates that several electron relaxation reactions occur within the nanoparticles. From this data, time constants can be determined, which help to understand the energy and electron transfer mechanism within QDs and may enable to predict the efficiency for certain optoelectronic applications. However, since several parameters affect the properties of QDs, e.g. composition, size, shape, ligands and surface defects, an exact classification of influencing parameters remains challenging.[34] For example, Garrett et al. have found an increased fluorescence decay with decreasing particle size for CdSe and CdS QDs in the

range between 2.3 and 6 nm.[40] Similar results have been observed in two other studies showing an extended lifetime with increasing diameter up to a size of 4 nm for CdSe QDs[41] and 3.5 nm for CdS QDs,[42] but starts to decrease with further increasing diameter. In contrast, Nirmal et al. and Hong et al. reported an contrary tendency, i.e. enhanced life time with reduced QD diameter.[43,44] The comparison of these studies illustrates the challenges in understanding the fundamental aspects of recombination processes within QDs. The different observation are probably attributed to the different QD qualities used for the studies. Furthermore, it is well known that QDs contain many surface disorders due to their high surface-to-volume ratio.[41,45,46] Such disorders can result in surface trap states that act as nonradiative recombination center and influence the optical and electrical properties.

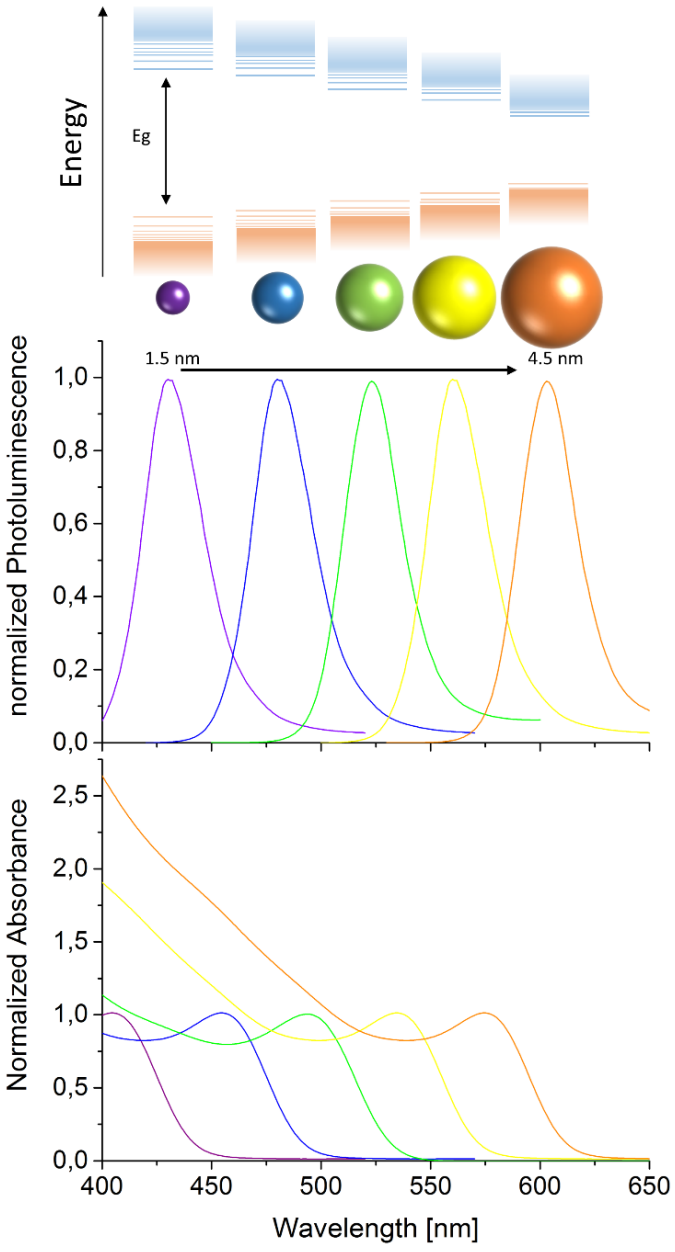

Figure 3. Schematic illustration of the energetic level and the corresponding fluorescence and absorbance spectra of five CdSe QD batches with different diameters between 1.5 and 4.5 nm.

Different strategies can be applied in order to passivate the QD surface and to reduce the formation of surface trap states. For instance stabilizing surface ligands (e.g. TOP and TOPO), which are usually used during QD synthesis, do not only support the nanoparticle growth and prevent particle aggregation, but also passivate free surface defects at the nanoparticle surface. Hartmann et al. have studied the influence of the dilution of surface ligands on TOP-capped CdSe QDs and found an increased fluorescence quenching rate after removal of surface ligands, which can be restored after addition of TOP ligands.[47] Another strategy to prevent surface defects is to grow a thin shell of a second semiconductor onto the QD core. These hybrid nanoparticles are called core-shell QDs. The most common core-shell QDs combine a large band gap semiconductor shell with a core material having a smaller band gap e.g. CdSe/ZnS, but also shell materials with a smaller band gap as compared to the core semiconductor have been reported e.g. ZnSe/CdSe.[48] The shell passivates the core and avoids the formation of free binding sites, resulting in an enhanced fluorescence.[49]

3.1.2.2 Nanowires

Semiconductor nanowires (NWs) are 1 D nanostructures with a diameter in the range of nanometers and an unconstrained length in the micrometer scale or even longer. NWs are typically composed of silicon, metal oxides such as TiO_2 and ZnO, and group III nitrides, including GaN and AlN. The NW synthesis can either be elaborated in a top-down approach via lithographic techniques, or in a bottom-up process via vapor-liquid-solid growth methods or solution-phase synthesis.[13] In analogy to QDs, also core-shell NWs have been synthesized and characterized. An additional covering with a second semiconductor material allows to control the surface defects, provides chemical passivation and prevents charge carrier recombination.[50]

Besides a large surface-to-volume ratio NWs provide an direct electron transfer in longitudinal direction, which facilitates a more efficient charge transfer than in nanoparticle films.[51] Moreover, the NW arrangement allows for light-trapping and scattering between the wires extending the traveling distance of the incident light within this structure and thus allows for more efficient light-harvesting. For instance, Cao et al. have shown that the capability of silicon to absorb solar radiation is increased by about 25%, if Si-NWs instead of a thin Si-film are applied.[52] Here, the absorbance properties of the NWs strongly depend on the NW diameter and the distance between the structures.

The InGaN NWs used in this thesis have so far been mainly studied in photonic applications for the construction of light emitting diodes (LEDs),[53] but also some solar cell or water splitting approaches have been reported.[54,55] The strong interest in using NWs of InGaN for photonic purposes can be explained by potential to tune the band gap and thus the emission wavelength of the material by adjusting the ration of InN and GaN

within the NWs. This theoretical allows to emit every wavelength between 3.51 eV[24] (band gap GaN) and 0.69 eV[56] (band gap InN) with a $In_xGa_{x-1}N$ alloy.

3.1.3 Organic semiconductors

Besides inorganic semiconductors also organic semiconductors have been investigated for their (photo-)electronic properties in respect to the construction of organic field effect transistors, light-emitting diodes and photovoltaic cells. These materials typical have delocalized π-electron systems, which can absorb light, and create and transport charge carriers.[57] The fundamental principle of charge carrier generation is based on the photoexcitation of delocalized π-electrons, which results in π- π* transitions, where the π-bonding orbital represents the highest occupied molecular orbital (HOMO) and the antibonding π* orbital is the lowest unoccupied molecular orbital (LUMO). In comparison to inorganic semiconductors the energetic states within organic semiconductors can be much more complex to calculate due to the absence of a three-dimensional crystal lattice, different intramolecular and intermolecular interactions, local structural disorders, amorphous and crystalline regions, and impurities.[58] These aspects have also strong implications on the charge transfer within organic semiconductors. While in highly ordered materials delocalized bands are formed, allowing a charge carrier transport in a band regime, disordering tends to localize the band states.[59] Thus, the charge carrier transport proceed in a hopping regime between the interacting molecules.[59] Intermolecular hopping processes are known to reduce the charge carrier mobility and are expected to limit the charge transport.[60,61] Therefore, the construction of highly ordered structures such as found in organic crystals has been the focus of recent studies in order to facilitate the propagation of charge carries within organic semiconductors.[62] So far, large number of different organic semiconductors have been reported, which can be divided into two classes according to their molecular weight. (1) Conjugated polycyclic compounds with a molecular weight below 1 kDa and (2) polyheterocycles with higher molecular weights.[63] Condensed aromatic systems such as anthracene, pentacene and perylene, metal-organic dyes such as phthalocyanines, porphyrins and ruthenium-complex containing dyes, heterocyclic oligomers such as oligothiophenes, and fullerenes belong to the first class of organic semiconductors. The second class is represented by conjugated polymers such as polythiophenes, polypyrrols and polyanilines.

Among the conjugated polymers, polyanilines (PANI) have attracted considerable interest due to the high environmental stability, low synthetic cost, and that the optical and electric properties can be controlled by oxidative doping, and doping with protonic acids.[21,64] Polyanilines are composed of alternatingly arranged units, which exist in the reduced state (benzoid) or in the oxidized state (quioid).[65] As illustrated in figure 4, PANI can exist in three oxidation states: fully reduced leucoemeraldine (LE) where y = 1, half oxidized emeraldine base (EB) where y = 0.5, and fully oxidized pernigraniline (PG)

where y = 0. EB is the most useful form of PANI due to its high stability at room temperature and the ability to become electrical conductive upon doping, while LE and PG are even after doping poor electrical conductors.[21,64] The electrical conductive state of EB is called emeraldine salt (ES). ES arises due to the protonation of the imine sites and is accompanied with the formation of a polaron, which ensures the charge transport within the polymer.[66] Besides doping with protonic acids, also the intrinsic doping via introduction of sulfonic acid groups into the PANI have been shown to be feasible.[67,68] This approach has some advantages over classical doping via acids, since on the one hand, the water solubility is significantly improved by the negatively charged sulfonic acid groups, and, on the other hand, conductivity can be provided in neutral and basic environments,[68,69] whereas unsubstituted PANI becomes insulating at a pH value above 4.[70]

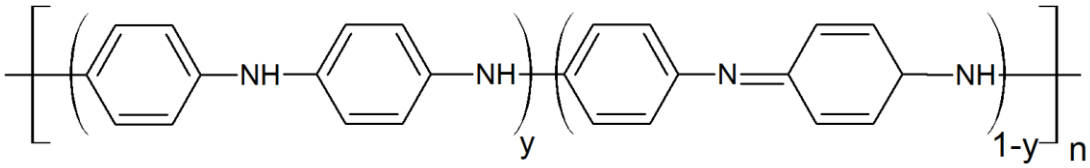

Figure 4. Chemical structure of polyaniline with different oxidation states: leucoemeraldine y =1, emeraldine base y = 0.5, pernigraniline y = 0, according to ref. [21].

3.1.4 Photosynthetic proteins

Another group of light-converting systems are photosynthetic proteins, which have found increasing interest during the last years for the construction of biosensors, solar-chemical producing systems and biophotovoltaic cells. In nature, photosynthetic proteins play a major role for the conversion of solar radiation in chemicals energy (photosynthesis) and can be found in plants, algae and photosynthetic bacteria.[7] While in plants, algae and cyanobacteria two photoactive proteins, i.e. photosystem 1 (PSI) and photosystem 2 (PSII), represent the light-harvesting components, in anoxygenic bacteria only one photoactive protein, i.e. bacteria reaction center (BRC), can be found.[71] Even if the structure of these photoactive proteins is different, the general principle of light-harvesting is the same and includes the light-induced charge carrier generation and the subsequent charge carrier separation. In detail photons are mainly absorbed by the light-harvesting complexes consisting of membrane proteins and photosynthetic pigments, which transfer the gained energy via FRET to the reaction center, where charge carrier separation takes place.[72] Here, small organic dyes such as chlorophyll a (PSI and PSII), bacteriochlorophyll and carotenoids (BRC) ensure the efficient exploitation of solar radiation. A peculiarity in comparison to semiconductors is that excited charge carriers are separated by an intramolecular electron transfer chain via several intrinsic redox centers, which reduces the unwanted charge carrier recombination.

PSII is the only known biological molecule, which is able to efficiently oxidize H_2O under illumination and therefore is an extensively studied subject.[73] However, the short-lived stability remains a big issue preventing its application in commercial water splitting systems. In contrast, PSI and BRC offer no catalytic activity, but serve primarily as an electron pump to lift electrons to a higher energetic state and deliver subsequent enzymatic reactions with electrons for the production of high energetic compounds.[74] Moreover, the better stability of PSI and BRC makes both photoactive proteins more promising for the application in light-converting systems than PSII.

3.2 Biohybrid light-converting electrodes for photobiocatalytic applications

The combination of photoactive materials with biological recognition elements such as antibodies, DNA, receptors, enzymes and cells has initiated new scientific research fields, which exploit the advantageous features of light-driven biohybrids in optical assays, biosensors, and in solar-to-current or solar-to-chemical converting systems.[15,16,75,17,76] These approaches are based on the optical, electrochemical and catalytic properties of photoactive materials.[16] The ability of photoactive materials to emit light have found application in optical assays allowing its use as label in binding assays for the parallel detection of different biomolecules.[6] Also electron transfer reactions between photoactive entities and electrodes can be established, which provides the basis for photoelectrochemical (PEC) systems. If such a PEC electrode is combined with a biological recognition element, the light-directed transduction of biological signals in PEC signals becomes feasible.[16] PEC transduction priniciples can be classified into two strategies, in which the photoactive entity is either used as light-switchable layer on electrodes or acts as a label for the analysis of recognition events.[16] The first strategy is based on the modulation of the photoelectrochemical signal in the presence of redox active molecules, allowing the determination of analyte concentrations. If additionally a recognition elements such as antibodies are attached to the photoactive layer of the PEC electrode, the analysis of binding events becomes feasible. As a result of target antigen binding the access of redox molecules to the photoactive layer is restricted and induces a changed photoelectrochemical signal allowing the label-free detection of binding events. Also a combination with redox enzymes is feasible, if electrons can be exchanged between the photoactive layer and the biocatalyst via redox molecules or direct electron transfer. The second strategy is typically based on a recognition element immobilized to an electrode and a target analyte, which is labeled with a photoactive entity. Upon binding, the photoactive entity is in close proximity to the electrode inducing the formation of a photoelectrochemical signal and thus enables the determination of the analyte.

In this chapter the focus is applied to PEC approaches, which combine the light-converting properties of photoactive entities with the biocatalytic features of enzymes. Moreover, photoactive materials with intrinsic catalytic activity towards several analytes will be introduced.

3.2.1 Functional principle and applications of PEC electrodes

PEC systems typically consist of an electrode, which is modified with a photoactive entity such as inorganic semiconductors, dyes or photoactive biomolecules. If the PEC electrode is excited with light, different electron transfer processes are activated, which can be divided in four main reactions: (1) charge carrier generation inside the photoactive material, (2) charge carrier separation via electron transfer between the light-sensitive entity and the electrode on the one hand and (3) between the photoactive entity and a redox active molecule in solution on the other hand, and (4) charge carrier recombination. For the generation of a photocurrent the separation of charge carriers should be the dominating processes, while the recombination pathways should be reduced. In figure 5, the basic principle of PEC electrodes is demonstrated. Under illumination and application of a positive potential an anodic photocurrent is induced, which is accompanied with an electron transfer from the conduction band of the photoactive entity to the electrode and the concomitant oxidation of a donor in solution. The cathodic photocurrent is favored under application of a negative bias leading to an electron flow from the electrode towards the excited photoactive material to an acceptor in solution. Besides the potential also the kind of photoactive material and the PEC electrode set up influences the direction of the photocurrent. It is crucial to adjust all electron transfer steps within such a signal cascade to each other in order to design efficient photobiocatalytic systems. Here, the electrode material, the energetic states within the photoactive material and the redox potential of the acceptor/donor play a major role ensuring efficient charge carrier transfer.[75]

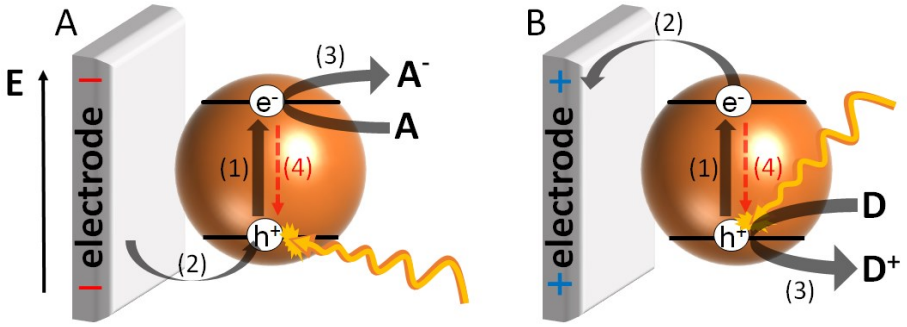

Figure 5. Light-initiated electron transfer processes at PEC electrodes, resulting in a generation of a cathodic **(A)** or an anodic photocurrent **(B)** upon illumination according to ref. [16]. The signal cascade includes: (1) charge carrier generation, (2) electron transfer between the photoactive entity and the electrode, (3) electron transfer between the photoactive entity and a donor D or acceptor molecule A in solution, and (4) charge carrier recombination.

The photocurrent represents a steady-state situation, where all electron transfer processes are in balance. If all conditions (e.g. potential, light intensity, pH etc.) are constant, the signal amplitude only depends on the concentration of acceptor and donor species in solution. This provides the basis for the determination of analytes by following the photocurrent of PEC electrodes. Therefore, either the catalytic activity for the oxidation or reduction of the analyte is provided by the photoactive entity itself or by combination with a catalyst or biocatalyst. Biocatalysts are often used due to their substrate specificity and high turnover rates. Several strategies have been developed for the transduction of a biocatalytic signal in a PEC signal, allowing the detection of enzyme inhibitors, phenolic compounds, sugars and nucleotides, or monitoring the enzyme activity (see chapter 3.2.4).

One advantage of PEC sensors compared to light-insensitive electrochemical systems can be seen in the separation of the analytical photocurrent signal from the background (dark) current, which can favor the signal-to-noise ratio and sensitivity.[17] Furthermore, light as trigger provides an additional tool to control electron transfer processes at electrodes extending the application range of electrochemical detection methods. Since the PEC signal chain is only switched on at the illuminated area, also multiplex analysis becomes feasible if different biocatalysts are immobilized spatially separated from each other on a PEC electrode (figure 6). By photoexcitation of the respective enzyme area with a spatial focused light beam the respective enzymatic substrates can be read-out individually.[16] Consequently, one PEC electrode could be used to detect several analytes by simply moving the light beam between the enzyme spots. The applicability of this concept has been recently demonstrated with a photocathode modified with three different antibodies, allowing the light-directed read-out of three different tumor markers with a laser.[77]

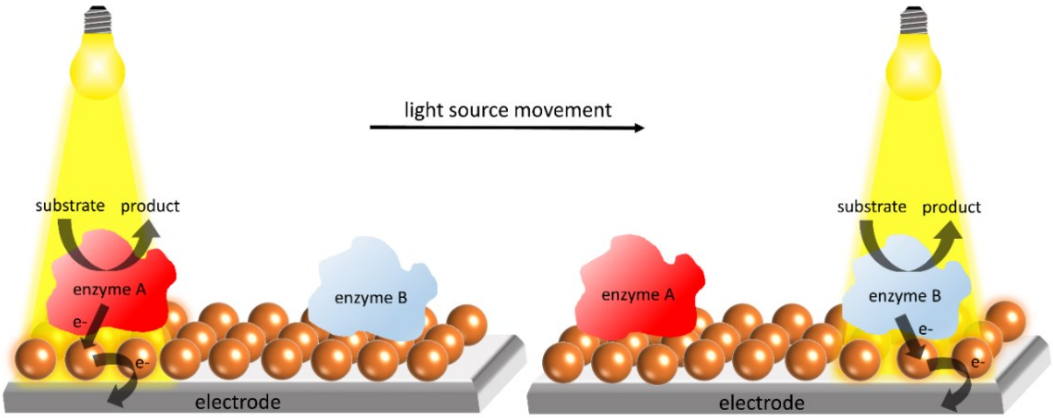

Figure 6. Schematic illustration of multiplex analysis with enzyme-modified PEC electrodes according to ref. [16]. The enzymes are immobilized spatially resolved on the electrode, and are read-out with a focused light beam, allowing the detection of the analyte.

Besides using light as reaction trigger, the energy gained during illumination can also improve the performance of biocatalytic electrodes. During photoexcitation high energetic states are generated, which modulate the potential behavior of the electrode.

While for light-insensitive electrodes the onset potential of a catalytic current is theoretically determined by the redox potential of the enzyme, PEC approaches can overcome this limitation. Here, electrons are not directly transferred between the electrode and the enzyme, but have to flow over the photoactive entity and thereby are lifted to higher energetic states under illumination. As schematically shown in figure 7, this can cause electrons to be subtracted from an oxidase and transferred to an electrode at more negative potentials. Conversely, PEC electrodes can also favor the electron transfer to reductases at more positive potentials. Consequently, the overpotential needed to drive the enzymatic reaction is decreased, which can improve the efficiency of biocatalytic reactions for the production of high energetic fuels or chemicals. Recently, first biophotocathodes harboring hydrogenases or carbon monoxide dehydrogenases have shown to generate H_2 and CO, respectively, under illumination at a reduced working potential compared to electrochemical approaches without photoexcitation.[78,79]

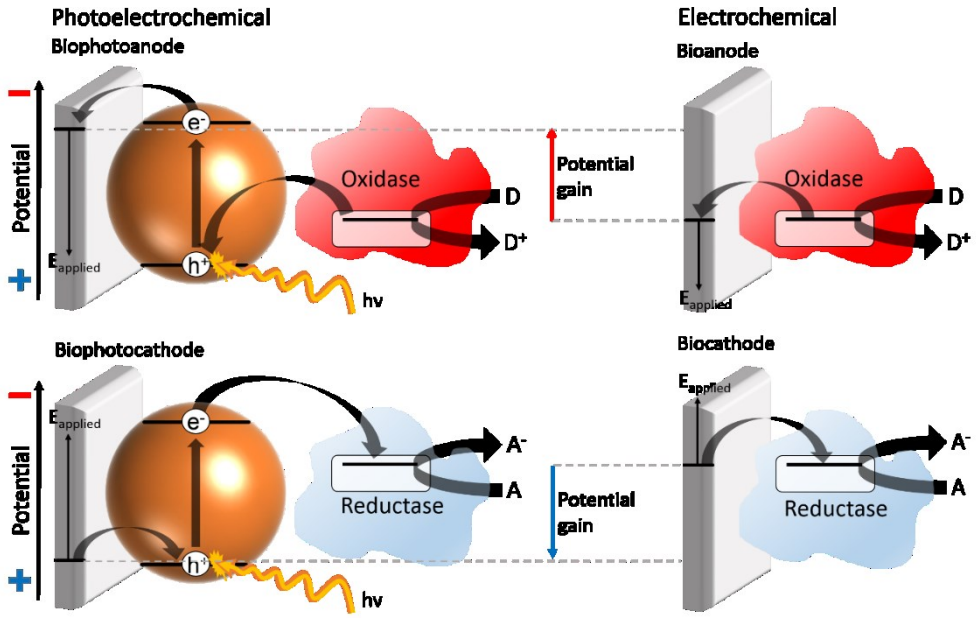

Figure 7. Schematic illustration of the electron transfer steps of PEC electrodes in combination with an enzyme compared to light-insensitive electrochemical electrodes. Biophotoanodes can promote an electron transfer from the enzyme to the electrode at more negative potentials due to photoexcitation as compared to the light-insensitive counterparts. In turn, biophotocathodes can induce an electron transfer from the electrode towards the photoactive entity to the enzyme at more positive potentials. Consequently, the overpotential needed to exchange electrons with the enzyme can be reduced with PEC approaches utilizing light energy.

In the future, biocatalytic PEC systems could also find application in biophotovoltaic devices for the generation of power from light energy combined with the enzymatic conversion of biomass. Such a PEC biofuel cell consists of an anode and a cathode, of which at least one electrode is light-sensitive and harbors the photoactive entity. If both electrodes are connected to each other, a voltage is gained and electrons flow from the anode to the cathode. This current can be used to power a load in an external circuit. Biophotanodes have been reported for the conversion of sugars under illumination, using

NAD-dependent glucose dehydrogenase (GDH) or glucose oxidase.[80–83] Although the principle can be successfully shown, these systems often fail in achieving low working potentials and high photocurrents, or integrating the enzyme functional into the photoanode. De la Garza et al. have constructed the first PEC biofuel cell by combination of a dye-sensitized photoanode with GDH in solution and an Hg/Hg_2SO_4 cathode in a two-compartment configuration.[80] Upon addition of glucose and NAD^+, the enzyme oxidizes glucose under concomitant reduction of NAD^+ to NADH. The generated NADH is subsequently oxidized at light-excited photoanode and electrons flow to the cathode, completing the circuit. This system achieves a cell voltage of 0.75 V and a current of 60 μA in the presence of glucose and under illumination.[80] If such a biophotoanode is linked to a cathode with an immobilized reductase the enzymatic reaction can be driven with light and without applying an external potential.[84] Consequently, only sun light and biofuels are needed to produce chemicals in a self-driven format. In this respect, also water-splitting photoanodes have been reported for driving cathodes hosting formate dehydrogenase or flavocytochrome c_3 reducing CO_2 to format or fumarate to succinate, respectively.[85,86]

However, irrespective of the application, the coupling of photoactive materials with biocatalysts on electrodes faces many challenges, which include:

(1) Achieving fast electron transfer between the electrode and the photoactive material

(2) Obtaining an efficient connection between the photoactive entity and the biocatalyst

(3) Preventing recombination pathways and side reactions

(4) Disturbing reactions with interfering molecules

(5) Stabilization of the photoactive material and the enzyme on the electrode

(6) Avoiding the needs for toxic light-harvesting materials

3.2.2 Strategies for the immobilization of light-sensitive entities

For the construction of biocatalytic PEC electrodes initially the photoactive entity needs to be attached to an electrode. Several immobilization strategies have been developed depending on the properties of the light-sensitive element, e.g. material composition and surface functionalities. Particularly, inorganic semiconductor nanostructures including QDs consisting of CdS,[87–90] CdSe,[91] CdTe,[92–94] CdS/ZnS,[95] CdSe/ZnS[96,81,97,98] and AgS,[99] and nanoparticle, nanowires and nanoporous films from different materials have found application in PEC systems.[100–102] Furthermore, semiconductor hybrids, which typically combine a large band gap semiconductor, e.g. TiO_2, SnO_2 and WO_3, with a small band

gap semiconductor nanoparticle or a dye have been reported for the construction of PEC systems.[80,103,104] Organic semiconductors such as ruthenium complex dyes,[82] porphyrins,[80] phthalocyanins,[105] flavins[106] and polythiophenes[107] represent another group of applied photoactive entities. Recently, also photosystem 1 has been integrated into light-driven biocatalytic systems.[83,108,109]

Semiconductor-based PEC electrodes rely on the synthesis of the nanostructure in a bottom-up or top-down process. Therefore, the nanostructure can either be directly grown on the electrode or is synthesized in solution and subsequently immobilized on the electrode. For instance semiconductor NWs are often directly grown on substrates via chemical vapor deposition, molecular beam epitaxy processes or hydrothermal methods.[13,102] Also the growth of QDs on electrodes has been followed by applying electrodeposition[110–112] or a successive ionic layer adsorption and reaction method.[113] These approaches provide the advantage of a direct contact between the photoactive material and the electrode without any spacing, avoiding the needs for further immobilization steps, which improves the reproducibility for the construction of PEC electrodes. However, the quality of the nanostructure, i.e. size distribution, surface defects etc., can be an issue, especially if small QDs are synthesized.[114] Therefore, QDs are mainly synthesized by self-assembly in organic solution in the presence of nonpolar capping ligands like trioctylphophine oxide.[115] This procedure results in monodisperse nanoparticle with pronounced optical properties, however, the organic capping ligands impede the reproducible immobilization to electrode surfaces and reduce the electron transfer ability with electrodes and enzymes.[96,116,117] To overcome this limitation a displacement of the organic ligands with other bifunctional molecules acting as linker between the QD and the electrode can be beneficial. The ligand exchange of the QDs can either be performed in solution or the linker molecule is first fixed to the electrode followed by the attachment of the nanoparticle to the premodified electrode surface via a partial displacement of the organic ligands.

The linker molecule have to provide at least two functional groups, of which one binds the QD and the second is attached to the electrode surface. While mainly thiols are applied for anchoring to the QD surface, the second functional group depends on the electrode material and the surface modification. Dithiol and dithiane compounds such as 1,6-hexandithiol, benzenedithiol and stilbenedithiol are often applied for the immobilization of QDs to gold electrodes.[118,119] Here, the quality of the interfacial dithiol films is fundamental for the stable fixation of a high amount of QDs on the electrode.[119] Furthermore, the linker length and composition (aliphatic or aromatic) influences the electron tunneling rate and the concomitant PEC performance.[118,116]

Thiols with a carboxyl-head group represent another group of linker molecules, which have found application for the fixation of QDs to electrodes. Here, the electrostatic attraction to positively charged surfaces,[120] covalent binding to amino group-modified electrodes[94] or complex coordination at metal oxide surfaces[117,121] can be exploited. For

instance, thioglycolic acid-functionalized CdTe QDs have been covalently coupled via carbodiimides to ITO electrodes modified with (3-aminopropyl)triethoxysilane, resulting in the generation of stable photocurrents.[94]

Dyes can either be extracted from natural sources or are synthesized in solution under controlled conditions. The latter offers the opportunity to adjust the chemical properties of the dye to the used electrode material. Dyes with several functional groups can be synthesized, including e.g. carboxylic acids, sulfonic acids, phosphonic acids, salicylic acids, pyridines, tetracyanate or catechols, allowing a versatile use of dyes on various electrode materials.[122] For instance, Tu et al. have coupled an iron-containing porphyrin with sulfonate functionalities directly to TiO_2 nanoparticles supported by the strong attraction between the sulfonic acid group and the metal oxide surface.[123] In this case the dyes binding group react with the surface hydroxyl groups of the metal oxide, establishing a reversible binding with high equilibrium binding constants.[124] Moreover, the conjugated π-system of dyes allow for the immobilization to reduced graphene oxide and CNTs via π-π-stacking interaction.[105,106]

Several immobilization strategies have been reported for the integration of photoactive proteins. The most approaches exploit the surface exposed charge-bearing amino acids for the electrostatic[125] or covalent binding[126,127] to electrodes. In another approach, the reconstitution of PSI to surface fixed vitamin K acting as molecular wire has been reported.[128] Moreover, the electrochemical communication between PSI and electrodes has been established via redox active compounds such as pyrroloquinoline quinone covalently bound to gold surfaces,[129] redox polymers[108] or the redox protein cyt *c*.[130]

Although various strategies for the efficient coupling of photoactive entities to electrodes have been developed, the amount of immobilized photoactive entities is often restricted to a monolayer limiting the overall photocurrent output. In order to enhance the number of photoactive entities different concepts have been elaborated, which include the construction of multilayers, the embedment within redox active matrices and the construction of 3D electrodes. For instance, it could be shown, that dithiols cannot only be used for the deposition of a single QD monolayer, but also enable the construction of multilayer arrangements by alternately incubation in dithiol and QD solutions.[131,132] These architectures give rise to amplified photocurrents, since electron transfer between the individual QD layers is found to be feasible and thus also charge carriers from the outer QD layers can be exchanged with the electrode. Göbel et al. have exploited the electrostatic attraction between negatively charged QDs and positively charged polyelectrolytes for the construction of QD multilayers by a layer-by-layer assembly approach, showing a 5-fold amplification of the photocurrent by comparing an electrode with five QD/polyelectrolyte bilayer with a monolayer electrode.[120] However, in some cases electrons cannot be transferred efficiently between the individual photoactive entity layers, which is why redox active molecules needs to be integrated into the multilayer arrangements to establish connectivity. Stieger et al. have applied cyt *c* for the wiring of

PSI integrated in (PSI:cyt c)/DNA multilayers.[133] Here, cyt *c* allows for electrode/cyt c electron transfer, intermolecular cyt *c*/cyt *c* electron self-exchange and cyt *c*/PSI electron transfer, resulting in a electron transport from the electrode towards the redox protein to PSI under generation of a cathodic photocurrent. In another study, PSI has been embedded into a matrix consisting of a redox polymer and crosslinking reagents, ensuring the efficient communication of a high amount of PSI molecules with the electrode via the redox-active moieties of the polymer.[134]

A further strategy to increase the amount of immobilized photoactive entities and thus to enhance the PEC performance is directed to the enlargement of the electrode surface area by the construction of 3D architectures. Often metal oxide nanoparticles are applied, which are firstly deposited on the electrode and subsequently sintered to compact and solid nanostructured films. For instance, nanostructured 3D TiO_2 architectures are widely used as substrates in solar cell approaches for the integration of high amounts of QDs and dyes, resulting in high photocurrents and low working potentials.[1,12] Also nanoparticular ITO electrodes have been exploited in combination with photoactive proteins to enhance the light-to-current conversion efficiency.[135–137] Here, special attention has been devoted to the construction of 3D ITO electrodes with an inverse opal structure. These architectures have macroscopic pores, which provide a beneficial morphology for the assembly of PSI and PSII.[109,136–138]

3.2.3 Photoactive materials with catalytic activity

Several studies have demonstrated the potential of photoactive materials for the oxidation and reduction of molecules. Such photoactive materials can either have an intrinsic catalytic activity or the activity is introduced by the combination with a second catalytic component. The direction of the reaction is determined by the electronic states of the photocatalyst and the redox potential of the molecule, and thus can be adjusted to each other by e.g. the choice of the photoactive material.

Hydrogen peroxide is an important biological analyte, which has triggered the interest for the construction of photoelectrochemical systems allowing the detection of this molecule. While electrodes modified with FePt nanoparticle decorated QDs,[119] gold nanoclusters[139] and NiO/BiOI[140] have shown a light-directed reduction of hydrogen peroxide, Pt/NiOOH-modified n-silicon,[141] TiO_2 nanowires,[102] WO_3 decorated core–shell TiC/C nanofibers[142] and nanoporous $BiVO_4$ films[143] have been found to catalyze the hydrogen peroxide oxidation. For example, Khalid et al. have explored the suitability of CdS QD electrodes for the photoelectrochemical detection of hydrogen peroxide.[119] However, since these QDs reveal no photocatalytic activity a further modification with FePt nanoparticles was found to be necessary to achieve H_2O_2 reduction and to provide sensitivities in the range between 1 and 30 µM.[119]

Thiols represent another group of analytes, which have been extensively investigated in various photoelectrochemical approaches. Pardo-Yissar et al. have reported a photoelectrochemical sensor allowing the detection of thiocholine via CdS QD-modified gold electrodes.[87] Also the amino acid cysteine has been investigated with various photoelectrochemical systems, e.g. methylviologen-modified QD electrodes,[144] protoporphyrin IX-functionalized WO_3-reduced graphene oxide ITO electrodes[103] and polythiophene-sensitized TiO_2 electrodes.[107] For all systems a rather similar detection range in the lower micro molar range has been evaluated. In another study glutathione has been analyzed at ITO electrodes modified with porphyrin-functionalized-TiO_2 nanoparticles allowing the oxidation in the range between 50 µM and 2.4 mM glutathione.[123] A further sensitivity improvement has been achieved with graphene-CdS nanocomposites showing a first signal response at 3 µM glutathione.[145] Also carbon dots have been evaluated for its photocatalytic activity towards the oxidation of glutathione.[146] Here, hybrid materials consisting of carbon dots and mesoporous silca exhibits the best sensing performance, achieving a lower limit of detection of 6.2 nM.[146]

Furthermore, bivalent cations such as Cu^{2+} [147–152,104] and Hg^{2+} [153,154] have been analyzed with light-driven systems. All systems share a rather similar electrode setup, i.e. CdS, CdTe or ZnS QDs are attached to an electrode, and the same detection mechanism, which is based on the formation of metal ion compounds on the QD surface (e.g. Cu_xS or Hg_xS). This results in an insertion of an exciton trapping site and a decrease of the photocurrent. Interestingly, these approaches are rather selective towards other interfering cations such as Mg^{2+}, Zn^{2+}, Ba^{2+}, Mn^{2+}, Na^+ and K^+.[147,149]

Photoelectrochemical electrodes have also been applied for the detection of phenolic compounds such as p-aminophenol,[155] p-phenyldiamine,[156] 4-nitrophenolate,[157] amoxicillin,[158] hydroquinone[158,159] and dopamine.[160–166] These approaches are mainly based on the direct oxidation of the phenolic compound and the concomitant generation of an anodic photocurrent. For example, Khalid et al. have exploited CdS QD-modified gold electrodes for the oxidation of p-aminophenol in the range between 25 µM and 1.5 mM p-aminophenol.[155] Besides CdS QDs several other photoactive materials have shown photocatalytic activity towards phenolic compounds such as nanostructured MoS_2[165] and WO_3 films,[163] TiO_2 nanotube photonic crystals,[166] TiO_2 nanostructures sensitized with graphene QDs,[161] g-C_3N_4 decorated graphene sheets,[162] and iron phthalocyanins.[164]

The enzymatic co-factor NADH is another interesting analyte, which has been analyzed with various photoelectrochemical systems. Here, a distinction can be made between systems which are of pure photoelectrochemical origin and oxidize NADH only during illumination,[80,167,81,168] and systems which already show a NADH-dependent current in the dark that is amplified upon illumination.[169–174,112,175] For the later systems it is often not clear whether the photoactive material is actually involved in the NADH oxidation, which complicates the understanding of electron transfer pathways. Moreover, these

systems often rely on the application of high overpotentials to ensure the NADH oxidation.[112,169,173] Exclusive light-driven systems have been reported for porphyrin sensitized SnO_2 electrodes,[80] dopamine sensitized TiO_2 electrodes,[167] and CdSe/ZnS QD-[81] or diaminodicyanoquinodimethane derivative-modified gold electrodes.[168] Besides using light-driven processes for the oxidation of NADH also the regeneration (i.e. reduction) of NAD^+ to NADH has been demonstrated for some photoactive materials.[176–179]

Photoactive materials have also found application for the enzyme-free detection of glucose. A broad range of different materials have been reported to oxidize glucose under illumination such as hydrogenated TiO_2 nanotubes,[180] NiO-based systems,[181,182] graphene CdS QD hybrids,[183] cubic CuO,[184] C_3N_4-modified WO_3,[185] bismuthoxychloride-graphene nanosheets,[186] gold nanorod sensitized TiO_2[187] and Pt nanoparticle-modified ZnO nanowires.[188] Such light-driven systems achieve high anodic photocurrents and provide sufficient sensitivities for a potential analysis of glucose in physiological samples. However, to promote the glucose oxidation often alkaline conditions have to be applied, which limits the sensor applicability.[189,190] Also the selectivity towards other sugars e.g. fructose and lactose remains challenging.[190]

Other photoelectrochemical systems have been reported for the detection of nitrite,[191] sulfide,[192] arecoline,[193] hexavalent chromium,[194,195] nucleotides such as AMP,[196] polychlorinated biphenyls,[197] pesticides such as dichlofenthion[198] and chlopyrifos,[199,200] and antioxidants such as ascorbic acid,[201,202,101,203] caffeic acid,[203] gallic acid[203,204] and folic acid.[205]

3.2.4 Strategies for connecting enzymes to photoactive materials

In recent years, a large number of different approaches have been developed for the electronic linkage of biocatalysts to photoactive materials. While initial attempts have concentrated on interaction studies in solution, the transfer of these solution-based systems to electrodes is more and more in focus. All of these approaches are based on three fundamental strategies: (1) detection of enzymatic co-substrates or products, (2) mediator-based electron transfer, and (3) direct electron transfer (DET). The first strategy relies on the coupling of an enzyme to a photoactive material, which is able to oxidize/reduce the corresponding enzymatic co-substrate or product. This approach is often easy to implement, but has also some limitations. Since the co-substrate or products are freely diffusing in solution the efficient communication between the enzyme and the photoactive material can be an issue. Also some co-substrates needed for the connection of the enzyme to the light-sensitive electrode are rather expensive. The second strategy is based on small redox molecules, which shuttle electrons from the enzyme to the light-sensitive entity or vice versa. The electron transfer can be achieved similar to the previous strategy via diffusible molecules or with mediators immobilized between the enzyme and

the photoactive material. The third strategy describes the direct exchange of electrons between the electroactive prosthetic group of the enzyme and the photoactive material. Thus, this approach pass over the needs for mediating molecules. However, DET can be difficult to achieve due to the random orientation of the enzyme on surfaces and/or too long electron transfer distances, hindering a fast enzyme/photoactive entity communication. Therefore, the material and surface modification of the light-sensitive entity needs to be carefully evaluated and adjusted to the enzyme properties.

3.2.4.1 Communication via enzymatic substrates or products

In three studies acetylcholine esterase has been attached to CdS QD-modified gold electrodes,[87] CdSe/ZnS QD graphene nanocomposites coated ITO electrodes[206] or Au-doped TiO_2 nanotubes[100] for the analysis of enzyme inhibitors. The enzyme catalyzes the conversion of acetylthiocholine to thiocholine, which is oxidized at the photoanode giving access to the evaluation of the enzyme activity and thus to the presence of inhibitors such as endogenous neurotoxins and organophosphorus pesticides.[100,206] In a very different approach, the inhibition of acetylcholine esterase has been analyzed via an enzyme-controlled synthesis of QDs on ITO electrodes.[207] Enzymatically generated thiocholine favors the deposition of CdS QDs in the presence of Cd^{2+} and S^{2-} ions and thus determines the photocurrent amplitude.[207] If an inhibitor is added the synthesis of QDs is disturbed due to the absence of thiocholine and the photocurrent is decreased. In a similar approach alkaline phosphatase (ALP) has been used for the catalysis of thiophosphate to hydrogen sulfide, resulting in a growth of CdS QDs in the presence of Cd^{2+} and the formation of a photoelectrochemical signal.[90] Zhao et al. have reported another photoelectrochemical inhibition assay based on ALP attached to TiO_2 nanoparticle-modified ITO electrodes.[101] The principle is based on the enzymatic conversion of ascorbic acid 2-phosphate to ascorbic acid, which interacts with the TiO_2 surface and results in an extension of the visible light excitation range giving access to an amplified photocurrent signal.[101] In another study, the catalytic activity of CdS QDs towards p-aminphenol for the combination with ALP is demonstrated to enable the detection of the p-aminophenylphosphate.[155]

Also glucose oxidase (GOx) has been integrated into several photoelectrochemical systems for the detection of glucose. One strategy is based on the oxygen sensitivity of photoactive materials, creating a competitive situation with GOx for oxygen in the presence of glucose. In a first study GOx has been immobilized onto CdSe/ZnS QD-modified gold electrodes via crosslinking compounds.[97] However, due to the rather small glucose detection range found, subsequently a layer-by-layer approach with polyelectrolytes and GOx has been studied enabling a better control of the amount of deposited enzyme.[97] If glucose is added, the oxygen-dependent part of the cathodic photocurrent starts to decrease allowing detection of glucose in the range between 0.1 and

5 mM.[97] Follow-up studies with CdTe,[92] CdS,[208] Ag_2S[99] or PbS[209] QD-modified electrodes have also exploited this concept for the combination with GOx and the detection of glucose reaching similar sensitivities. The universal applicability of this concept to other oxygen consuming enzymes has been demonstrated for sarcosine oxidase and the detection of sarcosine.[98]

The light-driven reduction of oxygen to reactive oxygen species e.g. superoxide and hydrogen peroxide has also been coupled to peroxygenases for the hydroxylation of chemicals.[210,211,106] Two studies have applied light-excited CdS QDs[210] or flavins[211] for the production of reactive oxygen species driving cytochrome P450 peroxygenases $P450_{Bs\beta}$ for myristic acid hydroxylation in solution. In another approach flavin has been attached to single-walled carbon nanotubes via π-π-stacking for the construction of a photoelectrochemical hydrogen peroxide generation platform supplying a heme-thiolate peroxygenase with hydrogen peroxide for the stereospecific conversion of ethylbenzene to (R)-1-phenylethanol.[106]

Another strategy is based on the photoelectrochemical detection of hydrogen peroxide produced by GOx. In chapter 3.2.3, various photoactive electrodes for the oxidation and reduction of hydrogen peroxide have been presented, but only a few have been applied for the combination with GOx.[102,139,140] For instance, Zhang et al. have followed the glucose turnover of GOx in solution with gold nanocluster-modified gold electrodes, giving a concentration-dependent cathodic photocurrent from 0.5 and 4 mM glucose.[139] Another approach demonstrated the covalent binding of GOx to aminosilane-modified TiO_2 nanowires reaching high anodic glucose-dependent photocurrents and a sufficient selectivity against common interfering compounds, but provides only a limited concentration range between 0.1 and 1 mM glucose.[102]

NAD-dependent glucose dehydrogenase (GDH) is a further glucose converting enzyme, which has found application in combination with various NADH-oxidizing photoanodes.[80,81,168,169,172,174,112,175] While first approaches have measured the glucose concentration with GDH and NAD^+ in solution,[80,81] other approaches have fixed the enzyme to the electrode via simple adsorption[169] or covalent binding with crosslinking reagents.[112,168,171,172,174,175] Metzger et al. have even integrated NAD^+ within a crosslinked GDH network on top of a photoactive electrode, which provides sensitivities in the higher molar range up to 300 mM glucose and pass over the needs for the addition of the expensive co-factor to the solution.[168] However, since the cofactor has to diffuse between the enzyme and the photoactive material to ensure conductivity also a leakage of NAD^+ from this network can be an issue for the system stability.

Furthermore, a photoelectrochemical multi-enzyme assay has been reported on the basis of NADH-sensitivity of CdS/ZnS QD-modified gold electrodes for the detection of guanosine monophosphate (GMP).[95] Therefore, guanylate kinase, pyruvate kinase and lactate dehydrogenase have been immobilized onto the electrode in a layer-by-layer

format with polyelectrolytes. GMP triggers an enzymatic signal cascade resulting finally in a consumption of NADH, which can be detected by a decline of the anodic photocurrent.[95] This principle allows the detection of GMP in the range between 0.05 and 1 mM GMP.

Several studies have exploited the photochemical regeneration of NAD^+ to NADH in solution for the production of methanol from CO_2 via the sequential reaction of three NAD-dependent enzymes, i.e. formate dehydrogenase, formaldehyde dehydrogenase and alcohol dehydrogenase.[176,177,212,178,213] This principle has also been applied for the regeneration of NADPH via the photosensitizer eosin Y supplying cytochrome P450 monooxygenases with reaction equivalents for the hydroxylation of chemicals.[179] Further examples following this approach have been found for the production of formic acid[214] and glutamate.[215,216]

3.2.4.2 Mediator-based systems

Only a few examples have shown the successful communication between enzymes and photoactive materials via mediators, and most of them have only been realized in solution. For example, methylviologen (MV) has been used as surrogate for the enzymatic co-factor NADH, transferring electrons from CdSe QDs to an old yellow enzyme homologue YqjM* for the reduction of ketoisophorone.[218] In a similar study two other old yellow enzymes have been electrically connected to an ruthenium complex-containing dye via MV in solution.[219] Also flavins such as FMN and FAD have been applied as mediators for the construction of photobiocatalyic systems in solution with an old yellow enzyme and a Baeyer-Villiger monooxygenase for the transformation of chemicals.[220,221] A photoelectrochemical approach with a p-type indium phosphide photocathode, a formate dehydrogenase, and MV in solution has demonstrated a electron transfer from the electrode to the enzyme via MV allowing the fixation of CO_2 and the production of formate.[222]

Recently, Efrati et al. have reported a new strategy for the connection of enzymatic reactions to photosystem 1 functionalized electrodes.[83] Instead of using free diffusing mediators a redox polymer has been assembled on top of a PSI-modified electrode, providing the electronic relay for the subsequently immobilized GOx.[83] In detail, electrons are transferred upon addition of glucose from the enzyme towards the redox polymer to PSI and are finally injected into the electrode under illumination. The system shows an anodic glucose-dependent response, however, the photocurrent amplitude is found to be rather modest, which is may be attributed to the short circuit found between the redox polymer and ITO electrode. The big advantage compared to previous reported

* The family of old yellow enzymes belongs to the NADPH oxidoreductases, which contain a flavin mononucleotide as prosthetic group and catalyze the asymmetric hydrogenation of C=C double bonds.[217]

mediator-based systems can be seen in the functional immobilization of all components, i.e. the photoactive entity, the enzyme and the mediator, on the electrode.

In a similar approach two different redox polymers have been applied to connect PSI with the electrode, on the one hand, and to mediate electrons between PSI and a hydrogenase on the other hand.[108] By applying a potential, electrons are initially transferred from the electrode towards a osmium complex-containing redox polymer to PSI. Upon illumination charge carriers are generated within PSI, resulting in the reduction of a cobaltocene-functionalized redox polymer. Subsequently, the electrons are further transferred to the hydrogenase, which reduces $2H^+$ to H_2 at a rather high onset potential of +0.38 V vs. SHE.[108]

3.2.4.3 Direct protein electrochemistry

During the last years, establishing direct protein electrochemistry with photoactive materials has become a great aim for the fabrication of efficient light-driven biohybrid systems, passing over the needs for co-substrates and mediators.

First studies have focused on the integration of small heme-containing redox proteins into photoactive assemblies. Stoll et al. have analyzed the DET of the redox protein cytochrome *c* in solution with CdSe/ZnS QDs-modified gold electrodes and found that the surface properties of the nanoparticle play a crucial role in order to achieve an efficient electron transfer.[96] Only after exchange of the hydrophobic surface ligands by mercaptopropionic acid or meracptosuccinic acid a QD-protein communication could be established.[96] The photocurrent amplitude and direction is found to depend on the applied potential, and the redox state and concentration of cyt *c*. In a follow-up study, the catalytic activity of cyt *c* towards superoxide has been exploited with the QD/cyt *c* system for the construction of a light-triggered radical sensor.[91] Also nitrate reductase and lactate dehydrogenase have been coupled to a QD/cyt *c* system giving access to the light-driven detection of nitrate and lactate, respectively.[88] The principle is based on the ability of cyt *c* to exchange electrons between the QDs and the enzymes. In this respect cyt *c* has also been used to connect PSI to gold[130] and ITO electrodes,[136] resulting in a generation of a cathodic photocurrent. Based on these systems sulfite oxidase (SOx) has been additionally integrated into PSI/cyt *c* photocathodes for the construction of a light-driven sulfite sensor.[109] The principle is based on a competitive situation between the electrode and SOx for supplying PSI with electrons, resulting in a suppression of the cathodic photocurrents if sulfite is present.[109] Recently, it has even been shown that cyt *c* itself can trigger a photocurrent under illumination if the heme group is substituted with tin and the protein is sandwiched between Au and Hg electrodes.[223] This may provide a basis for future cyt *c*-based photoelectrochemical sensors that are not dependent on additional photoactive materials.

Besides using redox proteins also heme-containing enzymes have been coupled to photoactive materials via direct protein electrochemistry. For instance, Soares et al. have exploited photoactivated methylene blue as reducing agent for horseradish peroxidase (HRP) in solution.[224] Also by immobilizing HRP on Pt-doped α-Fe_2O_3 thin film gold electrodes a light-directed direct electron transfer from the enzyme to the electrode has been achieved.[225]

In another report, ITO electrodes modified with polyethylenimine functionalized CdS QDs have demonstrated direct protein electrochemistry with SOx, showing an amplified sulfite-dependent current if the electrode is illuminated.[89] However, since already in the dark catalytic currents have been observed, probably a different electron transfer way is switched on under illumination.

Several groups have also reported on the DET of cytochrome P450 enzymes with different photoactive materials,[226,94,227,105,93,228] however, a clear evaluation of the mechanism remains difficult due to feasible intermediate reaction pathways with photoelectrochemical produced reactive oxygen species. One group developed hybrid P450 BM3 heme domains containing a covalently attached Ru(II) photosensitizer for the light-driven hydroxylation of lauric acid in solution.[226] Other studies have postulated direct protein electrochemistry of different P450 enzymes covalently coupled to CdTe QD-modified electrodes[93,94,227] and dye-sensitized macroporous silica electrodes.[105] Even if the clear reaction pathway is not fully understood, for all approaches metabolized products could be detected after the light-driven reaction.

Also flavin-based redox centers of enzymes have been used to establish light-triggered DET. One system has been reported for biohybrid complexes consisting of ferredoxin NADP-reductase attached to mercaptopropionic acid-modified CdSe QDs in solution.[229] Under illumination electrons are transferred from the QD to the enzyme leading to the reduction of $NADP^+$ to NADPH.[229] This light-driven NADPH regeneration system was further combined with alcohol dehydrogenase for the conversion of aldehydes into alcohols.[229] Another study has shown the photoreduction of enoate reductase via the photosensitizer rose bengal for the stereoselective hydrogenation of C=C bonds in solution.[230] Furthermore, an electrode-based system with immobilized CdS QDs has achieved the DET with formaldehyde dehydrogenase catalyzing the light-driven formaldehyde oxidation.[231] Tel-Vered et al. have covalently attached GOx to functionalized gold electrodes and subsequently modified the enzymes with a Ru(II) photosensitizer.[82] If glucose is added to the solution, electrons are transferred from the enzyme towards the light-excited photosensitizer and subsequently to the electrode, resulting in a generation of a anodic photocurrent.[82] This biohybid photoanode shows a concentration-dependent signal behavior up to a concentration of 70 mM glucose, but the photocurrent magnitude is found to be rather modest.[82]

Copper-containing enzymes such as laccases have also been extensively studied for their ability to transfer electrons with photoactive materials.[232–238] Four studies share a rather similar concept and have applied ruthenium complex-containing dyes,[232,236,237] porphyrins[234] or carbon dots[235] for supplying laccase with electrons triggering the light-driven oxygen reduction to water in solution. Another approach has reported on the construction of a biohybrid photocathode by immobilization of laccase on p-type silicon.[233] However, unfortunately no improvement of the onset potential of the biocatalytic oxygen reduction could be achieved under illumination.

There are also reports on laccase, which describe the reversal of the biocatalytic reaction, i.e. the electrooxidation of H_2O to molecular oxygen.[238,239] Tapia et al. have modified FTO-In_2S_3 photoanodes with laccase, which enables the light-induced laccase-catalyzed oxidation of water.[238] The onset potential of this light-directed process is +0.8 V vs. SHE, which is at least 0.4 V lower than compared to a light-insensitive approach with a laccase-modified graphite electrode.[238,239] This demonstrates the advantage of photoelectrochemical strategies for the reduction of the overpotential of biocatalytic reactions.

Much attention has also been drawn to the connection of hydrogenases to photoactive elements due to their interesting ability to produce H_2. A electrochemical approach with immobilized enzyme on CdS-modified electrodes have demonstrated DET, showing pronounced catalytic currents in the dark, which are amplified under illumination.[240] Moreover, a small shift in the onset potential to higher potentials is found for the biocatalytic H^+ reduction. In another study, hydrogenases have been integrated into a TiO_2-coated p-Si photocathode, displaying the visible light-driven production of H_2.[79] Also several approaches with photoactive entities and hydrogenase in solution have been reported. For example, TiO_2 nanoparticles modified with ruthenium-containing dyes or carbon nitride, where electrons are injected from the photosensitizer into the TiO_2 conduction band and subsequently to the enzyme, have been used for supplying the enzyme with electrons.[241,242] Also the direct electron transfer from photosensitizers such as CdS nanorods,[243] carbon dots,[244] polymeric carbon nitride,[245] eosin Y[246] or photosystem 1[247,248] to hydrogenases have been shown to be feasible in solution.

Another biophotocathode have been reported for a porous semiconducting NiO electrode modified with a dye harboring carbon monoxide dehydrogenase for the light-driven reduction of CO_2 to CO.[78] Here, the onset potential of the CO_2 reduction is shifted about 0.2 V in the positive direction under illumination in comparison to the reaction in the dark.[78] Furthermore, some approaches with carbon monoxide dehydrogenase in combination with ruthenium complex-modified TiO_2 nanoparticles[249,250] or with CdS nanocrystals[251] have shown the light-driven CO_2 conversion in solution.

Recently, also nitrogenase/CdS nanorod biohybrids have shown the ability to supply the enzyme with electrons under illumination for the conversion of N_2 into NH_3 in solution.[252]

The great number of reports studying the interaction between photoactive entities and enzymes displays the great interest in combining light-converting properties with biocatalytic features for sensing, power-supply and the production of chemicals. However, it can be stated that the full potential of this biohybrid approach has not yet been fully exploited, as it often still requires high overpotentials to exchange electrons between the photoactive element and the enzyme. Furthermore, so far many of the presented approaches operate only successful in solution, so that more work is necessary for the functional implementation of these systems on electrodes.

3.3 Enzymes

3.3.1 PQQ glucose dehydrogenase

The water-soluble PQQ glucose dehydrogenase (PQQ-GDH) belongs to the group of quinone-dependent dehydrogenases and is found in the cytoplasm of *Acinetobacter calcoaceticus*. The pI is 9.5 and the pH optimum has been determined to be 7.0.[253,254] As illustrated in figure 8, PQQ-GDH is a dimeric redox enzyme, consisting of two identical subunits with a molecular weight of about 50 kDa each.[253] One pyrroloquinoline quinone (PQQ) and three calcium ions (Ca^{2+}) are non-covalently bound to each monomer.[253,255] While two Ca^{2+} ions are located in the dimer interface and are needed for the functional dimerization, the third Ca^{2+} ion binds to the active site of the enzyme and is required for the activation of the co-factor.[256] The enzyme catalyzes the oxidation of monosaccharides such as glucose, allose, as well as disaccharides, such as lactose and maltose to the corresponding lactones leading to a reduction of PQQ to $PQQH_2$.[254,257]

The high activity and oxygen insensitivity makes the enzyme to a promising candidate for the construction of glucose biosensors and biofuel cells, however, the substrate specificity and stability can be an issue for a reliable glucose detection.[258] Therefore, great efforts have been put in protein engineering studies for improving the enzyme stability and specificity.[259–262] For instance, it could be shown that mutations in the PQQ binding pocket can greatly reduce the activity for allose, lactose, and maltose.[263]

The natural electron acceptor of soluble PQQ-GDH is unknown, however several artificial mediators have shown to undergo electron transfer with the enzyme. Based on these findings enzyme electrodes have been reported allowing glucose detection if combined with phenolic and heterocyclic compounds,[264–266] PQQ,[267] prussian blue,[268] ferrocenes[269–271] and redox polymers.[272–274] Also a connection via the redox protein cyt *c* to modified gold electrodes is feasible, if PQQ-GDH is in solution or integrated into an cyt *c* matrix.[275] Moreover, DET has been shown at various carbon surfaces such as carboxyl-functionalized single-walled carbon nanotubes,[276,277] polythiophene-[278] or polyaniline-modified MWCNTs,[279–282] and carbon cryogel,[283] but also PQQ-modified

gold nanoparticle[284] and semimetallic TiO_2 nanotubes[285] have demonstrated the potential for a direct interaction with PQQ-GDH. Polyanilines also convey the direct connection of the enzyme to gold and ITO electrodes.[286–289]

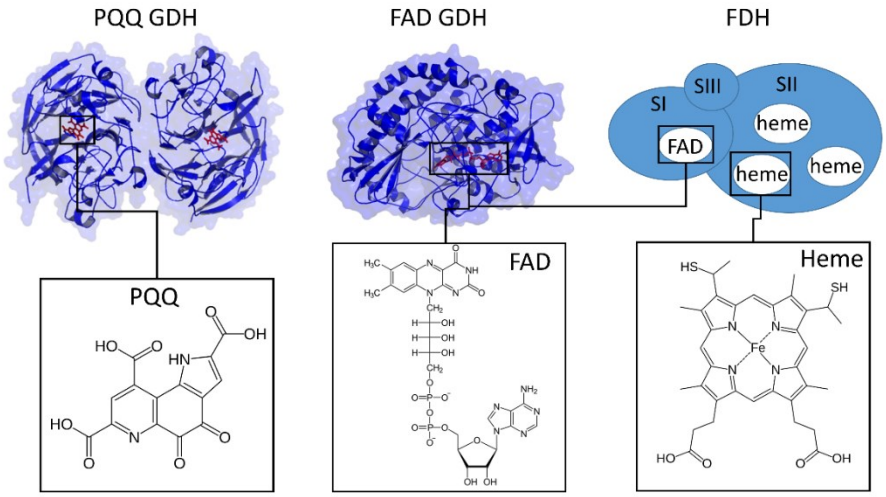

Figure 8. Crystal structure of PQQ and FAD-dependent glucose dehydrogenase as well as schematic visualization of fructose dehydrogenase with subunit I (SI), II (SII) and III (SIII) according to ref. [256,290,291]. Additionally, the respective enzymatic cofactors pyrroloquinoline quinone (PQQ), flavin adenine dinucleotide (FAD) and heme *c* are illustrated.

3.3.2 FAD-dependent glucose dehydrogenase

FAD-dependent glucose dehydrogenases (FAD-GDH) have been found in fungi, gram-negative bacteria and some insects, and can be divided according to their origin.[258] All enzymes contain a flavin adenine dinucleotide (FAD) as catalytic center, but differences have been found in the structure. For example, bacterial FAD-GDH holds an additional multi-heme cytochrome subunit,[292] which is not found in fungal enzymes.[293]

Fungal FAD-GDH from *Aspergillus sp.* has been first characterized in 1967,[293,294] however, so far only minor scientific informations are available for this enzyme. The enzyme has a rather narrow substrate spectrum and oxidize glucose with high specificity, but also 2-deoxy-D-glucose and xylose with significantly reduced activity to the respective lactone.[295] The selectivity of FAD-GDH for glucose is comparable with that of glucose oxidase, but much better than that of native PQQ-GDH.[258] Moreover, FAD-GDH is found to be rather insensitive to oxygen and provide a good thermostability.[294,296]

Fungal FAD-GDH accepts several mediators as electron acceptors such as 2,6-dichlorophenolindophenol,[294] β-naphthoquinone,[294] N-methylphenazonium methyl sulfate,[297,298] methylene blue[299] and ferricyanide,[300] but DET with electrodes has not been shown yet. The most reported enzyme electrodes hosting fungal FAD-GDH are constructed with osmium complex-containing redox polymers acting as wiring agent for the transfer of electrons to the electrode.[295,296,301] One approach with FAD-GDH and a

redox polymer integrated into mesoporous carbon electrodes achieved exceptionally high catalytic currents of 360 mA cm^{-2} in the presence of 500 mM glucose at solution temperatures of 55 °C and electrode rotation rates of 9000 rpm.[301] This demonstrates the great potential of FAD-GDH for the generation of power in biofuel cells. However, the high overpotential of 0.7 V vs. Ag/AgCl needed for the efficient subtraction of electrons remains an issue limiting the overall performance.[301] A reduction of the required potential have been achieved for quinone based redox polymers[302] and quinone-modified MWCNT papers,[303] reaching maximum currents of 3.3 mA cm^{-2} at 0 V vs. SCE and 5.38 mA cm^{-2} at 0.15 V vs. SCE, respectively, without electrode rotation or temperature support.

3.3.3 Fructose dehydrogenase

Fructose dehydrogenase (FDH) form *Gluconobacter sp.* is a heterotrimeric membrane associated flavohemo-protein with a molecular weight of about 140 kDa.[291] As schematically depicted in figure 8, the enzyme consists of three subunits I, II and III with a molecular weight of 67 kDa, 50.8 kDa and 19.7 kDa, respectively.[291] While subunit I and II own a covalently bound FAD and 3 heme *c* moieties, respectively, the function of subunit III is still unknown.[291] The formal potentials of the three heme *c* moieties have been recently determined to be -10 ± 4, 60 ± 8 and 150 ± 4 mV (vs. Ag/AgCl, sat. KCl) at pH 5.[304] FDH is highly specific towards the conversion of D-fructose, with a optimum pH of 4 for the substrate oxidation.[291] The fructose conversion proceeds at the FAD prosthetic group resulting in a reduction to $FADH_2$.[304] The electrons are subsequently transferred via intramolecular electron transfer to the heme *c* moieties.[304–306] It is expected that the electrons are under natural conditions further transferred from one of the heme *c* sites to the natural electron acceptor ubiquinone.[307,304]

The enzyme has gained great interest for the construction of biosensors and biofuel cells due to its ability to show not only mediator-based electron transfer with electrodes, but also to allow direct protein electrochemistry on various electrode materials. Mediator-based system have been reported for electrodes modified with benzoquinone,[308] tetrathiafulvalene,[309] MWCNTs with a adsorbed pyrene derivative of naphthoquinone,[306] ferricyanide,[310,311] ferrocene,[312,313] osmium redox mediator,[314] redox polymer,[315] and cyt *c*.[316,317] DET studies have demonstrated that the communication between the enzyme and the electrode is established via the heme *c* moieties.[304–306] A first fructose sensor based on DET has been reported for FDH immobilized on carbon paste electrodes.[318] Enhanced catalytic currents have been achieved on 3D carbon electrodes consisting of MWCNTs,[306,319] ketjen black[320] and carbon cryogel[321] reaching high currents up to 10 mA cm^{-2}. Also conductive polymers such as polypyrrole and sulfonated polyanilines have been used to convey DET with electrodes.[322,323] Besides carbon-based materials also modified gold electrodes or electrodes modified with gold nanoparticle allow the direct communication with FDH.[304,324–326]

4 Results

4.1 Connecting quantum dots with enzymes: mediator-based approaches for the light-directed read-out of glucose and fructose oxidation[†]

Authors: **M. Riedel**, N. Sabir, F. W. Scheller, W. J. Parak and F. Lisdat

Abstract: The combination of the biocatalytic features of enzymes with the unique physical properties of nanoparticles in a biohybrid system provides a promising approach for the development of advanced bioelectrocatalytic devices. This study describes the construction of photoelectrochemical signal chains based on CdSe/ZnS quantum dot (QD) modified gold electrodes as light switchable elements, and low molecular weight redox molecules for the combination with different biocatalysts. Photoelectrochemical and photoluminescence experiments verify that electron transfer can be achieved between the redox molecules hexacyanoferrate and ferrocene, and the QDs under illumination. Since for both redox mediators a concentration dependent photocurrent change has been found, light switchable enzymatic signal chains are built up with fructose dehydrogenase (FDH) and pyrroloquinoline quinone-dependent glucose dehydrogenase ((PQQ)GDH) for the detection of sugars. After immobilization of the enzymes at the QD electrode the biocatalytic oxidation of the substrates can be followed by conversion of the redox mediator in solution and subsequent detection at the QD electrode. Furthermore, (PQQ)GDH has been assembled together with ferrocenecarboxylic acid on top of the QD electrode for the construction of a functional biohybrid architecture, showing that electron transfer can be realized from the enzyme over the redox mediator to the QDs and subsequently to the electrode in a completely immobilized fashion. The results obtained here do not only provide the basis for light-switchable biosensing and bioelectrocatalytic applications, but may also open the way for self-driven point-of-care systems by combination with solar cell approaches (power generation at the QD electrode by enzymatic substrate consumption).

Introduction

During the last decade semiconductor nanoparticles (quantum dots) have gained much attention due to their unique photophysical properties, such as size-tunable photoluminescence properties, high fluorescence quantum yield, and stability against

[†] **Published in Nanoscale:** M. Riedel, N. Sabir, F. W. Scheller, W. J. Parak and F. Lisdat. Connecting quantum dots with enzymes: mediator-based approaches for the light-directed read-out of glucose and fructose oxidation. *Nanoscale* **2017**, 9, 2814-2823. DOI: 10.1039/C7NR00091J.

degradation and photobleaching.[327] These superior features of quantum dots (QDs) have initiated new light-driven research fields such as solar cells,[12] optical assays,[328] electrochemiluminescence-based detection schemes,[329] and photoelectrochemical (PEC) sensors.[16,17,75,330,331] All approaches rely on an excitation process of the semiconductor nanoparticle, e.g. by using light of sufficient energy, to transfer electrons from the valence band (VB) to the conduction band (CB) generating electron–hole pairs. While in solution often recombination processes of the electron–hole pairs inside the QDs are favored resulting in the emission of light, by fixation of the QDs to an electrode, electron transfer reactions can be enforced by applying a potential.[16] In such a PEC approach anodic photocurrents can be observed by electron subtraction from the CB of the QDs towards the electrode and subsequent oxidation of a donor at the VB of the QDs. In the reverse case, electrons can be supplied from the electrode via the QDs to an acceptor in solution, generating a cathodic photocurrent. Here, the direction and magnitude of the photocurrent depend not only on the potential but also on the concentration of the redox couple in solution. The use of light as an additional tool to control redox reactions at the electrode interface makes PEC systems a promising analytical approach with high sensitivity.[17] Light-triggered detection schemes also open a new way for multiplexing, when different biochemical recognition elements are immobilized spatially separated on a QD electrode.[16] This enables the individual read-out of analytes by photoexcitation of the respective QD electrode area with a focused light beam. Furthermore, the feasibility to combine the detection features of QD electrodes with solar cell approaches may enable the construction of self-driven sensorial systems for point-of-care diagnostics.[332]

Many efforts have been dedicated to the construction of PEC systems where the photocurrent can be manipulated by the presence of redox active molecules,[119,144,145] enzyme substrates,[81,87,97,98] DNA,[333] as well as binding partners of antibodies.[334–336] They display the great interest of using semiconductor nanostructures for light-triggered detection schemes. Amongst others, the construction of enzyme/nanoparticle hybrid systems has been followed in order to combine the biocatalytic features of enzymes with the unique and advantageous physical properties of nanoparticles.[337] Most enzymatic PEC systems are based on the reaction of enzymatic co-substrates or products such as oxygen,[97,98] hydrogen peroxide,[119] 4-aminophenol,[155] acethylthiocholine,[87] and nicotinamide adenine dinucleotide (NADH).[81,95] Furthermore, by controlling the surface properties of the QDs, direct electron transfer (DET) with the redox protein cytochrome c as well as a few enzymes has been achieved, allowing for the detection of superoxide,[91] sulfite,[89] as well as the production of drugs by P450 enzymes in a light-triggered fashion.[210] However, DET between enzymes and electrode materials with a high efficiency remains challenging due to the difficult directional orientation of enzymes. Hence, mediator-based enzymatic systems with redox mediators such as osmium,[338] ferrocene complexes[339,340] and hexacyanoferrate are still in the focus of research for biosensing,[341] biofuel cells,[342] enzyme kinetics,[343] and inhibition analysis,[344] since they

have demonstrated the ability to electrically communicate with a great variety of redox enzymes. Besides using the optical properties of redox mediators in spectral enzymatic assays, different metal and carbon electrodes can be used for the construction of enzyme sensors.

Until now only little attention has been paid to the redox behavior of mediators at semiconductor surfaces for light-triggered applications. Previously, hexacyanoferrate has been evaluated for its performance as a redox electrolyte in QD sensitized solar cells for maximizing solar energy conversion.[345] Most reports rely on mechanistic studies in solution to investigate complex energy and electron transfer processes between the redox species and the QDs by means of photoluminescence modulation.[346–348] However, until now the construction of such multistep signal chains on electrodes, in combination with biocatalysts, has not been shown.

In this study we investigate the light-triggered reaction of the redox molecules, hexacyanoferrate and ferrocenecarboxylic acid, at CdSe/ZnS quantum dot modified gold electrodes for light-driven applications. Therefore, we have characterized the photocurrent response upon addition of the redox species in dependence on the applied potential and concentration. Here, electron transfer between QDs and redox mediators has been found to be feasible. Additionally, photoluminescence measurements in solution demonstrate the strong interaction between the QDs and the redox species by quenching of QD fluorescence. Subsequently, the established QD–mediator systems have been combined with the enzymes, PQQ-dependent glucose dehydrogenase and fructose dehydrogenase, to demonstrate the feasibility of electrically contacted enzyme/QD biohybrids. This photoelectrochemical principle displays applicability for sensing and for driving QD electrodes by biocatalytic sugar consumption.

Experimental

Materials. 1,4-Benzeneditiol (BDT), poly(allylaminehydrochloride) (PAA, Mw = 17 500 g mol^{-1}), poly(styrenesulfonic acid) (PSS, Mw = 70 000 g mol^{-1}), N-(3-dimethylaminopropyl)-N′-ethylcarbodiimide hydrochloride (EDC), [N-(2-hydroxyethyl)piperazine- N-(2-ethansulfonic acid)] (99.5%; HEPES), ferrocenecarboxylic acid (Fc-COOH), hexacyanoferrate(II), hexacyanoferrate(III), D-fructose, D-glucose and fructose dehydrogenase (FDH) from Gluconobacter japonicus NBRCA3260 are purchased from Sigma-Aldrich (Steinheim, Germany). (PQQ) glucose dehydrogenase ((PQQ)GDH) (Acinetobacter calcoaceticus) was kindly gifted by Roche Diagnostics GmbH. CdSe/ZnS nanoparticles (QDs) with trioctylphosphine oxide as surface ligands were synthesized according to a modified protocol of Dabbousi et al..[49,95]

Electrode cleaning. Gold disk electrodes with an electrode surface area of 0.0314 cm^2 were firstly mechanically cleaned with abrasive paper (P3000). Subsequently, the electrodes were electrochemically cleaned by cyclic voltammetry in 1 M NaOH (-0.8 V

to +0.2 V vs. Ag/AgCl, 1 M KCl, scan rate 0.3 V s^{-1}) and 0.5 M H_2SO_4 (-0.2 V to +1.75 V vs. Ag/AgCl, 1 M KCl, scan rate 0.3 V s^{-1}). Afterwards the cleaned electrodes were extensively rinsed with deionized water.

Electrode preparation. The freshly cleaned electrodes were incubated in ethanolic solution with 5 mM 1,4-benzenedithiol. After removing unbound BDT by rinsing with ethanol, the electrodes were immersed in 10 µM QD solution overnight on a shaker (650 rpm).

Enzyme immobilization. To assemble the fructose dehydrogenase on top of the prepared QD electrode, PAA was adsorbed onto the electrode by immersing the electrode in 0.2 mg ml^{-1} PAA dissolved in HEPES buffer (5 mM, pH 7) for 1 h. Subsequently, the electrode was incubated with 0.5 mg ml^{-1} FDH solution in HEPES buffer (5 mM, pH 7) for 2 h.

(PQQ)GDH immobilization was achieved by incubation of the QD electrodes within 0.2 mg ml^{-1} PSS in HEPES buffer (5 mM, pH 7) for 1 h. Afterwards, the modified QD electrodes were immersed in 1 mg ml^{-1} (PQQ)GDH solution in HEPES buffer (5 mM, pH 7) for 2 h.

For the simultaneous assembly of (PQQ)GDH and ferrocenecarboxylic acid, a solution of both the enzyme (0.5 mg ml^{-1}) and the redox complex (2.5 mM) was mixed in the presence of 50 mM EDC and allowed to react for 20 min. Subsequently, the mediator-modified enzyme was incubated overnight at the QD electrodes.

Impedimetric measurements. Electrochemical impedance measurements were performed in the presence of 2 mM hexacyanoferrate(II/III) in 100 mM sodium phosphate buffer (pH 7) in the dark under the following conditions: 100 kHz–1 Hz frequency range, 5 mV AC amplitude, open circuit potential (OCP).

Photoelectrochemical measurements. Photoelectrochemical experiments were performed with a potentiostat from CHI (USA, Austin) and a halogen reflector lamp from Schott (Mainz, Germany) with a light intensity of about 13.9 mW cm^{-2}. The measurements were carried out in a three-electrode arrangement consisting of the QD working electrode, an Ag/AgCl reference electrode, and a platinum wire as the counter electrode. Photochronoamperometric experiments were performed at various potentials, while using an illumination time of 10 s. For wavelength-dependent measurements a monochromator (Polychrome V, Till Photonics) with a bandwidth of 15 nm was used. Chopped light voltammetry experiments were carried out in the bias range between -0.4 V and +0.4 V by applying a scan rate of 5 mV s^{-1} and an illumination time of 5 s. All measurements were performed in 100 mM HEPES (pH 7).

Photoluminescence measurements. QDs were dissolved in 1 ml ethanol (1 µM QDs) and placed in a quartz cuvette. The photoluminescence measurements were performed with a Cary Eclipse fluorescence spectrophotometer from Varian. QD–mediator

interactions were recorded during a stepwise addition of redox mediator solution (10 mM) to the QD solution. For the excitation a wavelength of 420 nm and 380 nm was used in experiments with hexacyanoferrate(II) and ferrocenecarboxylic acid, respectively. The emission spectra were recorded between 450 nm and 650 nm.

Results and discussion

Characterization of QD–mediator interactions. For the experiments, CdSe QDs with a ZnS shell and tritoctylphosphine oxide (TOPO) as a capping ligand have been synthesized.[95] The ZnS shell improves the photophysical properties of the QDs and passivates surface defects at the CdSe cores [349] The purified CdSe/ZnS QDs possess an absorption maximum at 535 nm, a fluorescence maximum at 561 nm and a quantum yield of 1.8% (see Fig. S1†). According to the spectral properties the diameter of the QDs is estimated to be around 2.8 nm.[37]

The QDs can be easily linked to 1,4-benzenedithiol-modified gold electrodes via partial ligand exchange of the nonpolar surface ligand TOPO by the immobilized dithiol.[119] Here, BDT acts as a linker molecule between the gold electrode and the QDs, which results in the formation of stable and functional QD layers. The QD electrode construction has been characterized by electrochemical impedance spectroscopy (EIS) measurements. A significant increase of the impedance signal can be followed after each modification step from the bare gold electrode to the BDT-modified electrode and finally to the QD electrode (see Fig. S3†). The results display the changing barrier for the interfacial charge transfer of the redox couple at the electrode, which can be explained by the enhanced blocking of the electrode due to BDT and subsequent QD assembly. This indicates the successful QD electrode construction. It has to be added here that the experiments have been performed in the dark; i.e. no charge carrier generation in the QDs.

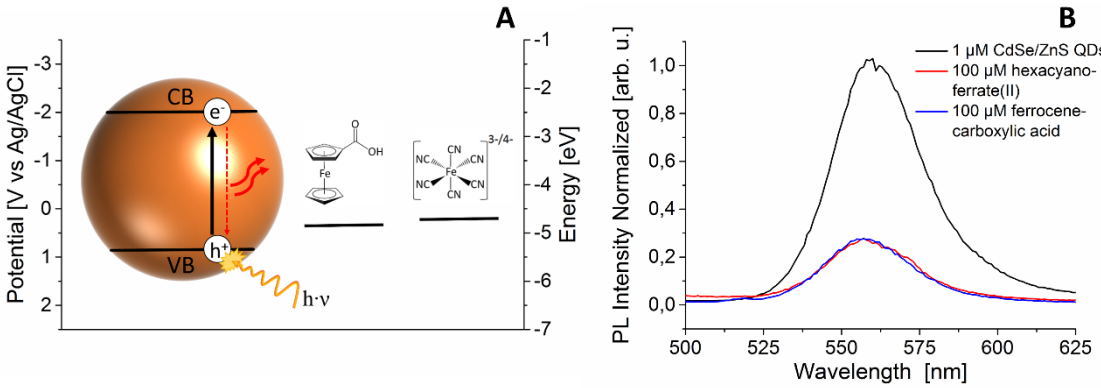

Fig. 1 (A) Energy level diagram of the used CdSe/ZnS QDs according to Jasieniak et al.[350] and ferrocenecarboxylic acid as well as hexacyanoferrate(II). **(B)** Normalized photoluminescence (PL) spectra of a 1 µM CdSe/ZnS QD solution in the absence and presence of hexacyanoferrate(II) or ferrocenecarboxylic acid with a ratio of 1 : 100. For hexacyanoferrate(II) and ferrocene carboxylic acid an excitation wavelength of 420 nm and 380 nm, respectively, has been used.

Comparative SEM measurements have been performed on planar gold chips (as for the photoelectrochemical studies gold disk electrodes are used). As shown in Fig. 2 the deposition of QDs can also be verified.

To investigate the photoelectrochemical properties of the QD electrodes, chopped light voltammetry has been carried out under modulated white light. As depicted in Fig. 3A it has been found that the magnitude and direction of the photocurrent depend on the applied potential and shifts at a potential of around +50 mV vs. Ag/AgCl from a cathodic to an anodic photocurrent, which is in good agreement with other QD-based studies on gold electrodes.[91,96] In contrast, the BDT-modified gold electrodes without QDs show no photocurrent response. Consequently, the signal can be attributed to the electron transfer between the gold electrode and the photoexcited immobilized QDs, whereby oxidation and reduction of the nanoparticles are controlled by the electrode potential. Additionally, wavelength-dependent measurements verify that the photocurrent follows the absorbance features of the QDs, which indicates that the nanoparticles retain their characteristic photophysical properties upon immobilization onto the gold electrode and after the transfer from the nonpolar solvent into buffer (see Fig. S4†).

The QD electrodes have been found to provide good signal stability in the cathodic direction, which can be attributed to the presence of oxygen as an electron acceptor in solution.[97,98,351] In comparison, anodic photocurrents show less stability due to the absence of electron donors, which may even result in a decomposition of the QDs. This however, can be avoided by changing the electrode polarization or by providing electron donors for the photoelectrochemical system.

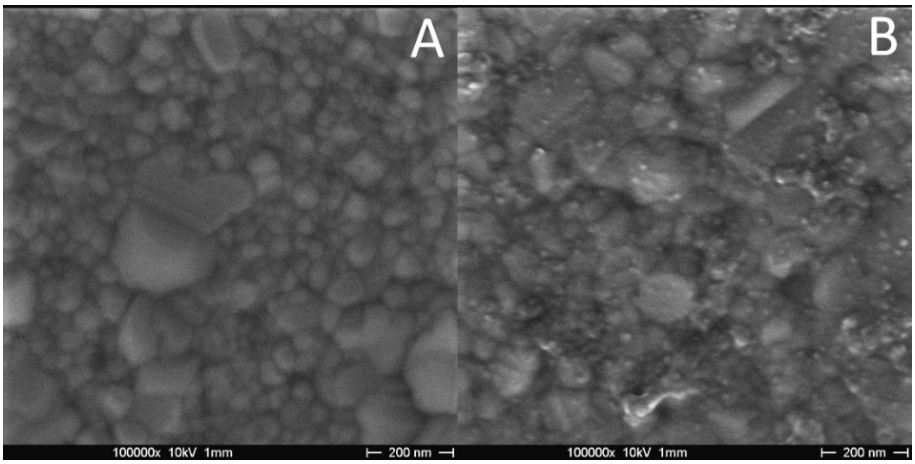

Fig. 2 SEM micrographs of a 1,4-benzenedithiol-modified gold chip electrode before **(A)** and after modification with QDs **(B)**. Here, it has to be mentioned that in contrast to the photoelectrochemical measurements for the SEM experiments planar gold-vaporized electrodes have been used, which can differ in the surface structure from the gold disk electrodes. Increased surface roughness can be observed after QD modification, which confirms the attachment of the nanoparticles to the gold electrode. SEM micrographs were obtained with a Zeiss DSM 982 GEMINI (Germany) scanning electron microscope at an acceleration voltage of 10 kV.

Before we study the photoelectrochemical interaction of the QDs immobilized on gold electrodes with the redox molecules hexacyanoferrate(II) and ferrocenecarboxylic acid,

we have initially evaluated the interaction by quenching studies via photoluminescence spectroscopy at room temperature. Therefore, we have followed the emission of the QDs upon addition of the redox mediator. For both redox mediators a decrease of the fluorescence emission can be observed with increasing concentrations of the respective compound (Fig. S5†). As depicted in Fig. 1B at a QD : mediator ratio of 1 : 100 for hexacyanoferrate(II) and ferrocenecarboxylic acid a similar photoluminescence decline of around 73% is achieved. This quenching behavior can be explained either by electron or energy transfer. However, energy transfer is energetically not favorable since: (1) the absorption wavelength range of the redox molecules does not overlap with the emission of the QDs (see Fig. S2†), and (2) the excitation wavelength was adapted to the absorption properties of the redox molecules (no absorption at the chosen excitation wavelength) to avoid joint excitation of the compounds. Consequently, the redox complexes should not get excited during the measurement and remain in their energetic ground state. Moreover, no formation of an additional fluorescence peak or changes of the peak shape have been observed. In contrast, a photoelectrochemical electron transfer from the QDs to a redox compound or the reverse can be explained by the calculated energetic levels (see Fig. 1A). For the used QDs the conduction band and the valence band have been determined to be at -2.055 V and 0.805 V (vs. Ag/AgCl, 1 M KCl), respectively, according to Jasieniak et al..[350] Thus, the energetic levels of ferrocenecarboxylic acid (0.244 V vs. Ag/AgCl, 1 M KCl) and hexacyanoferrate (0.2 V vs. Ag/AgCl, 1 M KCl) lie between the CB and VB of the QDs. Accordingly, both the reduction and the oxidation of the redox complexes at the QDs could be feasible, depending on the redox state of the molecules.

For ferrocene molecules photoluminescence quenching has been described as an electron transfer from the ferrocene to the excited QDs, which results in the formation of a nonluminescent charged QD.[347,352] A similar behavior can be expected for hexacyanoferrate(II), which could also act as an electron donor and inject charge carriers into the QDs. However, the quenching of hexacyanoferrate(II) at lower mediator concentrations (ratio 1 : 10) is less efficient than that of ferrocenecarboxylic acid (see Fig. S5†). Since a photoluminescence decrease by effects like displacement of the QD surface ligands is unlikely, (because of missing coordinating groups of the redox compounds) the differences of quenching efficiency may also be attributed to different electron transfer rates at the QDs. The photoluminescence experiments demonstrate that the electron transfer between the QDs and the redox compounds, hexacyanoferrate(II) and ferrocenecarboxylic acid, is feasible upon illumination and give the first hint for a feasible combination with QDs for the construction of enzymatic signal chains on electrodes.

Subsequently, the interaction between CdSe/ZnS QD modified gold electrodes and the redox molecules has been tested by chopped light voltammetric experiments. As shown in Fig. 3A, upon addition of 500 µM hexacyanoferrate(II) a strong increase of the photocurrent can be found over the entire investigated potential range. Here, the signal response increases with increasing anodic bias, but occurs even at potentials more

negative than the redox potential of hexacyanoferrate(II). The results demonstrate that hexacyanoferrate(II) can be oxidized at the photoexcited QDs, and that this reaction is determined by the position of the energy states within the QDs, allowing reliable hexacyanoferrate(II) detection over a larger potential range compared to metal electrodes. Furthermore, wavelength-dependent measurements verify that the photoelectrochemical oxidation of hexacyanoferrate(II) follows the absorbance features of the QDs (see Fig. S4†).

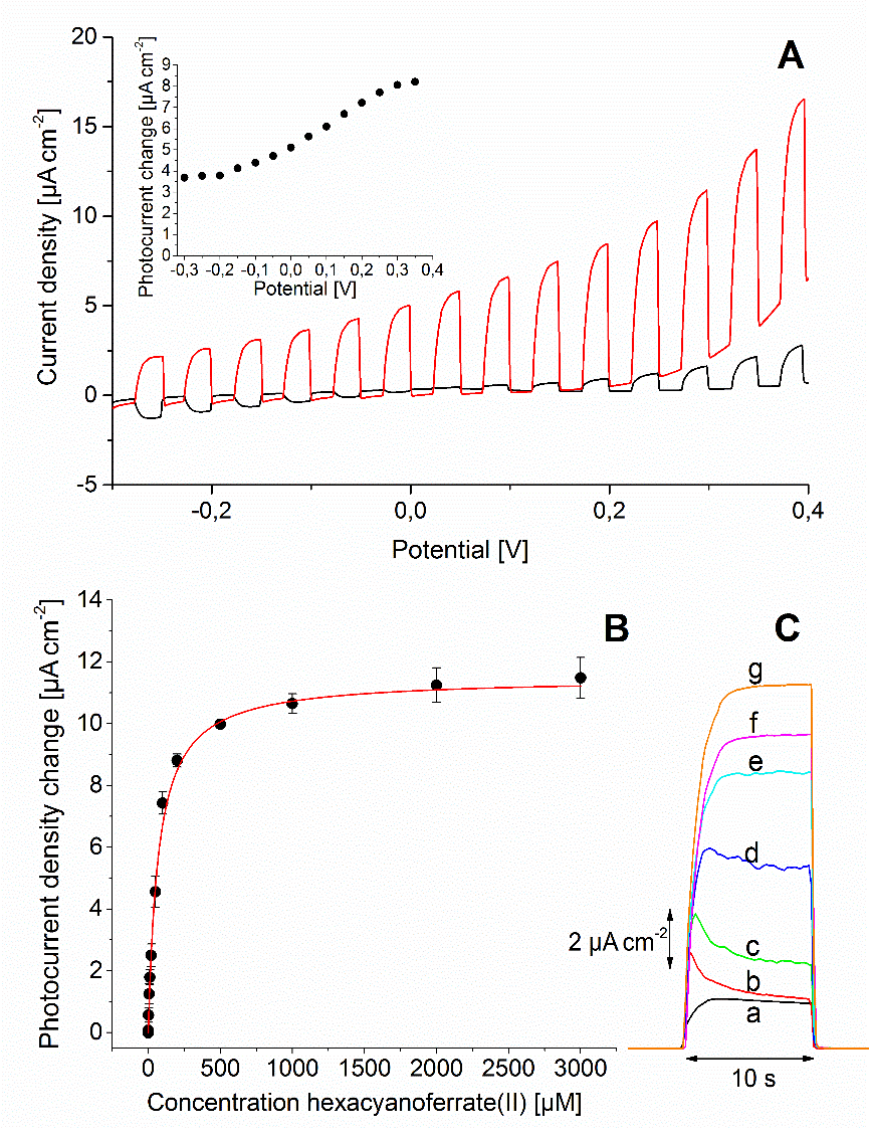

Fig. 3 (A) Chopped light voltammetry of a QD electrode in the absence (black curve) and presence of 500 µM hexacyanoferrate(II) (red curve). The inset illustrates the photocurrent density change after addition of 500 µM hexacyanoferrate(II) at different potentials (100 mM HEPES pH 7; light pulses of 5 s, scan rate 5 mV s^{-1}; potential vs. Ag/AgCl, 1 M KCl from -0.3 V to +0.4 V). Photocurrent density response **(B)** and photocurrent density measurement (C) of a QD electrode in solutions with different hexacyanoferrate(II) concentrations (a = 0 µM, b = 5 µM, c = 20 µM, d = 50 µM, e = 100 µM, f = 200 µM, g = 3 mM; 100 mM HEPES pH 7; +0.2 V vs. Ag/AgCl, 1 M KCl). Error bars result from 3 measurements.

In contrast, the addition of hexacyanoferrate(III) (oxidized species) results only in negligible photocurrent changes over the whole potential range (see ESI Fig. S6†). Consequently, the light-induced electron transfer between hexacyanoferrate(III) and the QD electrode is restricted. Similar results have been found in an electrochemical study of the redox process at undoped nanodiamond, showing fast oxidation of hexacyanoferrate(II), but slow reduction of hexacyanoferrate(III).[353] The study on hexacyanoferrate(II/III) demonstrates the necessity of investigating the individual behavior of redox molecules at semiconductor nanostructures since the behavior cannot simply be deduced from reactions at metal electrodes.

Subsequently, the photocurrent response of the QD electrode in dependence on the hexacyanoferrate(II) concentration has been analyzed (see Fig. 3B). Therefore, we have chosen a potential of +0.2 V (vs. Ag/AgCl, 1 M KCl), which provides a high signal output according to the voltammetric experiments. The anodic photocurrent is found to increase in the range between 1 μM and 1 mM hexacyanoferrate(II). The detection limit has been determined to be 1 μM, and the half maximal photocurrent is reached at 71 μM hexacyanoferrate(II). Consequently, the QD electrode enables the light-triggered detection of hexacyanoferrate(II) and is therefore promising for the combination with hexacyanoferrate reducing enzymes. It has to be emphasized here that a saturation-type of concentration dependence has been found, which is different from metal electrodes for the substance in this concentration range. This shows that the kinetics of electron transfer processes at the QD surface (QD – electrode and QD – mediator) are limiting the current flow. Such tendencies have also been found for other species.[81,96]

The interaction between QD electrodes and ferrocenecarboxylic acid has also been analyzed in dependence on the applied potential. The measurement in the absence and presence of 100 μM ferrocenecarboxylic acid is shown in Fig. 4A. Here, an enhancement of the cathodic photocurrent has been found up to potentials of +0.2 V (vs. Ag/AgCl, 1 M KCl), whereby higher potentials result in rising anodic photocurrents. The results indicate that ferrocenecarboxylic acid occurs in solution as reduced and oxidized species, and thus can be both reduced and oxidized at the illuminated QDs. Since the turning point from the anodic to the cathodic current lies close to the redox potential of ferrocenecarboxylic acid (0.244 V vs. Ag/AgCl, 1 M KCl), there is no gain in lowering the potential for the photoelectrochemical detection as has been observed for hexacyanoferrate(II). Wavelength-dependent measurements show that the photocurrent response still correlates with the optical properties of the nanoparticles (see ESI Fig. S7†).

To further characterize the ferrocenecarboxylic acid detection by QD electrodes the effect of the mediator concentration has been investigated. Increasing photocurrents have been observed in the range between 1 μM and 1 mM ferrocenecarboxylic acid with a detection limit of 1 μM.

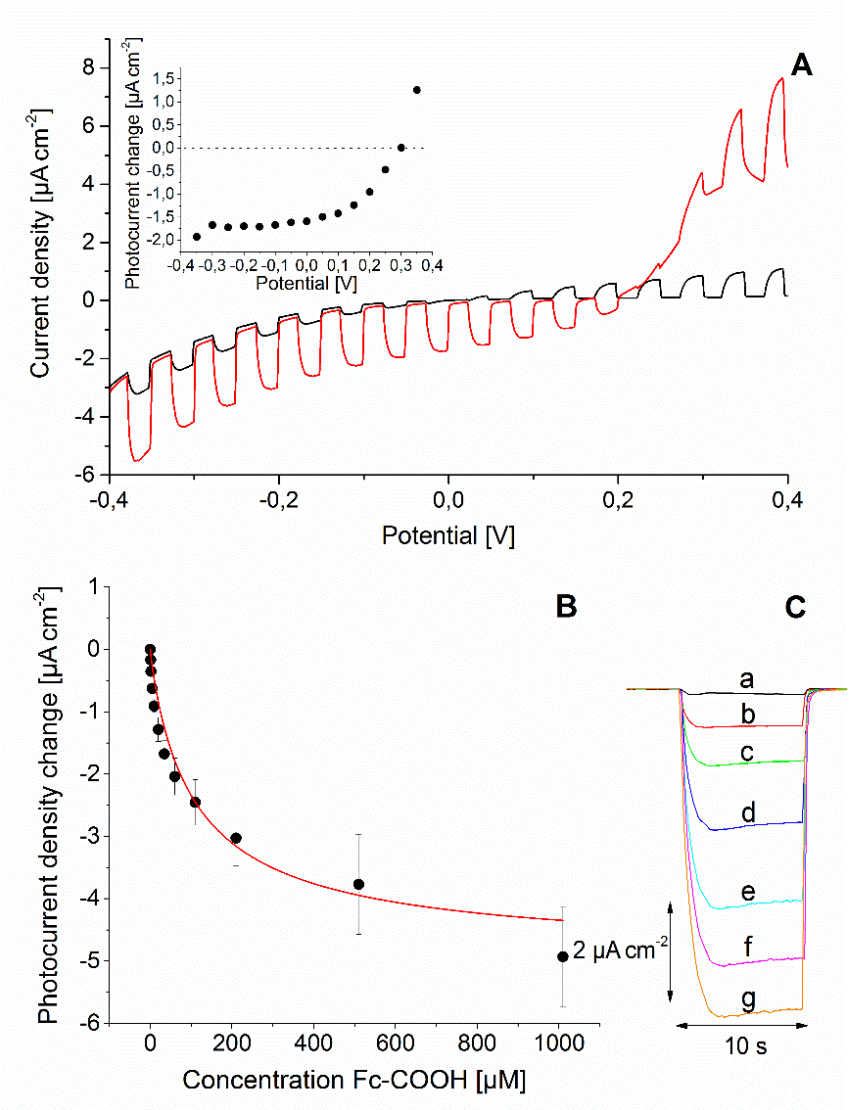

Fig. 4 (A) Chopped light voltammetry of a QD electrode in the absence (black curve) and presence of 100 µM ferrocenecarboxylic acid (red curve). The inset illustrates the photocurrent density change after addition of 100 µM ferrocenecarboxylic acid at different potentials (100 mM HEPES pH 7; light pulses of 5 s, scan rate 5 mV s^{-1}; potential vs. Ag/AgCl, 1 M KCl from -0.4 V to +0.4 V). Photocurrent density response **(B)** and photocurrent density measurement (C) of a QD electrode in solutions with different ferrocenecarboxylic acid concentrations (a = 0 µM, b = 5 µM, c = 20 µM, d = 110 µM, e = 510 µM, f = 1 mM, g = 1.5 mM; 100 mM HEPES pH 7; -0.1 V vs. Ag/AgCl, 1 M KCl). Error bars result from 3 measurements.

Although the redox potentials of ferrocenecarboxylic acid and hexacyanoferrate(II/III) are similar (see Fig. 1A), a different photoelectrochemical behavior at the QD electrode has been found for both mediators. The photocurrent experiments have been supported by photovoltage measurements in the absence of any applied driving force (see ESI Fig. S8†). By addition of increasing concentrations of ferrocenecarboxylic acid the photovoltage is enhanced compared to pure buffer pointing to a preferred cathodic reaction (from +25 mV to +47 mV (100 µM)). In comparison, the addition of hexacyanoferrate(II) results in a complete reversion of the photovoltage to -116 mV (100 µM). Consequently, for both redox mediators different charge transfer directions are

preferred at the QD electrode. Furthermore, larger photovoltage changes have been found for hexacyanoferrate(II). This suggests different mechanisms of charge transfer between the excited QDs and ferrocenecarboxylic acid and hexacyanoferrate(II) in terms of electron transfer rates for the oxidation and reduction process. However, further work is needed to better understand the kinetic limitations of charge transfer reactions of redox molecules at QD electrodes.

Mediator-based photoelectrochemical signal chains with immobilized enzymes. To evaluate the concept of using small redox molecules in combination with enzymes for the construction of light switchable signal chains on QD electrodes, firstly fructose dehydrogenase (FDH) has been coupled with hexacyanoferrate to verify that the photocurrent can be manipulated by the presence of the substrate fructose. We have chosen FDH since this enzyme has already shown to react well with hexacyanoferrate.[291] FDH is a hemoflavo-protein which consists of three subunits, containing one flavin-adenine-dinucleotide and 3 heme c as prosthetic groups, and catalyzes the oxidation of D-fructose to 5-keto-D-fructose. The principle of the photoelectrochemical signal chain to be established is illustrated in Scheme 1. Upon substrate addition FDH catalyzes the oxidation of fructose and transfers electrons to hexacyanoferrate(III) to form hexacyanoferrate(II). The reduced mediator can be oxidized at the excited QDs and can result in a photocurrent change.

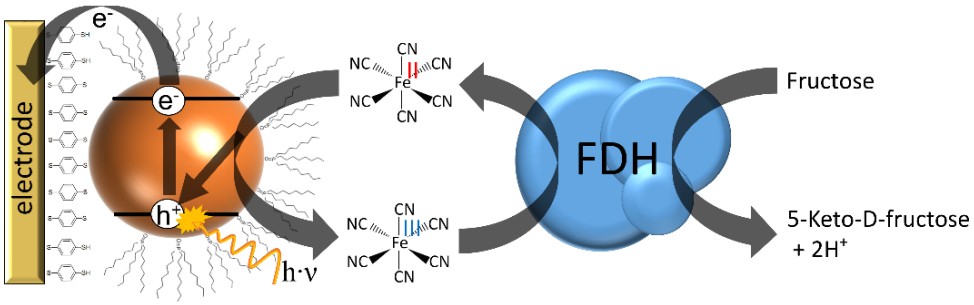

Scheme 1 Schematic illustration of the sensing principle of the QD electrode in combination with the redox system hexacyanoferrate(II/III) and the enzyme fructose dehydrogenase. Upon addition of fructose hexacyanoferrate(III) is reduced to hexacyanoferrate(II) by FDH, which can be subsequently oxidized at the excited QDs and can result in a change of the photocurrent.

For enzyme immobilization a polyelectrolyte interlayer on the QD electrode has been applied. Polyallylamine has been used, since FDH is an acidic enzyme with a pI of 5.0. Consequently, at pH 7 the electrostatic attraction between the positively charged PAA and the negatively charged enzyme facilitates the binding to the QD electrode according to the principle of the layer-by-layer deposition approach. Chopped light voltammetry experiments of the prepared QD electrode in the presence of 100 µM hexacyanoferrate(II) with 50 mM fructose show an enhancement of the anodic photocurrent over the whole potential range (see Fig. 5A). The signal increases with increasing anodic bias, similar to the experiments with hexacyanoferrate(II) alone. The measurement also indicates that after photooxidation of hexacyanoferrate(II) at the illuminated QDs the produced

hexacyanoferrate(III) is reduced back to hexacyanoferrate(II) by enzymatic conversion, which results in an amplification of the anodic photocurrent with a factor of around 1.6 at 0 mV (vs. Ag/AgCl, 1 M KCl). Furthermore, this proves that the FDH enzyme retains its catalytic activity after immobilization at the PAA-modified QD electrode. In contrast, control experiments without enzymes or redox mediators show no photocurrent changes upon addition of fructose.

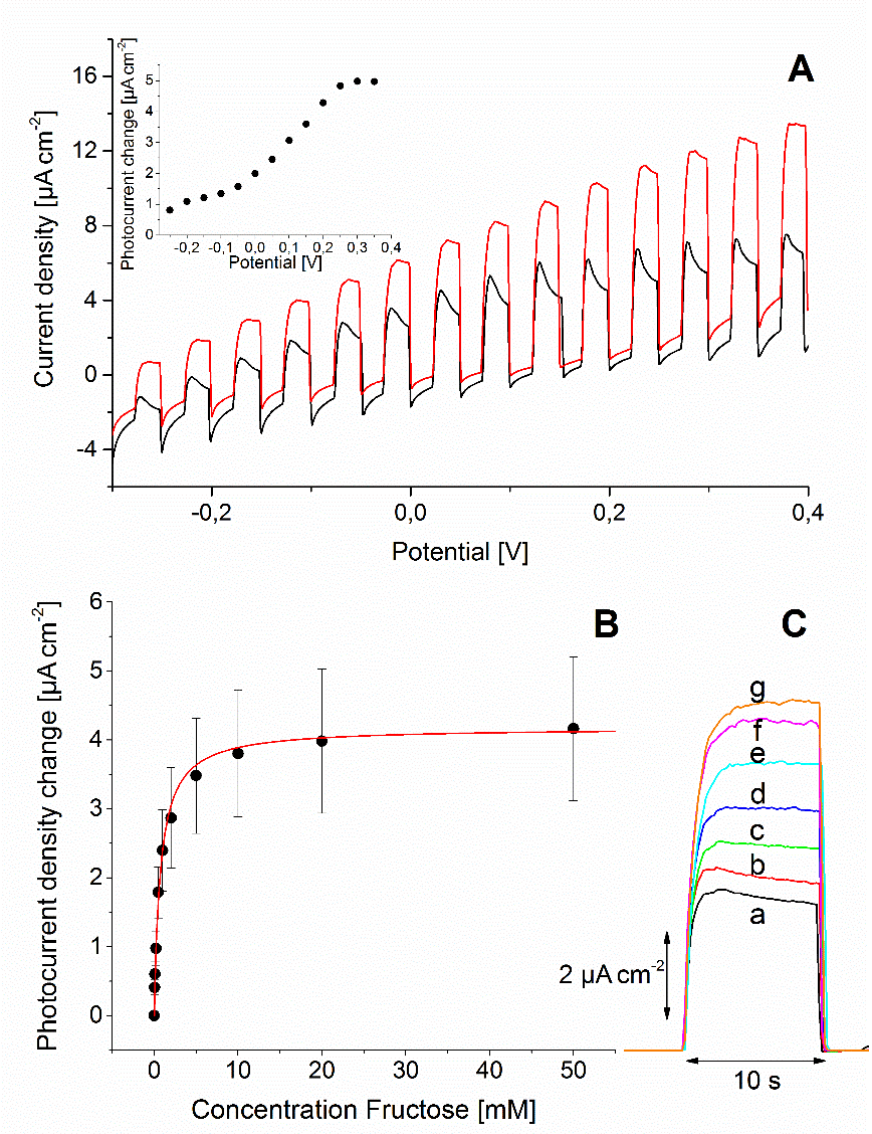

Fig. 5 (A) Chopped light voltammetry of a polyallylamine modified QD electrode with immobilized fructose dehydrogenase in the presence of 100 µM hexacyanoferrate(II) (black curve) and after addition of 50 mM fructose (red curve). The inset displays the potential dependence of the photocurrent density change in the presence of 100 µM hexacyanoferrate(II) and after addition of 50 mM fructose (100 mM HEPES; light pulses of 5 s, scan rate 5 mV s^{-1}; potential vs. Ag/AgCl, 1 M KCl from -0.3 V to +0.4 V) Photocurrent density response **(B)** and measurement (C) of a polyallylamine modified QD electrode with immobilized fructose dehydrogenase in solutions with 500 µM hexacyanoferrate(III) and successive addition of fructose (a = 0 µM, b = 50 µM, c = 200 µM, d = 500 µM, e = 2 mM, f = 10 mM, g = 50 mM; 100 mM HEPES pH 7; +0.2 V vs. Ag/AgCl, 1 M KCl). Error bars result from 3 measurements.

To further investigate the sensitivity of the system towards fructose, amperometric measurements have been performed in the presence of 500 µM hexacyanoferrate(III) at a potential of +0.2 V (vs. Ag/AgCl, 1 M KCl) by successively increasing the substrate concentration. A first signal response is found after addition of 50 µM fructose and enhances up to a concentration of 20 mM. The apparent Michaelis–Menten constant, $K_{M,app}$, is determined to be around 0.74 mM. It has to be mentioned here that these experiments have been performed at neutral pH in order to exclude pH effects and thus the apparent Michaelis–Menten constant, $K_{M,app}$, is smaller than the reported K_M values under acid conditions (K_M = 10 mM).[291] Furthermore, the concentration dependent photocurrent of hexacyanoferrate(II) shows a saturation type behaviour, which also limits the detection range of fructose.

The photoelectrochemical signal chain possesses similar sensitivity to other electrochemical systems with FDH, which are based on mediated or direct electron transfer,[317] but however enables fructose detection at much more negative potentials due to the properties of the QD electrode. Furthermore, the results demonstrate that the combination of a QD electrode with an enzymatic system can be beneficial to increase the power out-put (photocurrent) by biocatalytic consumption of substrates. In such a system substrate oxidation is realized by the enzyme and electrons are supplied by the enzyme via the mediator to the QDs (see Scheme 1). Subsequently, the QDs inject high energetic electrons into the electrode, resulting in an enhanced photoelectrochemical performance. Even if the photocurrents are currently modest this principle offers an alternative approach for the design of future photobiocatalytic solar cells, which are driven by fuels (enzymatic substrates) and may pass over the needs of environmentally dangerous electron donors.

Similar to the before described photoelectrochemical enzymatic signal chain, ferrocenecarboxylic acid has been combined with the enzyme (PQQ)GDH. This enzyme catalyzes the oxidation of glucose to gluconolactone and reduces ferrocenecarboxylic acid. For enzyme immobilization firstly polystyrene sulfonic acid has been assembled on top of the QD electrode, since this negatively charged polyelectrolyte is well known to allow electrostatic immobilization of (PQQ)GDH (pI 9.5) at pH 7 applying again the layer-by-layer method.[354] After enzyme attachment to the QD electrode the system is characterized by chopped light voltammetry. As illustrated in Fig. 6A, the photocurrent changes after addition of 1 mM glucose to a ferrocenecarboxylic acid containing solution. In detail, the cathodic photocurrent at negative potentials decreases in the presence of the substrate, and the potential of the turning point from a cathodic to an anodic photocurrent is shifted by about -0.1 V. Both effects can be attributed to the reduction of Fc-COOH+ by the enzyme, which changes the composition of the reduced/ oxidized mediator in front of the electrode and thus influences the photocurrent behavior.

In the absence of the enzyme or the redox mediator no signal changes have been found after addition of glucose. This proves that the photocurrent response is attributed to the

enzymatic conversion of ferrocenecarboxylic acid and subsequent detection at the QD electrode.

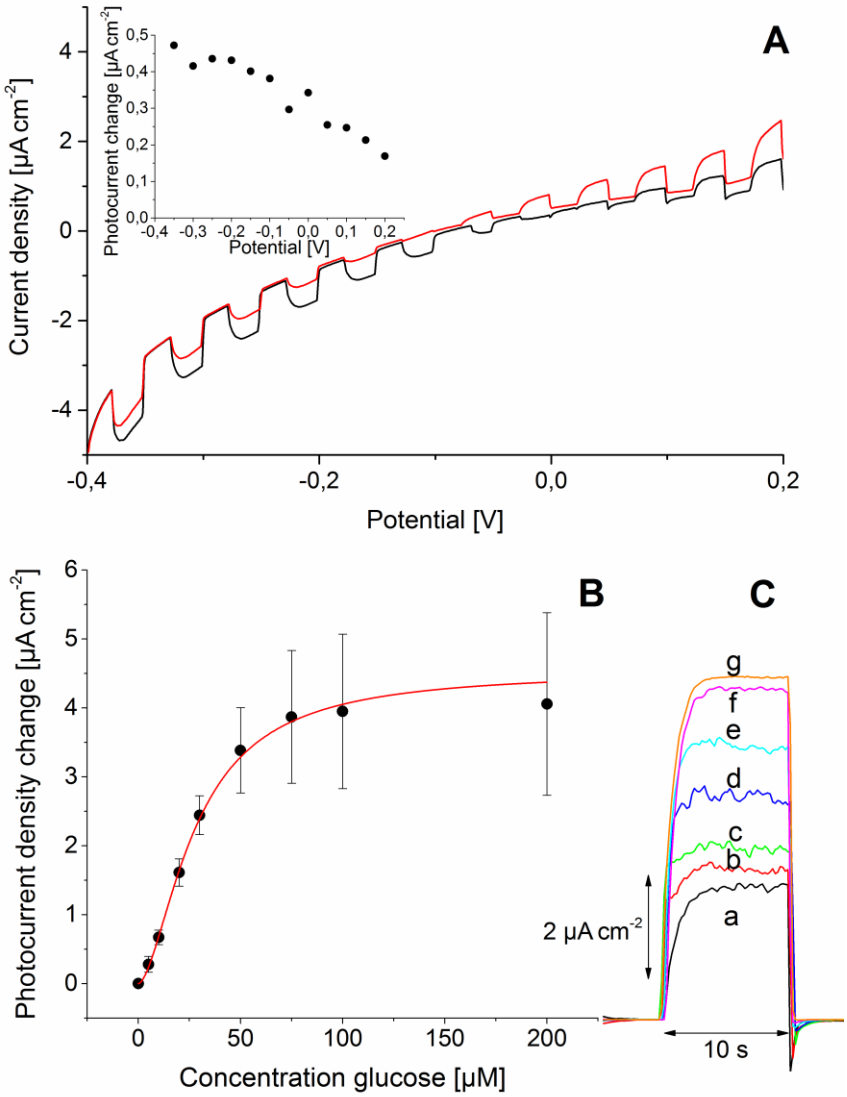

Fig. 6 (A) Chopped light voltammetry of a polystyrene sulfonic acid modified QD electrode with immobilized (PQQ) glucose dehydrogenase in the presence of 100 µM ferrocenecarboxylic acid (black curve) and after addition of 1 mM glucose (red curve). The inset displays the potential dependence of the photocurrent density change in the presence of 100 µM ferrocenecarboxylic acid before and after addition of 1 mM glucose (100 mM HEPES; light pulses of 5 s, scan rate 5 mV s^{-1}; potential vs. Ag/AgCl, 1 M KCl from -0.4 V to +0.2 V). Photocurrent density response **(B)** and photocurrent density measurements **(C)** of a polystyrene sulfonic acid modified QD electrode with immobilized (PQQ)GDH with 500 µM ferrocenecarboxylic acid in solution and successive addition of glucose (a = 0 µM, b = 5 µM, c = 10 µM, d = 20 µM, e = 30 µM, f = 50 µM, g = 100 µM; 100 mM HEPES pH 7; +0.1 V vs. Ag/AgCl, 1 M KCl). Error bars result from 3 measurements.

Concentration dependent measurements of the developed system with glucose in the presence of 500 µM ferrocenecarboxylic acid at +0.1 V (vs. Ag/AgCl, 1 M KCl) have shown the first signal responses in 5 µM glucose solution (see Fig. 6B). Increasing anodic photocurrents are found up to substrate concentrations of 100 µM and the $K_{M,app}$ has been

calculated to be around 28 μM. Since this value is smaller compared to experiments performed in solution[355] or on electrodes,[276,283] the whole charge transfer chain is probably limited by the rate of enzyme–mediator or mediator–QD electron transfer. A similar behavior has been observed by using cytochrome c as an electron shuttling molecule between (PQQ)GDH and a non-light triggered electrode.[275] However, even if only a small concentration dependent dynamic range can be provided, the construction of a light-controlled signal chain can be shown to be feasible with ferrocenecarboxylic acid and (PQQ)GDH.

Both enzyme-based approaches demonstrate the potential of using mediator-based signal chains for the light-triggered conversion of sugars at QD electrodes. The photocurrent is enhanced and can be used for detection or for power generation. On the basis of these experiments, the construction of functional photoelectrochemical biohybrid architectures is attempted by immobilization of both the enzyme and the redox mediator on top of the QDs.

Photoelectrochemical biohybrid architecture based on immobilized small redox molecules and enzymes. Based on the previous results we have tested whether the enzyme and the redox mediator can be immobilized together on top of the QD electrode for the construction of functional light-switchable biohybrid architectures. We have used (PQQ)GDH and ferrocenecarboxylic acid, since the carboxylic acid group of the mediator allows for simple coupling to functional groups via chemical reagents. Therefore, firstly (PQQ)GDH has been modified with ferrocenecarboxylic acid by EDC activation.[356] This has been performed in order to fix many ferrocene molecules around the enzyme and near the catalytic center, to allow for multistep electron transfer also between the ferrocene moieties and finally between ferrocene and the QD electrode.[357] The ferrocene-modified enzyme has been directly immobilized on the QD electrode. Here, we intend to exploit the nonpolar interaction between ferrocene moieties and the hydrophobic ligands at the QDs. The schematic electrode construction is depicted in Fig. 7A.

Subsequently, the signal response of the prepared QD electrode upon addition of glucose without adding a redox mediator into solution has been analyzed. As illustrated in Fig. 7B, changing photocurrents can be observed between 10 μM and 500 μM glucose. Since control experiments without the enzyme or Fc-COOH bound to the enzyme do not show a signal response, it can be confirmed that the assembly of both (PQQ)GDH and Fc-COOH results in a functional system showing glucose-dependent signals. In detail, electrons are transferred after substrate oxidation from the catalytic group of (PQQ)GDH to the bound Fc-COOH on the enzyme surface, and subsequently to the excited QDs. The results demonstrate that the enzyme remains stable even after chemical modification with Fc-COOH and immobilization to the nonpolar QD surface.

In order to address aspects of potential applications in sensing first investigations concerning the selectivity have been performed with diluted solutions of N-acetyl-4-

aminophenol, urea, glycine and fructose (see ESI Fig. S9†). For all these molecules only a negligible signal response has been found.

In comparison to the experiments with bound (PQQ)GDH and ferrocenecarboxylic acid in solution, the photocurrent change is smaller with the immobilized system, but the dynamic range for the detection of glucose is a little larger. This can be probably attributed to the different enzyme immobilization procedures of both approaches. Furthermore, it cannot be excluded at this point that some enzymes are not connected to the electrode after modification with ferrocenecarboxylic acid.

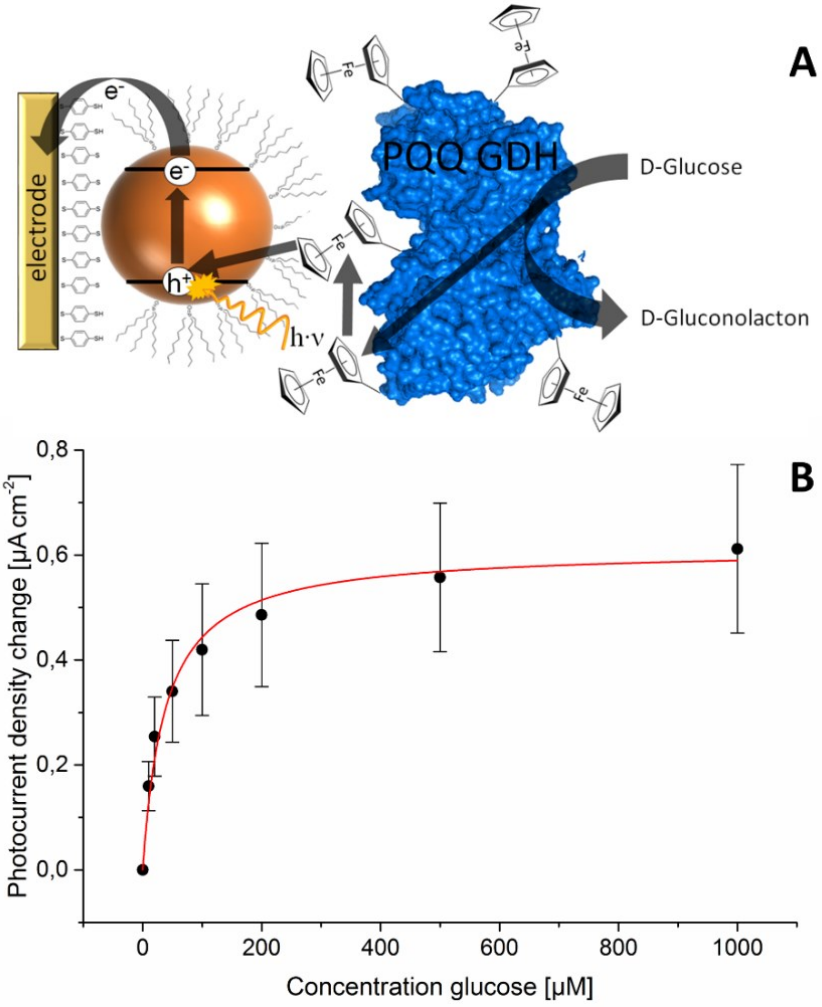

Fig. 7 (A) Schematic principle of the photoelectrochemical biohybrid architecture based on ferrocenecarboxylic acid modified (PQQ)GDH immobilized on QD electrodes. **(B)** Photocurrent density change of QD electrodes with immobilized (PQQ)GDH and ferrocenecarboxylic acid and successive addition of glucose (100 mM HEPES pH 7; +0.1 V vs. Ag/ AgCl, 1 M KCl). Error bars result from 3 measurements.

However, light-controlled and glucose-dependent signal chains can be shown in a completely immobilized state of the enzyme and redox mediator on the QD electrodes, which passes over the need for the addition of redox molecules into solution. The fact that in this work mediated electron transfer chains with small redox molecules and enzymes could be established at QD electrodes can be considered as the first example of

biohybrid QD systems where communication is not based anymore on the analysis of natural co-substrates of the enzyme. This may pave the way not only for the connection of QDs with a large number of enzymes by using redox mediators for light-controlled detection schemes, but also for potential light-induced production of biochemicals. In addition, a spatially resolved immobilization of different enzyme/mediator systems in combination with a localized read-out by means of a light beam seems to be feasible and would allow the detection of different analytes in parallel.

Conclusions

In summary, this work has shown a new concept to connect redox enzymes with quantum dots by means of small redox molecules for the development of photobioelectrocatalytic systems. Here, the photocurrent generation of a QD electrode has been efficiently combined with the redox mediators hexacyanoferrate and ferrocenecarboxylic acid enabling concentration dependent determination of both compounds. While for hexacyanoferrate only oxidation can be observed by enhancing photocurrents, for ferrocenecarboxylic acid both oxidation and reduction at the QD electrode are feasible. Furthermore, photoluminescence experiments in solution indicate a strong interaction between the QDs and the redox mediators. Based on these findings light-triggered biocatalytic signal chains have been constructed on QD electrodes by immobilization of fructose dehydrogenase and (PQQ) glucose dehydrogenase. It can be shown that concentration-dependent photocurrents are detected in the presence of the redox mediator and by addition of the substrate. Consequently, due to enzymatic substrate conversion the redox mediator is reduced and can afterwards be oxidized at the light-excited QDs, resulting in an enhanced photocurrent out-put. Finally, it is also shown that by covalent coupling of ferrocenecarboxylic acid to (PQQ)GDH a procedure has been found to assemble the whole system on top of a QD electrode for driving the photoelectrochemical reaction via glucose consumption. Consequently, the biohybrid approach introduced here allows for light-triggered sugar oxidations, which can be beneficial for sensing applications and power generation in a photobioelectrochemical solar cell format. This principle may also pave the way for the connection of other redox enzymes with semiconductor nanoparticles by the use of small redox molecules.

Acknowledgements

This work was supported by the German Research Foundation (DFG grants Li 706/8-1, PA794/15-1). N. S. acknowledges a fellowship from HEC/DAAD. The authors want to thank Roche Diagnostics (Penzberg, Germany) and mainly Dr. Meier and Dr. von der Eltz for cooperation on supplying us with the GDH enzyme.

4.2 InGaN/GaN nanowires as a new platform for photoelectrochemical sensors – detection of NADH‡

Authors: **M. Riedel**, S. Hölzel, P. Hille, J. Schörmann, M. Eickhoff, F. Lisdat

Abstract: InGaN/GaN nanowire heterostructures are presented as nanophotonic probes for the light-triggered photoelectrochemical detection of NADH. We demonstrate that photogenerated electron-hole pairs give rise to a stable anodic photocurrent whose potential- and pH-dependences exhibit broad applicability. In addition, the simultaneous measurement of the photoluminescence provides an additional tool for the analysis and evaluation of light-triggered reaction processes at the nanostructured interface. InGaN/GaN nanowire ensembles can be excited over a wide wavelength range, which avoids interferences of the photoelectrochemical response by absorption properties of the compounds to be analyzed by adjusting the excitation wavelength. The photocurrent of the nanostructures shows an NADH-dependent magnitude. The anodic current increases with rising analyte concentration in a range from 5 µM to 10 mM, at a comparatively low potential of 0 mV vs. Ag/ AgCl. Here, the InGaN/GaN nanowires reach high sensitivities of up to 91 µA mM^{-1} cm^{-2} (in the linear range) and provide a good reusability for repetitive NADH detection. These results demonstrate the potential of InGaN/GaN nanowire heterostructures for the defined conversion of this analyte paving the way for the realization of light-switchable sensors for the analyte or biosensors by combination with NADH producing enzymes.

Introduction

Semiconductor nanostructures are core components in many light-driven applications such as solar cells,[114] water splitting systems,[14] optical assays,[328] electrochemiluminescence-based detection schemes,[329] light addressable potentiometric sensors[358] and photoelectrochemical (PEC) sensor systems.[16,17,75] The latter applications are mainly based on semiconductor nanoparticles (quantum dots) and provide high sensitivity with light-triggered read-out. Until now only a small number of semiconductor materials, such as CdS,[87,88,155,119,89] CdSe,[91,96] CdTe,[94] CdS/ZnS,[95] CdSe/ZnS,[81,97,98] PbS[359] and TiO_2[101,167] has been used for the fabrication of PEC sensors, thus demonstrating the need for improved synthesis protocols but also for a better understanding of the physical parameters that determine their photoelectrochemical characteristics. Operation is based on light-induced charge carrier separation, enabling electron transfer from a donor molecule via the QDs towards the electrode or in opposite direction from the electrode via QDs to an acceptor molecule.

‡ **Published in Biosensors and Bioelectronics:** M. Riedel, S. Hölzel, P. Hille, J. Schörmann, M. Eickhoff, F. Lisdat. InGaN/GaN nanowires as a new platform for photoelectrochemical sensors – detection of NADH. *Biosens. Bioelectron.* **2017**, 94, 298-304. DOI: 10.1016/j.bios.2017.03.022.

First bioanalytical applications of PEC systems concentrate on the determination of small molecules, which occur as product or cofactor in enzymatic reactions, thus enabling the construction of enzymatic signal chains. They are based on the detection of e.g. oxygen,[97,98] hydrogen peroxide,[119] 4-aminophenol,[155] acethylthiocholine,[87] dopamine[161] and nicotinamide adenine dinucleotide (NADH). Furthermore, first mediator-based approaches have been developed to connect enzymes with QDs for the detection of sugars[360]. Direct electrochemistry with few redox proteins and enzymes has also been established, providing the base to build up sensor systems for O_2^-,[91] sulfite, [89] lactate and nitrate detection,[88] as well as for light-driven drug conversion by P450 enzymes.[94]

Despite many reports in literature, the QD-based approaches still possess problems due to particle aggregation during electrode preparation[361,362] and due to the strong influence of particle immobilization on the electrode performance, including the ill-understood effect of surface ligands on the PEC-behavior.[119,363] Therefore the synthesis of semiconductor nanostructures under defined conditions by means of bottom-up approaches such as physical and chemical vapor deposition,[364,365] chemical bath deposition[366] and electrodeposition[111] could be beneficial to overcome such problems and result in PEC sensorial systems of improved performance.

Sensors for NADH detection have gained much attention, since the molecule is of biochemical and medical interest.[367] NADH shows slow electron transfer kinetics at untreated electrodes, resulting in the necessity to apply high overpotentials during sensing.[367] Also, surface fouling by accumulation of adducts during NADH oxidation has been observed.[368] To overcome these problems several approaches have been followed by electrode modifications with e.g. redox mediators[369–372] and nanomaterials such as carbon nanotubes,[373] gold nanoparticles[374] and nanoporous TiO_2.[167] QD-modified electrodes have demonstrated the advantages of PEC-based NADH oxidation, since high potentials can be circumvented and multiplexing becomes feasible.[81]

The group III-Nitride (III-N) materials have been demonstrated to exhibit excellent material properties with respect to applications in electrochemical sensors. In particular the high pH-sensitivity[375] and electrochemical stability[55,376] of the related surfaces have been employed in different field-effect based biochemical sensors.[375,377,378] Recently, we have combined these specific material properties with the photoluminescence characteristics of III-N nanostructures to realize nanophotonic probes for pH detection or for probing the charge state of biomembranes grafted on InGaN/GaN structures by changes in the photoluminescence properties.[379–381] Particularly InGaN/GaN nanowires (NW) with a large contact area with the surrounding analyte and which can be excited by visible light, present a promising approach for the realization of PEC sensor systems that has not been explored by now.

In this study, we show the light-triggered detection of NADH at low potential employing InGaN/GaN NW ensembles. First, we characterize the basic photocurrent behavior of the

NWs in terms of wavelength, potential and pH dependence. Furthermore, the different parts of the NW heterostructures are analyzed with respect to NADH oxidation enabling clarification of the influence of the indium insertion on the photoelectrocatalytic activity. In consequence, the suitability of these semiconductor nanostructures for defined photocurrent measurements, analyzing the solution composition, is demonstrated. We intend this study to establish a novel platform for light directed sensing which is able to combine advantages of photoluminescence and photoelectrochemistry.

Experimental Section

Reagents. 4-(2-Hydroxyethyl)piperazine-1-ethanesulfonic acid (HEPES, 99,5%), β-Nicotinamide adenine dinucleotide reduced (NADH, 97%) for trace analysis are purchased from Sigma-Aldrich (Steinheim, Germany). β-Nicotinamide adenine dinucleotide oxidized (NAD^+, 98%) has been obtained from SERVA Electrophoresis GmbH (Heidelberg, Germany). The NAD/NADH-Glo Assay has been purchased from Promega. All solutions are prepared with ultrapure water.

Instruments. Photoelectrochemical measurements are performed with an integrated photoelectrochemical workstation from Zahner (CIMPS) consisting of a potentiostat (Zennium) for the electrochemical control and a second potentiostat (PP211) for controlling the light source. For illumination, a light source with a peak at 449 nm (half width 13 nm) or a monochromator for the investigation of the wavelength-dependence are used. All experiments are performed in a homemade electrochemical cell with a three-electrode arrangement using an Ag/ AgCl, 1 M KCl reference electrode, a platinum counter electrode and the investigated sample as working electrode. Photochronoamperometric measurements are carried out at different potentials (vs. Ag/AgCl, 1 M KCl) with an illumination time of 10 s and magnetic stirring. For chopped light voltammetry measurements a potential range from -500 mV to +500 mV vs. Ag/AgCl, 1 M KCl with a scan rate of 5 mV s^{-1} and an illumination time of 5 s is investigated. Electrochemical impedance spectroscopy measurements are carried out at 0 mV vs. Ag/AgCl, 1 M KCl by applying an AC amplitude of 10 mV in the frequency range between 0.1 Hz and 10 kHz in the dark or under illumination (10 mW cm^{-2}). The simultaneous photocurrent and photoluminescence measurements are performed in a three-electrode setup with the NWs samples operated as working electrode, an Ag/AgCl (3 M KCl) reference electrode and a platinum counter electrode. Here, the potential of the NW substrate with respect to the electrolyte was controlled via a potentiostat in combination with an external voltage source.

Photoluminescence measurements of InGaN/GaN NW heterostructures are carried out using a laser diode with a wavelength of 405 nm for excitation. The photoluminescence is measured in reflexion and the signal is focused on a USB-CCD-spectrometer (3648 px CCD). The photoluminescence measurements of GaN-NWs (basic electrode without Indium) are performed in a PL microscope setup using a HeCd laser at λ=325 nm. The

excitation light is focused by a 20x UV objective. The emitted PL light is collected with the same objective and detected with a charge-coupled device (CCD) camera in combination with a 250 mm spectrometer equipped with a grating of 3600 lines mm^{-1}.

All experiments are performed in 100 mM HEPES buffer at different pH values at room temperature. NADH has been added to the buffer from a concentrated stock solution under constant stirring. Structural characterization was carried out by high resolution x-ray diffraction (HRXRD) using a PANalytical X´Pert PRO MRD diffractometer.

InGaN/GaN nanowire electrode preparation. Vertically aligned InGaN/GaN nanowire heterostructures are grown on low resistivity n-type Si (111) substrates by plasma-assisted molecular beam epitaxy (PAMBE) under nitrogen-rich conditions. The nanowire heterostructures consist of a GaN nanowire base with a length of nominally 200 nm, grown according to a self-assembled and catalyst-free growth process,[382] followed by an extended InGaN section with a nominal length of 350 nm. The growth of the InGaN section with a detailed structural and optical analysis of InGaN/GaN NW heterostructures is presented in reference.[383] Sample preparation involved the deposition of an Ohmic backside contact (80 nm Al/100 nm Ag) by thermal evaporation onto the Si substrate after removing the native oxide layer in buffered HF solution.

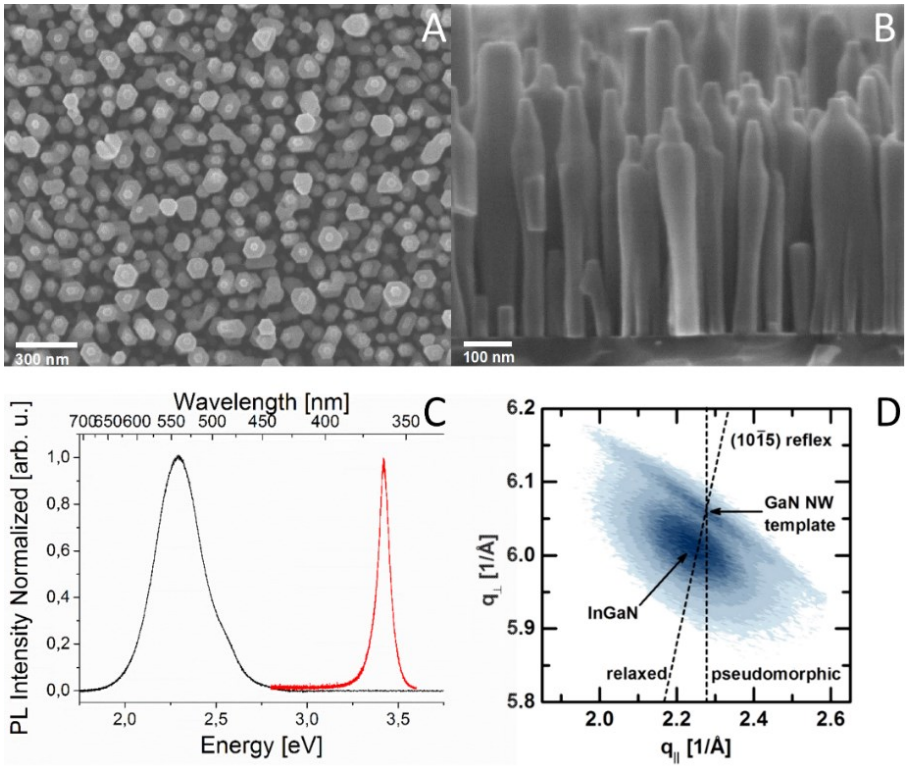

Fig. 1. Growth and optical characterization of InGaN/GaN NWs. Top **(A)** and side view **(B)** SEM images of InGaN NWs grown on GaN NW templates on n-Si(111) substrate. **(C)** Normalized photoluminescence spectra of InGaN/GaN (black curve) and GaN NWs (red curve) at room temperature. The excitation wavelengths for InGaN/GaN NWs are 405 nm and for GaN NWs are 325 nm, respectively. **(D)** Reciprocal space map of the (1015) reflex of an InGaN/GaN NW heterostructure. GaN and InGaN reflexes are labeled and the InGaN is relaxed to the GaN template indicated by the tilted dashed line. The structural analysis has been performed with HRXRD.

Results and discussion

Characterization of nanowires. The morphology of the InGaN/GaN nanowire electrode is presented in the SEM analysis in Fig. 1. The NWs have a hexagonal shape with an average diameter of 72 ± 20 nm and a length of about 550 nm, resulting in a high surface-to-volume ratio. In detail the GaN base, which serves as a template for the growth of the InGaN section corresponds to 36% of the total length (schematically shown in Fig. 2A) and provides an electrical contact of the InGaN NW to the substrate. Optical properties of InGaN/GaN and GaN base NW electrodes are investigated by photoluminescence spectroscopy at room temperature. While the GaN base gives rise to an emission peak at 363 nm, the InGaN part of the NW heterostructures shows an emission band around 535 nm (Fig. 1C).

HRXRD analysis has been performed for structural characterization of the nanowire electrodes. Fig. 1D shows the reciprocal space map (RSM) of the asymmetric (1015) reflex of the InGaN/GaN nanowire array. The reflexes plotted in the figure correspond to the GaN NW template and the InGaN top section. The position of the InGaN reflex relative to the GaN reflex reveals that the InGaN part is not compressively strained but has relaxed to its bulk lattice parameters. This is indicated by the dashed lines in the figure. The composition of the InGaN section has been estimated from the lattice parameter extracted from reciprocal space maps yielding an In-content of ≈10%.

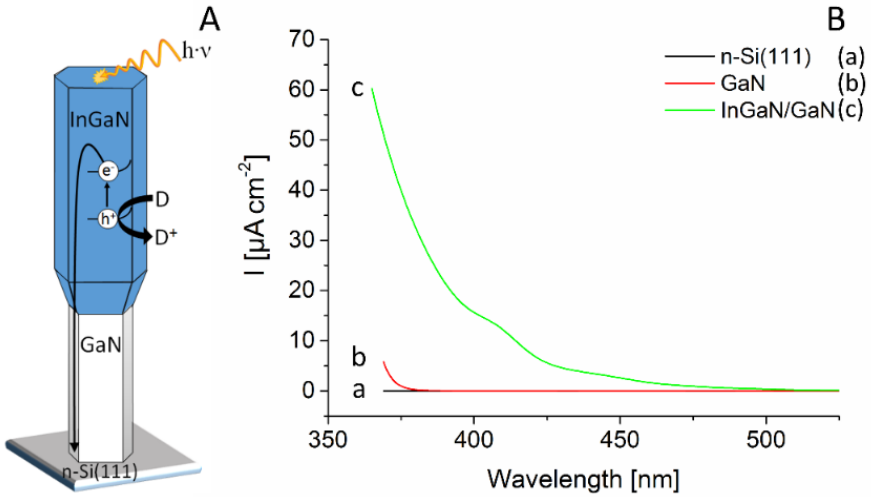

Fig. 2. (A) Schematic illustration of the charge carrier separation in InGaN/GaN NWs grown on Si substrate as a result of illumination. **(B)** Wavelength-dependence of the photocurrent of InGaN/GaN NWs grown on n-Si substrate (c), GaN NWs grown on n-Si substrate (b) and pure n-Si substrate (a). (100 mM HEPES pH 7; 5 mW cm^{-2}; 0 mV vs. Ag/AgCl, 1 M KCl).

Basic photoelectrochemical characterization of the InGaN/GaN NWs is performed in 100 mM HEPES pH 7. The wavelength-dependent photocurrent of the bare n-Si substrate (here the NW growth process has been interrupted directly after the initial nitridation step), and the GaN NW base have also been analyzed in comparison to the InGaN/GaN NW structures, as shown in Fig. 2B. The InGaN/GaN NWs exhibit an onset of a distinct

anodic photocurrent at a wavelength of around 500 nm that increases in magnitude with decreasing wavelength. In comparison the onset of the photocurrent for the GaN NW base electrode is observed below 380 nm and the bare n-Si electrode exhibits only negligible photocurrents in the entire wavelength range. These results show that the InGaN section of the InGaN/GaN NW heterostructures can be selectively excited, while parasitic photocurrents from the GaN NW base or from the Si substrate do not have to be considered. Furthermore, the wavelength study demonstrates that a photocurrent of sufficient magnitude can be generated in a wide wavelength range, allowing the adjustment of the excitation wavelength to the analyte to be detected and thus avoiding its direct excitation or the degradation of biomolecules by UV light.

The photocurrent kinetics of the InGaN/GaN NW electrodes are investigated by modulation of the light source with different frequencies and show a clear decrease of the photocurrent for frequencies above 5 Hz (Fig. S1). Since the electron transport inside the NWs can be excluded to be the limiting part, the electrode/donor electron transfer seems to slow down the system at higher modulation frequencies. However, this does not limit the applicability for biosensors.

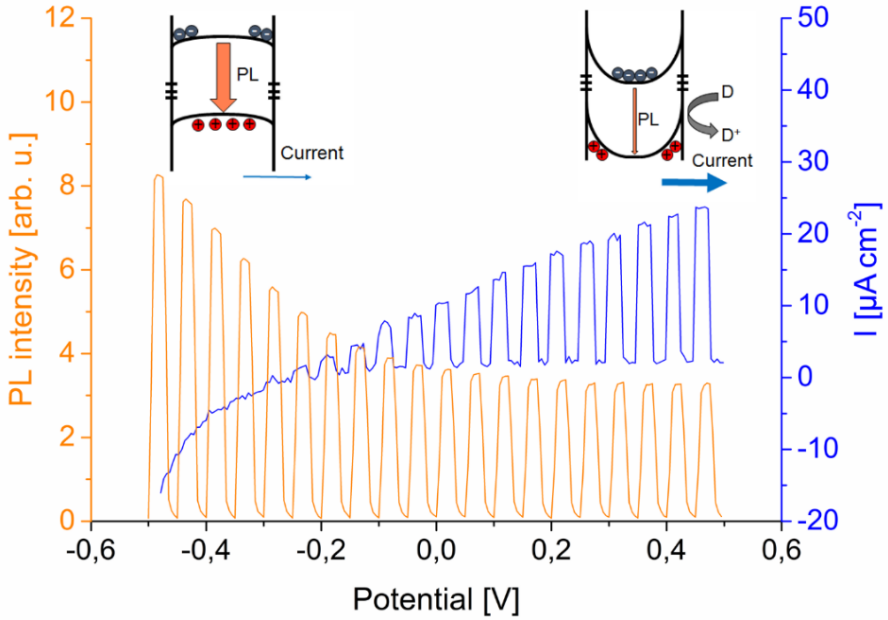

Fig. 3. Bias-dependence of the photocurrent and the photoluminescence intensity of an InGaN/GaN NW heterostructure ensemble. At cathodic bias at the nanowire-electrolyte contact, the PL intensity increases, because of hole concentration inside the NWs (left insert), while no photocurrent is present. For anodic bias a strong increase of the photocurrent due to photogenerated holes at the NW surface is found. (100 mM HEPES pH 7; light source 405 nm; output power 100 mW; light pulses of 5 s, scan rate 5 mV s^{-1}; potential vs. Ag/AgCl, 3 M KCl).

Although high photocurrents have been obtained with UV excitation further characterization has been performed with 449 nm ± 5 nm, since even under these conditions well defined photocurrents of sufficient magnitude are obtained. To investigate the bias-dependence of the InGaN/GaN NW photocurrent chopped light voltammetry has been performed, revealing exclusively anodic photocurrents starting at

around -400 mV vs. Ag/AgCl and enhancing with increasing applied potential (Fig. 3). This behavior can be explained by the formation of a Schottky barrier at the n-semiconductor/electrolyte interface. The potential-dependent photocurrent behavior is found to be independent on the wavelength used during illumination (Fig. S2). The photoelectrochemical properties of InGaN/GaN NWs are dominated by the recombination characteristics of photogenerated electron-hole pairs that are determined by the bias-dependent surface band bending in the NW electrodes. For anodic bias, the upward surface band bending is increased and the depletion layer is extended further into the NW, resulting in a more efficient separation of photogenerated electron-hole pairs and an increasing anodic photocurrent driven by holes as minority carriers. In contrast, the photoluminescence (PL) intensity for anodic bias decreases, as the confinement of holes as minority carriers inside the NWs is weakened.[381] With increasing cathodic bias the confinement of the holes inside the NW is improved, resulting in an increase of the radiative recombination rate, i.e. an increase of the PL intensity and a decrease of the photocurrent. Consequently, while the bias-dependence of the PL allows the optical detection of charge transfer at cathodic potentials, variations in the photocurrent enables photoelectrochemical sensing at anodic bias. Thus, the simultaneous measurement of the photocurrent and the PL with the InGaN/GaN sensing platform provides an additional tool to analyze and evaluate complex electron transfer schemes at the semiconductor/solution interface.

The influence of the excitation intensity on the amplitude of the anodic photocurrent is shown in Fig. 4A for different bias potentials. Here, an increasing anodic photocurrent with increasing light intensity as well as with increasing potential is observed. At small bias and low light intensities stable and fast establishing photocurrents are observed. The application of anodic potentials above 100 mV vs. Ag/AgCl also results in well-defined photocurrents but with a small drop of the current during illumination. In order to suppress the influence of such effects measurements have been carried out at small light intensities, e.g. 10 mW cm^{-2}, that already provide sufficient and stable photocurrents suitable for PEC detection in the entire investigated potential range.

The influence of the pH value on the photocurrent has been investigated by chopped light voltammetry and photochronoamperometric measurements (Fig. 4B and S3). For increasing pH, the photocurrent increases as further enhancement of the upward band bending in the NWs promotes the oxidation process. For more acidic conditions (lower pH) the photocurrent decreases, as the surface band bending is reduced and thus, the proton-hydroxide balance has a strong influence on the photocurrent magnitude, but also photocurrent kinetics. This explanation is in good agreement with previous findings on an increase of the PL intensity in more acidic pH.[381] Further enhancement of the photocurrent could also be caused by a higher photocatalytic conversion efficiency of hydroxide ions compared to water molecules, as it has also been shown for nanostructured

TiO_2 films.[384] These results may illustrate one advantage of InGaN/GaN NWs which allow pH detection by PEC and PL measurements.

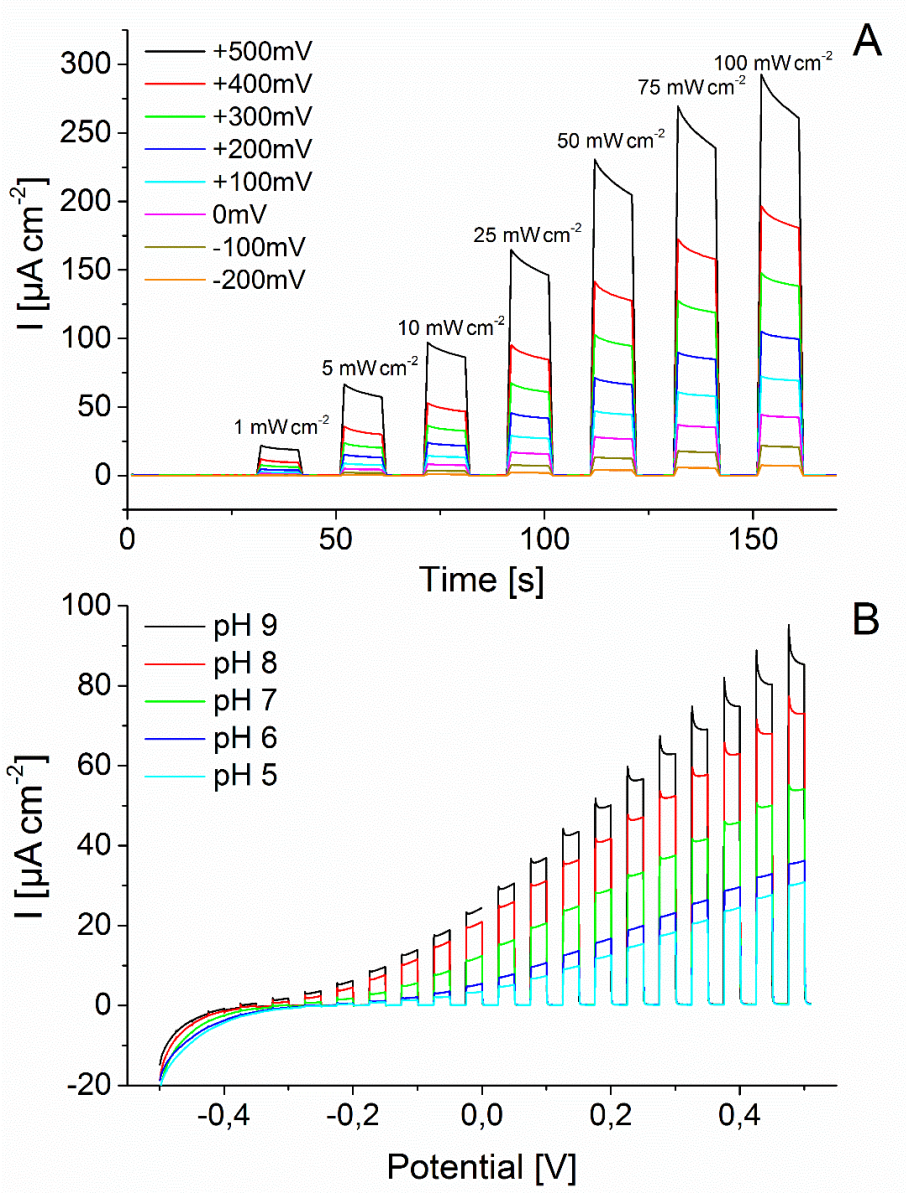

Fig. 4. (A) Photochronoamperometric measurements of an InGaN/GaN NW electrode at different light intensities and potentials. (100 mM HEPES pH 7; light source 449 nm ± 5 nm; light pulses of 10 s; potential vs. Ag/AgCl, 1 M KCl) **(B)** Chopped light voltammetry of the InGaN/GaN NWs grown on Si substrate in dependence on the solution pH. (100 mM HEPES; light source 449 nm ± 5 nm; 10 mW cm^{-2}; light pulses of 5 s, scan rate 5 mV s^{-1}; potential vs. Ag/AgCl, 1 M KCl).

Stability tests performed at pH 7 and 0 mV vs. Ag/AgCl with a light intensity of 10 mW cm^{-2} reveal that after 4-5 light pulses of 10 s a stable photocurrent is obtained, thus allowing precise evaluation of the baseline signal (before adding any analyte to the solution) (Fig. S4). Even after continuous illumination of 20 min only a minor photocurrent decrease of just 9% is observed that almost regenerates after returning to the initial pulse mode. However, it should be noted that the equilibration time extends with increasing potential and light intensity. Thus, a moderate light intensity of 10 mW cm^{-2} is beneficial and has been used for photoelectrochemical sensing of NADH.

Photoelectrochemical NADH sensing. One the basis of well-defined photocurrent generation, the photocatalytic oxidation of NADH at the InGaN/GaN nanowire heterostructure electrodes has been investigated. Since NADH possesses a strong absorption maximum at 340 nm, the photocurrents before and after addition of 1 mM NADH are investigated at different wavelengths. As shown in Fig. 5, the utilization of an illumination wavelength of 449 nm results in a photocurrent increase of about 250% (ΔI=16 µA cm^{-2}) in the presence of NADH, thus demonstrating the light-induced oxidation of NADH at the NWs. For a decreasing illumination wavelength the NADH-induced relative photocurrent is strongly attenuated. At 369 nm even a complete suppression of the initial photocurrent is found. This behavior is attributed to the strong absorbance of NADH in this spectral range and can be explained by a joint excitation of the electrode and the molecule to be analyzed, resulting in different electron transfer reactions compared to the ground state. These results demonstrate that the adjustment of the optical properties of the semiconductor to the absorption properties of the analyte is an essential tool for the design of efficient PEC sensor systems. Consequently, wavelengths above 398 nm can be used for the detection of NADH oxidation.

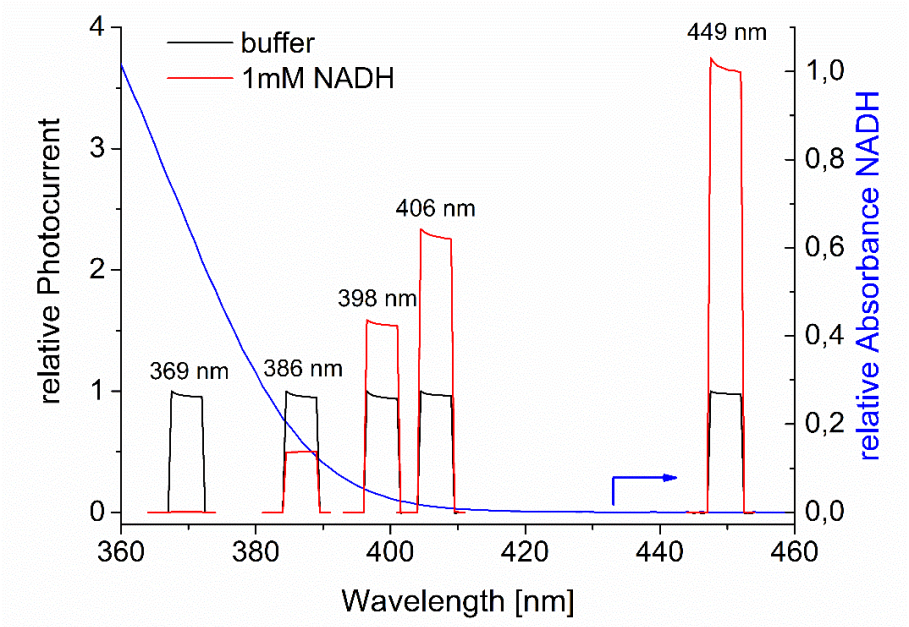

Fig. 5. Photocurrent response of an InGaN/GaN NW electrode before (black line) and after addition of 1 mM NADH (red line) at different wavelength. For a better comparison, the photocurrents are represented relative to the initial photocurrent I_0 at the respective wavelength; black line: I_0/I_0; red line: $I_{1\ mM\ NADH}/I_0$. Additionally, the relative absorption of NADH over the investigated wavelength range is illustrated as a blue curve. (100 mM HEPES pH 7; 10 mW cm^{-2}; light pulses of 10 s; 0 mV vs. Ag/AgCl, 1 M KCl).

In contrast to that, the addition of 1 mM NAD^+ - the oxidized form of the nucleotide - does not result in a photocurrent change, neither at 369 nm nor at 449 nm (Fig. S5 and S6). This shows that NADH can be selectively detected in the presence of the oxidized cofactor with InGaN/GaN NWs.

In order to verify the location of light-induced NADH oxidation at the InGaN/GaN NWs and to exclude a participation of the GaN base and the n-Si electrode to the NADH dependent signal, control experiments have been performed. Here for both, the GaN-base and the n-Si electrode a very small initial photocurrent and a tiny photocurrent increase in the presence of 1 mM NADH are observed, corresponding to about 0.3% of the signal obtained for the InGaN/GaN NW heterostructures (Figs. S7 and S8). Thus, the oxidation of NADH almost exclusively occurs at the InGaN section of the NW structure, as schematically shown in Fig. 2A. Furthermore, analysis of the solution after a defined time period of the photoelectrochemical experiment by means of an enzymatic assay demonstrate that NAD^+ is the main product of light-induced NADH oxidation at the InGaN/GaN NWs (see SI for further details).

We have also employed electrochemical impedance spectroscopy to analyze the charge transfer and transport at the InGaN/GaN NWs in the dark and under illumination with and without NADH (see Fig. S9). Due to the insulating properties of the NWs in the dark (i.e. no charge carrier generation) quite high impedance signals can be observed in buffer solution. Similar impedance spectra are obtained in the presence of NADH. Under illumination the impedance signal drastically decreases due to the light-induced charge carriers inside the InGaN/GaN NWs. A further decrease of the impedance can be observed in the presence of 1 mM NADH (under illumination) due to the additional supply of electrons.

To further evaluate the applicability of the InGaN/GaN NWs for the NADH sensing, we have investigated the potential- and pH-dependence of the photocurrent (Fig. 6). A first signal enhancement of around 1.5 μA cm^{-2} in the presence of 1 mM NADH is already observed at a potential of -300 mV vs. Ag/AgCl, which is remarkably low compared to other electrochemical and photoelectrochemical systems.[81,167,373,374] Further increase of the applied potential results in an increased NADH response up to an average photocurrent of 36 μA cm^{-2} at +500 mV vs. Ag/AgCl, allowing a reliable detection of NADH in a wide potential range. The observed pH-dependence (Fig. 6B) shows that InGaN/GaN NWs can be operated in moderate basic and acidic solutions, thus extending the application range for the combination with enzymes, as dehydrogenases show structural stability and catalytic activity at different pH values. A slightly higher NADH-dependent photocurrent can be detected in the acidic and neutral region. This is in contrast to what is expected, since it is known that the NADH oxidation is a 2 e^- process, accompanied by proton release, which can be thus expected to proceed preferably in alkaline media.[385] However, enhanced electrochemical NADH signals with decreasing pH have also been found in approaches with different redox mediators,[369,371,372] demonstrating the complex redox reaction of NADH at electrode surfaces. The results indicate that the rate-limiting process is not the proton release, but the electron transfer itself. However, analytical detection of the molecule is possible in the entire pH range studied.

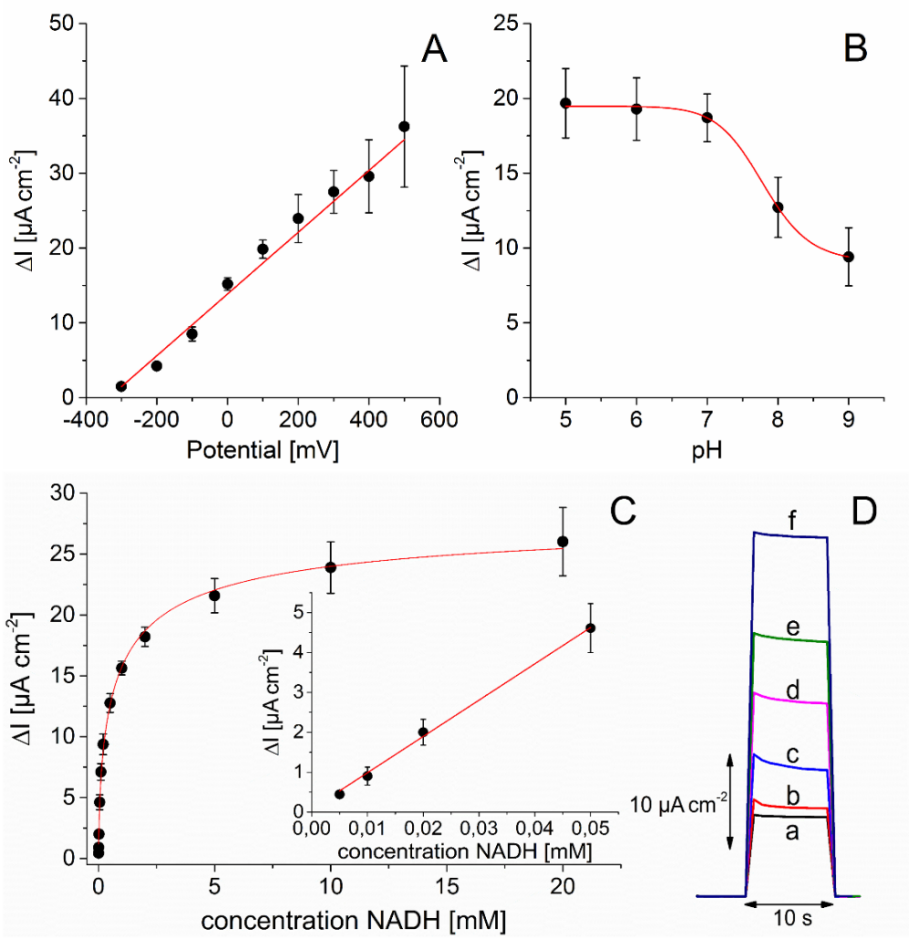

Fig. 6. (A) Photocurrent change ΔI of InGaN/GaN NW electrodes after addition of 1 mM NADH as a function of the applied potential. (100 mM HEPES pH 7; light source 449 nm ± 5 nm; 10 mW cm^{-2}; light pulses of 10 s; potential vs. Ag/AgCl, 1 M KCl; n=3 electrodes) **(B)** Photocurrent change ΔI of InGaN/GaN NW electrodes after addition of 1 mM NADH as a function of the pH in solution. (100 mM HEPES; light source 449 nm ± 5 nm; 10 mW cm^{-2}; light pulses of 10 s; 0 mV vs. Ag/AgCl, 1 M KCl; n=3 electrodes) **(C)** Photocurrent change ΔI of InGaN/GaN NW electrodes with increasing NADH concentration (n=3 electrodes) and time course of the photocurrent **(D)**. (a=0 µM, b=20 µM, c=100 µM, d=500 µM, e =2 mM, f =20 mM; 3 light pulses after substrate addition; 100 mM HEPES pH 7; light source 449 nm ± 5 nm; 10 mW cm^{-2}; light pulses of 10 s; 0 mV vs. Ag/AgCl, 1 M KCl).

Furthermore, the control of the light intensity used during illumination provides an additional tool to adjust the NADH dependent photocurrent response (Figs. S10 and S11).

The effect of the NADH concentration on the photocurrent response of the InGaN/GaN NWs has also been investigated and is shown in Fig. 6C. Even if NADH oxidation is already feasible at -300 mV vs. Ag/ AgCl we have chosen a slightly higher potential of 0 mV vs. Ag/AgCl to improve the signal-to-noise ratio (S/N). A linear photocurrent enhancement with a sensitivity of 91 µA mM^{-1} cm^{-2} NADH is found between 5 and 50 µM. The detection limit is estimated to be 1 µM (S/ N=3), revealing sufficient sensitivity for the combination with many important dehydrogenases e.g. glucose dehydrogenase or glycerol dehydrogenase. The relative change in photocurrent increases up to a concentration of 10 mM NADH and a half maximum photocurrent is reached at 0.73 mM. Thus, in comparison to other photoelectrochemical approaches the InGaN/GaN

NWs show a similar detection limit, but with a broader dynamic range at a small bias without the introduction of additional modifications on the semiconductor surface.[81,95,167,374] It should also be noted here that the basic current (in the dark) is not changing upon addition of NADH to the solution which demonstrates that the oxidation process is photo-induced at the InGaN part of the nanowires only (Fig. S12). Another observation is that after illumination and photoelectrochemical NADH oxidation the current returns fast to its initial state and the electrode can be used for further experiments. To demonstrate the repeatability of NADH detection with the InGaN/GaN NWs the detection of 200 µM NADH has been repeated 10 times with one electrode (see Fig. S13). Only a small standard deviation of 4.1% has been found, demonstrating the good reusability of the sensor for NADH detection. In contrast to other reports on NADH detection no electrode altering by effects like surface fouling (accumulation of adducts during the NADH oxidation) have been observed by the usage of InGaN/GaN NWs for sensing.

In order to investigate the influence of common interfering molecules on the photoelectrochemical detection of NADH, first experiments have been performed in the presence of ascorbic acid, uric acid and urea (200 µM each). While a clear signal response can be obtained after addition of 200 µM NADH, the successive addition of interfering molecules results only in negligible photocurrent changes (see Fig. S14). In contrast, a further increase of the NADH concentration can clearly be determined by an enhanced photocurrent. These results suggest that the InGaN/GaN NWs enable a sufficient discrimination of NADH in the presence of interfering biomolecules. Also the dark current is only negligibly affected by the interferences. Therefore, the elimination of unwanted electrode reactions improves the NADH dependent signal out-put under illumination. However, further work is needed to realize the application of the NWs in complex biological media.

In consequence, NADH detection and the analysis of a large number of substrates from different dehydrogenase reactions become feasible with the InGaN/GaN NWs, but also the realization of coupled multi-enzyme assays. In such systems an analyte can be specifically detected via sequential enzymatic conversions, resulting in NADH production or consumption, as has recently been exemplified for the analysis of GMP [95].

Conclusion

In this study InGaN/GaN nanowire heterostructures are investigated with respect to their application as photoelectrodes for analytical purposes. Stable and exclusively anodic photocurrents are selectively excited in the InGaN region starting from -400 mV vs. Ag/AgCl in the pH range between 5 and 9. This behavior is due to the Schottky-type barrier at the n-semiconductor-electrolyte interface and can be correlated to the photoluminescence properties of the structure.

In the presence of NADH a concentration-dependent photocurrent enhancement due to photocatalytic oxidation can be observed, allowing the detection in the range from 5 µM to 10 mM. The NW heterostructures provide an excellent sensitivity of 91 µA mM^{-1} cm^{-2} for NADH by applying a low electrode bias (0 mV vs. Ag/AgCl). Experiments at different wavelengths demonstrate the importance to adjust the excitation wavelength in order to avoid interferences by the optical properties of the analyte and/or prevent biomolecule degradation. By comparing InGaN/GaN NWs with GaN NWs only for the InGaN/GaN NWs a photocatalytic activity for the NADH oxidation is found. Consequently, InGaN/GaN NW structures pave the way for the combination with a wide variety of dehydrogenases to build up light-triggered biosensor electrodes. An enhancement of the functionality can be achieved by combining the photocurrent read-out in the anodic bias range with the photoluminescence read-out at cathodic bias. Furthermore, the spacing between the nanowires suppresses lateral diffusion of charge carriers, so that multiplex approaches by immobilization of different enzymes in separated spots and light-assisted read-out with high spatial resolution can be achieved. Hence, InGaN/ GaN NW electrodes provide a defined interface between the active semiconductor component and the underlying electrode support, resulting in a good stability and reproducibility for analytical applications.

Acknowledgements

This work was supported by the DFG (Li 706/8-1). Authors from JLU acknowledge financial support within the LOEWE program of excellence of the Federal State of Hessen (project initiative STORE-E). S. L. particularly acknowledges support from the “Graduiertenstipendium” of the Justus-Liebig-Universität Gießen.

4.3 Integration of enzymes in polyaniline-sensitized 3D inverse opal TiO_2 architectures for light-driven biocatalysis and light-to-current conversion[§]

Authors: **M. Riedel** and F. Lisdat

Abstract: Inspired by natural photosynthesis, coupling of artificial light-sensitive entities with biocatalysts in a biohybrid format can result in advanced photobioelectronic systems. Herein, we report on the integration of sulfonated polyanilines (PMSA1) and PQQ-dependent glucose dehydrogenase (PQQ-GDH) into inverse opal TiO_2 (IO-TiO_2) electrodes. While PMSA1 introduces sensitivity for visible light into the biohybrid architecture and ensures the efficient wiring between the IO-TiO_2 electrode and the biocatalytic entity, PQQ-GDH provides the catalytic activity for the glucose oxidation and therefore feeds the light-driven reaction with electrons for an enhanced light-to-current conversion. Here, the IO-TiO_2 electrodes with pores of around 650 nm provide a suitable interface and morphology needed for the stable and functional assembly of polymer and enzyme. The IO-TiO_2 electrodes have been prepared by a template approach applying spin coating, allowing an easy scalability of the electrode height and surface area. The successful integration of the polymer and the enzyme is confirmed by the generation of an anodic photocurrent, showing an enhanced magnitude with increasing glucose concentrations. Compared to flat and nanostructured TiO_2 electrodes, the three-layered IO-TiO_2 electrodes give access to a 24-fold and 29-fold higher glucose-dependent photocurrent due to the higher polymer and enzyme loading in IO films. The three-dimensional IO-TiO_2|PMSA1|PQQ-GDH architecture reaches maximum photocurrent densities of 44.7 ± 6.5 µA cm^{-2} at low potentials in the presence of glucose (for a three TiO_2 layer arrangement). The onset potential for the light-driven substrate oxidation is found to be at -0.315 V vs Ag/AgCl (1 M KCl) under illumination with 100 mW cm^{-2}, which is more negative than the redox potential of the enzyme. The results demonstrate the advantageous properties of IO-TiO_2|PMSA1|PQQ-GDH biohybrid architectures for the light-driven glucose conversion with improved performance.

Introduction

Exploiting light energy for bioelectrochemical applications has triggered extensive research efforts in recent years. Different directions can be seen in the development, such as conversion of solar into electrical energy,[114,386,387] usage of light for synthesis of valuable chemicals,[9,388] or for controlling electrochemical reactions at electrode interfaces

[§] **Published in ACS Applied Materials and Interfaces:** M. Riedel and F. Lisdat. Integration of enzymes in polyaniline-sensitized 3D inverse opal TiO_2 architectures for light-driven biocatalysis and light-to-current conversion. *ACS Appl. Mater. Interfaces* **2018**, 10, 267-277. DOI: 10.1021/acsami.7b15966.

in photoelectrochemical sensors.[16,17,389] Recently, the construction of light-driven biohybrid architectures on electrodes by the connection of light-sensitive elements with enzymes has shown to be promising for the design of advanced photobioelectrochemical systems.[82,83,95,97,98,138,168,360]

Upon illumination, electron-hole pairs are generated inside the light-sensitive element, allowing the electron transfer reaction with an electrode and also with enzymes. Photoinitiated electrons can be transferred to the enzyme, resulting in reduction of the substrate and the formation of a cathodic photocurrent. On the other hand, electrons from the biocatalytic conversion can fill up the photoinitiated hole for the generation of an anodic photocurrent. In both cases, the light-triggered initiation of highly energetic charge carriers is used to drive the biocatalytic reaction. This can be exploited in light-driven sensing[16] but also opens the way for the realization of self-powered point-of-care devices that rely on sun light.[332] This approach can be used to overcome limitations in applicable potentials to enzyme electrodes for oxidation and reduction of substrates or for an increased power output in photobioelectrochemical fuel cells.

Besides the integration of biocatalysts with intrinsic light sensitivity, such as native photocatalytic enzymes (e.g., photosystem I and II),[83,136,137] some light-insensitive enzymes, such as hydrogenase,[138] glucose oxidase,[82,83,97] sarcosine oxidase,[98] sulfite oxidase,[89] PQQ glucose dehydrogenase,[360] fructose dehydrogenase,[360] and cytochrome P450,[210,94] have been integrated in functional light-driven devices. Semiconductor nanostructures, such as quantum dots (QDs)[89,95,97,98,360] and nanowires[390] or organic dyes,[80,82] have shown the potential for photonically wiring light-insensitive enzymes. Therefore, different approaches have been developed to follow the biocatalytic reaction under illumination, including the detection of enzymatic cosubstrates and products,[97,98,95,87,119] or the detection of mediated or direct electron transfer reactions between the enzyme and the light-sensitive element.[82,83,88,89,96,360] However, the light-to-current conversion is currently rather low and a fast communication between enzymes and light-sensitive elements in a complete immobilized fashion and without the need for additional cofactors or mediators remains challenging.

For most photobioelectrochemical approaches, the photosensitive material is attached to conductive metal or heavily doped semiconductor electrodes (e.g., indium tin oxide (ITO)) and allows cathodic or anodic electron transfer processes, depending on the applied potential.[95,360] To favor the anodic direction, the utilization of the semiconductor TiO_2 has gained great interest for the construction of electrodes in solar cell and photocatalytic applications.[386,387,391] Here, the generation of electron-hole pairs is limited to the excitation with UV light. To expand the excitation range to visible light, TiO_2 is often combined with nanomaterials, such as QDs,[114] dyes[386,387] or polymers,[392] which are able to inject excited electrons into the conduction band (CB) of TiO_2, resulting in a generation of exclusively anodic photocurrents.

The idea of the present study is to use a polymer as a TiO_2 sensitizer and simultaneously as a wiring agent between an enzyme and TiO_2. We want to exploit that polyanilines enable a charge transfer to TiO_2 under visible light illumination[393] but also provide a beneficial interface for the connection with various redox enzymes.[394,64,289,323,395] Until now, the combination of TiO_2 with polyanilines and enzymes in a functional light-driven biohybrid system has not been shown.

Consequently, we have investigated the construction of macroporous inverse opal TiO_2 (IO-TiO_2) electrodes by a simple spin-coating procedure as platform for the incorporation of a sulfonated polyaniline (PMSA1) and the enzyme PQQ glucose dehydrogenase (PQQ-GDH) for the light-directed glucose oxidation. The final IO-TiO_2|PMSA1|PQQ-GDH architectures demonstrate the feasibility to transfer electrons from the biocatalytic reaction via the polymer toward the electrode under illumination. This photoelectrochemical signal cascade enables glucose oxidation at potentials below the enzymes redox potential for sensing and for an enhanced light-to-current conversion.

Experimental section

Materials. D-Glucose, 2-(N-morpholino)ethanesulfonic acid (MES), calcium chloride ($CaCl_2$), 2,6-dichlorophenolindophenol (DCPIP), and polystyrene latex beads (LB) (diameter 0.8 μm) were purchased from Sigma-Aldrich (Steinheim, Germany). HNO_3-stabilized TiO_2 anatase phase nanoparticles (NPs) with an average size of 4-8 nm were from PlasmaChem GmbH (Berlin, Germany). Poly(ethylene glycol) (PEG4000) was purchased from Carl Roth GmbH + Co. KG (Karsruhe, Germany). Pyrroloquinoline quinone disodium salt was obtained from Wako Chemicals GmbH (Neuss, Germany). PQQ glucose dehydrogenase (PQQ-GDH) (Acinetobacter calcoaceticus) was kindly gifted by Roche Diagnostics GmbH. Poly(2- methoxyaniline-5-sulfonic acid)-co-aniline polymer (PMSA1) was synthesized as reported before.[287,396]

Preparation of Macroporous IO-TiO_2 Electrodes. Fluorine doped tin oxide (FTO) slides were cleaned by ultrasonication in deionized water, isopropanol, and acetone for 15 min each. The cleaned electrodes were placed on a spin coater (SCC-200, KLM) directly after drying. A dispersion of 100 mg mL^{-1} TiO_2 nanoparticle (NP) and 100 mg mL^{-1} latex beads (LB, diameter 0.8 μm) was prepared in a 1:1 H_2O/ethanol mixture unless stated otherwise. First, 20 mg of TiO_2 nanoparticles was suspended in 200 μL volume, which results in a translucent TiO_2 NPs solution. Simultaneously, 1 mL of 20 mg mL^{-1} LB ethanol suspension was centrifuged at 25 000 g for 8 min. The supernatant was removed, and the LB pellet is resuspended in the before prepared TiO_2 NP solution. The mixture was ultrasonicated for at least 45 min in an ice bath before use. Fifteen microliters of the TiO_2 NP/LB mixture was dropped on the cleaned FTO slides and spin coated at 40 rps for 2 min unless stated otherwise. Subsequently, the area was limited to a circle with a diameter of 0.3 cm by wiping away the superfluous amount with a tissue.

The as-prepared electrodes were sintered at 450 °C for 1 h. For the preparation of further layers, the whole procedure was repeated.

The same preparation procedure was used for the construction of TiO_2 electrodes without LB or with poly(ethylene glycol) (PEG) by simply leaving out the LBs or exchanging the LB by the same amount of PEG (100 mg mL^{-1}). The molecular weight of the PEG used corresponds to around 4000 g mol^{-1}.

Preparation of Macroporous IO-TiO_2|PMSA1|PQQ-GDH Electrodes. The sintered macroporous IO-TiO_2 electrodes were first incubated in 2 mg mL^{-1} PMSA1 (dissolved in 5 mM MES + 5 mM $CaCl_2$ pH 6.5) for 1 h. For investigating the Ca^{2+} influence on the polymer assembly, the incubation was performed under different Ca^{2+} concentrations (5, 50, 100, and 200 mM) with 2 mg mL^{-1} PMSA in 5 mM MES pH 6.5. The polymer-modified IO-TiO_2 electrodes were subsequently rinsed with buffer to remove the weakly bound polymer. Before enzyme immobilization, the apo-enzyme was reconstituted with PQQ by a PQQ/enzyme ratio of 1 for 1 h in the dark. To assemble the PQQ-GDH on the PMSA1-modified IO-TiO_2 electrodes, a 2 mg mL^{-1} enzyme solution (5 mM MES + 5 mM $CaCl_2$ pH 6.5) was incubated for 1 h.

Estimation of the Enzyme Concentration. For the estimation of the PQQ-GDH concentration immobilized on the TiO_2 electrodes, we have assumed that the enzyme activity is not influenced by the immobilization procedure. The enzyme was first extracted with buffer of high ionic strength (5 mM MES + 200 mM KCl pH 6.5) by extensive rinsing to ensure a complete detachment of the adsorbed enzyme. Afterward, the activity of the removed enzyme was determined in a spectroscopic assay with DCPIP (600 nm) and correlated to experiments performed with a defined enzyme amount. Thus, we were able to estimate the enzyme concentration.

Determination of the Polymer Concentration. The polymer amount immobilized to the electrodes was determined by UV/vis. The PMSA1-modified IO-TiO_2 electrodes were dried and afterwards extensively rinsed with 10 µL of dimethyl sulfoxide (DMSO). The successful polymer removal was achieved after 1 min and could be recognized by a discoloration (from green to white) of the structure. After extraction of the polymer, the solution was spectroscopically investigated with a NanoDrop 2000 (Thermo Fisher Scientific Inc.), allowing the analysis of small sample volumes. The obtained data were correlated to the spectroscopic data of a known concentration of PMSA1 dissolved in DMSO. For the determination of the PMSA1 concentration, we have used the characteristic polymer peak at 320 nm.

Photoelectrochemical Experiments. Photoelectrochemical experiments were performed with an integrated photoelectrochemical workstation from Zahner (CIMPS). The device consists of a potentiostat (Zennium) for the electrochemical control and a second potentiostat (PP211) for controlling the light source. A white light source was

applied for the illumination of the electrodes unless stated otherwise. For wavelength-dependent experiments, a monochromator (Polychrome V, Till Photonics) with a bandwidth of 15 nm was used. The measurements were carried out in a homemade electrochemical cell in a three-electrode arrangement consisting of an IO-TiO_2 working electrode, an Ag/AgCl, 1 M KCl reference electrode, and a platinum wire as the counter electrode.

Scanning Electron Microscopy (SEM). The SEM images were prepared with a scanning electron microscope (JSM-6510; JEOL) at an acceleration voltage of 20 kV, with a 2500×, 8000×, and 25 000× magnification. For the determination of the layer height of the IO-TiO_2 architectures, a part of the structures was scratched away and the SEM images were recorded under an angle of 45° with a 2500× magnification.

Results and discussion

In this study, we have explored the construction of a biohybrid architecture for the photobiocatalytic glucose oxidation under visible light illumination. Here, we combine TiO_2 as cheap and transparent electrode material and sulfonated polyaniline as a biocompatible light-sensitive element and wiring agent for the enzyme PQQ-GDH. TiO_2 has to fulfill two requirements to provide the light-directed functionality of the whole system. On one hand, the large band gap of the material prevents electron transfer reactions between the electrode and the polymer in the dark. On the other hand, the separation of the light-induced charge carriers within the polymer is supported at the TiO_2/polymer interface and therefore supports the generation of anodic photocurrents. The whole principle is depicted in Figure 1C, showing the light-initiated electron transfer chain. Upon illumination, electron-hole pairs are generated inside the polymer. In detail, the photon-polymer interaction results in the excitation of electrons from the highest occupied molecular orbital (HOMO) into the lowest unoccupied molecular orbital (LUMO) state. The gained light energy is sufficient to enable the injection of excited electrons into the conduction band (CB) of TiO_2, which is at around −0.82 V vs SCE (pH 7).[393,397] On the other hand, the polymer can facilitate a direct electron transfer with the enzyme.[287,289] PQQ-GDH oxidizes glucose at the catalytic center (PQQ) to gluconolactone and subsequently transfers electrons to the polymer, resulting in enhanced photocurrents by filling up holes of the light-induced process.

Construction of IO-TiO_2 Structures. First, we have concentrated on the design and construction of three dimensional IO-TiO_2 electrodes to provide a beneficial morphology for the assembly of polymer and biomolecules. Such structures are characterized by a larger interface between the polymer and the semiconductor, which is essential for a defined photocurrent generation but also ensures a stable integration of a large amount of biomolecules while still allowing a sufficiently fast diffusion of substrates.

Even if there are several procedures for the construction of IO-TiO_2 structures, most of them are rather time-consuming or are difficult for controlling the layer thickness.[398–401] This is mainly attributed to the requirements of highly ordered structures for photonic purposes, which are not necessary for other applications. This is why we have developed a simple procedure to build up IO-TiO_2 electrodes with a defined height in a layered format. The stepwise preparation procedure is illustrated in Figure 1A and is based on the coassembly of a mixture of TiO_2 nanoparticles (NP) and latex beads (LB) by a spin-coating process onto FTO electrodes. The following sinter step at 450 °C results in a thermal decomposition of the LBs by leaving behind an inverse opal TiO_2 architecture with pores of a defined size. The procedure has been optimized for a homogeneous layer of IO-TiO_2 with open holes, allowing a good polymer and biomolecule penetration. Therefore, the influence of the amount and the ratio of the TiO_2 NP/LB mixture, the solvent, and the rotating speed used during spin coating on the final sintered TiO_2 layers has been evaluated by scanning electron microscopy measurements (for details, we refer to Figure S2, SI). As illustrated in Figure 1B, the final procedure (100 mg mL^{-1} TiO_2 NPs and 100 mg mL^{-1} LBs in 1/1 ethanol/H_2O, 40 rps) results in an inverse opal structure containing holes with a diameter of around 650 nm, with interconnecting channels between the pores. The structures are rather thin-walled so that even underlying chambers can be seen in the SEM image, which is expected to be beneficial for the propagation of light inside these structures.

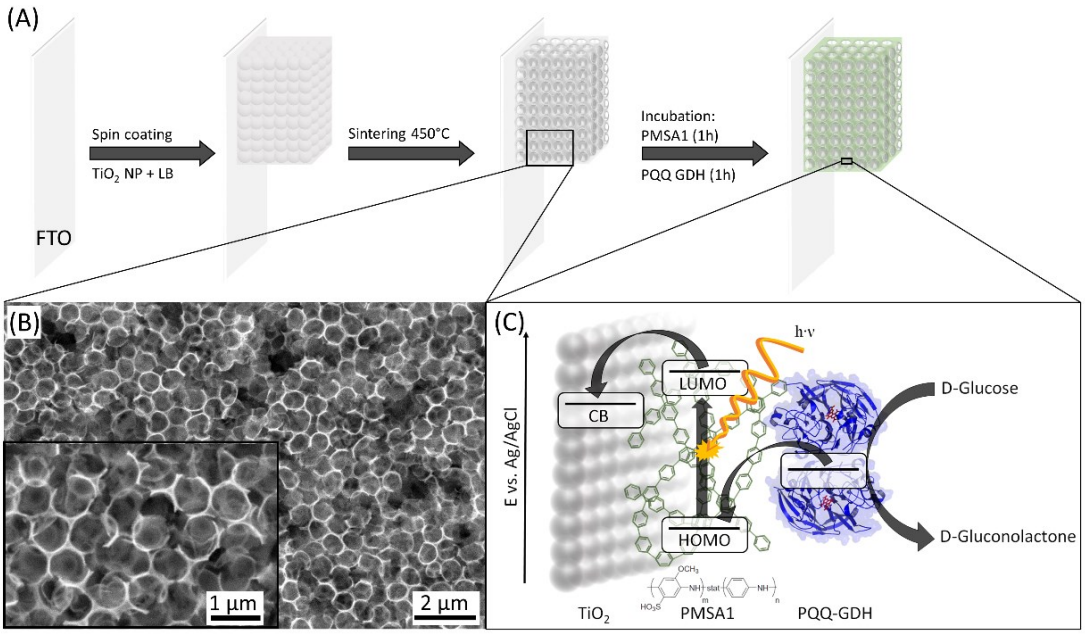

Figure 1. (A) Schematic illustration of the stepwise preparation of IO-TiO_2 architectures on FTO electrodes and the subsequent assembly of PMSA1 and PQQ-GDH. **(B)** SEM image of the IO-TiO_2 electrodes after sintering, demonstrating the open inverse opal structure with holes with a diameter of around 650 nm. **(C)** Energetic level of TiO_2, PMSA1, and PQQ-GDH, displaying the light-driven electron transfer chain for the composed biohybrid architecture. In the presence of glucose, the substrate is converted by the enzyme and the electrons from the biocatalytic reaction are transferred to the polymer. Upon illumination with visible light, the electrons inside the polymer are excited to a higher energetic state (LUMO) and are subsequently injected into the conduction band (CB) of TiO_2, resulting in an enhanced anodic photocurrent.

By using the spin-coating procedure, we have been able to control the thickness of the IO-TiO_2 architectures by simply tuning the number of layers deposited. However, to retain the integrity of the structures, a sintering step between the layers has been found to be necessary (Figure S2E, SI). Up to four layers have been deposited onto FTO, resulting in IO-TiO_2 architectures with a height of up to about 4.6 μm (Figure S3, SI). In the investigated range between one and four layers, a linear increase of the height with an average layer thickness of around 930 nm per layer has been found (Figure S4, SI), while maintaining the pore diameter and the uniform electrode morphology.

In UV/vis experiments, the optical properties of the prepared IO-TiO_2 architectures have been evaluated for the one- and two-layer electrodes (Figure S1, SI). The one-layer electrode shows a high light scattering starting from 300 nm and reaches the high transmittance of FTO of 85% at about 900 nm. For the two-layer electrode, a stronger scattering is observed over the whole recorded wavelength range but follows the course of the one-layer electrode. The promoted light scattering within such disordered structures can improve the optical absorption of the light-sensitive element due to the extended traveling distance of the incident light within this 3D structure, as reported before for different solar cell approaches.[402]

Photoelectrochemical Properties of IO-TiO_2 Structures. To evaluate the concept of using sulfonated polyanilines for the sensitization of IO-TiO_2, first, the interaction between both has been characterized photoelectrochemically. We have chosen the copolymer PMSA1, which has already shown the potential to efficiently wire various redox enzymes.[287,289,323,395] The polymer has been synthesized with two different types of monomers, an aniline and a methoxyaniline sulfonic acid, with a ratio of 1:5, resulting in a water soluble polymer with negatively charged functionalities. Besides exploiting the sulfonate groups for the electrostatic interaction with biomolecules, the insertion of these groups within the polyaniline is necessary to achieve polymer conductivity in the neutral pH range.[68,69] The UV/vis spectrum of PMSA1 in buffer solution is depicted in Figure 2A. The polymer is yellow-green and shows two characteristic peaks at 458 and 323 nm (Figure S6, SI), which can be associated with the polaron band and the π-π* band, respectively.[287,403] The spectral properties of PMSA1 reflect that the polymer exists in the conductive emeraldine salt state.

For sensitization of IO-TiO_2, the polymer has been assembled from an aqueous solution (5 mM MES with 5 mM $CaCl_2$ pH 6.5) for 1 h. Besides the preferred polymer assembly via adsorption to the electrode surface, we additionally assume to exploit the sulfonic acid groups of the polymer for the anchoring to the TiO_2 surface via bidentate binding, as reported for sulfonated dyes.[122] The successful binding of the polymer to the IO-TiO_2 architecture can be approved by the coloration of the structure from white to green (Figure S3E, SI).

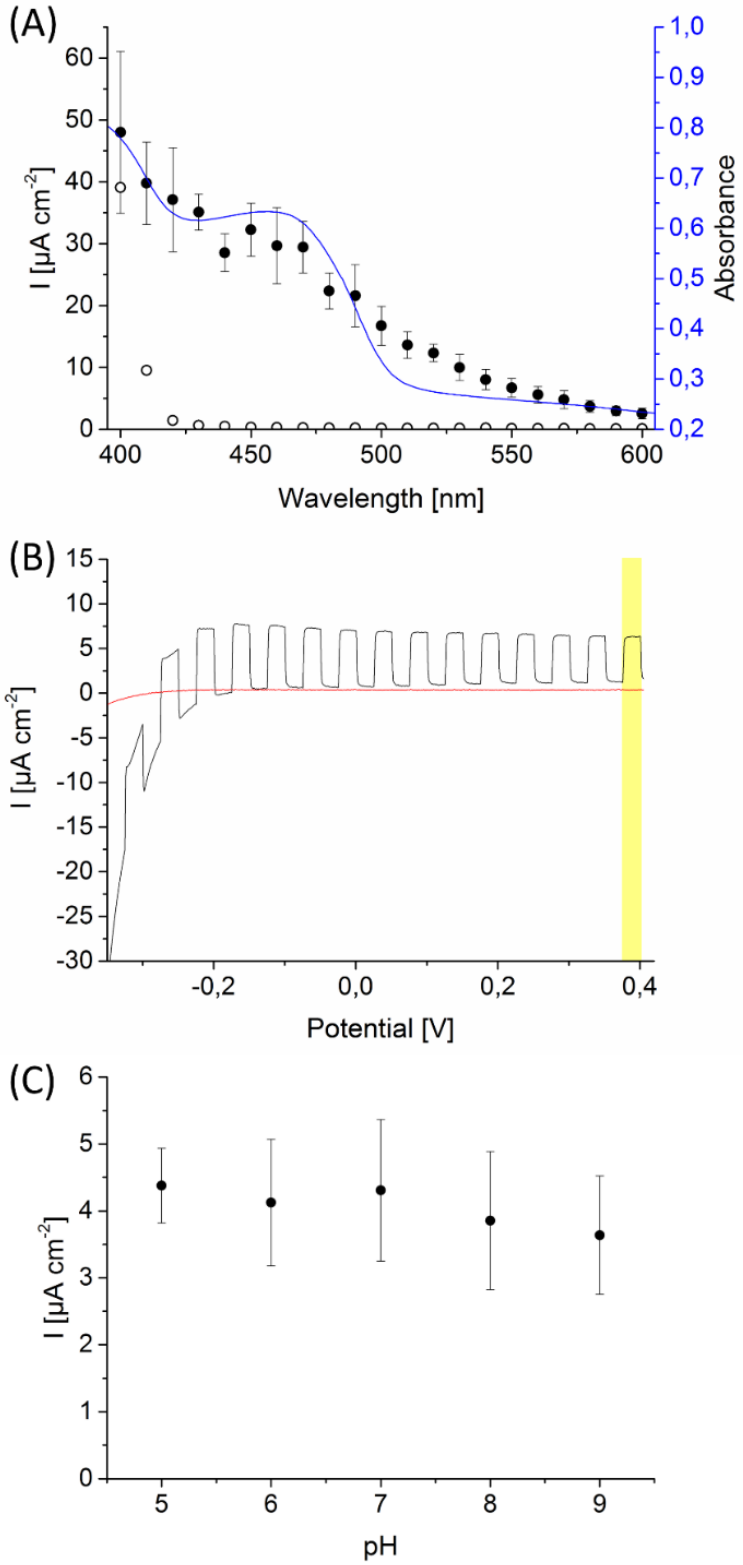

Figure 2. Photoelectrochemical experiments of IO-TiO_2|PMSA1 electrodes. **(A)** Wavelength-dependent photocurrent density of a three-layered IO-TiO_2 electrode with (closed circle) and without PMSA1 (open circle) (0 mV vs Ag/AgCl, 1 M KCl; 5 mM MES + 5 mM $CaCl_2$ pH 6.5). The blue curve corresponds to the UV/vis spectrum of PMSA1 in buffer solution. **(B)** Chopped light voltammetry of a three-layered IO-TiO_2 electrode with (black curve) and without PMSA1 (red curve) (white light source; 10 mW cm^{-2}; potential vs Ag/AgCl, 1 M KCl from -0.3 to +0.4 V; 5 mV s^{-1}; 5 mM MES + 5 mM $CaCl_2$ pH 6.5). **(C)** Photocurrent density of three layered IO-TiO_2|PMSA1 electrodes depending on the pH value (white light source; 10 mW cm^{-2}; 0 mV vs Ag/AgCl, 1 M KCl).

Basic photoelectrochemical characterizations have been performed with three-layered IO-TiO_2|PMSA1 electrodes. First, the photocurrent response of the final architecture has been analyzed wavelength-resolved with a monochromator at a potential of 0 V vs Ag/AgCl, 1 M KCl. As shown in Figure 2A, the photocurrent increases progressively from 600 to 400 nm. In comparison, IO-TiO_2 electrodes without polymer only show small photocurrents at wavelengths below 420 nm. Accordingly, the excitation range of the IO-TiO_2 electrodes is extended to the visible range due to the polymer integration. The photocurrent spectrum correlates well with the optical spectrum of PMSA1 in solution. At around 460 nm, a plateau is found, which can be attributed to the polaron band of the polymer. This confirms the light-induced electron injection from the LUMO of the polymer into the CB of TiO_2, with the concomitant generation of an anodic photocurrent. For further characterization, a white light source has been used.

Control experiments with a conductive FTO electrode covered with PMSA1 show no photocurrent upon illumination (0 V vs Ag/AgCl, 1 M KCl, and 10 mW cm^{-2}). The absence of a photocurrent for electrodes without TiO_2 demonstrates that FTO cannot efficiently separate the light-induced electron-hole pairs within the polymer. In contrast, such conductive materials allow electron transfer reactions with the polymer in the absence of light.[287,289] This is, however, not in the focus of the present study. It has also to be added here that unmodified three-layered IO-TiO_2 electrodes without polymer only give negligible photocurrents. Therefore, both IO-TiO_2 and PMSA1 are necessary to achieve clear anodic photocurrents in the visible light range.

By recording the photocurrent of IO-TiO_2|PMSA1 electrodes in dependence on the applied potential between -0.3 and +0.4 V vs Ag/AgCl, 1 M KCl over the entire investigated bias range, anodic photocurrents have been found (Figure 2B). As expected before, this displays that the IO-TiO_2|PMSA1 electrodes behave as photoanodes, allowing exclusively a unidirectional light-induced current flow from the polymer to the electrode. The photocurrent magnitude decreases slightly with positively shifting potential, which can be explained by the continuous oxidation of the polymer due to the absence of added electron donors in solution. This is supported by the fact that the transferred charge during long-term experiments at high light intensities correlates with the amount of immobilized PMSA1, indicating that the polymer may act as an electron reservoir for the photoelectrochemical reaction in the absence of any enzymatic reaction, and thus the photocurrent degrades consequently with time (for details, see Figure S13, SI). However, if a moderate light intensity of 10 mW cm^{-2} and short light pulses of 10 s are applied, the signal shows sufficient stability. Since our intention is to use a biocatalytic reaction to feed the photoelectrochemical process, all experiments have been performed without additional electron donor in solution (to avoid complex reaction capabilities).

The pH value used during the measurements is found to have little influence on the initial photocurrent response in the range between 5 and 9, with a slightly preferred reaction in the acidic region (Figure 2C). However, the functionality of the IO-TiO_2|PMSA1

architecture remains preserved over a wide pH range, which increases the potential application of these structures for the combination with different redox enzymes.

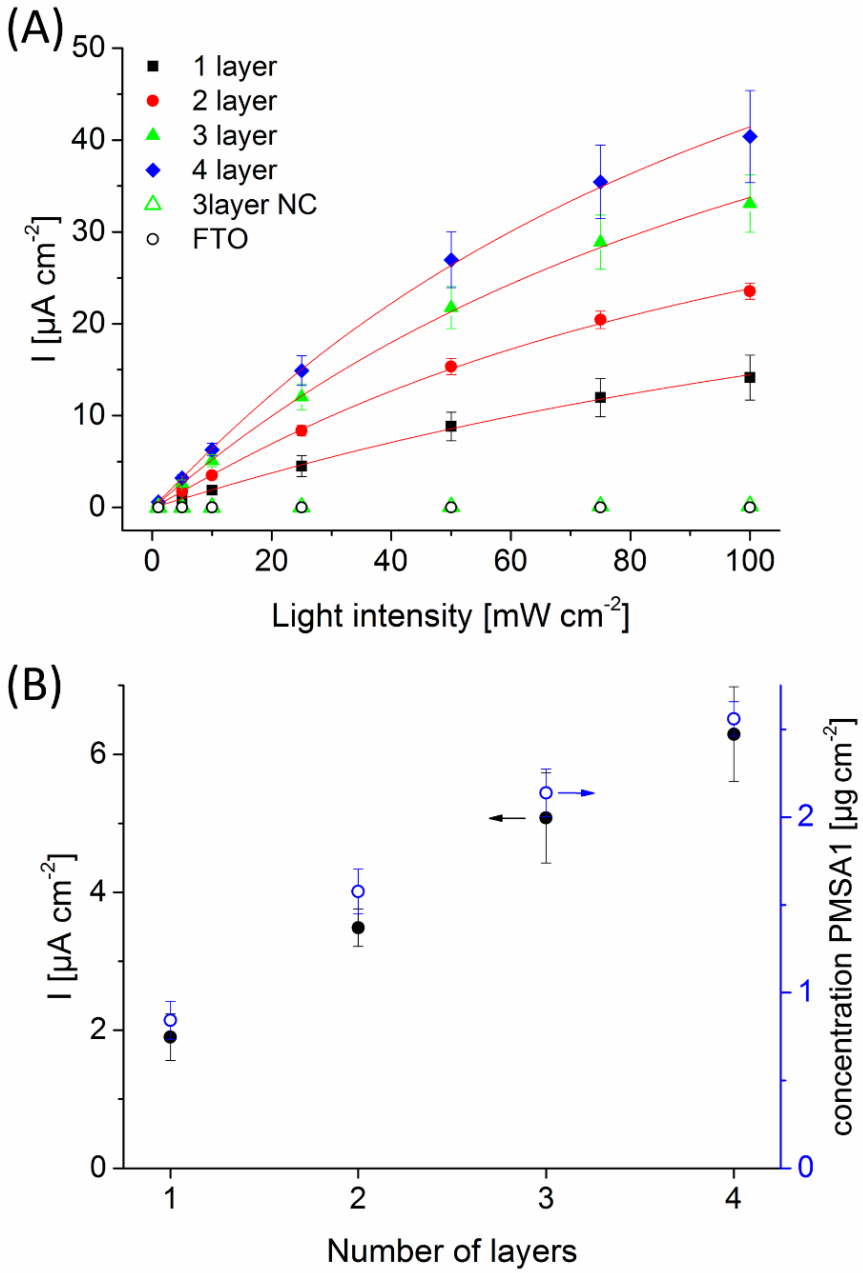

Figure 3. Photoelectrochemical experiments of IO-TiO_2|PMSA1 electrodes. **(A)** Photocurrent density of IO-TiO_2|PMSA1 electrodes for different numbers of layers at different light intensities. Additionally, the signal response of three-layered IO-TiO_2 electrodes without PMSA1 (open triangle, three-layer nanocrystalline) and of FTO after immobilization of PMSA1 (open circle) is shown (white light source; 0 mV vs Ag/AgCl, 1 M KCl; 5 mM MES + 5 mM $CaCl_2$ pH 6.5). **(B)** Photocurrent density (filled circle) and PMSA1 loading (open circle) of IO-TiO_2|PMSA1 electrodes for different numbers of layers (white light source; 10 mW cm^{-2}; 0 mV vs Ag/AgCl, 1 M KCl; 5 mM MES + 5 mM $CaCl_2$ pH 6.5).

Furthermore, the influence of the excitation intensity on the photocurrent density for three-layered IO-TiO_2|PMSA1 electrodes has been analyzed (Figure 3A). By fixing the potential to 0 mV vs Ag/AgCl, 1 M KCl first anodic signals of 0.5 ± 0.08 µA cm^{-2} have

already been obtained at rather low intensities of 1 mW cm^{-2}. A further signal enhancement is found with increasing light intensity up to 33.1 ± 3.1 μA cm^{-2} at 100 mW cm^{-2}. This suggests that the photoelectrochemical reaction is determined to a large extent by the charge carrier generation inside the polymer.

To determine the influence of the electrode height on the photoelectrochemical behavior, IO-TiO_2|PMSA1 architectures with 1-4 IO-TiO_2 layers have been analyzed. As illustrated in Figure 3A, the photocurrent density increases independently of the used light intensity with every IO-TiO_2 layer. This indicates that the propagation of light within these structures is not limited by the number of layers in the investigated range. In Figure 3B, the photocurrent response at a moderate light intensity of 10 mW cm^{-2} is plotted against the number of IO-TiO_2 layers, showing an almost ideal linear signal enhancement with increasing electrode height. For a better understanding, we have determined the amount of PMSA1 immobilized within these structures by extraction with DMSO and subsequent UV/vis measurements (Figure S14, SI). The surface concentration for different electrode thicknesses is depicted in Figure 3B, showing a linear increase of the polymer amount from 0.84 ± 0.11 μg cm^{-2} for one-layer electrodes up to 2.56 ± 0.1 μg cm^{-2} for four-layer electrodes. This suggests that we can exploit the additional surface area per layer for the integration of the polymer. Obviously, the polymer penetration into the IO-TiO_2 architecture is unhindered and thus also allows to fill up the underlying pores of thicker IO films. The results are supported by the photoelectrochemical data, indicating that a thicker TiO_2 structure gives rise to a larger polymer-TiO_2 interface area for an enhanced photocurrent density.

Integration of PQQ-GDH into IO-TiO_2|PMSA1 Architectures. Next, the integration of a biocatalytic entity into the IO-TiO_2|PMSA1 architecture has been investigated. Therefore, PQQ-GDH has been assembled onto the electrodes via electrostatic interactions in a layer-by-layer approach (first polymer then enzyme). Here, we intend to exploit the negatively charged functionalities (sulfonate groups) of the polymer for the immobilization of the basic enzyme (pI 9.5)[253] at pH 6.5.

In Figure 4A, the photocurrent density after addition of 10 mM glucose in dependence on the applied potential is shown. Here, an increasing anodic photocurrent is found in the presence of the substrate. In comparison, no response to glucose is obtained for IO-TiO_2|PMSA1 electrodes without enzyme or IO-TiO_2|PQQ-GDH electrodes without polymer. This confirms that the signal change is induced by the enzymatic reaction and that PMSA1 is essential for transferring electrons from the biocatalyst toward the IO-TiO_2 structure for enhanced anodic photocurrents, as schematically illustrated in Figure 1C. In the investigated bias range, the photocurrent change is found to be independent of the applied potential, indicating that the reaction is not controlled by the bias but by the kinetics of electron injection from the polymer into TiO_2.

To further evaluate the influence of the electrode morphology of IO-TiO_2 architectures for the construction of a functional biohybrid system consisting of TiO_2, PMSA1, and PQQ-GDH, the influence of these pore-like structures has been compared to that of flat TiO_2 electrodes and PEG-nanostructured TiO_2 electrodes. Therefore, the electrodes have been prepared identical to the IO-TiO_2 structures but without LB (resulting in flat TiO_2) or by exchanging the LB by the same amount of poly(ethylene glycol) (PEG-TiO_2). SEM experiments show that the first approach leads to a rather smooth layer with cracks, whereas the second one results in a nanostructured surface (Figure S5, SI). The PMSA1-modified flat and PEG-TiO_2 electrodes reach initial photocurrents of 2.3 ± 0.3 and 3.9 ± 0.3 μA cm^{-2} at 10 mW cm^{-2}, respectively. In comparison, the IO-TiO_2|PMSA1 architecture (three layered) gives signals of 5.1 ± 0.6 μA cm^{-2} (Figure S7, SI). The photoelectrochemical data fit well to the determined amount of PMSA1 immobilized onto the electrodes (Figure 4B, inset), demonstrating that the IO-TiO_2 electrodes allow a higher polymer loading for an increased light-to-current conversion.

In Figure 4B, the photocurrent response after addition of glucose for the different TiO_2 electrode types modified with polymer and enzyme is illustrated. Here, a photocurrent density increase of 1.08 ± 0.2 μA cm^{-2} for the IO-TiO_2 architectures, 0.044 ± 0.04 μA cm^{-2} for the flat TiO_2 electrodes, and 0.037 ± 0.02 μA cm^{-2} for the PEG-TiO_2 electrodes have been found. Thus, the IO-TiO_2 architectures give rise to a 24-fold and 29- fold higher glucose-dependent photocurrent response, compared to that of the flat and PEG-TiO_2 electrodes, respectively. For quantification, the bound enzyme has been removed from the electrodes with a high ionic strength buffer and afterwards, the activity has been determined (for details, see Experimental Section). A noticeable higher surface concentration of PQQ-GDH is found in IO-TiO_2 architectures (31 ± 3 pmol cm^{-2}), whereas the flat and PEG-TiO_2 electrodes allow for much less enzyme loading of 6 ± 2 and 2 ± 0.3 pmol cm^{-2}, respectively. The differences in the enzyme surface concentrations can be explained by the different surface morphologies of the electrodes. The pores of the IO-TiO_2 electrodes enable the filling with both the polymer and the enzyme. In contrast, for the PEG-TiO_2 electrodes, only the polymer can be sufficiently integrated into the electrode, whereas the enzyme loading remains rather small. As indicated in the SEM experiments, this is probably due to the very small pores in the nanometer range for such TiO_2 electrodes.[404,405] Although the procedure results in electrodes with a high surface area, the penetration of larger biomolecules in such nanostructured electrodes can be restricted.[406] By comparing the glucose-dependent photocurrent response of the different electrode types with the estimated enzyme concentration, it can be shown that the IO-TiO_2| PMSA1 electrodes not only cause an integration of more enzymes but also result in a higher amount of electrically connected biocatalysts (IO-TiO_2: 35 nA $pmol^{-1}$ enzyme, flat TiO_2: 7 nA $pmol^{-1}$ enzyme, and PEG-TiO_2: 21 nA $pmol^{-1}$ enzyme). Therefore, both the flat and the PEG-TiO_2 electrodes provide a less beneficial surface for the incorporation of PQQ-GDH, indicating that the open pore structure of the IO-TiO_2

electrodes is needed to obtain a stable functional biohybrid architecture based on TiO_2, PMSA1, and PQQ-GDH.

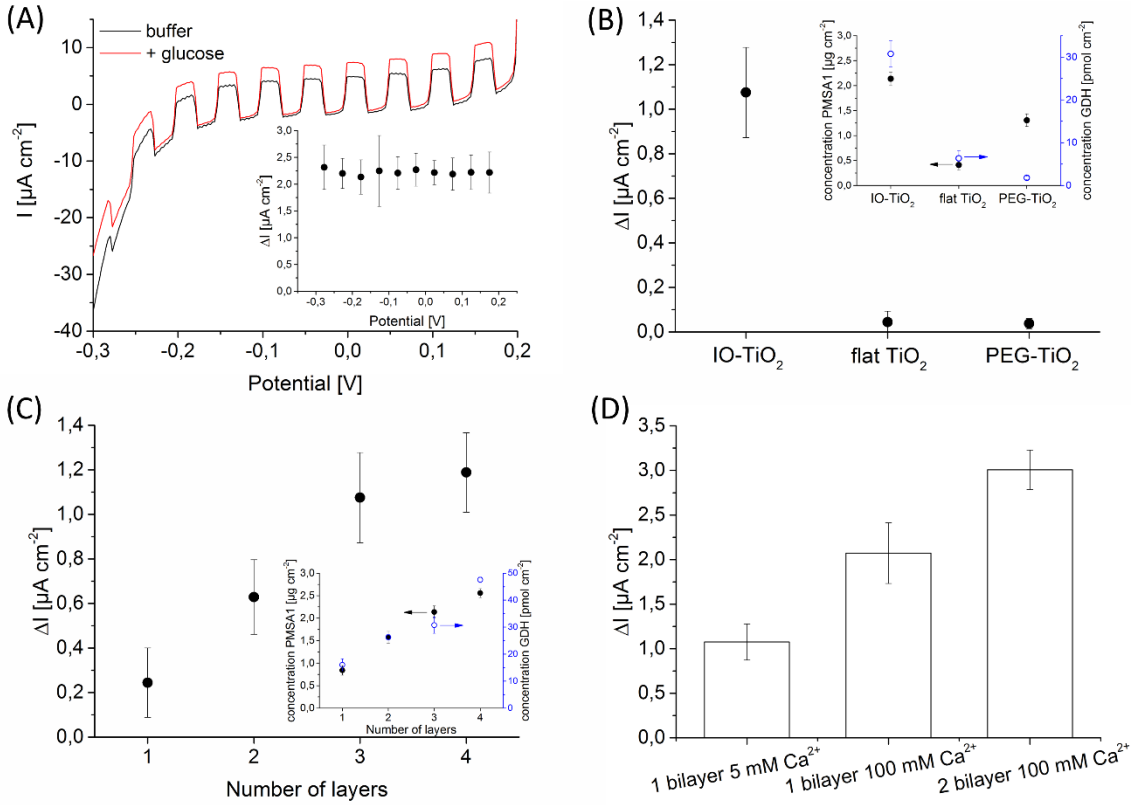

Figure 4. Photoelectrochemical experiments of IO-TiO_2|PMSA1 electrodes with immobilized PQQ-GDH. **(A)** Chopped light voltammetry of a three-layered IO-TiO_2|PMSA1|PQQ-GDH electrode in the absence and presence of 10 mM glucose. Inset: photocurrent density change ΔI after addition of 10 mM glucose, dependent on the applied potential (white light source; 10 mW cm^{-2}; potential vs Ag/AgCl, 1 M KCl from +0.2 to -0.3 V; 50 mV s^{-1}; 5 mM MES + 5 mM $CaCl_2$ pH 6.5). **(B)** Photocurrent density change ΔI after addition of 10 mM glucose for three-layered IO-TiO_2, flat TiO_2 (prepared without LB), and PEG-TiO_2 electrodes (prepared with PEG instead of LB), with immobilized PMSA1 and PQQ-GDH. Inset: surface concentration of PMSA1 (filled circle) and PQQ-GDH (open circle) for three-layered IO-TiO_2, flat TiO_2, and PEG-TiO_2 electrodes (white light source, 10 mW cm^{-2}; 0 mV vs Ag/AgCl, 1 M KCl; 5 mM MES + 5 mM $CaCl_2$ pH 6.5). **(C)** Photocurrent density change ΔI after addition of 10 mM glucose of IO-TiO_2|PMSA1|PQQ-GDH electrodes for different numbers of layers. Inset: surface concentration of PMSA1 (filled circle) and PQQ-GDH (open circle) for IO-TiO_2 electrodes with different numbers of layers (white light source, 10 mW cm^{-2}; 0 mV vs Ag/AgCl, 1 M KCl; 5 mM MES + 5 mM $CaCl_2$ pH 6.5). **(D)** Photocurrent density change ΔI after addition of 10 mM glucose for different assembly strategies of PMSA1 and PQQ-GDH onto three-layered IO-TiO_2 electrodes: one bilayer with 2 mg mL^{-1} PMSA1 (5 mM Ca^{2+}) and 2 mg mL^{-1} PQQ-GDH; one bilayer with 2 mg mL^{-1} PMSA1 (100 mM Ca^{2+}) and 2 mg mL^{-1} PQQ-GDH; two bilayers with 2 mg mL^{-1} PMSA1 (100 mM Ca^{2+}) and 2 mg mL^{-1} PQQ-GDH (white light source, 10 mW cm^{-2}; 0 mV vs Ag/AgCl, 1 M KCl; 5 mM MES + 5 mM $CaCl_2$ pH 6.5).

Next, we have evaluated the influence of the IO-TiO_2 layer thickness on the glucose-dependent photocurrent. As illustrated in Figure 4C, the signal response is enhanced with increasing number of layers from 0.24 ± 0.16 up to 1.19 ± 0.18 µA cm^{-2} at a moderate light intensity of 10 mW cm^{-2} and a potential of 0 mV vs Ag/AgCl, 1 M KCl. This indicates that the increasing surface area with every layer can be used for the

photobiocatalytic reaction. The enzyme surface concentration rises continuously from 16 ± 2 pmol cm^{-2} for the one-layer electrodes up to 48 ± 1 pmol cm^{-2} for the four-layer electrodes. The rising PQQ-GDH amount and the enhanced photocatalytic signal with every additional layer suggest that the integration of the enzyme but also the substrate diffusion are not limited by the layer number. Assuming that a fully packed enzyme monolayer on a flat electrode corresponds to about 3.2 pmol cm^{-2},[283] we can estimate that we are able to integrate up to 15 enzyme monolayers into the 4-layered IO-TiO_2|PMSA1 electrode. Interestingly, the enzyme/polymer ratio integrated into the IO-TiO_2 architectures remains rather constant for all layer numbers (1 layer: 19 pmol μg^{-1}, 2 layer: 17 pmol μg^{-1}, 3 layer: 14 pmol μg^{-1}, and 4 layer: 19 pmol μg^{-1}), giving a further hint for the unrestricted assembly of both enzyme and polymer into the IO architecture.

To further improve the light-directed glucose oxidation of the IO-TiO_2|PMSA1|PQQ-GDH electrodes, different strategies for the assembly of polymer and enzyme have been analyzed with three-layered IO-TiO_2 electrodes (Figure 4D). From previous reports, it is known that Ca^{2+} ions can coordinate sulfonate moieties in emeraldine salt polyanilines by screening the negative SO_3^- charges.[403,407] The reduced electrostatic repulsion between the sulfonate groups is thought to change the PMSA1 conformation, which may help to fill up the IO-TiO_2 pores with more polymers for an enhanced photoelectrochemical response.

Therefore, we have compared the photocurrent response of IO-TiO_2|PMSA1 electrodes prepared under low (5 mM $CaCl_2$, previously used) and high Ca^{2+} concentrations (100 mM $CaCl_2$). The enzyme incubation and measurements have been further performed in 5 mM MES, with 5 mM $CaCl_2$ at pH 6.5. Although for the initial photocurrent response in the absence of glucose no clear differences have been obtained for the two different Ca^{2+} concentrations used during polymer immobilization (Figure S8, SI), the glucose-dependent signal is strongly influenced by the higher Ca^{2+} concentration (Figure 4D). The glucose-dependent signal is found to be around 2-fold higher by using 100 mM Ca^{2+} during polymer assembly (2.07 ± 0.34 μA cm^{-2}). Higher Ca^{2+} concentrations result in no further enhancement of the photocurrent response (Figure S9, SI). The polymer loading of the IO-TiO_2|PMSA1 electrodes prepared with 5 and 100 mM $CaCl_2$ has been calculated to be 2.14 ± 0.14 and 8 ± 0.16 μg cm^{-2} PMSA1, respectively. This corresponds to a 3.7-fold higher integration of PMSA1. These results are supported by quartz crystal microbalance with dissipation monitoring measurements on gold chips, showing that the polymer adsorption is drastically increased for Ca^{2+} concentrations above 50 mM (Figure S10, SI). In contrast, high concentrations of monovalent cations such as Na^+ do not favor the polymer assembly (500 mM Ca^{2+}: 600 Hz; 500 mM Na^+: 30 Hz). This underlines the outstanding role of Ca^{2+} for the coordination at the sulfonate groups and for the controlled immobilization of the polymer.

Similar to the improved polymer loading, also an increased enzyme loading of 90 ± 13 pmol cm^{-2} for IO-TiO_2|PMSA1| PQQ-GDH electrodes prepared with 100 mM $CaCl_2$

compared with 31 ± 3 pmol cm^{-2} for electrodes prepared with 5 mM $CaCl_2$ can be found. These results display the improved conditions found for the integration of the polymer and the enzyme into the IO-TiO_2 electrodes and demonstrate the favorable role of PMSA1 in connecting the enzyme with the TiO_2 electrodes for the light-directed glucose oxidation with improved performance.

We have tried to build up two PMSA1/PQQ-GDH bilayers inside the IO-TiO_2 architectures by repeated incubations with polymer (100 mM $CaCl_2$) and the enzyme. A clear enhancement of the glucose-dependent signal up to 3 ± 0.22 µA cm^{-2} has been achieved by applying two repeated incubation steps (Figure 4D). The stronger green coloring of the two-bilayer modified IO-TiO_2 electrode compared to the one-bilayer electrode additionally confirms a higher polymer loading. The results successfully demonstrate the principle of using repetitive incubation cycles of polymer and enzyme for the enhanced deposition of both entities inside the IO-TiO_2 pores. However, further experiments are needed to better understand the limitations of this approach.

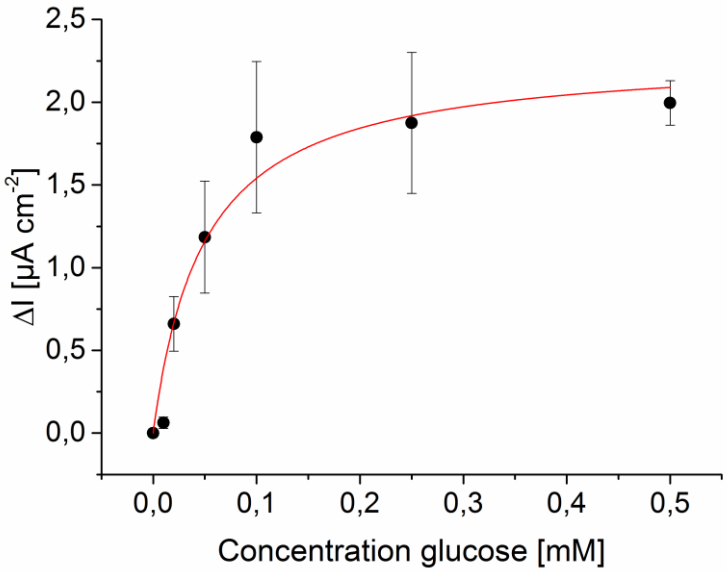

Figure 5. Photocurrent density change ΔI of three-layered IO-TiO_2| PMSA1|PQQ-GDH electrodes after addition of different glucose concentrations. Error bars result from three individual electrodes (white light source, 10 mW cm^{-2}; 0 mV vs Ag/AgCl, 1 M KCl; 5 mM MES + 5 mM $CaCl_2$ pH 6.5).

Performance of IO-TiO_2|PMSA1|PQQ-GDH Architectures. The following experiments have been performed with three-layered IO-TiO_2|PMSA1|PQQ-GDH electrodes consisting of one polymer/enzyme bilayer (100 mM $CaCl_2$). Concentration-dependent measurements of the biohybrid system with glucose at 0 V vs Ag/AgCl, 1 M KCl show first signal responses at 10 µM and level off at 250 µM (Figure 5). From the sensitivity plot, the apparent $K_{M,app}$ value has been calculated to be 49 µM. This value is much smaller than the value for free PQQ-GDH in solution (K_M ~ 25 mM)[408,259,283] but is comparable to values which have been reported for the enzyme on electrode

surfaces.[409,360] This may illustrate that the changed transport conditions and the electrical connection of the enzyme can significantly alter the concentration behavior. This is also supported by the fact that higher $K_{M,app}$ values (0.33 mM) have been reported for PMSA1/PQQ-GDH films on ITO electrodes.[289] However, even if the dynamic range is currently rather small, the principle of light-directed glucose detection at low potentials can be successfully shown for the developed biohybrid system.

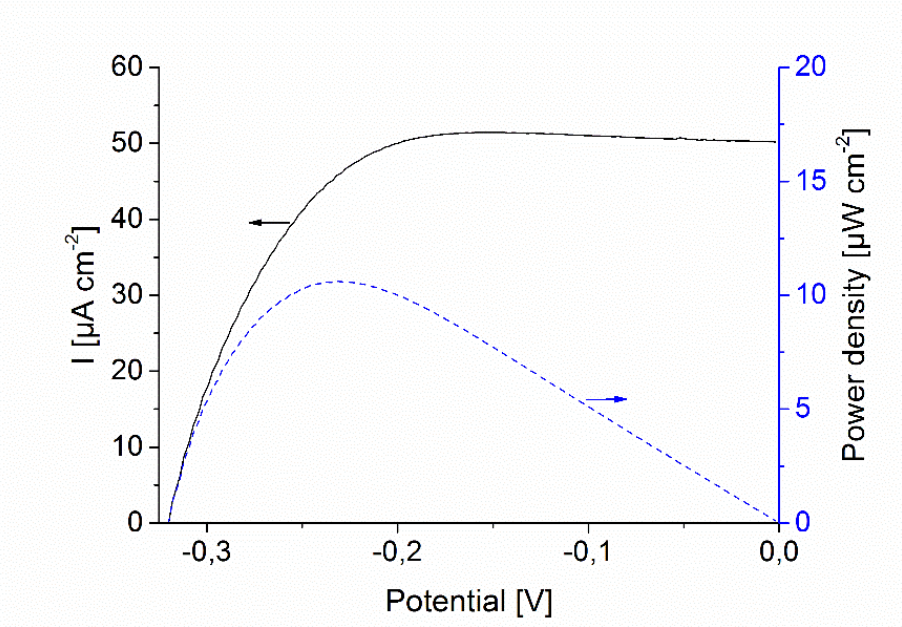

Figure 6. Current and power density of three-layered IO-TiO_2| PMSA1|PQQ-GDH electrodes dependent on the applied potential in the presence of 10 mM glucose and under continuous illumination with 100 mW cm^{-2}. The maximum power output has been determined by using the IO-TiO_2|PMSA1|PQQ-GDH electrode as a working electrode, a Pt wire as the counter electrode, and an Ag/AgCl, 1 M KCl reference electrode (white light source, 100 mW cm^{-2}; 5 mV s^{-1}; potential vs Ag/AgCl, 1 M KCl; 5 mM MES + 5 mM $CaCl_2$ pH 6.5).

On the other hand, glucose can also be considered as a fuel for the generation of electrical power, as already introduced for (photo)-biofuel cells.[410,411,83,168] To evaluate the performance of our biohybrid system as a photoanode we have recorded I-V curves under continuous illumination with a maximum intensity of 100 mW cm^{-2} in the presence of glucose (Figure 6). The maximum current (I_{max}) corresponds to 44.7 ± 6.5 µA cm^{-2} and the open circuit potential (OCP) is found to be -0.315 ± 0.007 V vs Ag/AgCl, 1 M KCl. The maximum power output is determined to be around 10.5 µW cm^{-2} at -0.232 V vs Ag/ AgCl, 1 M KCl. From that data the fill factor (compares the maximum power output with the product of OCP and maximum current) is calculated to be 0.66 ± 0.02. This demonstrates that high efficiency can be found at the redox potential of the enzyme but also that electrons from the biocatalytic reaction can already be transferred to the electrode about 0.1 V below this potential (by assuming a redox potential between -0.188 and -0.226 V vs Ag/AgCl, 1 M KCl).[412,283] Since no anodic current is found in the dark (Figure S11, SI), this can be attributed to the utilization of light energy to drive the biocatalytic reaction and is realized by the efficient charge carrier separation at the

polymer/TiO_2 interface. In comparison, flat FTO|PMSA1|PQQ-GDH electrodes allow the first gain of electrons from the biocatalytic reaction in the dark only when potentials more positive than -0.07 V vs Ag/AgCl, 1 M KCl are applied (Figure S12, SI), which is in good agreement with previous reports on IO-ITO electrodes.[289] Accordingly, the IO-TiO_2|PMSA1|PQQ-GDH biohybrid architectures give rise to lowering of the working potential of about 200 mV due to the light-harvesting feature, which reflects an advantage of light-sensitive electrodes over light-insensitive electrodes for power supply.

By continuously illuminating the IO-TiO_2|PMSA1|PQQGDH electrodes with a maximum light intensity of 100 mW cm^{-2} for 30 min, a strong difference between the situation in the absence or presence of glucose is found (Figure S13, SI). While 27.3 mC cm^{-2} are transferred to the electrode in the presence of glucose, only 3.3 mC cm^{-2} are collected in the absence of substrate. This shows the necessity to feed the photoelectrochemical reaction with electrons from the biocatalytic glucose oxidation for an enhanced generation of electrical power.

By assuming that only PMSA1 contributes to the photocurrent and excluding the scattering effects of the electrode, the internal quantum efficiency (IQE) can be calculated from the UV/vis spectra of PMSA1 in buffer solution corrected for the amount of polymer within the three-layered IO-TiO_2 electrodes. At a potential of 0 V vs Ag/AgCl, 1 M KCl and a wavelength of 460 nm, an IQE of 2.2 and 2.7% has been determined in the absence and presence of glucose, respectively, which is indicative of an improved efficiency as a result of the biocatalytic reaction.

Compared with other photobioelectrochemical anodes using glucose as fuel, the overall performance of the IO-TiO_2|PMSA1| PQQ-GDH electrode is higher and provides a step toward the utilization of light-driven biosensors and biofuels cells.[82,83,168,360] However, the photocurrent is currently moderate and needs further optimization to achieve light-driven biohybrid systems with higher efficiencies, but seems to be already useful for light-triggered sensing.

This approach is particularly promising because a variety of redox enzymes has already been shown to interact with sulfonated polyanilines, giving access to the light-triggered oxidation of a large number of different substrates.[323,395,396] Also, the good biocompatibility of TiO_2 and polyanilines represents an advance to other photoelectrochemical systems, which are based on toxic light-sensitive materials or mediators.

Conclusions

The present study has introduced an approach for the construction of a light-driven biohybrid architecture based on IO-TiO_2 electrodes, PMSA1 as light-sensitive element and wiring agent, and PQQ-GDH. Therefore, a spin-coating protocol for the preparation of IO-TiO_2 electrodes with scalable height and open pores of 650 nm diameter has been

established. The final electrodes have shown to provide a suitable platform for the integration of polymer and enzyme due to the advantageous surface morphology. The addition of glucose results in enhanced anodic photocurrents, demonstrating the functionality of the light-induced signal chain, starting from the biocatalytic glucose oxidation and subsequent electron transfer via the polymer to the IO-TiO_2 architecture. The magnitude of the glucose-dependent signal is concentration-dependent and can be controlled by the number of IO-TiO_2 layers. Compared with flat and nanostructured TiO_2 electrodes, a significant higher integration of polymer and enzyme is realized by using IO-TiO_2 architectures, resulting in enhanced photocurrents for an improved light-to-current conversion. Furthermore, the reported biohybrid architecture allows photobioelectrocatalytic glucose oxidation at potentials below the redox potential of the enzyme and therefore gives access to an increased power output if glucose is used as the fuel. We anticipate that this approach will push forward the development and design of new concepts for combining biocatalytic features of enzymes with the photophysical properties of light-sensitive entities for advanced photoelectrochemical applications.

Acknowledgement

The authors are grateful to Roche Diagnostics (Penzberg, Germany) and mainly Dr. Meier and Dr. von der Eltz for cooperation for supplying the GDH enzyme. Furthermore, the authors would like to thank Dr. Schulz and Dr. Xu from the University of Potsdam (Potsdam, Germany) for the synthesis of the polymer.

4.4 Light as Trigger for Biocatalysis: Photonic Wiring of Flavin Adenine Dinucleotide-Dependent Glucose Dehydrogenase to Quantum Dot-Sensitized Inverse Opal TiO_2 Architectures via Redox Polymers[**]

Authors: **M. Riedel**, W. J. Parak, A. Ruff, W. Schuhmann and F. Lisdat

Abstract: The functional coupling of photo-active nanostructures with enzymes creates a novel strategy for the design of light-triggered biocatalysts. This study highlights the efficient wiring of FAD-dependent glucose dehydrogenase (FAD-GDH) to PbS QD-sensitized inverse opal TiO_2 electrodes (IO-TiO_2) by means of an Os-complex-containing redox polymer for the light-driven glucose oxidation. A new template approach for the construction of IO-TiO_2 scaffolds has been developed, enabling the tunability of the surface area and a high loading capacity for the integration of QDs, redox polymer and enzyme. The biohybrid signal chain can be switched on with light, generating charge carriers within the QDs, triggering a multistep electron transfer cascade from the enzyme towards the redox polymer via the QDs and finally to the IO-TiO_2 electrode. The resulting anodic photocurrent can be modulated by the potential, the excitation intensity, and the glucose concentration, providing a new degree of freedom for the control of biocatalytic reactions at electrode interfaces. Maximum photocurrents of 207 µA cm^{-2} have been achieved in the presence of glucose and a first gain of electrons from the biocatalytic reaction is found at -540 mV vs. Ag/AgCl, 1 M KCl, which lowers the working potential by more than 500 mV as compared to light-insensitive electrodes. The biohybrid system combines the advantages of a high surface area of IO-films, an efficient charge carrier generation and separation at the QDs/TiO_2 interface, and an efficient wiring of FAD-GDH to the QDs via a redox polymer, resulting in photo(bio)anodes of high performance for sensing and power-supply.

Introduction

Mimicking photosynthetic proteins by combination of light-insensitive enzymes with artificial light-harvesting entities in a functional biohybrid system has gained great interest in the last decade.[210,168,83,360] Such approaches combine both, biocatalytic activity and photophysical properties in one integrated system with potential applications for sensing,[413,414] light-to-current,[9,127,83,137,136] or light-to-chemical conversion.[210,241,138] Introducing light-sensitivity offers the possibility to switch on/off enzymatic reactions and thus to manipulate electron transfer reactions at electrode interfaces, but can also be

[**] **Published in ACS Catalysis:** M. Riedel, W. J. Parak, A. Ruff, W. Schuhmann and F. Lisdat. Light as Trigger for Biocatalysis: Photonic Wiring of Flavin Adenine Dinucleotide-Dependent Glucose Dehydrogenase to Quantum Dot-Sensitized Inverse Opal TiO_2 Architectures via Redox Polymers. *ACS Catal.*, **2018**, 8 (6), pp 5212–5220. DOI: 10.1021/acscatal.8b00951.

useful for bioenergetics. Light triggers the generation of electron-hole pairs within the light-sensitive entity and thus, allows electron transfer reactions from the enzyme towards the light-sensitive element to the electrode (anodic direction) or vice versa (cathodic direction).

Besides nanomaterials such as dyes,[82,415,168] gold nanoclusters,[139] and polymers[416] or biomolecules such as photosynthetic proteins (e.g. photosystem I (PSI))[247,83,108,109], particularly quantum dots (QDs)[89,360] have been used for photonic wiring of light-insensitive enzymes. Therefore, first the light-sensitive entity needs to be attached to the electrode, which is often realized via electrostatic attraction, chemisorption, or covalent binding.[413] However, QD-based approaches are often limited by particle aggregation[361,362] and the stabilizing ligands,[119] influencing not only particle assembly, but also the interaction with enzymes. An alternative way can be seen in the synthesis of QDs directly on top of the electrode material via successive ionic layer adsorption and reaction (SILAR).[113,417,418] This easy and low-cost procedure allows to control the QD growth by means of the number of SILAR cycles and pass over the needs for surface ligands.

The design of efficient photo-reducing or oxidizing systems are based on a biocatalyst electronically linked to a light-harvesting entity. First approaches have exploited the activity of the light-active element itself for the detection of enzymatic co-substrates or products, giving information about the enzyme activity and analyte concentration.[87,97,95,139,390] Until now, only a few examples have demonstrated the direct or mediated electron transfer between enzymes and the light-active entities in a light-directed operation.[96,82,89,83,168,360,416]

However, most of these approaches are characterized by some drawbacks: e.g. limited wavelength excitation range, the need for freely diffusing mediators or a low efficiency for the light-to-current conversion. The efficiency is often limited by an insufficient charge-carrier separation as a result of recombination processes at the electrode/photoactive entity interface. In nature, the electron/hole separation has been optimized by a cascade of electron transfer steps, resulting in higher quantum efficiencies. Such pathways can be simulated in artificial systems by combination of different semiconducting materials. Here, a large band gap semiconductor (e.g. TiO_2) with a conduction band acting as electron trap for excited electrons of a second visible-light sensitive semiconducting material (e.g. QDs, dyes or polymers) has proven to be promising for solar cell and photocatalytic applications.[386,387,391]

Another optimization parameter arises from the electronic linkage of the light-sensitive entity to the biocatalyst. Even if the direct electron transfer with biocatalysts is a desired task, such electrodes often lack in efficiency due to inhomogeneous orientation of the enzyme and the restriction of enzyme immobilization to a monolayer. One strategy to overcome such limitations can be the entrapment of the enzyme within a redox-active

polymer.[419,301,296] The biocatalysts are efficiently wired within the polymer matrix independent of the orientation. A further efficiency boost can be expected if enzyme/redox polymer matrices are integrated into 3D electrode architectures.[136,137]

Here, we report on a novel high-performance glucose oxidizing photoanode, which combines the advantages of efficient charge carrier separation within a multicomponent semiconductor electrode, and the efficient wiring of the biocatalyst via a redox polymer to QDs in a functional system. Therefore, a new strategy for the construction of hierarchical invers opal TiO_2 architectures has been investigated. Visible-light sensitivity has been introduced by the growth of PbS QDs via a SILAR approach directly on top of the IO-TiO_2 electrodes. Finally, FAD-GDH has been integrated within the architectures by means of a redox polymer, resulting in an efficient linkage of the biocatalyst to the QDs. The IO-TiO_2|PbS|P_{Os}|FAD-GDH architectures demonstrate the potential of light-driven electron transfer chains. Here the electrons are transferred via several steps from the enzyme via the redox polymer towards the QDs and finally to the IO-TiO_2 electrode, giving access to pronounced glucose-dependent anodic photocurrents.

Experimental section

Materials. [N-(2-hydroxyethyl)piperazine-N-(2-ethansulfonic acid)] (99.5%; HEPES), D-glucose, fluorine-doped tin oxide-coated glass slides (7 Ω cm^{-1}; FTO), lead(II) nitrate (99.999%; $Pb(NO_3)_2$), ammonium sulfide solution (20% in H_2O; $(NH_4)_2S$), polystyrene latex beads (LBs, diameter 0.8 µm) and titaniumtetraisopropoxide (97%; TTIP) were purchased from Sigma-Aldrich (Steinheim, Germany). Poly(1-vinylimidazole-co-allylamine)-Os(bipy)$_2$Cl-redox polymer has been synthesized as reported before.[420] FAD-dependent glucose dehydrogenase from *Aspergillus sp.* has been obtained from SEKISUI CHEMICAL.

Construction of IO-TiO_2 electrodes. Firstly, FTO-coated glass slides have been successively immersed in deionized water, isopropanol and acetone for 15 min each under ultrasonification. The cleaned slides have been dried before further use. A mixture of 100 mg mL^{-1} latex beads (LB; 0.8 µm diameter) and 100 mg mL^{-1} titaniumtetraisopropoxide (TTIP) in isopropanol has been prepared: Therefore, 200 µL of aqueous 100 mg mL^{-1} LB dispersion was mixed with 800 µL ethanol and centrifuged at 25000 g for 8 min in order to remove the water. The supernatant has been discarded and the LB pellet has been suspended in 1 mL ethanol followed by one second centrifugation at 25000 g for 8 min. After removing the supernatant the pellet has been suspended in 180 µL isopropanol in an ultrasonication bath for 5 min. Finally, 20 µL TTIP has been added fast to the LB suspension, which has been again ultrasonicated for 5 min. Afterwards 6 µL per layer of the LB/TTIP-mixture has been dropped onto the cleaned FTO slides and spin coated at 80 rps with a waiting time of 15 s between the deposition steps. The electrode area has been then limited to 0.071 cm^2 by wiping away the

superfluous material. The prepared electrodes have been sintered at 450°C under air for 2 h, resulting in the final IO-TiO_2 electrodes. Flat TiO_2 electrodes have been prepared identical like the IO-TiO_2 electrodes, but without LBs.

Synthesis of PbS QDs. PbS QDs have been directly synthesized on the final IO-TiO_2 electrodes with a SILAR approach.[113,417,418] Therefore, the electrodes have been alternately immersed in aqueous 0.02 M $Pb(NO_3)_2$ and aqueous 0.02 M $(NH_4)_2S$ for 1 min each, starting the SILAR process with the Pb^{2+} precursor. Between the deposition steps the electrode has been carefully rinsed with deionized water and ethanol in order to remove unbound precursors. In this respect one cycle is defined as one reaction with Pb^{2+} and S^{2-}, respectively. IO-TiO_2|PbS electrodes with up to 8 cycles have been prepared according to this procedure.

Assembly of redox polymer and FAD-GDH. 4 µL of a mixture containing 5 mg mL^{-1} Poly(1-vinylimidazole-co-allylamine)-Os(bipy)$_2$Cl-redox polymer and 5 mg mL^{-1} FAD-GDH in 5 mM HEPES pH 7 has been directly drop casted on the IO-TiO_2|PbS electrode and allowed to incubate for 15 min at room temperature in the dark. The drop spread over the whole IO-film, indicating the filling of the pores with P_{Os} and FAD-GDH due to capillary forces. Subsequently, the modified electrode has been extensively rinsed with buffer in order to remove unbound material.

SEM and HR-TEM experiments. Scanning electron microscopy (SEM) measurements have been performed with a JSM-6510 from JEOL at an acceleration voltage of 30 kV with a 2500-fold, 8000-fold, and 25000-fold magnification. The layer height of the IO-TiO_2 electrode has been determined by scratching away a part of the structure and recording the IO-film under an angle of 45° with a 2500-fold magnification. HR-TEM measurements have been performed with a FEI TITAN 80-300 transmission electron microscope (TEM).

Photoelectrochemical experiments. Photoelectrochemical measurements have been performed with an integrated photoelectrochemical workstation from Zahner, containing a potentiostat for the light control and a second potentiostat (Zennium) for the electrochemical control. For the illumination a white light source (410-800 nm) has been used unless stated otherwise. Wavelength-resolved measurements have been performed with a monochromator (Polychrome V, Till Photonics) with a bandwidth of 15 nm. All electrochemical experiments have been performed in a homemade electrochemical cell with a three-electrode arrangement, consisting of an IO-TiO_2 working electrode, a platinum wire as counter electrode, and an Ag/AgCl, 1 M KCl reference electrode.

Results and discussion

The artificial signal chain is depicted in Scheme 1 consisting of three components: 1) a light-active component (TiO_2 electrode and PbS QDs), 2) an electron shuttling component between the QDs and enzyme (Os-complex modified polymer, P_{Os}), and 3) a biocatalytic

component (FAD-dependent glucose dehydrogenase, FAD-GDH). Under illumination with visible light the signal chain is switched on and electrons from the enzymatic glucose conversion are transferred from the enzyme towards P_{Os} to the QDs and finally to the TiO_2 electrode with a concomitant generation of an anodic photocurrent. The TiO_2/QD interface is of importance for the light-directed functionality of the whole biohybrid system, since electron-hole pairs are firstly generated within the QDs and are subsequently efficiently separated at the TiO_2 electrode via injection of excited electrons from the QD into the TiO_2 conduction band.[421] If the light source is switched off, no free charge carriers are available within the semiconductor (QD) and the signal chain is interrupted with no current flow. In the dark the redox polymer remains completely reduced due to the lack of light-directed oxidation, thus the enzyme can no longer transfer electrons and is switched off. Therefore, the whole IO-TiO_2|PbS|P_{Os}|FAD-GDH architecture can be controlled with light as trigger for glucose oxidation.

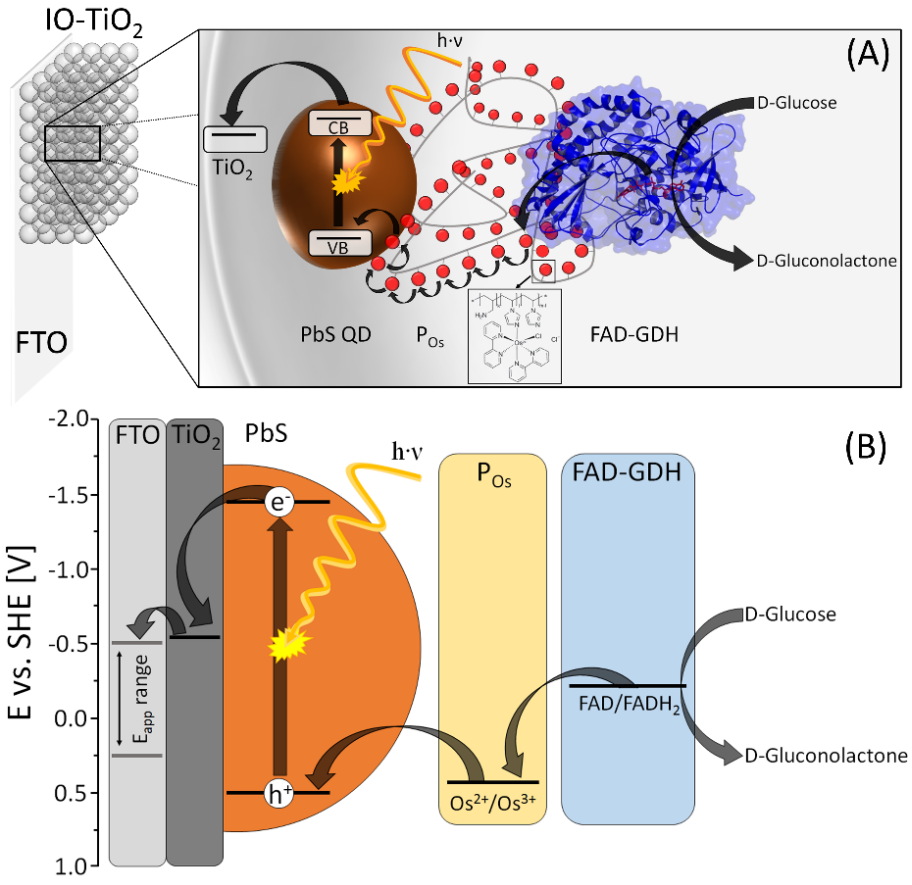

Scheme 1 Schematic illustration of **(A)** the electron transfer steps within the light-driven signal cascade and **(B)** the energetic level E of TiO_2, PbS QDs, the osmium-containing redox polymer (P_{Os}) and of the FAD-dependent glucose dehydrogenase (FAD-GDH). For FAD-GDH a redox potential of free FAD has been assumed, since the redox potential of the enzyme is not yet known. VB = valence band, CB = conduction band.

Synthesis and characterization of the light-sensitive entity. The light-sensitive entity consisting of TiO_2 and PbS QDs has been successively synthesized on a transparent fluorine-doped tin oxide (FTO) electrode. Firstly, we have established a new procedure

for the construction of TiO_2 electrodes with a macroporous inverse opal structure. TiO_2 has been chosen due to its favorable energetic states, which promote the charge carrier separation within the QDs and thus, increase the light-to-current efficiency.[114] The application of a macroporous structure is assumed to be beneficial for the stable integration of a large amount of polymer and enzyme.

The IO-TiO_2 electrodes have been prepared using a template approach: By spin-coating a mixture of latex beads and titaniumtetraisopropoxide (TTIP) onto a cleaned FTO slide, followed by a sintering step, an inverse opal TiO_2 scaffold is formed (see details in experimental section).

The morphology of the final IO-TiO_2 electrodes has been investigated with scanning electron microscopy. As illustrated in Figure 1A the procedure results in an inverse opal TiO_2 film with pores with a diameter of around 650 nm. The pores are open and interconnected with differently sized channels. This procedure allows scalability of the electrode height by deposition of several layers without the need for a sintering step between the layers while maintaining its unique morphology. Up to 8 layers have been deposited, resulting in IO-films with a maximum height of 9 ± 0.7 µm. In the range between 2 and 8 layers the height per layer is found to increase linearly (1.2 ± 0.1 µm per layer) without indication of a limitation (SI, Figure S1E). Control experiments of electrodes prepared without latex beads show that both, TTIP and latex beads, are needed for the successful construction of the IO-TiO_2 film (SI, Figure S1).

The optical features of the IO-TiO_2 electrodes have been investigated with UV/VIS absorption spectroscopy. The IO-TiO_2 films are of high transparency, which decreases linearly with increasing number of layers (SI, Figure S2&S3). Interestingly, the transmittance of the IO-film is found to be noticeably higher than the planar TiO_2 film (prepared without LB, SI Figure S4), which can be attributed to the absence of dense agglomerates within the IO-TiO_2 structure. In comparison to IO-films prepared in a template approach with TiO_2 nanoparticles the structures produced in this work show a higher transparency.[416,422,423] This significantly expands the field of applications of our IO-films. Also the fast construction and easy scalability of the electrodes is a clear advantage compared to other approaches.[398–400]

The PbS QDs have been synthesized directly on top of the IO-TiO_2 film with a SILAR approach as reported before.[113,418] For this, the electrode is immersed alternately in Pb^{2+} and S^{2-} containing solutions, resulting in a growth of PbS QDs with increasing number of cycles (a cycle is defined as one reaction with Pb^{2+} and S^{2-}, respectively). The successful synthesis of the QDs within the IO-TiO_2 electrode can be confirmed by a coloration of the structure from white to brown. The UV/VIS absorption spectra of a 4 layered IO-TiO_2 electrode exhibit an increase of the absorbance over the whole visible wavelength range with increasing number of cycles from 2 up to 8 cycles (SI, Figure S5). High resolution (HR)-TEM measurements show that the QDs reach a diameter between 3 and 4 nm after

4 cycles (Figure 1B), which is in good agreement with a previous report.[418] According to this the band gap is in the range of 1.92 – 1.47 eV.[350] Consequently, the energy gained during illumination is high enough to inject excited electrons into the conduction band of TiO_2[386,421] and thus, to provide visible light sensitivity for the light-driven signal chain.

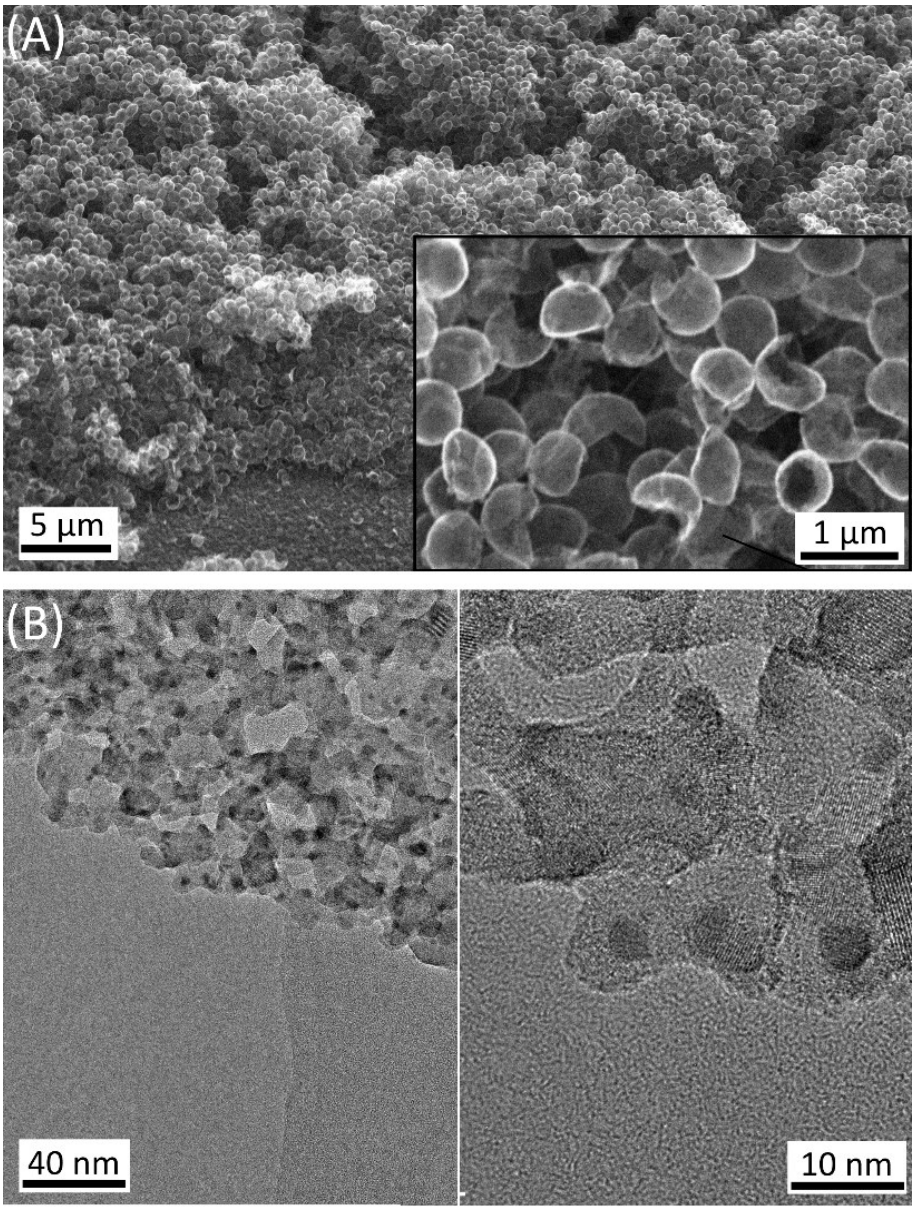

Figure 1 (A) SEM image of an IO-TiO_2 electrode under an angle of 45° with a 2500-fold magnification by applying an acceleration voltage of 30 kV. Inset: Top view with a 25000-fold magnification. **(B)** HR-TEM image of PbS QDs synthesized on IO-TiO_2 electrodes.

Next the functionality of IO-TiO_2|PbS electrodes has been investigated in photochronoamperometric measurements at 0 mV vs. Ag/AgCl, 1 M KCl using a white light source without a UV share (410 – 800 nm). Therefore, the photocurrent response of a 4 layered IO-TiO_2 electrode before and after deposition of PbS QDs (4 cycles) in buffer has been compared (SI, Figure S6). As expected no photocurrent response is obtained for the pure IO-TiO_2 (which can be attributed to the large band gap of TiO_2, enabling only

excitation at a wavelength <400 nm).[386] In contrast, a pronounced anodic photocurrent is found for the IO-TiO_2|PbS_{4cycle} system, demonstrating the successful visible-light sensitization of the electrode.

Integration of the biocatalytic entity. As biocatalyst FAD-GDH from *Aspergillus sp.* has been used, which catalyzes the oxidation of D-glucose to D-gluconolactone. The wiring of the enzyme has been realized with the $Os^{2+/3+}$ containing poly(1-vinylimidazole-co-allylamine)-Os(bipy)$_2$Cl-redox polymer, which has already demonstrated a good interaction with various biocatalysts.[83,137,424] We have chosen this redox polymer due to its favourable redox potential and chemical properties. Here, it has to be mentioned that P_{Os} does not only enable an intermolecular electron exchange with the enzyme, but also charge transfer within the polymer as an electron hopping mechanism between the redox-active $Os^{2+/3+}$ moieties. Furthermore, the functional groups of P_{Os} (amino group and imidazole group) cause a cationic nature of the polymer at pH 7, which should also be beneficial for the electrostatic interaction with the negatively charged enzyme (pI 4.4)[††]. The amino groups are further expected to favor the anchoring of P_{Os} to the QD surface[363,425] and thus to stabilize the QDs and the polymer within the IO-film.

For the integration of P_{Os} and FAD-GDH into the IO-TiO_2|PbS architecture a mixture of both is drop-casted on top of the electrodes and incubated in the dark (for details see experimental section). Figure 2A shows the photocurrent response of the final 4 layered IO-TiO_2|PbS_{4cycle}|P_{Os}|FAD-GDH electrode before and after addition of glucose. While in buffer anodic photocurrents of 8.2 ± 2 µA cm^{-2} are obtained, the presence of glucose results in a 2-fold enhancement of the signal (17 ± 2.4 µA cm^{-2}), giving a first hint for the functional construction of the biohybrid architecture. In this respect no dark currents have been observed, which can be explained by the blocking behavior of the TiO_2-film.

In order to clarify the origin of the glucose-dependent photocurrent modulation and the mechanism of the whole light-driven signal chain, we have performed a set of control experiments. Neither the IO-TiO_2|PbS_{4cycle}|P_{Os} electrodes without FAD-GDH nor the IO-TiO_2|PbS_{4cycle}|FAD-GDH electrodes without polymer show a signal response after addition of glucose (SI, Figure S7&S8). This confirms that both, P_{Os} and FAD-GDH, are needed to provide the biocatalytic activity and the efficient wiring to the IO-TiO_2|PbS electrode. Interestingly, IO-TiO_2|P_{Os}|FAD-GDH electrodes without PbS QDs yield small anodic photocurrents of 0.5 ± 0.1 µA cm^{-2} and 1 ± 0.3 µA cm^{-2} in the absence and presence glucose, respectively. This can be explained by a direct excitation of P_{Os} under illumination with visible light (see UV/VIS absorption spectrum SI, Figure S14), resulting in an electron injection from P_{Os} into the conduction band of TiO_2 as previously reported for osmium-containing dyes.[426] However, the signal response of this signal chain

[††] The information on the pI of the enzyme is given by the supplier of FAD-GDH.

is found to be 17-fold smaller than of electrodes with QDs and thus is significantly less efficient for the photoelectrochemical glucose oxidation. Consequently, the whole IO-TiO_2|PbS_{4cycle}|P_{Os}|FAD-GDH architecture gives rise to an efficient P_{Os}/QD-interaction as the dominant electron transfer pathway, while the direct interaction between TiO_2 and P_{Os} has only a minor contribution. All control experiments indicate an electron transfer cascade of the IO-TiO_2|PbS_{4cycle}|P_{Os}|FAD-GDH biohybrid system as illustrated in Scheme 1.

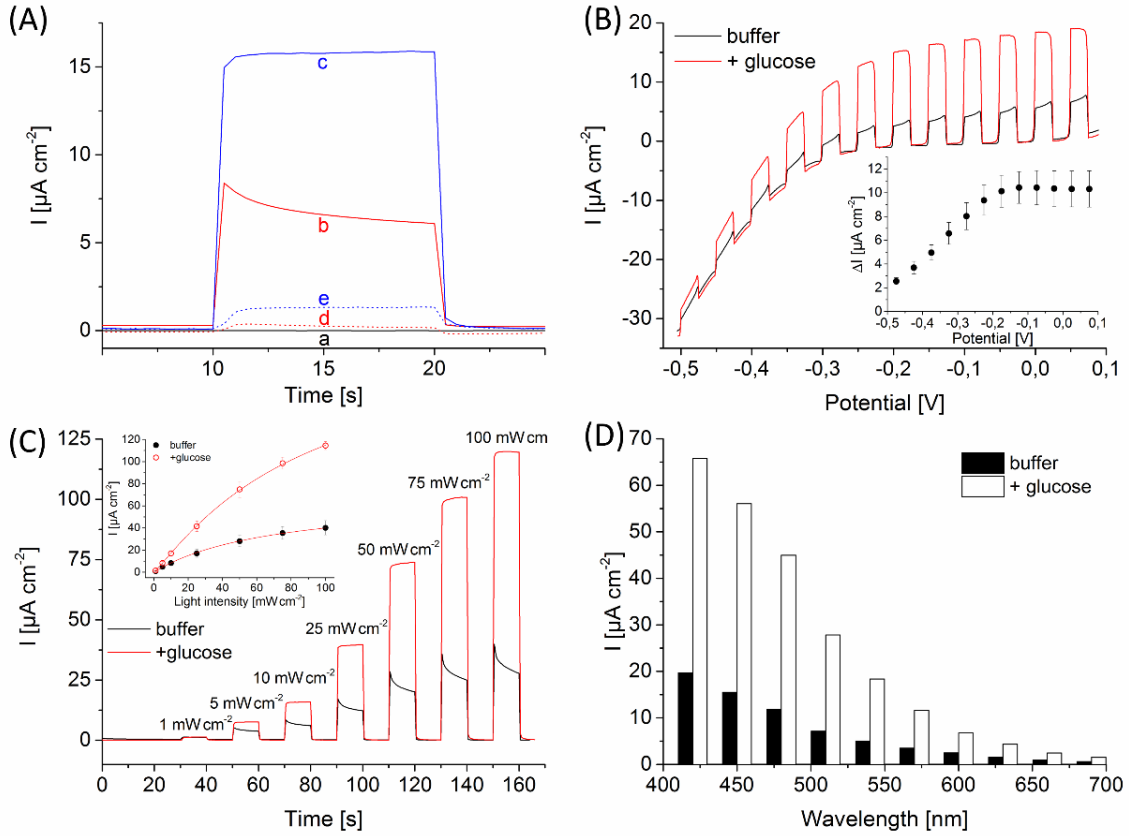

Figure 2 (A) Photochronoamperometric measurement of 4 layered IO-TiO_2 electrodes after different modification steps: (a) blank IO-TiO_2 electrode; (b) IO-TiO_2|PbS_{4cycle}|P_{Os}|FAD-GDH in buffer; (c) IO-TiO_2|PbS_{4cycle}|P_{Os}|FAD-GDH after addition of 10 mM glucose; (d) IO-TiO_2|P_{Os}|FAD-GDH without QDs in buffer; (e) IO-TiO_2|P_{Os}|FAD-GDH without QDs after addition of 10 mM glucose. (white light source is switched on from 10 s to 20 s; 10 mW cm^{-2}; 0 mV vs. Ag/AgCl, 1 M KCl; 5 mM HEPES pH 7) **(B)** Chopped light voltammetry of a 4 layered IO-TiO_2|PbS_{4cycle}|P_{Os}|FAD-GDH electrode in the presence and absence of 10 mM glucose. (white light source; 10 mW cm^{-2}; potential vs. Ag/AgCl, 1 M KCl; 5 mV s^{-1}; 5 mM HEPES pH 7) **(C)** Photochronoamperometric measurement and photocurrent density (inset) of a 4 layered IO-TiO_2|PbS_{4cycle}|P_{Os}|FAD-GDH electrode at different light intensities in the absence and presence of 10 mM glucose. (chopped white light source; 0 mV vs. Ag/AgCl, 1 M KCl; 5 mM HEPES pH 7) **(D)** Wavelength-dependent photocurrent density of a 4 layered IO-TiO_2|PbS_{4cycle}|P_{Os}|FAD-GDH electrode in the absence and presence of 10 mM glucose. (0 mV vs. Ag/AgCl, 1 M KCl; 5 mM HEPES pH 7)

Subsequently, the properties of 4 layered IO-TiO_2|PbS_{4cycle}|P_{Os}|FAD-GDH electrodes have been evaluated in additional photoelectrochemical experiments. As depicted in Figure 2B, chopped light voltammetry measurements under illumination with 10 mW cm^{-}

^{2} show exclusively anodic photocurrents and reveal the unidirectionality of the system. In the whole potential range between -500 mV and 0 mV vs. Ag/AgCl, 1 M KCl a strong increase of the signal can be achieved by addition of 10 mM glucose. The glucose-dependent component of the photocurrent increases with rising potential and levels off at -200 mV vs. Ag/AgCl, 1 M KCl.

The photocurrent response can be modulated by the light intensity used during illumination (Figure 2C). Enhancing anodic signals have been obtained with increasing excitation intensities in the range between 1 mW cm^{-2} and 100 mW cm^{-2}, achieving maximum photocurrents of 40.1 ± 6.4 µA cm^{-2} and 114.5 ± 3.7 µA cm^{-2} in buffer and 10 mM glucose, respectively. The biocatalytic glucose turnover is found to distinctly improve the light-to-current conversion and demonstrates that the QDs can even be supplied with enzymatic electrons at high excitation intensities i.e. high turnover rates at the QD/P_{Os} interface. In this context, wavelength-dependent measurements with and without glucose show the wide excitation range found for the IO-TiO_2|PbS_{4cycle}|P_{Os}|FAD-GDH electrodes (Figure 2D). The biohybrid system displays a strong glucose sensitivity in the visual range between 400 nm and 700 nm.

Stability measurements over 30 min in a pulse mode with 20 s light pulses reveal the excellent stability of the biohybrid architecture, showing no decrease of the photocurrent in the presence of 10 mM glucose (SI, Figure S9). Even after rinsing the electrode with high ionic strength buffer (5 mM HEPES + 200 mM KCl pH 7) for 2 min the light-directed functionality remains preserved, showing 94% (ΔI = 10.2 µA cm^{-2}) of the glucose-dependent photoresponse without treatment. Obviously, the IO-TiO_2 electrode provides a favourable surface for the stabilization of all components within the IO-film. The importance of the electrode morphology for the functionality can also be confirmed by comparing the photoelectrochemical response of IO-TiO_2|PbS_{4cycle}|P_{Os}|FAD-GDH electrodes with flat TiO_2|PbS_{4cycle}|P_{Os}|FAD-GDH electrodes, resulting in low photocurrent stability, magnitude and smaller glucose response (SI, Figure S10). Furthermore, we suppose a protection of the QDs from degradation at moderate light intensities by the redox polymer in combination with the biocatalytic electron supply, since pure IO-TiO_2|PbS electrodes without polymer and enzyme yields a rather fast photocurrent decline (SI, Figure S9).

Influence of SILAR cycle number and IO-TiO_2 layer number. Next, factors such as the number of SILAR cycles, the number of IO-TiO_2 layers and their influence on the photoelectrochemical response of the biohybrid system have been evaluated. Initially, 4 layered IO-TiO_2|PbS|P_{Os}|FAD-GDH electrodes prepared with different number of SILAR cycles (0, 2, 4, 6 and 8 cycle) have been compared. Figure 3A illustrates the photocurrent density change after addition of 10 mM glucose. The photoresponse in the presence of glucose shows a continuous signal magnification with rising cycle number. The enhanced photocurrent per SILAR cycle can be explained by the increasing

absorbance of the PbS QDs with every cycle (SI, Figure S5), leading to a higher photon absorbance yield. Furthermore, the increased deposition of QDs results in a larger interface for the interaction with P_{Os} and is expected to improve the signal output. This is also reflected by an improved external quantum efficiency (EQE) with increasing number of SILAR cycles (Table 1).

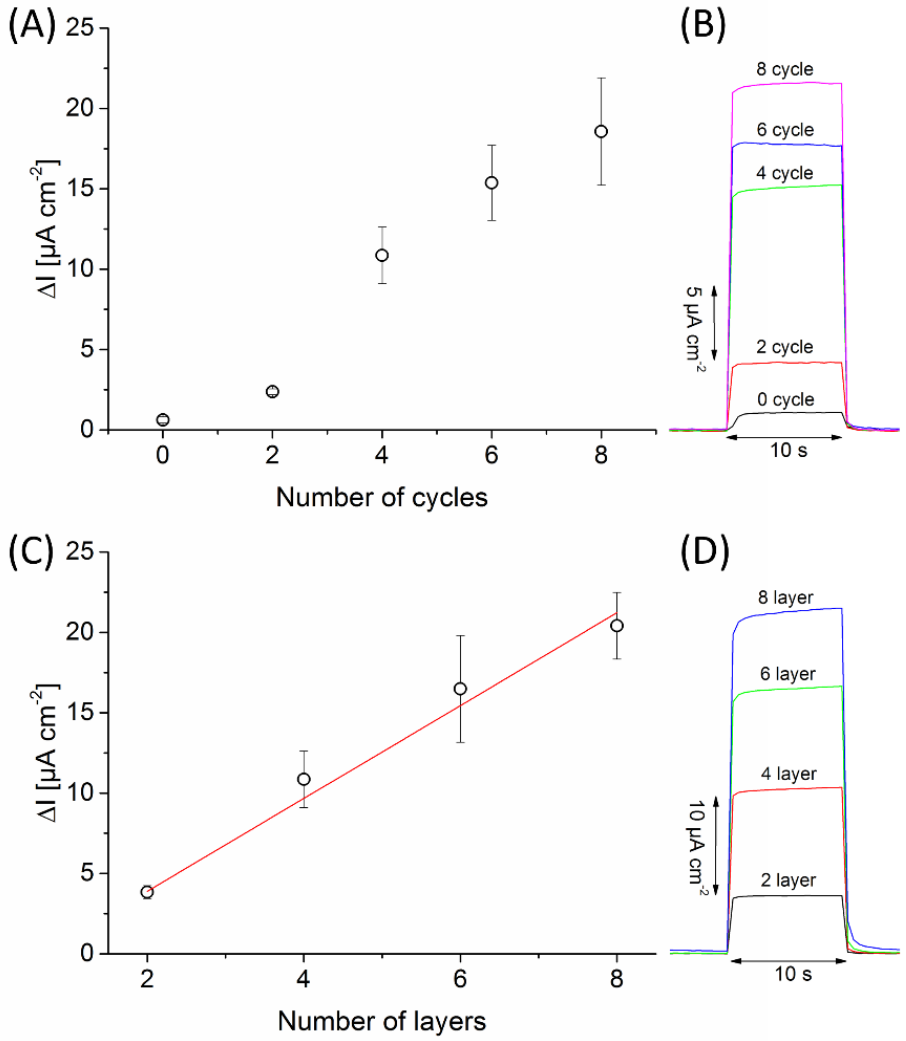

Figure 3 (A) Photocurrent density change ΔI and **(B)** photocurrent pulse of 4 layered IO-TiO_2|PbS_{Xcycle}|P_{Os}|FAD-GDH electrodes for different number of SILAR cycles after addition of 10 mM glucose. **(C)** Photocurrent density change ΔI and **(D)** photocurrent pulse of IO-TiO_2|PbS_{4cycle}|P_{Os}|FAD-GDH electrodes for different number of IO-TiO_2 layers after addition of 10 mM glucose. Inset: Photocurrent density of the respective electrodes in buffer. (white light source switched on for 10 s; 10 mW cm^{-2}; 0 mV vs. Ag/AgCl, 1 M KCl; 5 mM HEPES pH 7)

Figure 3C shows the photoresponse of IO-TiO_2|PbS_{4cycle}|P_{Os}|FAD-GDH electrodes for different numbers of IO-film layers. The photocurrent density change after addition of 10 mM glucose rises linearly with 2.9 ± 0.2 μA cm^{-2} per layer, when the electrode thickness is increased. Also an increasing EQE with the layer number has been found (Table 1). The results suggest that the increasing surface area per layer can be exploited for the growth of the QDs, as well as for the integration of enzymes and polymers without any indication of a limitation. Even for IO-films with a height of 10 μm (8 layer) the

propagation of light within the structure seems to be little affected, which can be attributed to the high transparency of the IO-TiO_2 films. Accordingly, the biohybrid approach presented here allows for good scalability through the number of IO-film layers deposited, giving rise to a tunable photoelectrochemical response.

Table 1 EQE of IO-TiO_2|PbS|P_{Os}|FAD-GDH electrodes in dependence of the number of SILAR cycles and the number of IO-TiO_2 layers in the presence of 10 mM glucose, under illumination with 10 mW cm^{-2} with a white light source and by applying 0 mV vs. Ag/AgCl, 1 M KCl. For the investigation of the cycle dependence 4 layered IO-TiO_2 electrodes have been used, while for the layer dependence 4 SILAR cycles have been applied.

No.	cycle	layer
0	0.023 ± 0.007	-
2	0.1 ± 0.002	0.12 ± 0.01
4	0.38 ± 0.05	0.38 ± 0.05
6	0.43 ± 0.05	0.57 ± 0.11
8	0.52 ± 0.09	0.72 ±0.08

Performance of IO-TiO_2|PbS|P_{Os}|FAD-GDH electrodes. To evaluate the performance of the biohybrid architecture, further photoelectrochemical experiments have been performed with 8 layered IO-TiO_2|PbS_{4cycle}|P_{Os}|FAD-GDH electrodes. As illustrated in Figure 4A concentration-dependent measurements have been carried out by gradually increasing the glucose concentration (at 0 mV vs. Ag/AgCl, 1 M KCl and using an excitation intensity of 10 mW cm^{-2}). The biohybrid architecture shows a first signal response of 0.61 ± 0.19 µA cm^{-2} at low substrate concentrations of 10 µM and increases up to 29.2 ± 2.8 µA cm^{-2} at 100 mM glucose. The photocurrent response is found to be linear between 10 µM and 200 µM glucose, reaching a sensitivity of 31 µA mM^{-1} cm^{-2}. The concentration dependency follows the Michaelis-Menten kinetics and the apparent $K_{M,app}$ is determined to be 2.9 ± 0.5 mM. Thus, the $K_{M,app}$ value of our light-controlled biohybrid system is lower than the value reported by the supplier (50 mM), but comparable to previous reported $K_{M,app}$ values for fungal FAD-GDH immobilized on light-insensitive electrodes (4 - 40 mM).[297,295,302,303] Compared to other photoelectrochemical sensors using glucose as analyte the IO-TiO_2|PbS_{4cycle}|P_{Os}|FAD-GDH electrodes provide higher sensitivity, a larger dynamic measuring range, and pass over the needs for freely diffusing co-substrates or redox mediators.[82,97,139,168,360]

In order to evaluate the suitability as photo(bio)anode for the construction of (photo)-biofuel cells, we have characterized the 8 layered IO-TiO_2|PbS_{4cycle}|P_{Os}|FAD-GDH electrodes with respect to their maximum performance in the presence of 100 mM glucose. In the inset in Figure 5A, the influence of the excitation intensity on the photoresponse is shown. A saturation-type behavior is found, reaching already a half maximum current at 29 mW cm^{-2}.

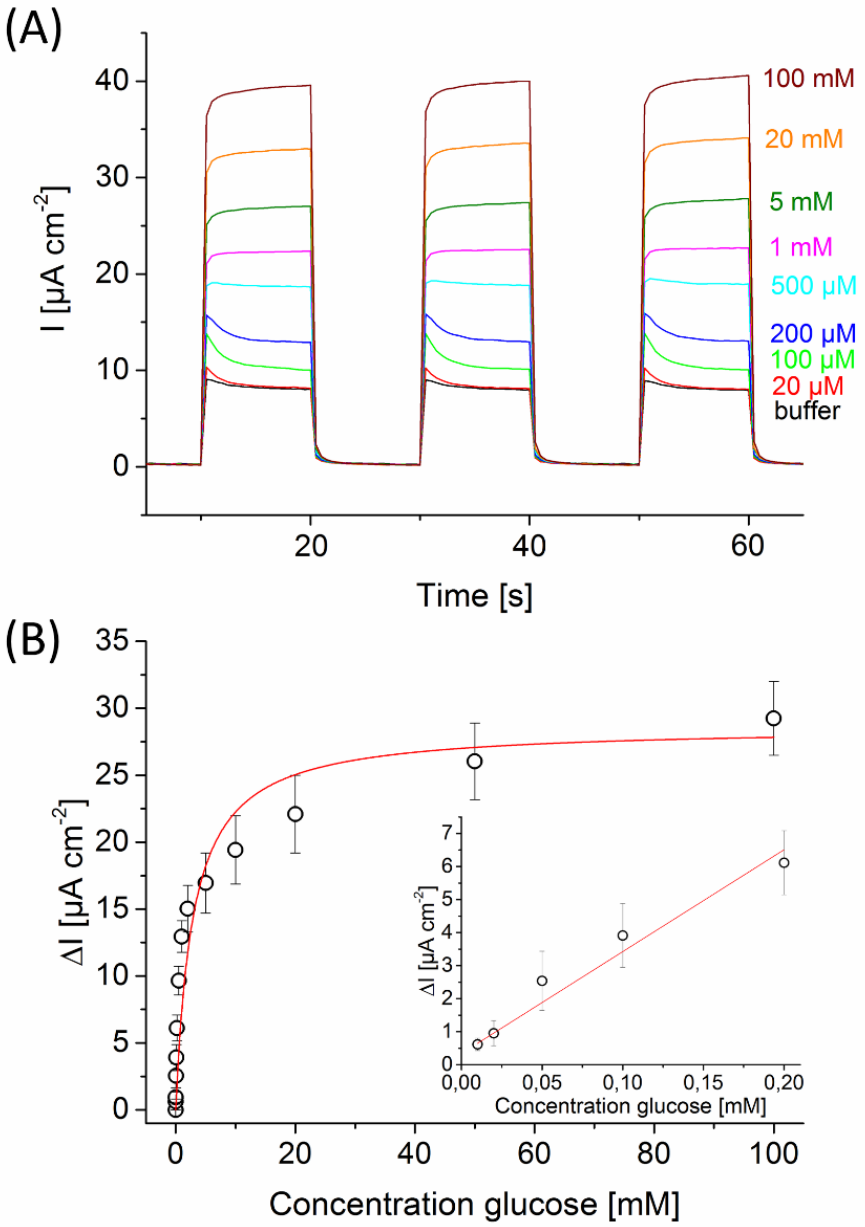

Figure 4 (A) Photochronoamperometric measurement and **(B)** photocurrent density change ΔI of 8 layered IO-TiO_2|PbS_{4cycle}|P_{Os}|FAD-GDH electrodes before and after addition of different glucose concentrations. (white light source chopped in 10 s intervals; 10 mW cm^{-2}; 0 mV vs. Ag/AgCl, 1 M KCl; 5 mM HEPES pH 7)

By recording I-V curves under continuous illumination (100 mW cm^{-2}) a maximum current (J_{max}) of 207 ± 17 µA cm^{-2} and open circuit potential (OCP) of -540 ± 14 mV vs. Ag/AgCl, 1 M KCl has been determined (Figure 5B; for measurements without glucose or illumination we refer to the SI, Figure S11). A maximum power density of 31.3 ± 2.7 µW cm^{-2} is achieved at -287 ± 80 mV vs. Ag/AgCl, 1 M KCl and the fill factor (FF) is calculated to be 0.28 ± 0.002. These results display the high performance of the photo(bio)anode for glucose oxidation, which can be attributed to the favourable combination of light-harvesting functionality and high biocatalytic activity. Remarkably, the biohybrid architecture allows a first gain of electrons from the biocatalytic reaction at

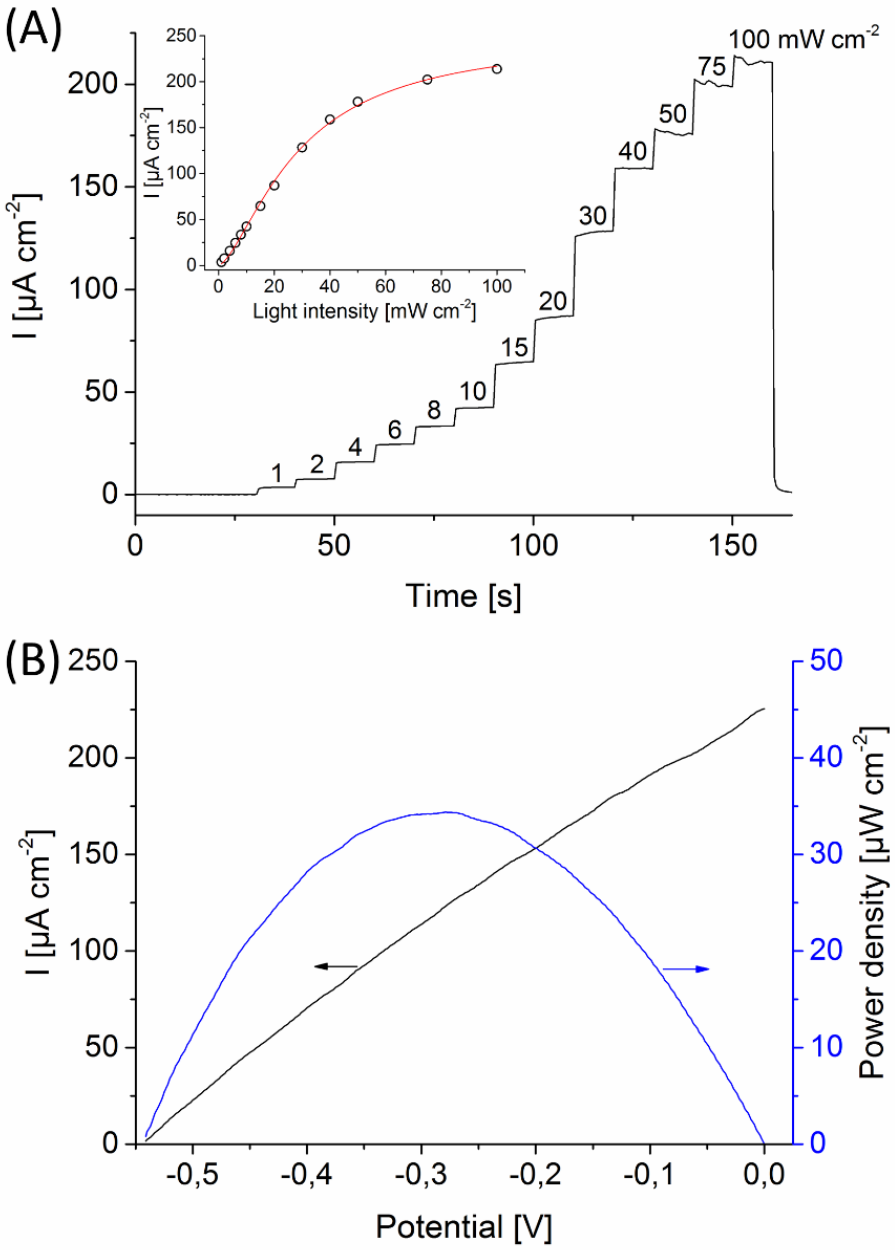

Figure 5 (A) Photochronoamperometric measurement of an 8 layered IO-TiO_2|PbS_{4cycle}|P_{Os}|FAD-GDH electrode under continuous illumination with stepwise enhancement of the light intensity from 0 mW cm^{-2} up to 100 mW cm^{-2} in 100 mM glucose. (white light source; 0 mV vs. Ag/AgCl, 1 M KCl; 5 mM HEPES pH 7) **(B)** Current and power density of an 8 layered IO-TiO_2|PbS_{4cycle}|P_{Os}|FAD-GDH electrode in dependence of the applied potential and under continuous illumination with 100 mW cm^{-2} in the presence of 100 mM glucose. The maximum power output has been determined by using the 8 layered IO-TiO_2|PbS_{4cycle}|P_{Os}|FAD-GDH electrode as a working electrode, a Pt wire as counter electrode and an Ag/AgCl, 1 M KCl reference electrode. (white light source; 100 mW cm^{-2}; potential vs. Ag/AgCl, 1 M KCl; 5 mV s^{-1}; 5 mM HEPES pH 7)

quite negative potentials of -540 mV vs. Ag/AgCl, 1 M KCl, which to our knowledge has never been reported before. In contrast, flat FTO|P_{Os}|FAD-GDH electrodes without TiO_2 and PbS QDs (i.e., without light sensitivity) show a first deduction of biocatalytic electrons in the dark at a potential of around +50 mV vs. Ag/AgCl, 1 M KCl (SI, Figure

S12). This corresponds to an improvement of the potential of more than 500 mV by using the IO-TiO_2|PbS_{4cycle}|P_{Os}|FAD-GDH architecture and light-directed read-out. Consequently, the biohybrid architecture provides both, a high driving force for the withdrawal of electrons from the enzyme by the redox polymer and a low working potential under illumination, resulting in a unique light-directed electrode arrangement with high performance. Long-term experiments with glucose in solution and under illumination with high intensity (100 mW cm^{-2}) reveal a rather constant electron transfer rate at the electrode, yielding a transferred charge of 220 mC cm^{-2} in 30 min (SI, Figure S13).

Under these conditions the cumulative anodic photocurrent output in the presence of glucose is found to be at least 70-fold higher than in previous studies with immobilized light-sensitive entity and enzyme on rather flat electrodes[82,83,360] and 5-fold higher than on 3D electrodes.[416] This can be attributed to the high surface area of the IO-TiO_2 architectures, but also to the efficient charge carrier generation and separation at the QD/TiO_2 interface and the efficient wiring of FAD-GDH to the QDs via P_{Os}. Thus, our developed architecture gives access to an overall improved photo(bio)anode and may stimulate the interest in developing light-triggered biosensors, solar-to-energy and solar-to-chemical converting biohybrid devices.

Conclusion

In summary, this work has introduced a new concept for the coupling of biocatalytic reactions to the light-triggered read-out of QD electrodes. Here, a procedure for the scalable construction of IO-TiO_2 electrodes has been established, serving as electrode platform for the integration of PbS QDs, a redox polymer, and FAD-GDH. Under illumination electron-hole pairs are generated within the PbS QDs and separated at the TiO_2 interface, leaving behind holes which oxidize P_{Os}. As a result of glucose turnover P_{Os} becomes regenerated, supplying the photoelectrochemical reaction with new electrons from the biocatalytic reaction for an enhanced photocurrent output. The signal response can be modulated by the potential, the light-intensity, and the wavelength used during illumination, allowing the accurate control of the biohybrid system. Increasing glucose-dependent photocurrents have been obtained with rising QD loading and electrode height, showing a concentration-dependent behavior between 10 µM and 50 mM glucose. A first gain of electrons from the biocatalytic reaction has been found at a quite negative potential of around -540 mV vs. Ag/AgCl, 1 M KCl, giving access to the design of high performance photobioelectrochemical cells using glucose as fuel.

Such light-driven biohybrids are desirable due to their unique electrode properties, combining the photophysical features of the IO-TiO_2|PbS electrode for charge carrier generation and separation with the efficient wiring of a specific enzymatic reaction via a redox polymer. This approach provides the basis for the efficient photonic wiring of other light-insensitive biocatalysts for light-directed sensing and power-supply.

Acknowledgment

This work was supported by the German Research Foundation (DFG grants Li 706/8-1 and Pa 794/15-1).

5 Discussion

In the following chapter the results of this thesis will be discussed, compared with each other and ranked according to the state of the art. The thesis is composed of the four topics listed below:

- Enzymes coupled to QD-modified gold electrodes via redox mediators (P4.1, chapter 4.1)
- InGaN/GaN NWs for the detection of NADH (P4.2, chapter 4.2)
- 3D IO-TiO_2 electrodes with integrated sulfonated polyanilines and PQQ glucose dehydrogenase (P4.3, chapter 4.3)
- 3D IO-TiO_2 electrodes with integrated PbS QDs, osmium complex-containing redoxpolymer and FAD-dependent glucose dehydrogenase (P4.4, chapter 4.4)

A schematic structure overview of the individual PEC systems is illustrated in figure 9. All studies share the same concept of using photoactive elements for the coupling with enzymatic reactions or at least enzymatic cofactors, giving access to the construction of light-driven signal chains for sensing and power-supply. In the first part, the different strategies for the construction of light-sensitive electrodes will be discussed and key functions of these PEC electrodes such as the influence of the electrode material on the photocurrent direction and the excitation wavelength range will be elaborated. The second part of the discussion is dealing with the performance of the constructed photocatalytic anode for the oxidation of NADH (P4.2) and three biophotocatalytic anodes for the oxidation of glucose (P4.1, P4.3 and P4.4). To compare the performance of these systems with each other, but also with previous NADH or sugar converting PEC approaches, important PEC parameter have been evaluated, including the maximum photocurrent response, the onset potential for the analyte oxidation and the detection range. Here, it has to be mentioned that a quantitative comparison with previous PEC reports is challenging, since often different conditions, e.g. light source, light intensity and applied bias, have been used and thus only a rough evaluation of the PEC systems can be given. The most important parameter of all PEC electrodes constructed in this thesis are summarized in table 1.

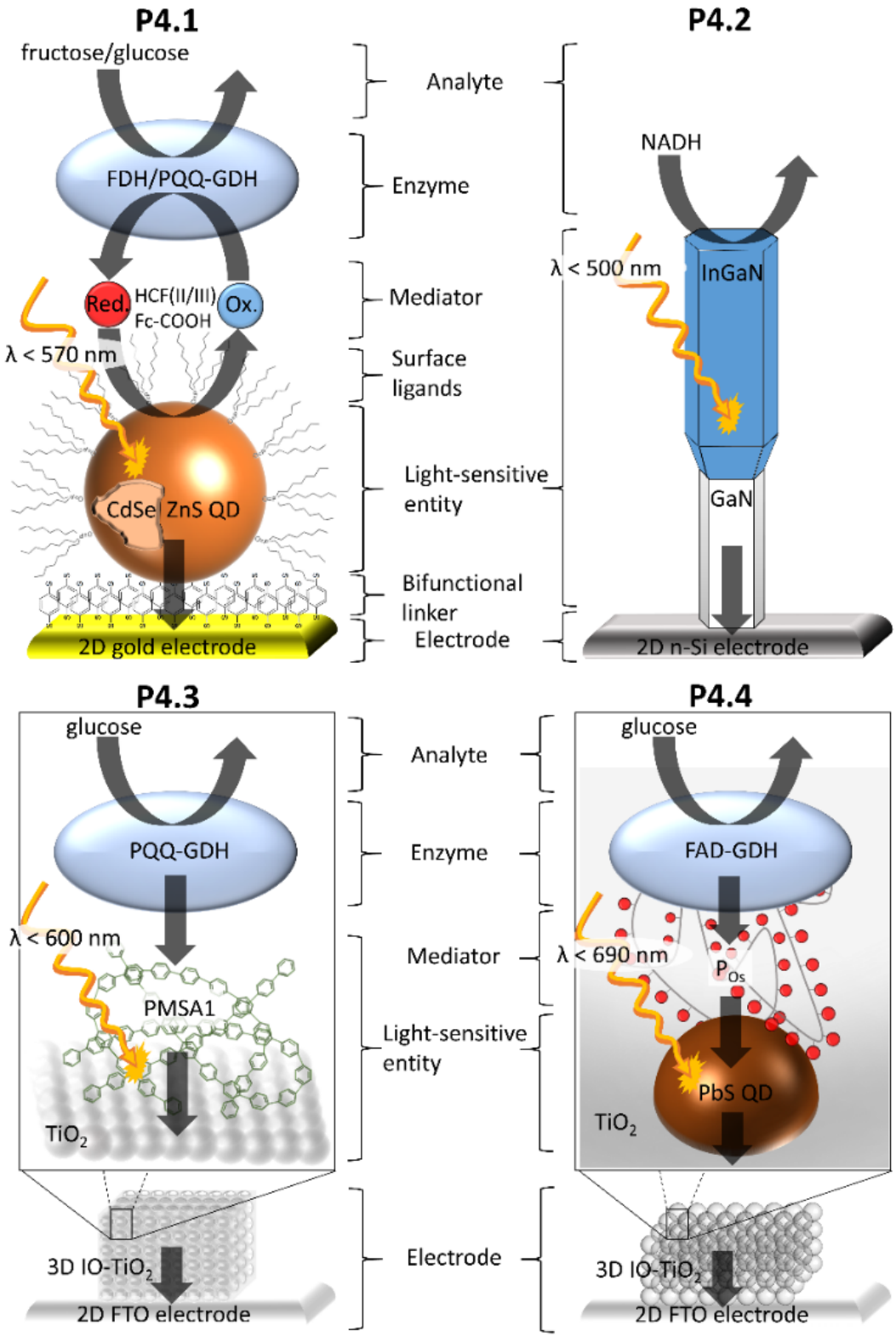

Figure 9. Schematic overview of the constructed PEC electrodes, showing the main components of P4.1, P4.2, P4.3 and P4.4.

Table 1. PEC parameter of the light-switchable electrodes constructed in this thesis.

Paper	Analyte	J_{max} [μA cm^{-2}]	U_{onset} vs. Ag/AgCl [V]	Dynamic detection range [mM]	$K_{M,app}$ [mM]
P4.1(1) Au|QDs|Fc-$COOH^{S.}$|PQQ-GDH	glucose	6	-	0.005 - 0.1	0.028
P4.1(2) Au|QDs|Fc-$COOH^{I.}$|PQQ-GDH	glucose	0.6	-	0.01 - 0.5	0.033
P4.1(3) Au|QDs| $HCF^{S.}$|FDH	fructose	8	-	0.05 - 10	0.74
P4.2 n-Si|InGaN/GaN NWs	NADH	104	-0.3	0.001 - 10	0.73
P4.3 FTO|IO-TiO_2| PMSA1|PQQ-GDH	glucose	44.7	-0.315	0.01 – 0.25	0.049
P4.4 FTO|IO-TiO_2|PbS |P_{Os}|FAD-GDH	glucose	207	-0.54	0.01 - 50	2.9

$^{S.}$ - soluble, $^{I.}$ - immobilized

5.1 Connecting photoactive entities with electrodes

The contact of the electrode with the photoactive entity is of great importance for the separation of generated charge carriers and thus the formation of a photocurrent. Therefore, a good connection is key for the construction of efficient PEC electrodes. Different immobilization strategies have been applied and characterized within this thesis, which can be divided into three approaches: 1) Assembly of light-sensitive entities to electrodes via bifunctional reagents (P4.1), 2) assembly of light-sensitive entities to electrodes without bifunctional reagents (P4.3), and 3) direct synthesis of light-sensitive entities on electrodes (P4.2 and P4.4).

P4.1 follows a rather popular and widespread approach, starting with the synthesis of QDs in solution, followed by a binding of the nanocrystals to the electrode via dithiol compounds.[91,96,119] The advantage of this strategy is mainly attributed to the production of high quality QDs by solution-based synthesis protocols in terms of optical features, quantum efficiency and monodispersity.[49] This allows an accurate control of the energetic states within the semiconductor nanocrystals and can be important for the adjustment of the respective electrode components to each other. Furthermore, the QD immobilization via bifunctional linkers is not only limited to a certain electrode material e.g. gold, but can be adapted to other electrode materials by simply exchanging the coupling agents. One drawback is the need for stabilizing surface ligands in order to prevent particle aggregation. In P4.1 the CdSe/ZnS QDs are modified with hydrophobic trioctylphophine

oxide (TOPO) ligands and thus do not favor the stable immobilization of the nanoparticles to gold electrodes by itself, but instead need a ligand exchange with bifunctional reagents. The attachment of the QDs to the electrode has been realized via dithiols, which is often difficult to control due to the tendency of dithiols to bind with both thiol groups to the surface.[119] SEM experiments (P4.1, Fig. 2) reveal a rather homogeneous distribution of the QDs at the BDT-modified electrode. However, obviously some nanoparticles tend to form small aggregates, which is probably attributed to the interaction between the hydrophobic alkane chains of the TOPO surface ligands. This could be one of the reasons for the variations found between the prepared QD electrodes. Nevertheless, the PEC performance of the electrode seems to be less affected and gives rise to pronounced photocurrents. The photocurrent amplitude and behavior in the absence of redox molecules is comparable to previous reports on QD electrodes using bifunctional linkers for the nanoparticle fixation.[97,98]

In order to overcome the limitation of linker molecules for the attachment of photoactive materials, different concepts have been used in this thesis. In P4.2 InGaN/GaN NWs have been synthesized directly on top of 2D n-doped Si electrodes by plasma-assisted molecular beam epitaxy. This method allows the controlled growth of the NWs and thereby provides a direct interaction between the electrode and the photoactive material. Moreover, the NWs with a length of 550 nm and a diameter of about 72 nm give rise to an enlarged surface area of the photoactive entity compared to P4.1, where QDs with a diameter of 2.8 nm have been assembled on 2D gold electrodes. A comparison between P4.1 and P4.2 is difficult, because of the different light sources and intensities used during the experiments. While the InGaN/GaN NWs have been illuminated with monochromatic light of 449 ± 5 nm, the QDs have been excited with a white light source. Regardless, it can be stated that the overall PEC performance in terms of the signal strength and the noise level could be significantly improved by application of InGaN/GaN NW electrodes (see P4.2, Fig. 6D).

In analogy to P4.1, in P4.3 the photoactive entity, i.e. sulfonated polyanilines (PMSA1), has been firstly synthesized in solution and subsequently immobilized to TiO_2 electrodes, but without the utilization of linker molecules. In this case the photoactive entity itself enables the stable fixation to the electrode surface, which is realized via physical adsorption and is supported by the sulfonic groups of the polymer ensuring a high attraction to the TiO_2 surface.[122] This overcomes the needs for additional surface modifications of the bare electrode and therefore simplifies the PEC electrode construction compared to P4.1. Similar approaches have been reported for dye molecules allowing the direct assembly to nanostructured SnO_2 surfaces,[80] however, the utilization of a polymer as photoactive entity for the construction of biocatalytic PEC systems is a unique approach. Moreover, in P4.3 a further strategy for the enlargement of the electrode surface area has been elaborated. Here, not the photoactive entity itself increase the surface area as demonstrated for the InGaN/GaN NWs in P4.2, but a 3D inverse opal TiO_2

electrode has been constructed allowing the harboring of higher amounts of PMSA1 and therefore help to increase the PEC performance as compared to flat electrodes.

In P4.4, PbS QDs has been synthesized via a SILAR approach on IO-TiO_2 electrodes. The SILAR approach has often been applied for the construction of solar cells due to its easy applicability and the feasibility to control the amount and size of QDs deposited via the number of performed SILAR cycles. Despite this, QDs prepared via SILAR approaches are often rather polydisperse compared to QDs synthesized via solution-based procedures. The polydispersity of QDs can be an issue if the electronic states within the QDs have to be exactly adjusted to a potential reactant, however, for the most PEC applications highly monodisperse QDs are not required. Therefore, the SILAR process provides a good alternative for the easy, fast and low-cost synthesis of QDs on electrodes, which overcomes the complex, and costly synthesis and purification of QDs prepared via solution-based protocols as well as the nanoparticle immobilization. Moreover, the IO-TiO_2|PbS electrode combines the advantages of InGaN/GaN NWs and IO-TiO_2|PMSA1 electrodes in one approach, i.e. the direct synthesis of the photoactive entity on the electrode without any linker molecules and the large surface area of a 3D IO-TiO_2 electrode.

5.2 Photocurrent direction

At this point the influence of the used electrode material on the photocurrent direction needs to be discussed. While in P4.1 gold has been used as electrode material, in the other studies semiconductor electrodes consisting of n-doped silicon (P4.2) and TiO_2 modified FTO (P4.3 and P4.4) have been applied. In agreement with previous reports, PEC systems based on metal electrodes give rise to anodic and cathodic photocurrents depending on the applied potential.[96,98,279] Therefore, metal electrodes can be exploited for the construction of photoanodes and photocathodes, which allow the photoxidation or photoreduction of molecules with one PEC electrode. However, the bidirectionality can also limit the applicability of metal electrodes in PEC systems if only one direction should run preferred. In P4.2, n-Si has been used as substrate for the InGaN/GaN NWs. The final electrode construction favors the formation of a Schottky barrier at the semiconductor/electrolyte interface leading to the exclusive generation of anodic photocurrents. Also in P4.3 (IO-TiO_2|PMSA1) and P4.4 (IO-TiO_2|PbS QDs) only anodic signals have been obtained, which, however, is attributable to the large band gap of TiO_2, defining the direction of the photocurrent. Here, the TiO_2 conduction band represents an electron trap for excited electrons of the photoactive entity, transporting the charge carriers to the underlying FTO electrode. For the combination with electron-donating enzymes the construction of such unidirectional photoanodes represent an advantage compared to the QD-modified gold electrodes in P4.1, since oxidative reactions can be

favored and unwanted cathodic reactions are reduced. This is reflected in higher anodic PEC performances obtained with InGaN/GaN NWs, IO-TiO_2|PMSA1 and IO-TiO_2|PbS QD electrodes.

Moreover, in P4.3 (IO-TiO_2|PMSA1) it is found that the choice of the electrode material is not only important for the photocurrent direction, but also has a fundamental impact whether light-induced charge carriers can be separated at the electrode/PMSA1 interface under concomitant photocurrent generation or not. It can be demonstrated that PMSA1 is reliant to the electronic structure of TiO_2 for an efficient charge carrier separation, while at unmodified conducting FTO electrodes no photosignal has been achieved. This is probably attributed to the fast charge carrier recombination at the FTO/polymer interface. Such synergistic effects have already been reported previously, for instance for dopamine sensitized TiO_2, which exhibit only photocurrents under illumination with visible light if both components are present.[167]

5.3 Excitation range

Besides the immobilization procedure and the electrode material also the photoactive material itself defines the performance of a PEC electrode. Particularly, the wavelength range that can be exploited for the excitation and electron-hole pair generation is important. For energetics, the PEC system should be able to use a large part of the sunlight spectrum in order to increase the photon-to-current conversion efficiency. In contrast, for sensing the wavelength range don't have to cover the whole solar spectrum, but needs to be broad enough to allow an adjustment of the excitation wavelength to the absorbance properties of the analyte to prevent the joint excitation of the electrode and the molecule. For the combination with biomolecules it is also important to exclude UV light for the photoexcitation in order to avoid biomolecule degradation. All photoactive materials applied in this thesis are able to use visible light for the generation of a photocurrent. Here, the maximum usable wavelength range could be successively extended from wavelength smaller than 500 nm for InGaN/GaN NWs (P4.2) to wavelength below 690 nm by utilization of PbS QDs (P4.4). CdSe/ZnS QDs (P4.1) allow an excitation below 570 nm and PMSA1 (P4.3) generates first photocurrents at about 600 nm. The differences are attributed to the material properties of the respective photoactive entities determining the band gap and thus the needed excitation energy. Consequently, PbS as a small band gap semiconductor exhibits the widest excitation range found for all photoactive materials used in this thesis. A comparison with previous PEC studies remains difficult since only a few reports have evaluated the wavelength-dependent excitation range of their systems. Conclusions can only be drawn on the basis of the used photoactive materials, the absorbance spectra and the applied light source. For instance, CdS is an often utilized photoactive material in PEC system bearing a band gap of 2.4 eV

as bulk material.[23] This theoretically corresponds to a minimum wavelength of 515 nm required for the excitation, however, since QDs are often applied the usable solar range is shifted to the lower wavelength according to the quantum confinement effect. The excitation range of these systems is thus comparable with that of the InGaN/GaN NWs used in this thesis, but smaller than of the photoactive elements used in P4.1, P4.3 and P4.4. Also other reported PEC systems with diaminodicyanoquinodimethane derivatives,[168] gold nanocluster[139] and TiO_2 NWs[102] seems to be less efficient in exploiting the visible wavelength range and rely on a UV light to ensure a sufficient excitation. Only for approaches using PSI as photoactive entity a similar wide excitation range as compared to P4.4 can be achieved,[83,108,427] indicating that the photoactive materials used in this thesis belong to the most efficient sun light-converting systems reported so far for biophotocatalytic electrodes. The rather wide excitation range provided for all systems is also important for sensing in order to bypass the analyte absorption of the excitation light by adapting the wavelength of the light source as demonstrated with InGaN/GaN NWs for the quantification of NADH (see P4.2, figure 5).

5.4 Photocatalytic activity for the oxidation of NADH

The cofactor NADH has been extensively analyzed in electrochemical studies due to its important role in the metabolism and the potential for the combination with NADH-converting enzymes. However, often high overpotentials of around 1 V have to be applied to achieve electrochemical oxidation, although the redox potential of NADH is rather negative (-0.56 V vs. SCE, pH 7).[367] The InGaN/GaN NWs overcome this limitation due to the gained light energy allowing a first oxidation of NADH at potentials of around -0.3 V vs. Ag/AgCl, 1 M KCl. So far only one of ten previously published NADH-oxidizing PEC electrodes achieves similar onset potentials (-0.37 V vs. Ag/AgCl).[80] All other reports have either not determined this parameter or need at least 0.2 V higher potentials to initiate the photooxidation of NADH.[81,112,167,170–175] The InGaN/GaN NWs reach high photocurrents of around 104 µA cm^{-2} after addition of 1 mM NADH at a low potential of 0 mV vs. Ag/AgCl, 1 M KCl. Only ZnS-CdS QDs electrodeposited on graphite electrodes (630 µA cm^{-2})[112] or on MWCNT-modified glassy carbon electrodes (1060 µA cm^{-2})[175] give rise to higher NADH-dependent photocurrents. However, these studies already show in the dark a NADH-dependent current response, which accounts for more than 50% of the total current under illumination. Similar observations have also been reported in five other approaches.[169–173] Furthermore, many of these systems need high overpotentials to ensure a sufficient NADH oxidation. This raises the question where the NADH oxidation actually takes place and whether these systems can be considered as PEC approaches. In contrast, for the InGaN/GaN NWs the NADH oxidation can be precisely controlled by switching on/off the light, demonstrating that the reaction proceeds exclusively at the photoactive entity. Further pure PEC approaches for the NADH oxidation have so far

only been reported for porphyrin-sensitized SnO_2,[80] CdSe/ZnS QD-modified gold electrodes[81] and dopamine sensitized nanoporous TiO_2,[167] which, however, lack to reach the high photocurrents of the InGaN/GaN NWs. The dynamic detection range provided with the InGaN/GaN NWs is between 1 µM and 10 mM NADH, which is comparable with the other PEC approaches. Lower detection limits have only been obtained for thionine-modified MWCNTs (0.05 µM)[169], dopamine sensitized nanoporous TiO_2 (0.5 µM)[167] and polymethylene blue-modified glassy carbon electrodes (0.1 µM).[171] Consequently, the InGaN/GaN NWs represents currently one of the PEC electrodes with the highest photocatalytic performance for the oxidation of NADH. This provides a solid basis for the light-controlled detection of NADH and the future combination with NADH-producing enzymes.

5.5 Performance of biophotoelectrodes for the conversion of glucose

In this thesis, different strategies for the integration of the glucose converting enzymes such as PQQ glucose dehydrogenase (P4.1, P4.3) and FAD-dependent glucose dehydrogenase (P4.4) into PEC systems have been developed. As described in chapter 3.2.4 the strategies for establishing a photoactive entity/enzyme communication can be classified in three generations. According to this, P4.1 and P4.4, belong to the 2nd generation of biocatalytic PEC electrodes, since redox mediators and redox polymers, respectively, have been applied to mediate the electron transfer between the enzyme and the photoactive entity. In contrast, in P4.3 a biophotoanode of the 3rd generation could be constructed due to DET established between the enzyme and PMSA1 as light-sensitive element.

So far twelve biophotoanodes and six biophotocathodes have been previously reported for the light-directed detection of glucose, of which sixteen can be classified to the 1st generation, one to the 2nd generation and one to the 3rd generation of biophotoelectrodes. The biophotocathodes are based on the oxygen sensitivity of various photoactive materials, leading to a competitive situation for oxygen if combined with oxygen consuming glucose oxidase.[92,97,99,208,209] This principle allows the detection of glucose via a reduction of the cathodic photocurrent, but is not suitable for the generation of power from light and enzymatic substrates, since electrons from the enzymatic reaction get lost after transfer to oxygen and therefore are not available for the PEC circuit. Another set of publications overcome this loss of electrons by simply using H_2O_2, which is formed by glucose oxidase during glucose turnover, as electron donor for the generation of anodic photocurrents.[102,139] However, one limitation of these two approaches can be seen in the dependence on the oxygen concentration in solution, which has to be kept constant in order to ensure a reliable operation for sensing and power supply. Moreover, the

production of reactive oxygen species can influence the enzymatic and PEC processes. An alternative can be seen in the combination of oxygen insensitive NAD-dependent glucose dehydrogenase with NADH oxidizing photoactive materials, which represent the most widely studied biophotoanodes for the detection of glucose. Here, PEC concepts with enzyme and NAD^+ in solution,[80,81] immobilized enzyme and only NAD^+ in solution,[112,169,172,174,175] and with both, enzyme and NAD^+, attached to the electrode have been presented.[168] Even if these approaches can reach rather high photocurrent densities a drawback is that the expensive cofactor NAD^+ has to be added to ensure an electron transfer between the enzyme and the photoactive entity. Also the electron transfer pathways of some systems are not clear due to high dark currents observed after addition of glucose.[112,169,172,174,175] Recently, Willner et al. have reported a mediator-based biophotoanode, using glucose oxidase wired via a redox polymer to PSI-modified electrodes.[83] In the same group also an electron transfer between ruthenium complex-containing dyes and glucose oxidase has been demonstrated.[82] Even if in both studies the principle of light-driven electron transfer between photoactive entities and enzymes could be shown, these systems do not provide a high performance with respect to the photocurrent magnitude, the onset potential and the detection range for glucose.

The large number of glucose converting biophotoelectrodes reported so far, demonstrates the strong interest in exploiting light-driven processes for sensing and feeding the photoelectrochemical reactions with electrons from enzymatic reactions, but also reveals that only little attention has been paid to the further development of 2nd and 3rd generation biophotoelectrodes. Here, it has to be added that also for biophotoelectrodes harvesting non-glucose converting enzymes only a few 2nd and 3rd generation PEC systems have been reported, yet. Accordingly, the mediator-based and DET approaches presented in P4.1, P4.3 and P4.4 can be evaluated as a progress supporting the further development of enzymatic PEC electrodes.

5.5.1 Current density

In P4.1 the electronic linkage of PQQ-GDH to QD-modified electrodes has been realized via the mediator ferrocenecarboxylic acid. The diffusible mediator can efficiently shuttle electrons from the immobilized enzyme towards the photoactive element resulting in enhanced anodic photocurrents up to 6 $\mu A\ cm^{-2}$ in the presence of glucose. In order to overcome the limitation of a diffusible mediator, ferrocenecarboxylic acid has been chemically coupled to the enzyme and assembled to the PEC electrode. This functional biohybrid system shows an electron transfer via the coupled ferrocene moieties to the photoexcited QDs if glucose is in solution, but the PEC efficiency is about 10-fold decreased compared to the situation with mediator in solution (0.6 $\mu A\ cm^{-2}$). Obviously, the coupled ferrocene moieties lack in connecting all immobilized enzymes with the photoactive material. Also a partial inactivation of the enzymes due to the chemical

coupling can be a reason for the reduced performance. To further improve the mediated approach, in P4.4 a redox polymer has been used for connecting the biocatalyst with the photoanode in a completely immobilized fashion. Therefore, the enzyme has been embedded into an osmium complex-containing redox polymer (P_{Os}) without any coupling agents. First approaches with embedded PQQ-GDH have resulted in a 20-fold amplification of the PEC signal compared to P4.1 with ferrocenecarboxylic acid coupled to PQQ-GDH. (12 µA cm^{-2}, data not shown). However, if FAD-GDH is used much higher glucose-dependent photocurrents have been achieved, although similar enzyme activities have been used for the embedment into the redox polymer. This suggests that FAD-GDH exhibit a faster electron transfer to the redox polymer than PQQ-GDH does. The best IO-TiO_2|PbS|P_{OS}|FAD-GDH biophotoanode constructed in P4.4 reached maximum photocurrents of 207 µA cm^{-2} at a low potential of 0 V vs. Ag/AgCl, which exceeds the output obtained in P4.1 with diffusible and immobilized mediator about 34.5-fold and 345-fold, respectively. A similar mediator-based biophotoanode based on PSI, redox polymers and glucose oxidase shows two orders of magnitude lower photocurrents (2 µA cm^{-2}) compared to P4.4.[83] Only one biophotoanode consisting of TiO_2 NWs modified with glucose oxidase achieved distinctly higher photocurrents of about 1000 µA cm^{-2}, but at a potential of +0.3 V vs. Ag/AgCl.[102] This system oxidizes enzymatically produced H_2O_2 at the excited TiO_2 NWs giving rise to its extraordinary performance. However, it has to be mentioned that the TiO_2 NWs already exhibit a glucose response if no enzyme is immobilized, which indicates that besides the H_2O_2 oxidation also a direct oxidation of glucose could be feasible.

In P4.3, the DET between PQQ-GDH and PMSA1 as photoactive element has been established in a light-triggered fashion for the oxidation of glucose. This approach gives rise to 44.7 µA cm^{-2} at 0 V vs. Ag/AgCl, 1 M KCl, in the presence of glucose. Consequently, the maximum photocurrent of P4.3 exceeds the PEC signal of P4.1 with immobilized mediator 75-fold, but is about 5-fold smaller than the QD sensitized IO-TiO_2 electrode with redox polymer and FAD-GDH (P4.4). Compared to a previously published biophotoanode based on a ruthenium dye-modified electrode with glucose oxidase (2 µA cm^{-2}), the signal response of the IO-TiO_2|PMSA1|PQQ-GDH electrode is found to be about 22-fold higher.[82]

5.5.2 Onset potential

Another important parameter which needs to be discussed is the onset potential for glucose oxidation. While in P4.1 the onset potential has not been determined, IO-TiO_2|PMSA1|PQQ-GDH electrodes (P4.3) enable a first gain of electrons form the biocatalytic reaction at -0.315 V vs. Ag/AgCl, 1 M KCl, which is about 0.1 V below the redox potential of PQQ-GDH (by assuming a redox potential between -0.188 and -0.226 V vs. Ag/AgCl, 1 M KCl).[283,412] This demonstrates the advantage of using the light-

harvesting features of PMSA1-sensitized IO-TiO_2 electrodes for overcoming the limitation of the PQQ-GDH redox potential, resulting in an enhanced power output. A further reduction of the onset potential to -0.54 V vs. Ag/AgCl, 1 M KCl could be achieved with IO-TiO_2|PbS|P_{Os}|FAD-GDH electrodes (P4.4). This corresponds currently to the lowest onset potentials ever reported for the biocatalytic oxidation of glucose. Also the high performance TiO_2 NWs modified with glucose oxidase provide only an onset potential of -0.3 V vs. Ag/AgCl, which is even higher than of IO-TiO_2|PMSA1|PQQ-GDH electrodes.[102]

5.5.3 Detection range

Besides the photocurrent response and the onset potential, also the glucose detection range is of great interest for biosensorial aspects. Particularly, monitoring the blood sugar level is important for the handling of diabetes patients. Therefore, the sensor should allow the determination of glucose concentrations of about 5 mM glucose.[428] The QD-modified gold electrodes with ferrocenecarboxylic acid and PQQ-GDH (P4.1) provide a detection range of 0.005 - 0.1 mM and 0.01 - 0.5 mM glucose with diffusible or immobilized mediators, respectively. Also for IO-TiO_2|PMSA1|PQQ-GDH electrodes (P4.3) a similar detection range between 0.01 and 0.25 mM glucose has been achieved, which is not sufficient for detecting glucose concentrations in blood. Therefore, only diluted samples could be analyzed, because of the high sensitivity found in P4.1 and P4.3. This raises the question why only low glucose concentrations can be detected using these biophotoanodes, although the K_M value of PQQ-GDH in solution is much higher ($K_{M,sol}$ ~ 25 mM).[408,259,283] Generally, it can be suggested that at least one electron transfer step within the light-driven signal chain limits the performance. This can either be the electron transfer of the QDs with the electrode or with the enzyme. A rather small concentration range is not a peculiarity of light-triggered PEC approaches, but have already been reported previously for light insensitive electrodes harboring PQQ-GDH.[409,289,275,276,429] This may give a hint that a restricted detection range is mainly induced by a rather slow electron subtraction from the substrate-reduced PQQ-GDH limiting the overall performance, but less by the electron transfer between the photoactive entity and the electrode. This is supported by the finding that IO-TiO_2|PbS biophotoanodes prepared with PQQ-GDH and an redox polymer also lead to relatively small detection ranges up to 0.5 mM glucose (data not shown), while under identical conditions biophotoanodes prepared with FAD-GDH allow a detection up to 50 mM glucose and thereby exhibit significantly larger currents (see P4.4). Nonetheless, more experiments are needed to fully enlighten this aspect. However, by using biophotoanodes prepared with FAD-GDH (P4.4) the detection range could be distinctly enlarged to 0.01 mM - 50 mM glucose, which is suitable for the detection of relevant glucose

concentrations found in blood. Compared to previous published biophotoelectrodes, P4.4 provides the broadest glucose detection range of all systems.

In summary, it can be stated that the performance of biophotoanodes in terms of signal stability, excitation range, photocurrent response, onset potential and detection range could be successively improved within this thesis. This paves the way for the application of these concepts for light-directed sensing, but also for the generation of power from sun light and sugars.

6 Summary

This thesis explores different strategies for the construction of light-converting photoanodes and studies their interaction with enzymatic reactions or enzymatic co-factors for the application in light-driven biosensors and biophotoelectrochemical cells.

In the first part of the thesis (P4.1), presynthesized QDs have been coupled by a dithiol to gold electrodes, resulting in the generation of pronounced photocurrents under illumination. Wavelength-dependent measurements verify that the photocurrent follows the absorbance features of the QDs in solution, which indicates that the nanoparticles retain their characteristic photophysical properties upon immobilization onto the gold electrode. First photocurrents have been observed at wavelength below 570 nm. To electronically connect redox enzymes to the QD-modified electrodes the capability of small redox molecules to transfer and shuttle electrons between biocatalysts and photoexcited QDs have been analyzed. The QD electrodes show a photocurrent response in the presence of the redox mediators hexacyanoferrate and ferrocenecarboxylic acid, giving rise to the concentration-dependent determination of both compounds. It is found that for hexacyanoferrate exclusively the oxidation can be followed via generation of an amplified anodic photocurrent, while for ferrocenecarboxylic acid both, oxidation and reduction, can be observed depending on the applied bias. These findings have provided the basis for the construction of light-triggered biocatalytic signal chains by immobilization of the enzymes PQQ glucose dehydrogenase (PQQ-GDH) or fructose dehydrogenase (FDH) to the QD electrode and electron-shuttling mediators in solution. Upon addition of substrate the enzymatic reaction is switched on, resulting in the reduction of the mediator that is subsequently oxidized at the excited QD electrode under concomitant generation of an enhanced anodic photocurrent. This approach gives access to the concentration-dependent determination of fructose and glucose by combination of FDH with hexacyanoferrate and PQQ-GDH with ferrocenecarboxylic acid, respectively. The study also reveals that both, PQQ-GDH and ferrocenecarboxylic acid, can be assembled together onto QD electrodes via chemical coupling of the redox mediator to the enzyme, allowing the electron transfer from the biocatalyst towards the mediator to the QDs in a complete immobilized fashion at a potential of 0.1 V vs. Ag/AgCl, 1 M KCl. This passes over the needs for soluble mediators and demonstrates one strategy for the functional integration of both, mediator and biocatalyst, into photoelectrochemical electrodes.

The second part of the thesis (P4.2) is dedicated to the photoelectrochemical analysis of the enzymatic co-factor NADH by means of InGaN/GaN nanowire heterostructures. Furthermore, this study was also aimed to overcome some limitations found in P4.1 such as the challenging immobilization of the QDs by the direct growth of the NWs to an n-Si substrate via molecular beam epitaxy. The excited InGaN/GaN NWs give rise to the

formation of stable anodic photocurrents in a rather large potential and pH-range revealing its broad applicability. The unidirectional photocurrent can be attributed to the formation of a Schottky-type barrier at the n-semiconductor/electrolyte interface, which is also reflected in the photoluminescence properties of the NWs. Here, the NWs allow the photoexcitation with visual light at wavelength below 500 nm. The rather wide excitation range found is crucial for the light-triggered detection of NADH, since the strong absorbance of NADH in the UV region impedes the generation of a photocurrent, but can be overcome by application of wavelength above 400 nm. The photocatalytic NADH oxidation starts at rather negative potentials of -0.3 V vs. Ag/AgCl, 1 M KCl, allowing the detection of NADH in the range between 5 µM and 10 mM at low electrode bias. Here, the InGaN/GaN NWs exhibit an excellent sensitivity of 91 µA mM^{-1} cm^{-2} for NADH. Thus, some previously reported limitations for the NADH oxidation at electrodes, including the needs for high overpotentials or surface fouling of the electrode, can be prevented by application of the InGaN/GaN NWs and light-directed read-out. This makes the InGaN/GaN NWs not only interesting for the detection of NADH, but also provides the basis for the combination with NADH-producing biocatalysts and the analysis of enzymatic substrates.

In the third part of this thesis (P4.3), sulfonated polyanilines (PMSA1) and PQQ-GDH have been integrated into inverse opal TiO_2 electrodes. Here, PMSA1 provides photoactivity for visible light and ensures the efficient electronic linkage of the enzymatic reaction to the IO-TiO_2 electrode. The IO-TiO_2 electrodes have been prepared by a template approach and spin coating allowing the scalability of the IO-film thickness and thus a tunability of surface area for the integration of high amounts of PMSA1 and PQQ-GDH. Upon illumination an anodic photocurrent is formed, which is enhanced in the presence of glucose, confirming the successful assembly of PMSA1 and PQQ-GDH. Here, the biohybrid electrode exhibit a photocurrent onset at a wavelength of around 600 nm. It is also found that the 3D structure of the IO-TiO_2 electrode is fundamental to provide the functionality of the whole biohybrid system, i.e. to generate large photocurrents and to ensure glucose sensitivity. Moreover, the influence of the IO-film thickness and the assembly strategy used for PMSA1 and PQQ-GDH integration on the glucose-dependent photocurrent has been evaluated. The final IO-TiO_2|PMSA1|PQQ-GDH architecture reaches maximum photocurrent densities of 44.7 µA cm^{-2} at a comparable low potential of 0 V vs. Ag/AgCl, 1 M KCl and allows a first gain of electrons from the biocatalytic glucose conversion at -0.315 V vs. Ag/AgCl, 1 M KCl under illumination with 100 mW cm^{-2}. Therefore, the biohybrid architecture allows the photobiocatalytic substrate oxidation at potentials below the enzymatic redox potential, which demonstrates the beneficial conditions found for the light-driven conversion of glucose.

In the fourth part of this thesis (P4.4), the high surface area of IO-TiO_2 electrodes has been exploited for the integration of PbS QDs, an osmium complex-containing redox

polymer and FAD-dependent glucose dehydrogenase (FAD-GDH). In this case electron-hole pairs are generated within the QDs upon photoexcitation, resulting in an electron injection into the TiO_2 conduction band and the oxidation of the redox polymer. The oxidized redox polymer is regenerated by the enzymatic reaction in the presence of glucose and therefore feeds the photoelectrochemical reaction with electrons from the glucose turnover. This results in amplified anodic photocurrents, allowing the concentration-dependent glucose detection between 10 µM and 50 mM glucose. Here, the biohybrid architecture provide a wide excitation range and enables a first generation of photocurrents at a wavelength of 690 nm. Moreover, the glucose-dependent photocurrent can be controlled by the IO-film thickness, the QD loading, the applied potential and the light intensity. The optimized biohybrid system give rise to high photocurrents of about 207 µA cm^{-2} at 0 mV vs. Ag/AgCl, 1 M KCl, and exhibit a first gain of electrons from the biocatalytic reaction at quite negative potentials of -0.54 V vs. Ag/AgCl, 1 M KCl, which is outstanding low compared to previous studies. The biohybrid system combines the advantages of a high surface area of IO-films, an efficient charge carrier generation and separation at the QDs/TiO_2 interface, and an efficient wiring of FAD-GDH to the QDs via a redox polymer, resulting in biophotoanodes of high performance for sensing and power-supply.

In conclusion, it can be stated that within this thesis improvements in the construction of photobioelectrochemical electrodes have been achieved with respect to the stability of the photocurrent signal, the photocurrent magnitude and also the onset potential of the light-directed photocatalytic NADH oxidation and biophotocatalyic glucose conversion. Also the dynamic range for the detection of glucose could be successively improved in this thesis. Moreover, the four constructed photoelectrodes provide a wide wavelength range for the excitation, which allow an adjustment to the absorption properties of the analyte by simply adapting the illumination wavelength. Therefore, this thesis has been dealing with different aspects of photobioelectrochemical systems. On the one hand, different photoactive materials such as CdSe/ZnS and PbS QDs, InGaN/GaN NWs and sulfonated polyanilines have been studied. On the other hand, the coupling of these photoactive entities to electrodes via linker molecules, physical adsorption or the direct growth of photoactive nanostructures on electrodes have been analyzed. The interaction of photoelectrochemical electrodes with diffusible and immobilized redox molecules has been a further focus of this work. Moreover, new strategies for the efficient electronic linkage of enzymes to photoactive entities could be shown in a mediated fashion or via direct electron transfer.

The approaches presented in this thesis may provide the basis for the photonic wiring of other interesting redox enzymes and the detection of the respective enzymatic substrates. This offers new perspectives for sensing, since multiplexing by spatially resolved immobilization of different enzymes in combination with a localized read-out by means of a light beam seems to be feasible and would allow the detection of several analytes in

parallel. Furthermore, the developed biophotoanodes could be applied in bioenergetic systems, allowing the generation of power from sun light and energy-rich compounds.

7 References

1 L.-L. Li and E. W.-G. Diau, *Chem. Soc. Rev.*, 2012, **42**, 291–304.
2 M.-S. Choi, T. Aida, T. Yamazaki and I. Yamazaki, *Angew. Chem.*, 2001, **113**, 3294–3298.
3 K. J. Channon, G. L. Devlin and C. E. MacPhee, *J. Am. Chem. Soc.*, 2009, **131**, 12520–12521.
4 Y. Ishida, T. Shimada, D. Masui, H. Tachibana, H. Inoue and S. Takagi, *J. Am. Chem. Soc.*, 2011, **133**, 14280–14286.
5 A. P. Alivisatos, *Science*, 1996, **271**, 933–937.
6 I. L. Medintz, H. T. Uyeda, E. R. Goldman and H. Mattoussi, *Nat. Mater.*, 2005, **4**, 435–446.
7 N. S. Lewis and D. G. Nocera, *Proc. Natl. Acad. Sci.*, 2006, **103**, 15729–15735.
8 J. Li and N. Wu, *Catal. Sci. Technol.*, 2015, **5**, 1360–1384.
9 T. W. Woolerton, S. Sheard, Y. S. Chaudhary and F. A. Armstrong, *Energy Environ. Sci.*, 2012, **5**, 7470–7490.
10 null Willner and null Katz, *Angew. Chem. Int. Ed Engl.*, 2000, **39**, 1180–1218.
11 C. Léger and P. Bertrand, *Chem. Rev.*, 2008, **108**, 2379–2438.
12 G. H. Carey, A. L. Abdelhady, Z. Ning, S. M. Thon, O. M. Bakr and E. H. Sargent, *Chem. Rev.*, 2015, **115**, 12732–12763.
13 W. Lu and C. M. Lieber, *J. Phys. Appl. Phys.*, 2006, **39**, R387.
14 X. Chen, S. Shen, L. Guo and S. S. Mao, *Chem. Rev.*, 2010, **110**, 6503–6570.
15 R. Gill, M. Zayats and I. Willner, *Angew. Chem. Int. Ed Engl.*, 2008, **47**, 7602–7625.
16 F. Lisdat, D. Schäfer and A. Kapp, *Anal. Bioanal. Chem.*, 2013, **405**, 3739–3752.
17 W.-W. Zhao, J.-J. Xu and H.-Y. Chen, *Chem. Soc. Rev.*, 2015, **44**, 729–741.
18 C. Kittel, *Am. J. Phys.*, 1967, **35**, 547–548.
19 R. A. Marcus, *Angew. Chem. Int. Ed. Engl.*, 1993, **32**, 1111–1121.
20 L. Stryer, *Annu. Rev. Biochem.*, 1978, **47**, 819–846.
21 K. Molapo, P. Ndangili, R. Ajayi, G. Mbambisa, S. Mailu, N. Njomo, M. Masikini, P. Baker and E. Iwuoha, *Int. J. Electrochem. Sci.*, 2012, **7**, 11859–11875.
22 C. A. Gueymard, *Sol. Energy*, 2004, **76**, 423–453.
23 Y. Xu and M. A. A. Schoonen, *Am. Mineral.*, 2000, **85**, 543–556.
24 I. Vurgaftman and J. R. Meyer, *J. Appl. Phys.*, 2003, **94**, 3675–3696.
25 S. Strite and H. Morkoç, *J. Vac. Sci. Technol. B Microelectron. Nanometer Struct. Process. Meas. Phenom.*, 1992, **10**, 1237–1266.
26 W. Shan, W. Walukiewicz, E. E. Haller, B. D. Little, J. J. Song, M. D. McCluskey, N. M. Johnson, Z. C. Feng, M. Schurman and R. A. Stall, *J. Appl. Phys.*, 1998, **84**, 4452–4458.
27 S. Nakamura, M. Senoh, S. Nagahama, N. Iwasa, T. Yamada, T. Matsushita, H. Kiyoku, Y. Sugimoto, T. Kozaki, H. Umemoto, M. Sano and K. Chocho, *Appl. Phys. Lett.*, 1998, **72**, 211–213.
28 P. G. Moses and C. G. V. de Walle, *Appl. Phys. Lett.*, 2010, **96**, 021908.
29 U. Diebold, *Appl. Phys. A*, 2003, **76**, 681–687.
30 M. A. Henderson, *Surf. Sci. Rep.*, 2011, **66**, 185–297.
31 Y. Wang and N. Herron, *J. Phys. Chem.*, 1991, **95**, 525–532.
32 null Takagahara and null Takeda, *Phys. Rev. B Condens. Matter*, 1992, **46**, 15578–15581.

33 X. Zhao, C. M. Wei, L. Yang and M. Y. Chou, *Phys. Rev. Lett.*, 2004, **92**, 236805.
34 S. Kundu and A. Patra, *Chem. Rev.*, 2017, **117**, 712–757.
35 C. de M. Donegá, *Chem. Soc. Rev.*, 2011, **40**, 1512–1546.
36 L. Brus, *J. Phys. Chem.*, 1986, **90**, 2555–2560.
37 W. W. Yu, L. Qu, W. Guo and X. Peng, *Chem. Mater.*, 2003, **15**, 2854–2860.
38 X. Gao, Y. Cui, R. M. Levenson, L. W. K. Chung and S. Nie, *Nat. Biotechnol.*, 2004, **22**, 969–976.
39 U. Resch-Genger, M. Grabolle, S. Cavaliere-Jaricot, R. Nitschke and T. Nann, *Nat. Methods*, 2008, **5**, 763–775.
40 M. D. Garrett, A. D. Dukes III, J. R. McBride, N. J. Smith, S. J. Pennycook and S. J. Rosenthal, *J. Phys. Chem. C*, 2008, **112**, 12736–12746.
41 J. Zhang, X. Zhang and J. Y. Zhang, *J. Phys. Chem. C*, 2009, **113**, 9512–9515.
42 I. Yagi, K. Mikami, K. Ebina, M. Okamura and K. Uosaki, *J. Phys. Chem. B*, 2006, **110**, 14192–14197.
43 M. Nirmal, C. B. Murray and M. G. Bawendi, *Phys. Rev. B*, 1994, **50**, 2293–2300.
44 M. Hong, M. Guo-Hong, W. Wen-Jun, G. Xue-Xi and M. Hong-Liang, *Chin. Phys. B*, 2008, **17**, 1280.
45 J.-Y. Zhang, X.-Y. Wang, M. Xiao, L. Qu and X. Peng, *Appl. Phys. Lett.*, 2002, **81**, 2076–2078.
46 C. de Mello Donegá, S. G. Hickey, S. F. Wuister, D. Vanmaekelbergh and A. Meijerink, *J. Phys. Chem. B*, 2003, **107**, 489–496.
47 L. Hartmann, A. Kumar, M. Welker, A. Fiore, C. Julien-Rabant, M. Gromova, M. Bardet, P. Reiss, P. N. W. Baxter, F. Chandezon and R. B. Pansu, *ACS Nano*, 2012, **6**, 9033–9041.
48 E. Petryayeva, W. R. Algar and I. L. Medintz, *Appl. Spectrosc.*, 2013, **67**, 215–252.
49 B. O. Dabbousi, J. Rodriguez-Viejo, F. V. Mikulec, J. R. Heine, H. Mattoussi, R. Ober, K. F. Jensen and M. G. Bawendi, *J. Phys. Chem. B*, 1997, **101**, 9463–9475.
50 C. M. Lieber, *MRS Bull.*, 2011, **36**, 1052–1063.
51 Q. Zhang and G. Cao, *Nano Today*, 2011, **6**, 91–109.
52 L. Cao, P. Fan, A. P. Vasudev, J. S. White, Z. Yu, W. Cai, J. A. Schuller, S. Fan and M. L. Brongersma, *Nano Lett.*, 2010, **10**, 439–445.
53 R. Yan, D. Gargas and P. Yang, *Nat. Photonics*, 2009, **3**, 569–576.
54 A. G. Bhuiyan, K. Sugita, A. Hashimoto and A. Yamamoto, *IEEE J. Photovolt.*, 2012, **2**, 276–293.
55 B. AlOtaibi, H. P. T. Nguyen, S. Zhao, M. G. Kibria, S. Fan and Z. Mi, *Nano Lett.*, 2013, **13**, 4356–4361.
56 J. Wu, W. Walukiewicz, W. Shan, K. M. Yu, J. W. Ager, S. X. Li, E. E. Haller, H. Lu and W. J. Schaff, *J. Appl. Phys.*, 2003, **94**, 4457–4460.
57 S. Günes, H. Neugebauer and N. S. Sariciftci, *Chem. Rev.*, 2007, **107**, 1324–1338.
58 D. Wöhrle and D. Meissner, *Adv. Mater.*, 1991, **3**, 129–138.
59 V. Coropceanu, J. Cornil, D. A. da Silva Filho, Y. Olivier, R. Silbey and J.-L. Brédas, *Chem. Rev.*, 2007, **107**, 926–952.
60 Y.-J. Cheng, S.-H. Yang and C.-S. Hsu, *Chem. Rev.*, 2009, **109**, 5868–5923.
61 R. A. Street, J. E. Northrup and A. Salleo, *Phys. Rev. B*, 2005, **71**, 165202.
62 C. Wang, H. Dong, L. Jiang and W. Hu, *Chem. Soc. Rev.*, 2018, **47**, 422–500.
63 H. E. Katz, Z. Bao and S. L. Gilat, *Acc. Chem. Res.*, 2001, **34**, 359–369.
64 C. Dhand, M. Das, M. Datta and B. D. Malhotra, *Biosens. Bioelectron.*, 2011, **26**, 2811–2821.
65 J. Y. Shimano and A. G. MacDiarmid, *Synth. Met.*, 2001, **123**, 251–262.

66 S. Stafström, J. L. Brédas, A. J. Epstein, H. S. Woo, D. B. Tanner, W. S. Huang and A. G. MacDiarmid, *Phys. Rev. Lett.*, 1987, **59**, 1464–1467.
67 J. Yue and A. J. Epstein, *J. Am. Chem. Soc.*, 1990, **112**, 2800–2801.
68 J. Yue, Z. H. Wang, K. R. Cromack, A. J. Epstein and A. G. MacDiarmid, *J. Am. Chem. Soc.*, 1991, **113**, 2665–2671.
69 X.-L. Wei, Y. Z. Wang, S. M. Long, C. Bobeczko and A. J. Epstein, *J. Am. Chem. Soc.*, 1996, **118**, 2545–2555.
70 A. G. Macdiarmid, J. C. Chiang, A. F. Richter and A. J. Epstein, *Synth. Met.*, 1987, **18**, 285–290.
71 M. T. Giardi and E. Pace, *Trends Biotechnol.*, 2005, **23**, 257–263.
72 Y.-C. Cheng and G. R. Fleming, *Annu. Rev. Phys. Chem.*, 2009, **60**, 241–262.
73 J. P. McEvoy and G. W. Brudvig, *Chem. Rev.*, 2006, **106**, 4455–4483.
74 N. Plumeré and M. M. Nowaczyk, in *Biophotoelectrochemistry: From Bioelectrochemistry to Biophotovoltaics*, Springer, Cham, 2016, pp. 111–136.
75 Z. Yue, F. Lisdat, W. J. Parak, S. G. Hickey, L. Tu, N. Sabir, D. Dorfs and N. C. Bigall, *ACS Appl. Mater. Interfaces*, 2013, **5**, 2800–2814.
76 S. H. Lee, D. S. Choi, S. K. Kuk and C. B. Park, *Angew. Chem. Int. Ed Engl.*, , DOI:10.1002/anie.201710070.
77 J. Wang, J. Long, Z. Liu, W. Wu and C. Hu, *Biosens. Bioelectron.*, 2017, **91**, 53–59.
78 A. Bachmeier, S. Hall, S. W. Ragsdale and F. A. Armstrong, *J. Am. Chem. Soc.*, 2014, **136**, 13518–13521.
79 C.-Y. Lee, H. S. Park, J. C. Fontecilla-Camps and E. Reisner, *Angew. Chem. Int. Ed.*, 2016, **55**, 5971–5974.
80 L. de la Garza, G. Jeong, P. A. Liddell, T. Sotomura, T. A. Moore, A. L. Moore and D. Gust, *J. Phys. Chem. B*, 2003, **107**, 10252–10260.
81 K. Schubert, W. Khalid, Z. Yue, W. J. Parak and F. Lisdat, *Langmuir*, 2010, **26**, 1395–1400.
82 R. Tel-Vered, H. B. Yildiz, Y.-M. Yan and I. Willner, *Small*, 2010, **6**, 1593–1597.
83 A. Efrati, C.-H. Lu, D. Michaeli, R. Nechushtai, S. Alsaoub, W. Schuhmann and I. Willner, *Nat. Energy*, 2016, **1**, 15021.
84 M. Hambourger, M. Gervaldo, D. Svedruzic, P. W. King, D. Gust, M. Ghirardi, A. L. Moore and T. A. Moore, *J. Am. Chem. Soc.*, 2008, **130**, 2015–2022.
85 S. Y. Lee, S. Y. Lim, D. Seo, J.-Y. Lee and T. D. Chung, *Adv. Energy Mater.*, 2016, **6**, n/a-n/a.
86 A. Bachmeier, B. J. Murphy and F. A. Armstrong, *J. Am. Chem. Soc.*, 2014, **136**, 12876–12879.
87 V. Pardo-Yissar, E. Katz, J. Wasserman and I. Willner, *J. Am. Chem. Soc.*, 2003, **125**, 622–623.
88 E. Katz, M. Zayats, I. Willner and F. Lisdat, *Chem. Commun.*, 2006, 1395–1397.
89 T. Zeng, S. Leimkühler, J. Koetz and U. Wollenberger, *ACS Appl. Mater. Interfaces*, 2015, **7**, 21487–21494.
90 J. Barroso, L. Saa, R. Grinyte and V. Pavlov, *Biosens. Bioelectron.*, 2016, **77**, 323–329.
91 C. Stoll, C. Gehring, K. Schubert, M. Zanella, W. J. Parak and F. Lisdat, *Biosens. Bioelectron.*, 2008, **24**, 260–265.
92 W. Wang, L. Bao, J. Lei, W. Tu and H. Ju, *Anal. Chim. Acta*, 2012, **744**, 33–38.
93 L. Jiang, Y. Li, W. Wei, A. Liu, Y. Zhang and S. Liu, *J. Electroanal. Chem.*, 2016, **781**, 345–350.
94 X. Xu, J. Qian, J. Yu, Y. Zhang and S. Liu, *Chem. Commun.*, 2014, **50**, 7607–7610.

95 N. Sabir, N. Khan, J. Völkner, F. Widdascheck, P. del Pino, G. Witte, M. Riedel, F. Lisdat, M. Konrad and W. J. Parak, *Small*, 2015, **11**, 5844–5850.
96 C. Stoll, S. Kudera, W. J. Parak and F. Lisdat, *Small*, 2006, **2**, 741–743.
97 J. Tanne, D. Schäfer, W. Khalid, W. J. Parak and F. Lisdat, *Anal. Chem.*, 2011, **83**, 7778–7785.
98 M. Riedel, G. Göbel, A. M. Abdelmonem, W. J. Parak and F. Lisdat, *ChemPhysChem*, 2013, **14**, 2338–2342.
99 X. Zhang, M. Liu, H. Liu and S. Zhang, *Biosens. Bioelectron.*, 2014, **56**, 307–312.
100 W. Zhu, Y.-R. An, X.-M. Luo, F. Wang, J.-H. Zheng, L.-L. Tang, Q.-J. Wang, Z.-H. Zhang, W. Zhang and L.-T. Jin, *Chem. Commun. Camb. Engl.*, 2009, 2682–2684.
101 W.-W. Zhao, Z.-Y. Ma, J.-J. Xu and H.-Y. Chen, *Anal. Chem.*, 2013, **85**, 8503–8506.
102 J. Tang, Y. Wang, J. Li, P. Da, J. Geng and G. Zheng, *J. Mater. Chem. A*, 2014, **2**, 6153–6157.
103 B. Sun, K. Zhang, L. Chen, L. Guo and S. Ai, *Biosens. Bioelectron.*, 2013, **44**, 48–51.
104 K. Feng, M. Yang, F. Xie, G. Diao, M. Ou and H. Huang, *Anal. Methods*, 2017, **9**, 6754–6759.
105 J. Lu, Y. Shen and S. Liu, *Chem. Commun.*, 2016, **52**, 7703–7706.
106 D. S. Choi, Y. Ni, E. Fernández-Fueyo, M. Lee, F. Hollmann and C. B. Park, *ACS Catal.*, 2017, **7**, 1563–1567.
107 Y. Wang, W. Wang, S. Wang, W. Chu, T. Wei, H. Tao, C. Zhang and Y. Sun, *Sens. Actuators B Chem.*, 2016, **232**, 448–453.
108 C. Tapia, R. D. Milton, G. Pankratova, S. D. Minteer, H.-E. Åkerlund, D. Leech, A. L. De Lacey, M. Pita and L. Gorton, *ChemElectroChem*, 2017, **4**, 90–95.
109 D. Ciornii, M. Riedel, K. R. Stieger, S. C. Feifel, M. Hejazi, H. Lokstein, A. Zouni and F. Lisdat, *J. Am. Chem. Soc.*, 2017, **139**, 16478–16481.
110 C. Lu, X.-F. Wang, J.-J. Xu and H.-Y. Chen, *Electrochem. Commun.*, 2008, **10**, 1530–1532.
111 X.-Y. Yu, J.-Y. Liao, K.-Q. Qiu, D.-B. Kuang and C.-Y. Su, *ACS Nano*, 2011, **5**, 9494–9500.
112 B. Ertek, C. Akgül and Y. Dilgin, *RSC Adv.*, 2016, **6**, 20058–20066.
113 H. M. Pathan and C. D. Lokhande, *Bull. Mater. Sci.*, 2004, **27**, 85–111.
114 P. V. Kamat, *J. Phys. Chem. C*, 2008, **112**, 18737–18753.
115 A. J. Nozik, M. C. Beard, J. M. Luther, M. Law, R. J. Ellingson and J. C. Johnson, *Chem. Rev.*, 2010, **110**, 6873–6890.
116 I.-S. Liu, H.-H. Lo, C.-T. Chien, Y.-Y. Lin, C.-W. Chen, Y.-F. Chen, W.-F. Su and S.-C. Liou, *J. Mater. Chem.*, 2008, **18**, 675–682.
117 J. B. Sambur, S. C. Riha, D. Choi and B. A. Parkinson, *Langmuir*, 2010, **26**, 4839–4847.
118 E. P. A. M. Bakkers, A. L. Roest, A. W. Marsman, L. W. Jenneskens, L. I. de Jong-van Steensel, J. J. Kelly and D. Vanmaekelbergh, *J. Phys. Chem. B*, 2000, **104**, 7266–7272.
119 W. Khalid, M. El Helou, T. Murböck, Z. Yue, J.-M. Montenegro, K. Schubert, G. Göbel, F. Lisdat, G. Witte and W. J. Parak, *ACS Nano*, 2011, **5**, 9870–9876.
120 G. Göbel, K. Schubert, I. W. Schubart, W. Khalid, W. J. Parak and F. Lisdat, *Electrochimica Acta*, 2011, **56**, 6397–6400.
121 I. Robel, V. Subramanian, M. Kuno and P. V. Kamat, *J. Am. Chem. Soc.*, 2006, **128**, 2385–2393.
122 L. Zhang and J. M. Cole, *ACS Appl. Mater. Interfaces*, 2015, **7**, 3427–3455.
123 W. Tu, Y. Dong, J. Lei and H. Ju, *Anal. Chem.*, 2010, **82**, 8711–8716.

124 H. Hug, M. Bader, P. Mair and T. Glatzel, *Appl. Energy*, 2014, **115**, 216–225.
125 I. Lee, J. W. Lee and E. Greenbaum, *Phys. Rev. Lett.*, 1997, **79**, 3294–3297.
126 C. J. Faulkner, S. Lees, P. N. Ciesielski, D. E. Cliffel and G. K. Jennings, *Langmuir*, 2008, **24**, 8409–8412.
127 S. C. Feifel, K. R. Stieger, H. Lokstein, H. Lux and F. Lisdat, *J. Mater. Chem. A*, 2015, **3**, 12188–12196.
128 N. Terasaki, N. Yamamoto, T. Hiraga, Y. Yamanoi, T. Yonezawa, H. Nishihara, T. Ohmori, M. Sakai, M. Fujii, A. Tohri, M. Iwai, Y. Inoue, S. Yoneyama, M. Minakata and I. Enami, *Angew. Chem. Int. Ed Engl.*, 2009, **48**, 1585–1587.
129 A. Efrati, O. Yehezkeli, R. Tel-Vered, D. Michaeli, R. Nechushtai and I. Willner, *ACS Nano*, 2012, **6**, 9258–9266.
130 K. R. Stieger, S. C. Feifel, H. Lokstein and F. Lisdat, *Phys. Chem. Chem. Phys. PCCP*, 2014, **16**, 15667–15674.
131 T. Nakanishi, B. Ohtani and K. Uosaki, *J. Phys. Chem. B*, 1998, **102**, 1571–1577.
132 R. Koole, B. Luigjes, M. Tachiya, R. Pool, T. J. H. Vlugt, C. de Mello Donegá, A. Meijerink and D. Vanmaekelbergh, *J. Phys. Chem. C*, 2007, **111**, 11208–11215.
133 K. R. Stieger, D. Ciornii, A. Kölsch, M. Hejazi, H. Lokstein, S. C. Feifel, A. Zouni and F. Lisdat, *Nanoscale*, 2016, **8**, 10695–10705.
134 A. Badura, D. Guschin, T. Kothe, M. J. Kopczak, W. Schuhmann and M. Rögner, *Energy Environ. Sci.*, 2011, **4**, 2435–2440.
135 M. Kato, T. Cardona, A. W. Rutherford and E. Reisner, *J. Am. Chem. Soc.*, 2013, **135**, 10610–10613.
136 K. R. Stieger, S. C. Feifel, H. Lokstein, M. Hejazi, A. Zouni and F. Lisdat, *J. Mater. Chem. A*, 2016, **4**, 17009–17017.
137 K. P. Sokol, D. Mersch, V. Hartmann, J. Z. Zhang, M. M. Nowaczyk, M. Rögner, A. Ruff, W. Schuhmann, N. Plumeré and E. Reisner, *Energy Environ. Sci.*, 2016, **9**, 3698–3709.
138 D. Mersch, C.-Y. Lee, J. Z. Zhang, K. Brinkert, J. C. Fontecilla-Camps, A. W. Rutherford and E. Reisner, *J. Am. Chem. Soc.*, 2015, **137**, 8541–8549.
139 J. Zhang, L. Tu, S. Zhao, G. Liu, Y. Wang, Y. Wang and Z. Yue, *Biosens. Bioelectron.*, 2015, **67**, 296–302.
140 L. Zhang, Y.-F. Ruan, Y.-Y. Liang, W.-W. Zhao, X.-D. Yu, J.-J. Xu and H.-Y. Chen, *ACS Appl. Mater. Interfaces*, , DOI:10.1021/acsami.7b17647.
141 H. Li, W. Hao, J. Hu and H. Wu, *Biosens. Bioelectron.*, 2013, **47**, 225–230.
142 X. Zhang, L. Li, X. Peng, R. Chen, K. Huo and P. K. Chu, *Electrochimica Acta*, 2013, **108**, 491–496.
143 M. Liu, Y.-X. Yu and W.-D. Zhang, *Electroanalysis*, 2017, **29**, 305–311.
144 Y.-T. Long, C. Kong, D.-W. Li, Y. Li, S. Chowdhury and H. Tian, *Small*, 2011, **7**, 1624–1628.
145 X. Zhao, S. Zhou, Q. Shen, L.-P. Jiang and J.-J. Zhu, *The Analyst*, 2012, **137**, 3697.
146 Z. Li, J. Zhang, Y. Li, S. Zhao, P. Zhang, Y. Zhang, J. Bi, G. Liu and Z. Yue, *Biosens. Bioelectron.*, 2018, **99**, 251–258.
147 G.-L. Wang, J.-J. Xu and H.-Y. Chen, *Nanoscale*, 2010, **2**, 1112–1114.
148 Q. Shen, X. Zhao, S. Zhou, W. Hou and J.-J. Zhu, *J. Phys. Chem. C*, 2011, **115**, 17958–17964.
149 P. Wang, X. Ma, M. Su, Q. Hao, J. Lei and H. Ju, *Chem. Commun.*, 2012, **48**, 10216–10218.
150 F. Huang, F. Pu, X. Lu, H. Zhang, Y. Xia, W. Huang and Z. Li, *Sens. Actuators B Chem.*, 2013, **183**, 601–607.

151 H. Xu, J. Yan, X. She, L. Xu, J. Xia, Y. Xu, Y. Song, L. Huang and H. Li, *Nanoscale*, 2014, **6**, 1406–1415.
152 I. Ibrahim, H. N. Lim, O. K. Abou-Zied, N. M. Huang, P. Estrela and A. Pandikumar, *J. Phys. Chem. C*, 2016, **120**, 22202–22214.
153 G.-L. Wang, K.-L. Liu, Y.-M. Dong, Z.-J. Li and C. Zhang, *Anal. Chim. Acta*, 2014, **827**, 34–39.
154 G. Wen, X. Wen, M. M. F. Choi and S. Shuang, *Sens. Actuators B Chem.*, 2015, **221**, 1449–1454.
155 W. Khalid, G. Göbel, D. Hühn, J.-M. Montenegro, P. Rivera-Gil, F. Lisdat and W. J. Parak, *J. Nanobiotechnology*, 2011, **9**, 46.
156 Y. Zhu, K. Yan, Y. Liu and J. Zhang, *Anal. Chim. Acta*, 2015, **884**, 29–36.
157 H. Li, J. Li, Q. Xu, Z. Yang and X. Hu, *Anal. Chim. Acta*, 2013, **766**, 47–52.
158 S. Trashin, V. Rahemi, K. Ramji, L. Neven, S. M. Gorun and K. D. Wael, *Nat. Commun.*, 2017, **8**, 16108.
159 H. Wu, J. Hu, H. Li and H. Li, *Sens. Actuators B Chem.*, 2013, **182**, 802–808.
160 G.-L. Wang, H.-J. Jiao, K.-L. Liu, X.-M. Wu, Y.-M. Dong, Z.-J. Li and C. Zhang, *Electrochem. Commun.*, 2014, **41**, 47–50.
161 Y. Yan, Q. Liu, X. Du, J. Qian, H. Mao and K. Wang, *Anal. Chim. Acta*, 2015, **853**, 258–264.
162 Z. Cai, M. Rong, T. Zhao, L. Zhao, Y. Wang and X. Chen, *J. Electroanal. Chem.*, 2015, **759**, 32–37.
163 S. A. Alves, L. L. Soares, L. A. Goulart and L. H. Mascaro, *J. Solid State Electrochem.*, 2016, **20**, 2461–2470.
164 S. Yotsumoto Neto, R. de C. S. Luz and F. S. Damos, *Electrochem. Commun.*, 2016, **62**, 1–4.
165 X. Hun, S. Wang, S. Wang, J. Zhao and X. Luo, *Sens. Actuators B Chem.*, 2017, **249**, 83–89.
166 Y. Xin, Z. Li, W. Wu, B. Fu, H. Wu and Z. Zhang, *Biosens. Bioelectron.*, 2017, **87**, 396–403.
167 G.-L. Wang, J.-J. Xu and H.-Y. Chen, *Biosens. Bioelectron.*, 2009, **24**, 2494–2498.
168 T. S. Metzger, C. G. Chandaluri, R. Tel-Vered, R. Shenhar and I. Willner, *Adv. Funct. Mater.*, 2016, **26**, 7148–7155.
169 L. Deng, Y. Wang, L. Shang, D. Wen, F. Wang and S. Dong, *Biosens. Bioelectron.*, 2008, **24**, 951–957.
170 Y. Dilgin, L. Gorton and G. Nisli, *Electroanalysis*, 2007, **19**, 286–293.
171 Y. Dilgin, D. G. Dilgin, Z. Dursun, H. İ. Gökçel, D. Gligor, B. Bayrak and B. Ertek, *Electrochimica Acta*, 2011, **56**, 1138–1143.
172 F. Jafari, A. Salimi and A. Navaee, *Electroanalysis*, 2014, **26**, 1782–1793.
173 K. Wang, J. Wu, Q. Liu, Y. Jin, J. Yan and J. Cai, *Anal. Chim. Acta*, 2012, **745**, 131–136.
174 D. G. Dilgin and H. İ. Gökçel, *Anal. Methods*, 2015, **7**, 990–999.
175 B. Ertek and Y. Dilgin, *Bioelectrochemistry*, 2016, **112**, 138–144.
176 A. Dibenedetto, P. Stufano, W. Macyk, T. Baran, C. Fragale, M. Costa and M. Aresta, *ChemSusChem*, 2012, **5**, 373–378.
177 R. K. Yadav, G. H. Oh, N.-J. Park, A. Kumar, K. Kong and J.-O. Baeg, *J. Am. Chem. Soc.*, 2014, **136**, 16728–16731.
178 X. Ji, Z. Su, P. Wang, G. Ma and S. Zhang, *Small Weinh. Bergstr. Ger.*, 2016, **12**, 4753–4762.
179 J. H. Lee, D. H. Nam, S. H. Lee, J. H. Park, C. B. Park and K. J. Jeong, *J. Ind. Eng. Chem.*, 2016, **33**, 28–32.

180 S. Li, J. Qiu, M. Ling, F. Peng, B. Wood and S. Zhang, *ACS Appl. Mater. Interfaces*, 2013, **5**, 11129–11135.
181 Y. Wang, J. Tang, Z. Peng, Y. Wang, D. Jia, B. Kong, A. A. Elzatahry, D. Zhao and G. Zheng, *Nano Lett.*, 2014, **14**, 3668–3673.
182 Y. Yang, K. Yan and J. Zhang, *Electrochimica Acta*, 2017, **228**, 28–35.
183 X. Zhang, F. Xu, B. Zhao, X. Ji, Y. Yao, D. Wu, Z. Gao and K. Jiang, *Electrochimica Acta*, 2014, **133**, 615–622.
184 H. Li, J. Li, D. Chen, Y. Qiu and W. Wang, *Sens. Actuators B Chem.*, 2015, **220**, 441–447.
185 D. Chen, D. Jiang, X. Du, L. Zhou, L. Huang, J. Qian, Q. Liu, N. Hao, Y. Li and K. Wang, *Electrochimica Acta*, 2016, **215**, 305–312.
186 A. Gopalan, N. Muthuchamy and K. Lee, *Biosens. Bioelectron.*, 2017, **89**, 352–360.
187 L. Guo, Z. Li, K. Marcus, S. Navarro, K. Liang, L. Zhou, P. D. Mani, S. J. Florczyk, K. R. Coffey, N. Orlovskaya, Y.-H. Sohn and Y. Yang, *ACS Sens.*, 2017, **2**, 621–625.
188 C.-L. Hsu, J.-H. Lin, D.-X. Hsu, S.-H. Wang, S.-Y. Lin and T.-J. Hsueh, *Sens. Actuators B Chem.*, 2017, **238**, 150–159.
189 S. Park, H. Boo and T. D. Chung, *Anal. Chim. Acta*, 2006, **556**, 46–57.
190 K. Tian, M. Prestgard and A. Tiwari, *Mater. Sci. Eng. C*, 2014, **41**, 100–118.
191 F. W. P. Ribeiro, F. C. Moraes, E. C. Pereira, F. Marken and L. H. Mascaro, *Electrochem. Commun.*, 2015, **61**, 1–4.
192 D. G. Shchukin, D. V. Sviridov and A. I. Kulak, *Sens. Actuators B Chem.*, 2001, **76**, 556–559.
193 H. Dai, S. Zhang, G. Xu, L. Gong, M. Fu, X. Li, S. Lu, C. Zeng, Y. Jiang, Y. Lin and G. Chen, *RSC Adv.*, 2014, **4**, 11099–11102.
194 R. Siavash Moakhar, G. K. L. Goh, A. Dolati and M. Ghorbani, *Electrochem. Commun.*, 2015, **61**, 110–113.
195 R. Siavash Moakhar, G. K. L. Goh, A. Dolati and M. Ghorbani, *Appl. Catal. B Environ.*, 2017, **201**, 411–418.
196 A. Ikeda, M. Nakasu, S. Ogasawara, H. Nakanishi, M. Nakamura and J. Kikuchi, *Org. Lett.*, 2009, **11**, 1163–1166.
197 H. Shi, J. Zhao, Y. Wang and G. Zhao, *Biosens. Bioelectron.*, 2016, **81**, 503–509.
198 H. Li, J. Li, Z. Yang, Q. Xu and X. Hu, *Anal. Chem.*, 2011, **83**, 5290–5295.
199 H. Li, J. Li, Q. Xu and X. Hu, *Anal. Chem.*, 2011, **83**, 9681–9686.
200 J. Qian, Z. Yang, C. Wang, K. Wang, Q. Liu, D. Jiang, Y. Yan and K. Wang, *J. Mater. Chem. A*, 2015, **3**, 13671–13678.
201 J. A. Cooper, M. Wu and R. G. Compton, *Anal. Chem.*, 1998, **70**, 2922–2927.
202 J. A. Cooper, K. E. Woodhouse, A. M. Chippindale and R. G. Compton, *Electroanalysis*, 1999, **11**, 1259–1265.
203 W. Ma, D. Han, M. Zhou, H. Sun, L. Wang, X. Dong and L. Niu, *Chem. Sci.*, 2014, **5**, 3946–3951.
204 W. Ma, D. Han, S. Gan, N. Zhang, S. Liu, T. Wu, Q. Zhang, X. Dong and L. Niu, *Chem. Commun.*, 2013, **49**, 7842–7844.
205 H. Dai, Y. Li, S. Zhang, L. Gong, X. Li and Y. Lin, *Sens. Actuators B Chem.*, 2016, **222**, 120–126.
206 X. Li, Z. Zheng, X. Liu, S. Zhao and S. Liu, *Biosens. Bioelectron.*, 2015, **64**, 1–5.
207 T. Hou, L. Zhang, X. Sun and F. Li, *Biosens. Bioelectron.*, 2016, **75**, 359–364.
208 G.-L. Wang, K.-L. Liu, Y.-M. Dong, X.-M. Wu, Z.-J. Li and C. Zhang, *Biosens. Bioelectron.*, 2014, **62**, 66–72.

209 W.-X. Dai, L. Zhang, W.-W. Zhao, X.-D. Yu, J.-J. Xu and H.-Y. Chen, *Anal. Chem.*, 2017, **89**, 8070–8078.
210 B. I. Ipe and C. M. Niemeyer, *Angew. Chem. Int. Ed.*, 2006, **45**, 504–507.
211 M. Girhard, E. Kunigk, S. Tihovsky, V. V. Shumyantseva and V. B. Urlacher, *Biotechnol. Appl. Biochem.*, 2013, **60**, 111–118.
212 J. Liu, R. Cazelles, Z. P. Chen, H. Zhou, A. Galarneau and M. Antonietti, *Phys. Chem. Chem. Phys.*, 2014, **16**, 14699–14705.
213 S. K. Kuk, R. K. Singh, D. H. Nam, R. Singh, J.-K. Lee and C. B. Park, *Angew. Chem. Int. Ed.*, 2017, **56**, 3827–3832.
214 R. K. Yadav, J.-O. Baeg, G. H. Oh, N.-J. Park, K. Kong, J. Kim, D. W. Hwang and S. K. Biswas, *J. Am. Chem. Soc.*, 2012, **134**, 11455–11461.
215 C. Beum Park, S. Ha Lee, E. Subramanian, B. B. Kale, S. Mi Lee and J.-O. Baeg, *Chem. Commun.*, 2008, **0**, 5423–5425.
216 J. Liu, J. Huang, H. Zhou and M. Antonietti, *ACS Appl. Mater. Interfaces*, 2014, **6**, 8434–8440.
217 R. Stuermer, B. Hauer, M. Hall and K. Faber, *Curr. Opin. Chem. Biol.*, 2007, **11**, 203–213.
218 T. N. Burai, A. J. Panay, H. Zhu, T. Lian and S. Lutz, *ACS Catal.*, 2012, **2**, 667–670.
219 M. K. Peers, H. S. Toogood, D. J. Heyes, D. Mansell, B. J. Coe and N. S. Scrutton, *Catal. Sci. Technol.*, 2015, **6**, 169–177.
220 F. Hollmann, A. Taglieber, F. Schulz and M. T. Reetz, *Angew. Chem. Int. Ed.*, 2007, **46**, 2903–2906.
221 M. Mifsud, S. Gargiulo, S. Iborra, I. W. C. E. Arends, F. Hollmann and A. Corma, *Nat. Commun.*, 2014, **5**, 3145.
222 B. A. Parkinson and P. F. Weaver, *Nature*, 1984, **309**, 148.
223 S. Nakamaru, F. Scholz, W. E. Ford, Y. Goto and F. von Wrochem, *Adv. Mater. Deerfield Beach Fla*, , DOI:10.1002/adma.201605924.
224 V. A. Soares, D. Severino, H. C. Junqueira, I. L. S. Tersariol, C. S. Shida, M. S. Baptista, O. R. Nascimento and I. L. Nantes, *Photochem. Photobiol.*, 2007, **83**, 1254–1262.
225 K. Kamada, A. Moriyasu and N. Soh, *J. Phys. Chem. C*, 2012, **116**, 20694–20699.
226 N.-H. Tran, D. Nguyen, S. Dwaraknath, S. Mahadevan, G. Chavez, A. Nguyen, T. Dao, S. Mullen, T.-A. Nguyen and L. E. Cheruzel, *J. Am. Chem. Soc.*, 2013, **135**, 14484–14487.
227 J. Qian, W. Zhu, L. Mi, X. Xu, J. Yu, D. Cui, Y. Xue and S. Liu, *J. Electroanal. Chem.*, 2014, **733**, 27–32.
228 X. Fang, Y. Duan, Y. Liu, G. Adkins, W. Zang, W. Zhong, L. Qiao and B. Liu, *Anal. Chem.*, 2017, **89**, 7365–7372.
229 K. A. Brown, M. B. Wilker, M. Boehm, H. Hamby, G. Dukovic and P. W. King, *ACS Catal.*, 2016, **6**, 2201–2204.
230 S. H. Lee, D. S. Choi, M. Pesic, Y. W. Lee, C. E. Paul, F. Hollmann and C. B. Park, *Angew. Chem. Int. Ed Engl.*, 2017, **56**, 8681–8685.
231 W. Vastarella and R. Nicastri, *Talanta*, 2005, **66**, 627–633.
232 A. J. Simaan, Y. Mekmouche, C. Herrero, P. Moreno, A. Aukauloo, J. A. Delaire, M. Réglier and T. Tron, *Chem. – Eur. J.*, 2011, **17**, 11743–11746.
233 K. Skorupska, H. J. Lewerenz, P. Ugarte Berzal, I. A. Rutkowska and P. J. Kulesza, *J. Mater. Chem.*, 2012, **22**, 15267–15274.
234 T. Lazarides, I. V. Sazanovich, A. J. Simaan, M. C. Kafentzi, M. Delor, Y. Mekmouche, B. Faure, M. Réglier, J. A. Weinstein, A. G. Coutsolelos and T. Tron, *J. Am. Chem. Soc.*, 2013, **135**, 3095–3103.

235 H. Li, S. Guo, C. Li, H. Huang, Y. Liu and Z. Kang, *ACS Appl. Mater. Interfaces*, 2015, **7**, 10004–10012.
236 L. Schneider, Y. Mekmouche, P. Rousselot-Pailley, A. J. Simaan, V. Robert, M. Réglier, A. Aukauloo and T. Tron, *ChemSusChem*, 2015, **8**, 3048–3051.
237 V. Robert, E. Monza, L. Tarrago, F. Sancho, A. De Falco, L. Schneider, E. Npetgat Ngoutane, Y. Mekmouche, P. R. Pailley, A. J. Simaan, V. Guallar and T. Tron, *ChemPlusChem*, 2017, **82**, 607–614.
238 C. Tapia, S. Shleev, J. C. Conesa, A. L. De Lacey and M. Pita, *ACS Catal.*, 2017, **7**, 4881–4889.
239 M. Pita, D. M. Mate, D. Gonzalez-Perez, S. Shleev, V. M. Fernandez, M. Alcalde and A. L. De Lacey, *J. Am. Chem. Soc.*, 2014, **136**, 5892–5895.
240 A. Bachmeier, V. C. C. Wang, T. W. Woolerton, S. Bell, J. C. Fontecilla-Camps, M. Can, S. W. Ragsdale, Y. S. Chaudhary and F. A. Armstrong, *J. Am. Chem. Soc.*, 2013, **135**, 15026–15032.
241 E. Reisner, D. J. Powell, C. Cavazza, J. C. Fontecilla-Camps and F. A. Armstrong, *J. Am. Chem. Soc.*, 2009, **131**, 18457–18466.
242 C. A. Caputo, L. Wang, R. Beranek and E. Reisner, *Chem. Sci.*, 2015, **6**, 5690–5694.
243 K. A. Brown, M. B. Wilker, M. Boehm, G. Dukovic and P. W. King, *J. Am. Chem. Soc.*, 2012, **134**, 5627–5636.
244 G. A. M. Hutton, B. Reuillard, B. C. M. Martindale, C. A. Caputo, C. W. J. Lockwood, J. N. Butt and E. Reisner, *J. Am. Chem. Soc.*, 2016, **138**, 16722–16730.
245 C. A. Caputo, M. A. Gross, V. W. Lau, C. Cavazza, B. V. Lotsch and E. Reisner, *Angew. Chem.*, 2014, **126**, 11722–11726.
246 T. Sakai, D. Mersch and E. Reisner, *Angew. Chem. Int. Ed.*, 2013, **52**, 12313–12316.
247 C. E. Lubner, P. Knörzer, P. J. N. Silva, K. A. Vincent, T. Happe, D. A. Bryant and J. H. Golbeck, *Biochemistry (Mosc.)*, 2010, **49**, 10264–10266.
248 C. E. Lubner, A. M. Applegate, P. Knörzer, A. Ganago, D. A. Bryant, T. Happe and J. H. Golbeck, *Proc. Natl. Acad. Sci.*, 2011, **108**, 20988–20991.
249 T. W. Woolerton, S. Sheard, E. Reisner, E. Pierce, S. W. Ragsdale and F. A. Armstrong, *J. Am. Chem. Soc.*, 2010, **132**, 2132–2133.
250 T. W. Woolerton, S. Sheard, E. Pierce, S. W. Ragsdale and F. A. Armstrong, *Energy Environ. Sci.*, 2011, **4**, 2393–2399.
251 Y. S. Chaudhary, T. W. Woolerton, C. S. Allen, J. H. Warner, E. Pierce, S. W. Ragsdale and F. A. Armstrong, *Chem. Commun.*, 2011, **48**, 58–60.
252 K. A. Brown, D. F. Harris, M. B. Wilker, A. Rasmussen, N. Khadka, H. Hamby, S. Keable, G. Dukovic, J. W. Peters, L. C. Seefeldt and P. W. King, *Science*, 2016, **352**, 448–450.
253 P. Dokter, J. Frank and J. A. Duine, *Biochem. J.*, 1986, **239**, 163–167.
254 A. J. J. Olsthoorn and J. A. Duine, *Biochemistry (Mosc.)*, 1998, **37**, 13854–13861.
255 O. Geiger and H. Görisch, *Biochem. J.*, 1989, **261**, 415–421.
256 A. Oubrie, H. J. Rozeboom, K. H. Kalk, J. A. Duine and B. W. Dijkstra, *J. Mol. Biol.*, 1999, **289**, 319–333.
257 S. Igarashi, T. Ohtera, H. Yoshida, A. B. Witarto and K. Sode, *Biochem. Biophys. Res. Commun.*, 1999, **264**, 820–824.
258 S. Ferri, K. Kojima and K. Sode, *J. Diabetes Sci. Technol.*, 2011, **5**, 1068–1076.
259 K. Sode, T. Ootera, M. Shirahane, A. B. Witarto, S. Igarashi and H. Yoshida, *Enzyme Microb. Technol.*, 2000, **26**, 491–496.
260 K. Sode, S. Igarashi, A. Morimoto and H. Yoshida, *Biocatal. Biotransformation*, 2002, **20**, 405–412.

261 S. Igarashi and K. Sode, *Mol. Biotechnol.*, 2003, **24**, 97–103.
262 S. Igarashi, T. Hirokawa and K. Sode, *Biomol. Eng.*, 2004, **21**, 81–89.
263 S. Igarashi, J. Okuda, K. Ikebukuro and K. Sode, *Arch. Biochem. Biophys.*, 2004, **428**, 52–63.
264 V. Laurinavičius, B. Kurtinaitienė, V. Liauksminas, B. Puodžiūnaitė, R. Jančienė, L. Kosychova and R. Meškys, *Monatshefte Für Chem. Chem. Mon.*, 1999, **130**, 1269–1281.
265 V. Laurinavicius, B. Kurtinaitiene, V. Liauksminas, A. Ramanavicius, R. Meskys, R. Rudomanskis, T. Skotheim and L. Boguslavsky, *Anal. Lett.*, 1999, **32**, 299–316.
266 A. Malinauskas, J. Kuzmarskyt≐, R. Meškys and A. Ramanavičius, *Sens. Actuators B Chem.*, 2004, **100**, 387–394.
267 W. Jin, U. Wollenberger and F. W. Scheller, *Biol. Chem.*, 1998, **379**, 1207–1211.
268 V. Laurinavicius, B. Kurtinaitiene and R. Stankeviciute, *Electroanalysis*, 2008, **20**, 1391–1395.
269 J. Razumiene, R. Meškys, V. Gureviciene, V. Laurinavicius, M. D. Reshetova and A. D. Ryabov, *Electrochem. Commun.*, 2000, **2**, 307–311.
270 J. Razumiene, A. Vilkanauskyte, V. Gureviciene, V. Laurinavicius, N. V. Roznyatovskaya, Y. V. Ageeva, M. D. Reshetova and A. D. Ryabov, *J. Organomet. Chem.*, 2003, **668**, 83–90.
271 V. Laurinavicius, J. Razumiene, A. Ramanavicius and A. D. Ryabov, *Biosens. Bioelectron.*, 2004, **20**, 1217–1222.
272 L. Ye, M. Haemmerle, A. J. J. Olsthoorn, W. Schuhmann, H. L. Schmidt, J. A. Duine and A. Heller, *Anal. Chem.*, 1993, **65**, 238–241.
273 M. Alkasrawi, I. C. Popescu, B. Mattiasson, E. Csöregi and V. Laurinavicius, *Anal. Commun.*, 1999, **36**, 395–398.
274 V. Flexer and N. Mano, *Anal. Chem.*, 2014, **86**, 2465–2473.
275 C. Wettstein, H. Möhwald and F. Lisdat, *Bioelectrochemistry*, 2012, **88**, 97–102.
276 D. Ivnitski, P. Atanassov and C. Apblett, *Electroanalysis*, 2007, **19**, 1562–1568.
277 R. J. Lopez, S. Babanova, K. Artyushkova and P. Atanassov, *Bioelectrochemistry*, 2015, **105**, 78–87.
278 G. Fusco, G. Göbel, R. Zanoni, E. Kornejew, G. Favero, F. Mazzei and F. Lisdat, *Electrochimica Acta*, 2017, **248**, 64–74.
279 C. Tanne, G. Göbel and F. Lisdat, *Biosens. Bioelectron.*, 2010, **26**, 530–535.
280 G. Göbel, I. W. Schubart, V. Scherbahn and F. Lisdat, *Electrochem. Commun.*, 2011, **13**, 1240–1243.
281 I. W. Schubart, G. Göbel and F. Lisdat, *Electrochimica Acta*, 2012, **82**, 224–232.
282 V. Scherbahn, M. T. Putze, B. Dietzel, T. Heinlein, J. J. Schneider and F. Lisdat, *Biosens. Bioelectron.*, 2014, **61**, 631–638.
283 V. Flexer, F. Durand, S. Tsujimura and N. Mano, *Anal. Chem.*, 2011, **83**, 5721–5727.
284 M. Zayats, E. Katz, R. Baron and I. Willner, *J. Am. Chem. Soc.*, 2005, **127**, 12400–12406.
285 D. Sarauli, M. Riedel, C. Wettstein, R. Hahn, K. Stiba, U. Wollenberger, S. Leimkühler, P. Schmuki and F. Lisdat, *J. Mater. Chem.*, 2012, **22**, 4615–4618.
286 O. A. Raitman, F. Patolsky, E. Katz and I. Willner, *Chem. Commun.*, 2002, **0**, 1936–1937.
287 D. Sarauli, C. Xu, B. Dietzel, B. Schulz and F. Lisdat, *Acta Biomater.*, 2013, **9**, 8290–8298.
288 D. Sarauli, C. Xu, B. Dietzel, B. Schulz and F. Lisdat, *J. Mater. Chem. B*, 2014, **2**, 3196–3203.

289 D. Sarauli, K. Peters, C. Xu, B. Schulz, D. Fattakhova-Rohlfing and F. Lisdat, *ACS Appl. Mater. Interfaces*, 2014, **6**, 17887–17893.
290 H. Yoshida, G. Sakai, K. Mori, K. Kojima, S. Kamitori and K. Sode, *Sci. Rep.*, 2015, **5**, 13498.
291 M. Ameyama, E. Shinagawa, K. Matsushita and O. Adachi, *J. Bacteriol.*, 1981, **145**, 814–823.
292 I. Lee, N. Loew, W. Tsugawa, C.-E. Lin, D. Probst, J. T. La Belle and K. Sode, *Bioelectrochemistry*, 2018, **121**, 1–6.
293 T.-G. Bak, *Biochim. Biophys. Acta BBA - Enzymol.*, 1967, **139**, 277–293.
294 T.-G. Bak, *Biochim. Biophys. Acta BBA - Enzymol.*, 1967, **146**, 317–327.
295 M. N. Zafar, N. Beden, D. Leech, C. Sygmund, R. Ludwig and L. Gorton, *Anal. Bioanal. Chem.*, 2012, **402**, 2069–2077.
296 M. N. Zafar, X. Wang, C. Sygmund, R. Ludwig, D. Leech and L. Gorton, *Anal. Chem.*, 2012, **84**, 334–341.
297 R. Monošík, M. Streďanský, K. Lušpai, P. Magdolen and E. Šturdík, *Enzyme Microb. Technol.*, 2012, **50**, 227–232.
298 K. Sode, N. Loew, Y. Ohnishi, H. Tsuruta, K. Mori, K. Kojima, W. Tsugawa, J. T. LaBelle and D. C. Klonoff, *Biosens. Bioelectron.*, 2017, **87**, 305–311.
299 N. Tsuruoka, T. Sadakane, R. Hayashi and S. Tsujimura, *Int. J. Mol. Sci.*, , DOI:10.3390/ijms18030604.
300 S. Tsujimura, S. Kojima, K. Kano, T. Ikeda, M. Sato, H. Sanada and H. Omura, *Biosci. Biotechnol. Biochem.*, 2006, **70**, 654–659.
301 S. Tsujimura, K. Murata and W. Akatsuka, *J. Am. Chem. Soc.*, 2014, **136**, 14432–14437.
302 R. D. Milton, D. P. Hickey, S. Abdellaoui, K. Lim, F. Wu, B. Tan and S. D. Minteer, *Chem. Sci.*, 2015, **6**, 4867–4875.
303 A. J. Gross, X. Chen, F. Giroud, C. Abreu, A. Le Goff, M. Holzinger and S. Cosnier, *ACS Catal.*, 2017, **7**, 4408–4416.
304 S. Kawai, T. Yakushi, K. Matsushita, Y. Kitazumi, O. Shirai and K. Kano, *Electrochem. Commun.*, 2014, **38**, 28–31.
305 S. Kawai, Y. Kitazumi, O. Shirai and K. Kano, *Electrochimica Acta*, 2016, **210**, 689–694.
306 M. Kizling and R. Bilewicz, *ChemElectroChem*, 2018, **5**, 166–174.
307 S. Kawai, M. Goda-Tsutsumi, T. Yakushi, K. Kano and K. Matsushita, *Appl. Environ. Microbiol.*, 2013, **79**, 1654–1660.
308 T. Ikeda, F. Matsushita and M. Senda, *Agric. Biol. Chem.*, 1990, **54**, 2919–2924.
309 S. Campuzano, M. Pedrero, F. J. M. de Villena and J. M. Pingarrón, *Electroanalysis*, 2004, **16**, 1385–1392.
310 K. Damar and D. Odaci Demirkol, *Talanta*, 2011, **87**, 67–73.
311 J. Biscay, E. Costa Rama, M. B. González García, A. Julio Reviejo, J. M. Pingarrón Carrazón and A. C. García, *Talanta*, 2012, **88**, 432–438.
312 M. Boujtita and N. El Murr, *Appl. Biochem. Biotechnol.*, 2000, **89**, 55–66.
313 J. Tkáč, I. Voštiar, E. Šturdík, P. Gemeiner, V. Mastihuba and J. Annus, *Anal. Chim. Acta*, 2001, **439**, 39–46.
314 P. A. Paredes, J. Parellada, V. M. Fernández, I. Katakis and E. Domínguez, *Biosens. Bioelectron.*, 1997, **12**, 1233–1243.
315 R. Antiochia, G. Vinci and L. Gorton, *Food Chem.*, 2013, **140**, 742–747.
316 E. E Ferapontova and L. Gorton, *Bioelectrochemistry Amst. Neth.*, 2005, **66**, 55–63.
317 C. Wettstein, K. Kano, D. Schäfer, U. Wollenberger and F. Lisdat, *Anal. Chem.*, 2016, **88**, 6382–6389.

318 T. Ikeda, F. Matsushita and M. Senda, *Biosens. Bioelectron.*, 1991, **6**, 299–304.
319 M. Tominaga, S. Nomura and I. Taniguchi, *Biosens. Bioelectron.*, 2009, **24**, 1184–1188.
320 Y. Kamitaka, S. Tsujimura and K. Kano, *Chem. Lett.*, 2006, **36**, 218–219.
321 S. Tsujimura, A. Nishina, Y. Hamano, K. Kano and S. Shiraishi, *Electrochem. Commun.*, 2010, **12**, 446–449.
322 C. A. B. Garcia, G. de Oliveira Neto and L. T. Kubota, *Anal. Chim. Acta*, 1998, **374**, 201–208.
323 D. Sarauli, C. Wettstein, K. Peters, B. Schulz, D. Fattakhova-Rohlfing and F. Lisdat, *ACS Catal.*, 2015, **5**, 2081–2087.
324 K. T. Kinnear and H. G. Monbouquette, *Anal. Chem.*, 1997, **69**, 1771–1775.
325 S. Yabuki and F. Mizutani, *Electroanalysis*, 1997, **9**, 23–25.
326 K. Murata, M. Suzuki, K. Kajiya, N. Nakamura and H. Ohno, *Electrochem. Commun.*, 2009, **11**, 668–671.
327 X. Michalet, F. F. Pinaud, L. A. Bentolila, J. M. Tsay, S. Doose, J. J. Li, G. Sundaresan, A. M. Wu, S. S. Gambhir and S. Weiss, *Science*, 2005, **307**, 538–544.
328 R. Freeman and I. Willner, *Chem. Soc. Rev.*, 2012, **41**, 4067–4085.
329 W.-W. Zhao, J. Wang, Y.-C. Zhu, J.-J. Xu and H.-Y. Chen, *Anal. Chem.*, 2015, **87**, 9520–9531.
330 A. Devadoss, P. Sudhagar, C. Terashima, K. Nakata and A. Fujishima, *J. Photochem. Photobiol. C Photochem. Rev.*, 2015, **24**, 43–63.
331 W.-W. Zhao, X.-D. Yu, J.-J. Xu and H.-Y. Chen, *Nanoscale*, 2016, **8**, 17407–17414.
332 K. Yan, Y. Yang, O. K. Okoth, L. Cheng and J. Zhang, *Anal. Chem.*, 2016, **88**, 6140–6144.
333 R. Freeman, J. Girsh and I. Willner, *ACS Appl. Mater. Interfaces*, 2013, **5**, 2815–2834.
334 Y.-J. Li, M.-J. Ma and J.-J. Zhu, *Anal. Chem.*, 2012, **84**, 10492–10499.
335 W.-W. Zhao, Z.-Y. Ma, P.-P. Yu, X.-Y. Dong, J.-J. Xu and H.-Y. Chen, *Anal. Chem.*, 2012, **84**, 917–923.
336 X. Zeng, W. Tu, J. Li, J. Bao and Z. Dai, *ACS Appl. Mater. Interfaces*, 2014, **6**, 16197–16203.
337 I. Willner, B. Basnar and B. Willner, *FEBS J.*, 2007, **274**, 302–309.
338 R. Kumar and D. Leech, *Bioelectrochemistry*, 2015, **106**, **Part A**, 41–46.
339 M. Saleem, H. Yu, L. Wang, Zain-ul-Abdin, H. Khalid, M. Akram, N. M. Abbasi and J. Huang, *Anal. Chim. Acta*, 2015, **876**, 9–25.
340 N. P. Godman, J. L. DeLuca, S. R. McCollum, D. W. Schmidtke and D. T. Glatzhofer, *Langmuir*, 2016, **32**, 3541–3551.
341 A. Chaubey and B. D. Malhotra, *Biosens. Bioelectron.*, 2002, **17**, 441–456.
342 P. Pinyou, A. Ruff, S. Pöller, S. Ma, R. Ludwig and W. Schuhmann, *Chem. – Eur. J.*, 2016, **22**, 5319–5326.
343 J. W. Gallaway and S. A. Calabrese Barton, *J. Am. Chem. Soc.*, 2008, **130**, 8527–8536.
344 M. E. Ghica and C. M. A. Brett, *Microchim. Acta*, 2008, **163**, 185–193.
345 R. M. Evangelista, S. Makuta, S. Yonezu, J. Andrews and Y. Tachibana, *ACS Appl. Mater. Interfaces*, 2016, **8**, 13957–13965.
346 M. Sykora, M. A. Petruska, J. Alstrum-Acevedo, I. Bezel, T. J. Meyer and V. I. Klimov, *J. Am. Chem. Soc.*, 2006, **128**, 9984–9985.
347 D. Dorokhin, N. Tomczak, A. H. Velders, D. N. Reinhoudt and G. J. Vancso, *J. Phys. Chem. C*, 2009, **113**, 18676–18680.

348 M. H. Stewart, A. L. Huston, A. M. Scott, A. L. Efros, J. S. Melinger, K. B. Gemmill, S. A. Trammell, J. B. Blanco-Canosa, P. E. Dawson and I. L. Medintz, *ACS Nano*, 2012, **6**, 5330–5347.
349 M. A. Hines and P. Guyot-Sionnest, *J. Phys. Chem.*, 1996, **100**, 468–471.
350 J. Jasieniak, M. Califano and S. E. Watkins, *ACS Nano*, 2011, **5**, 5888–5902.
351 F. Koberling, A. Mews and T. Basché, *Adv. Mater.*, 2001, **13**, 672–676.
352 A. K. Gooding, D. E. Gómez and P. Mulvaney, *ACS Nano*, 2008, **2**, 669–676.
353 K. B. Holt, C. Ziegler, J. Zang, J. Hu and J. S. Foord, *J. Phys. Chem. C*, 2009, **113**, 2761–2770.
354 N. Loew, F. W. Scheller and U. Wollenberger, *Electroanalysis*, 2004, **16**, 1149–1154.
355 A. Oubrie, H. J. Rozeboom and B. W. Dijkstra, *Proc. Natl. Acad. Sci.*, 1999, **96**, 11787–11791.
356 S. S. Wong, *Chemistry of Protein Conjugation and Cross-Linking*, CRC Press, 1991.
357 I. Willner, A. Riklin, B. Shoham, D. Rivenzon and E. Katz, *Adv. Mater.*, 1993, **5**, 912–915.
358 T. Yoshinobu, K. Miyamoto, T. Wagner and M. J. Schöning, *Sens. Actuators B Chem.*, 2015, **207**, **Part B**, 926–932.
359 G.-L. Wang, J.-X. Shu, Y.-M. Dong, X.-M. Wu, W.-W. Zhao, J.-J. Xu and H.-Y. Chen, *Anal. Chem.*, 2015, **87**, 2892–2900.
360 M. Riedel, N. Sabir, F. W. Scheller, W. J. Parak and F. Lisdat, *Nanoscale*, 2017, **9**, 2814–2823.
361 J. Aldana, Y. A. Wang and X. Peng, *J. Am. Chem. Soc.*, 2001, **123**, 8844–8850.
362 M. Green, *J. Mater. Chem.*, 2010, **20**, 5797–5809.
363 D. A. Hines and P. V. Kamat, *J. Phys. Chem. C*, 2013, **117**, 14418–14426.
364 Y. C. Kong, D. P. Yu, B. Zhang, W. Fang and S. Q. Feng, *Appl. Phys. Lett.*, 2001, **78**, 407–409.
365 G. Su, V. G. Hadjiev, P. E. Loya, J. Zhang, S. Lei, S. Maharjan, P. Dong, P. M. Ajayan, J. Lou and H. Peng, *Nano Lett.*, 2015, **15**, 506–513.
366 W. Lee, S. K. Min, V. Dhas, S. B. Ogale and S.-H. Han, *Electrochem. Commun.*, 2009, **11**, 103–106.
367 I. Katakis and E. Domínguez, *Microchim. Acta*, 1997, **126**, 11–32.
368 J. Moiroux and P. J. Elving, *Anal. Chem.*, 1978, **50**, 1056–1062.
369 L. Gorton, G. Johansson and A. Torstensson, *J. Electroanal. Chem. Interfacial Electrochem.*, 1985, **196**, 81–92.
370 L. Gorton and E. Domı́nguez, *Rev. Mol. Biotechnol.*, 2002, **82**, 371–392.
371 F. Pariente, F. Tobalina, G. Moreno, L. Hernández, E. Lorenzo and H. D. Abruña, *Anal. Chem.*, 1997, **69**, 4065–4075.
372 F. Ni, H. Feng, L. Gorton and T. M. Cotton, *Langmuir*, 1990, **6**, 66–73.
373 M. Musameh, J. Wang, A. Merkoci and Y. Lin, *Electrochem. Commun.*, 2002, **4**, 743–746.
374 A. K. Samantara, S. C. Sahu, B. Bag, B. Jena and B. K. Jena, *J. Mater. Chem. A*, 2014, **2**, 12677–12680.
375 G. Steinhoff, M. Hermann, W. J. Schaff, L. F. Eastman, M. Stutzmann and M. Eickhoff, *Appl. Phys. Lett.*, 2003, **83**, 177–179.
376 K. Aryal, B. N. Pantha, J. Li, J. Y. Lin and H. X. Jiang, *Appl. Phys. Lett.*, 2010, **96**, 052110.
377 B. Baur, J. Howgate, H.-G. von Ribbeck, Y. Gawlina, V. Bandalo, G. Steinhoff, M. Stutzmann and M. Eickhoff, *Appl. Phys. Lett.*, 2006, **89**, 183901.

378 G. M. Müntze, B. Baur, W. Schäfer, A. Sasse, J. Howgate, K. Röth and M. Eickhoff, *Biosens. Bioelectron.*, 2015, **64**, 605–610.
379 N. Frenkel, J. Wallys, S. Lippert, J. Teubert, S. Kaufmann, A. Das, E. Monroy, M. Eickhoff and M. Tanaka, *Adv. Funct. Mater.*, 2014, **24**, 4927–4934.
380 J. Teubert, S. Koslowski, S. Lippert, M. Schäfer, J. Wallys, G. Dimitrakopulos, T. Kehagias, P. Komninou, A. Das, E. Monroy and M. Eickhoff, *J. Appl. Phys.*, 2013, **114**, 074313.
381 J. Wallys, J. Teubert, F. Furtmayr, D. M. Hofmann and M. Eickhoff, *Nano Lett.*, 2012, **12**, 6180–6186.
382 F. Furtmayr, M. Vielemeyer, M. Stutzmann, J. Arbiol, S. Estradé, F. Peirò, J. R. Morante and M. Eickhoff, *J. Appl. Phys.*, 2008, **104**, 034309.
383 T. Kehagias, G. P. Dimitrakopulos, P. Becker, J. Kioseoglou, F. Furtmayr, T. Koukoula, I. Häusler, A. Chernikov, S Chatterjee, T. Karakostas, H.-M. Solowan, U. T. Schwarz, M. Eickhoff and P. Komninou, *Nanotechnology*, 2013, **24**, 435702.
384 S. Crawford, E. Thimsen and P. Biswas, *J. Electrochem. Soc.*, 2009, **156**, H346–H351.
385 W. J. Blaedel and R. A. Jenkins, *Anal. Chem.*, 1975, **47**, 1337–1343.
386 M. Grätzel, *Nature*, 2001, **414**, 338–344.
387 M. Grätzel, *Inorg. Chem.*, 2005, **44**, 6841–6851.
388 M. G. Walter, E. L. Warren, J. R. McKone, S. W. Boettcher, Q. Mi, E. A. Santori and N. S. Lewis, *Chem. Rev.*, 2010, **110**, 6446–6473.
389 N. Zhang, L. Zhang, Y.-F. Ruan, W.-W. Zhao, J.-J. Xu and H.-Y. Chen, *Biosens. Bioelectron.*, 2017, **94**, 207–218.
390 M. Riedel, S. Hölzel, P. Hille, J. Schörmann, M. Eickhoff and F. Lisdat, *Biosens. Bioelectron.*, 2017, **94**, 298–304.
391 J. Schneider, M. Matsuoka, M. Takeuchi, J. Zhang, Y. Horiuchi, M. Anpo and D. W. Bahnemann, *Chem. Rev.*, 2014, **114**, 9919–9986.
392 G. Li, R. Zhu and Y. Yang, *Nat. Photonics*, 2012, **6**, 153–161.
393 Z. Liu, J. Zhou, H. Xue, L. Shen, H. Zang and W. Chen, *Synth. Met.*, 2006, **156**, 721–723.
394 N. Mano, J. E. Yoo, J. Tarver, Y.-L. Loo and A. Heller, *J. Am. Chem. Soc.*, 2007, **129**, 7006–7007.
395 D. Sarauli, A. Borowski, K. Peters, B. Schulz, D. Fattakhova-Rohlfing, S. Leimkühler and F. Lisdat, *ACS Catal.*, 2016, **6**, 7152–7159.
396 D. Sarauli, C. Xu, B. Dietzel, K. Stiba, S. Leimkühler, B. Schulz and F. Lisdat, *Soft Matter*, 2012, **8**, 3848–3855.
397 A. Hagfeldt and M. Graetzel, *Chem. Rev.*, 1995, **95**, 49–68.
398 G. I. N. Waterhouse and M. R. Waterland, *Polyhedron*, 2007, **26**, 356–368.
399 E. S. Kwak, W. Lee, N.-G. Park, J. Kim and H. Lee, *Adv. Funct. Mater.*, 2009, **19**, 1093–1099.
400 L. Liu, S. K. Karuturi, L. T. Su and A. I. Y. Tok, *Energy Environ. Sci.*, 2010, **4**, 209–215.
401 S.-J. Ha and J. H. Moon, *J. Phys. Chem. C*, 2017, **121**, 12046–12052.
402 Q. Zhang, D. Myers, J. Lan, S. A. Jenekhe and G. Cao, *Phys. Chem. Chem. Phys.*, 2012, **14**, 14982–14998.
403 Y. Pornputtkul, E. V. Strounina, L. A. P. Kane-Maguire and G. G. Wallace, *Macromolecules*, 2010, **43**, 9982–9989.
404 C. J. Barbé, F. Arendse, P. Comte, M. Jirousek, F. Lenzmann, V. Shklover and M. Grätzel, *J. Am. Ceram. Soc.*, 1997, **80**, 3157–3171.
405 Y. Saito, S. Kambe, T. Kitamura, Y. Wada and S. Yanagida, *Sol. Energy Mater. Sol. Cells*, 2004, **83**, 1–13.

406 S. Frasca, T. von Graberg, J.-J. Feng, A. Thomas, B. M. Smarsly, I. M. Weidinger, F. W. Scheller, P. Hildebrandt and U. Wollenberger, *ChemCatChem*, 2010, **2**, 839–845.
407 T. Borrmann, A. Dominis, A. J. McFarlane, J. H. Johnston, M. J. Richardson, L. A. P. Kane-Maguire and G. G. Wallace, *J. Nanosci. Nanotechnol.*, 2007, **7**, 4303–4310.
408 K. Matsushita, E. Shinagawa, O. Adachi and M. Ameyama, *Biochemistry (Mosc.)*, 1989, **28**, 6276–6280.
409 C. Lau, S. Borgmann, M. Maciejewska, B. Ngounou, P. Gründler and W. Schuhmann, *Biosens. Bioelectron.*, 2007, **22**, 3014–3020.
410 I. Willner, Y.-M. Yan, B. Willner and R. Tel-Vered, *Fuel Cells*, 2009, **9**, 7–24.
411 M. Rasmussen, S. Abdellaoui and S. D. Minteer, *Biosens. Bioelectron.*, 2016, **76**, 91–102.
412 A. Sato, K. Takagi, K. Kano, N. Kato, J. A. Duine and T. Ikeda, *Biochem. J.*, 2001, **357**, 893–898.
413 Z. Yue, F. Lisdat, W. J. Parak, S. G. Hickey, L. Tu, N. Sabir, D. Dorfs and N. C. Bigall, *ACS Appl. Mater. Interfaces*, 2013, **5**, 2800–2814.
414 W.-W. Zhao, J.-J. Xu and H.-Y. Chen, *Biosens. Bioelectron.*, 2017, **92**, 294–304.
415 E. T. Hwang, K. Sheikh, K. L. Orchard, D. Hojo, V. Radu, C.-Y. Lee, E. Ainsworth, C. Lockwood, M. A. Gross, T. Adschiri, E. Reisner, J. N. Butt and L. J. C. Jeuken, *Adv. Funct. Mater.*, 2015, **25**, 2308–2315.
416 M. Riedel and F. Lisdat, *ACS Appl. Mater. Interfaces*, 2018, **10**, 267–277.
417 H. Lee, M. Wang, P. Chen, D. R. Gamelin, S. M. Zakeeruddin, M. Grätzel and M. K. Nazeeruddin, *Nano Lett.*, 2009, **9**, 4221–4227.
418 H. Lee, H. C. Leventis, S.-J. Moon, P. Chen, S. Ito, S. A. Haque, T. Torres, F. Nüesch, T. Geiger, S. M. Zakeeruddin, M. Grätzel and M. K. Nazeeruddin, *Adv. Funct. Mater.*, 2009, **19**, 2735–2742.
419 A. Heller, *Curr. Opin. Chem. Biol.*, 2006, **10**, 664–672.
420 A. Badura, D. Guschin, B. Esper, T. Kothe, S. Neugebauer, W. Schuhmann and M. Rögner, *Electroanalysis*, 2008, **20**, 1043–1047.
421 B.-R. Hyun, Y.-W. Zhong, A. C. Bartnik, L. Sun, H. D. Abruña, F. W. Wise, J. D. Goodreau, J. R. Matthews, T. M. Leslie and N. F. Borrelli, *ACS Nano*, 2008, **2**, 2206–2212.
422 J.-H. Shin, J.-H. Kang, W.-M. Jin, J. H. Park, Y.-S. Cho and J. H. Moon, *Langmuir*, 2011, **27**, 856–860.
423 Y. G. Seo, K. Woo, J. Kim, H. Lee and W. Lee, *Adv. Funct. Mater.*, 2011, **21**, 3094–3103.
424 D. Pankratov, F. Conzuelo, P. Pinyou, S. Alsaoub, W. Schuhmann and S. Shleev, *Angew. Chem. Int. Ed.*, 2016, **55**, 15434–15438.
425 C. Giansante, I. Infante, E. Fabiano, R. Grisorio, G. P. Suranna and G. Gigli, *J. Am. Chem. Soc.*, 2015, **137**, 1875–1886.
426 Sauvé Geneviève, M. E. Cass, G. Coia, S. J. Doig, I. Lauermann, K. E. Pomykal and N. S. Lewis, *J. Phys. Chem. B*, 2000, **104**, 6821–6836.
427 D. Ciornii, M. Riedel, K. R. Stieger, S. C. Feifel, M. Hejazi, H. Lokstein, A. Zouni and F. Lisdat, *J. Am. Chem. Soc.*, , DOI:10.1021/jacs.7b10161.
428 *Diabetes Care*, 2011, **34**, S11–S61.
429 X. Chen, M. Shao, S. Pöller, D. Guschin, P. Pinyou and W. Schuhmann, *J. Electrochem. Soc.*, 2014, **161**, H3058–H3063.

Appendix

Supporting Information: Connecting quantum dots with enzymes: mediator-based approaches for the light-directed read-out of glucose and fructose oxidation

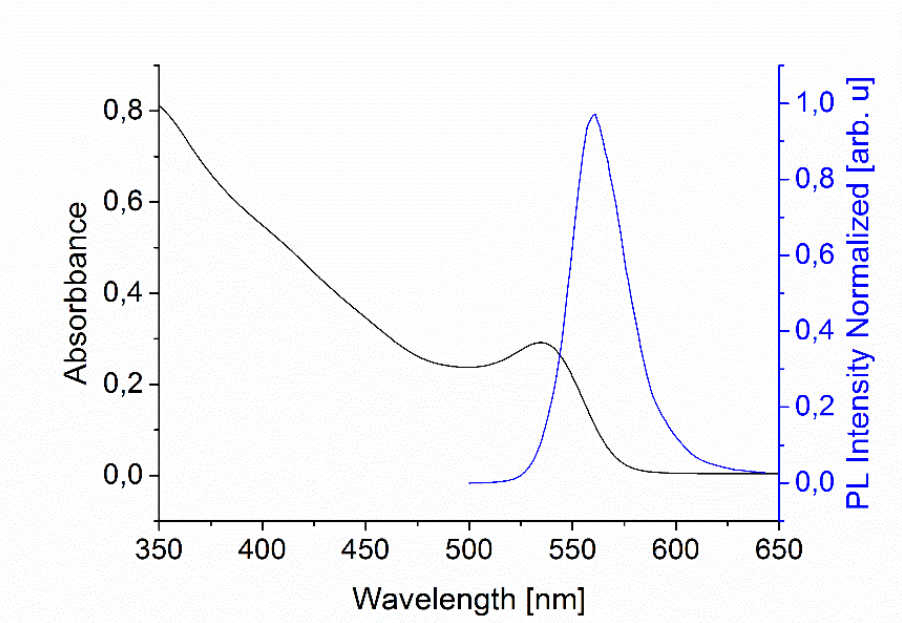

Fig. S1 Absorption and fluorescence spectra of CdSe/ZnS QDs in chloroform.

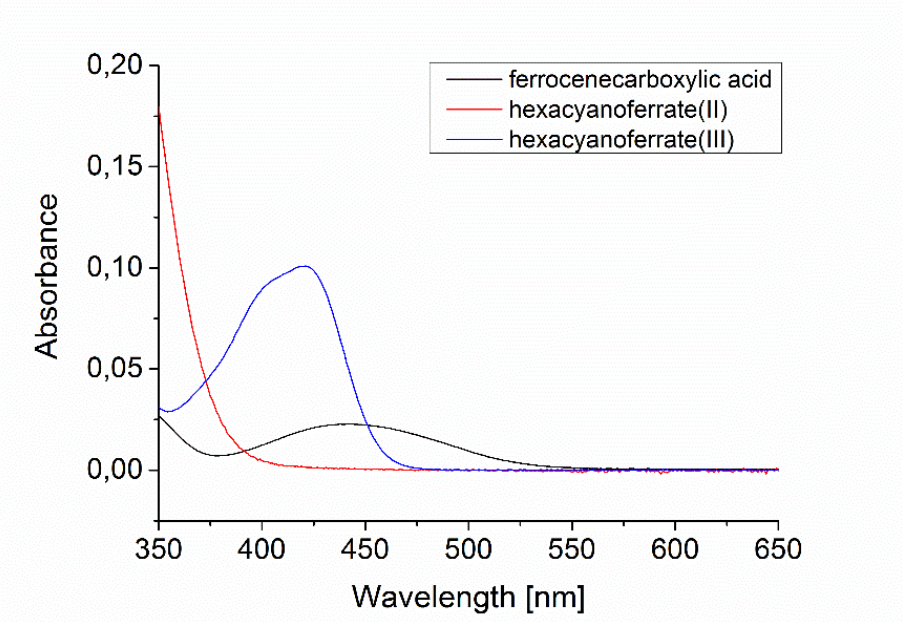

Fig. S2 Absorption spectra of 100 µM ferrocenecarboxylic acid, hexacyanoferrate(II) and hexacyanoferrate(III) in 100 mM HEPES pH 7.

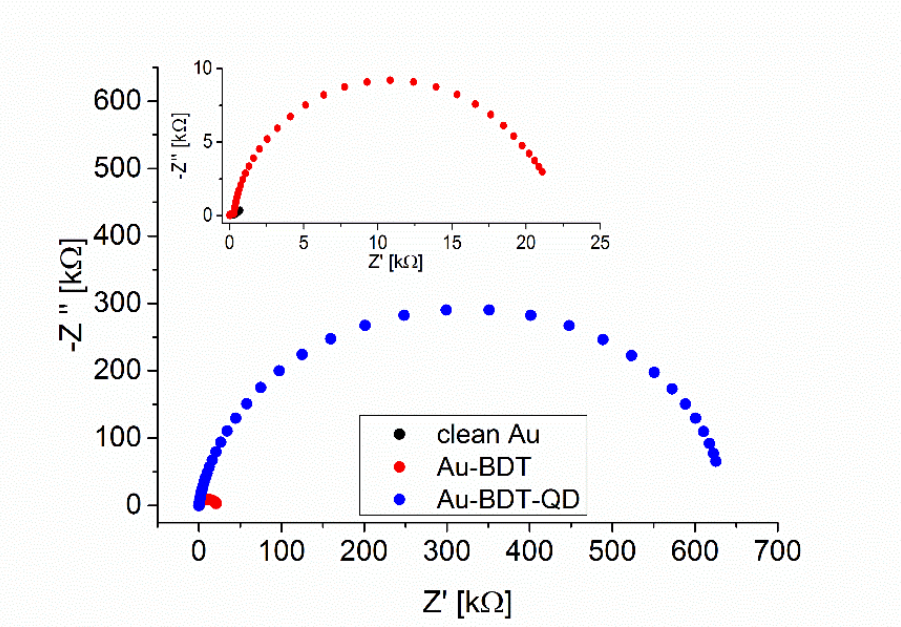

Fig. S3 Impedance spectra of a clean gold electrode (black symbols) and after modification with BDT (red symbols) and QDs (blue symbols) in the dark depicted as Nyquist plot. Inset: Magnification of the Impedance spectra. (100 mM sodium phosphate buffer pH 7, 2 mM hexacyanoferrate(II/III), 100 kHz – 1 Hz, 5 mV AC amplitude, OCP vs. Ag/AgCl, 1 M KCl)

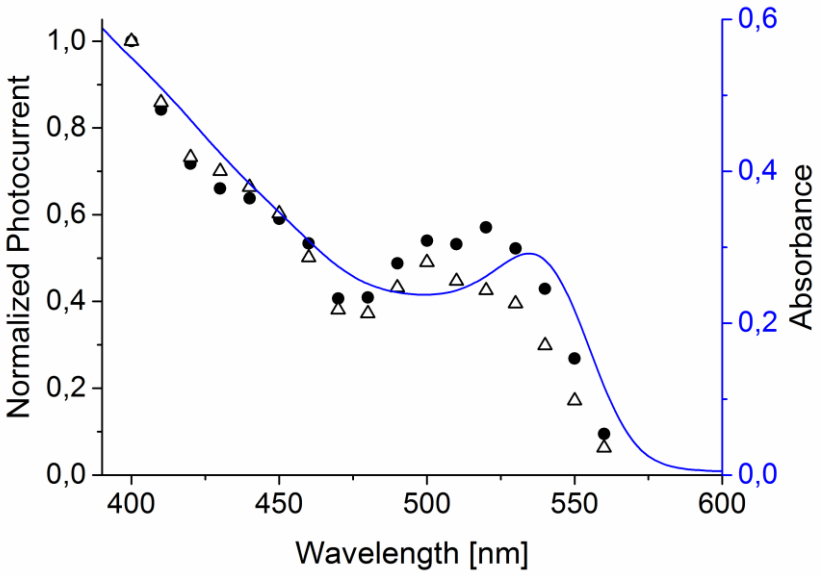

Fig. S4 Wavelength dependence of the photocurrent change ΔI of a CdSe/ZnS-modified gold electrode in buffer (black circle) and after addition of 200 µM hexacyanoferrate(II) (open triangle). For a better comparison the photocurrent is normalized to the value at 400 nm. (100 mM HEPES pH 7, -0.2 V vs. Ag/AgCl, 1 M KCl) Additionally the absorbance spectra of the used CdSe/ZnS QDs dissolved in chloroform is depicted (blue line).

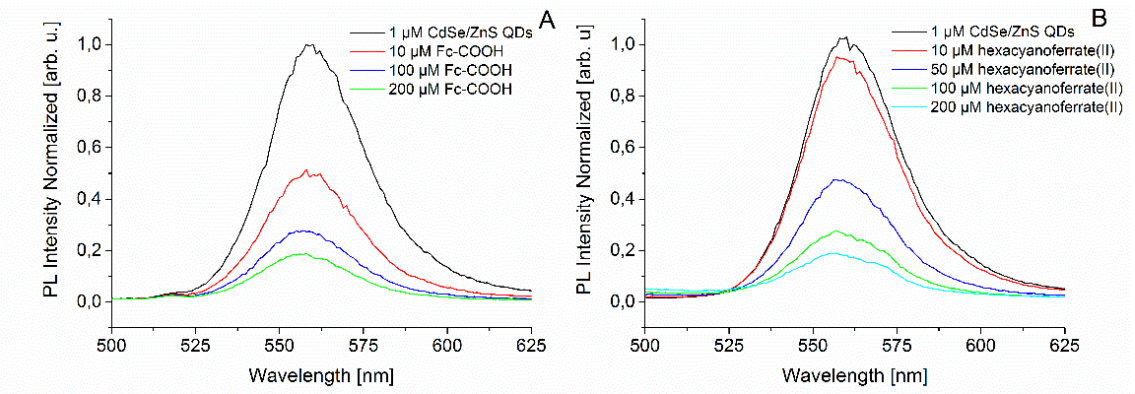

Fig. S5 Normalized photoluminescence spectra of a 1 µM CdSe/ZnS QDs solution in the absence and presence of ferrocenecarboxylic acid (A) and hexacyanoferrate(II) (B) with different ratios. For hexacyanoferrate(II) and ferrocenecarboxylic acid an excitation wavelength of 420 nm and 380 nm, respectively has been used.

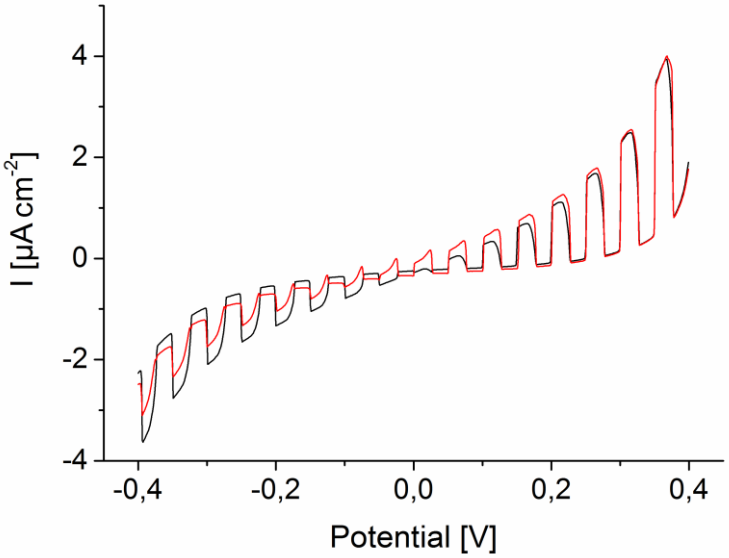

Fig. S6 Chopped light voltammetry of a QD electrode in the absence (black curve) and presence of 500 µM hexacyanoferrate(III) (red curve). (100 mM HEPES pH7; light pulses of 5 s, scan rate 5 mV s^{-1}; potential vs. Ag/AgCl, 1 M KCl from +400 mV to -400mV)

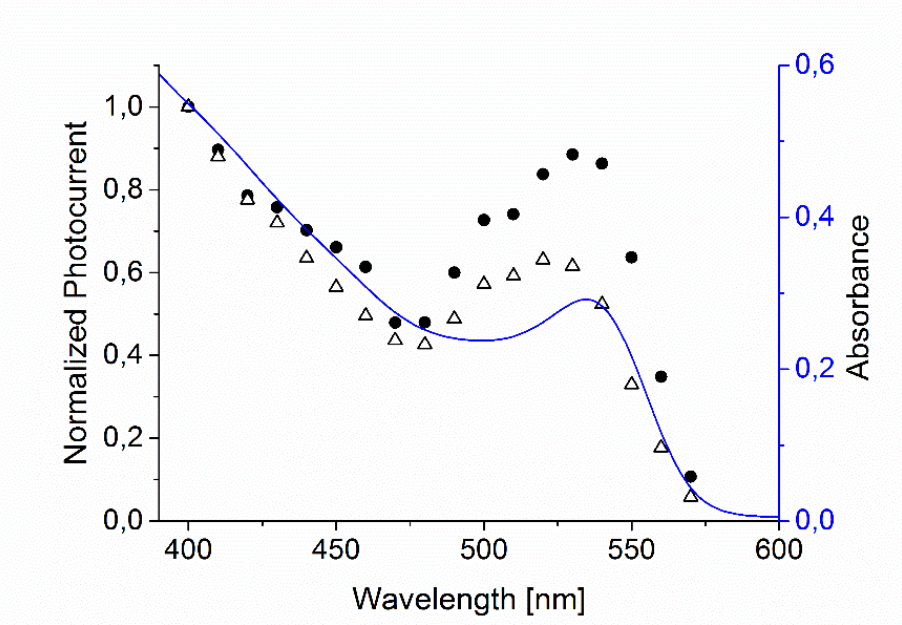

Fig. S7 Wavelength dependence of the photocurrent change ΔI of a CdSe/ZnS-modified gold electrode in buffer (black circle) and after addition of 100 µM ferrocenecarboxylic acid (open triangle). For a better comparison the photocurrent is normalized to the value at 400 nm. (100 mM HEPES pH 7, -0.2 V vs. Ag/AgCl, 1 M KCl) Additionally the absorbance spectra of the used CdSe/ZnS QDs dissolved in chloroform is depicted (blue line).

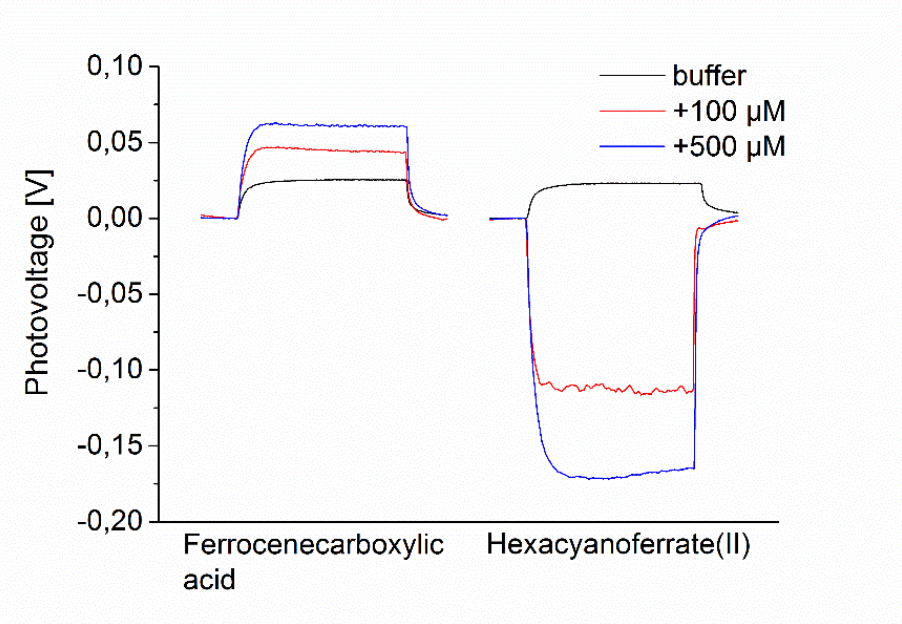

Fig. S8 Photovoltage measurements of a QD electrode in buffer (black curve) and in the presence of 100 µM (red curve) and 500 µM redox mediator (blue curve). (100 mM HEPES pH 7, light pulses of 20 s)

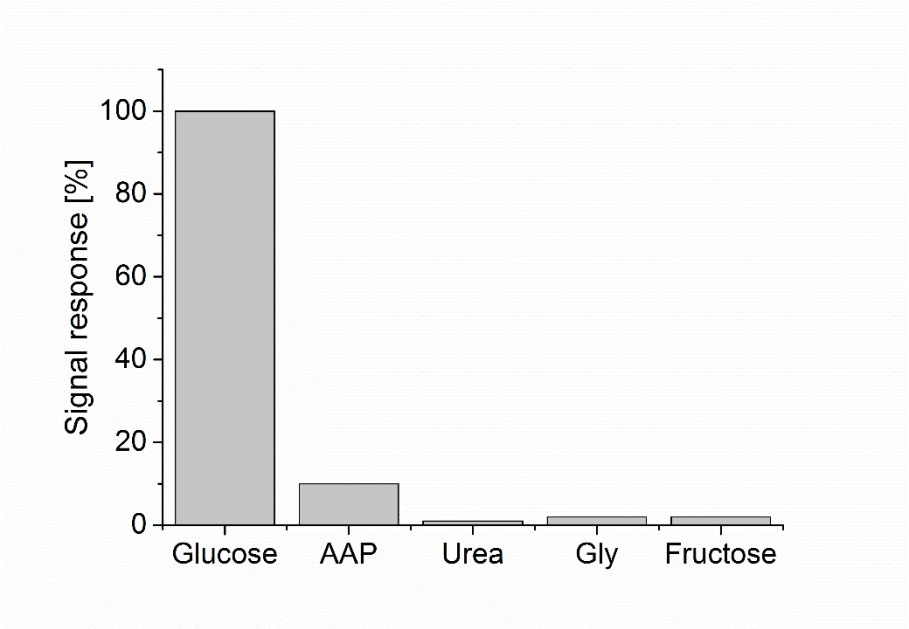

Fig. S9 Normalized photocurrent response of QD electrodes with immobilized (PQQ)GDH and ferrocenecarboxylic acid after addition of 100 µM glucose, 50 µM 4-acetylaminophenol (AAP), 50 µM urea, 50 µM glycine and 100 µM fructose. All values are normalized to the signal response after addition of 100 µM glucose (100 mM HEPES pH 7; +0.1 V vs. Ag/AgCl, 1 M KCl).

Supporting Information: InGaN/GaN nanowires as a new platform for photoelectrochemical sensors – detection of NADH

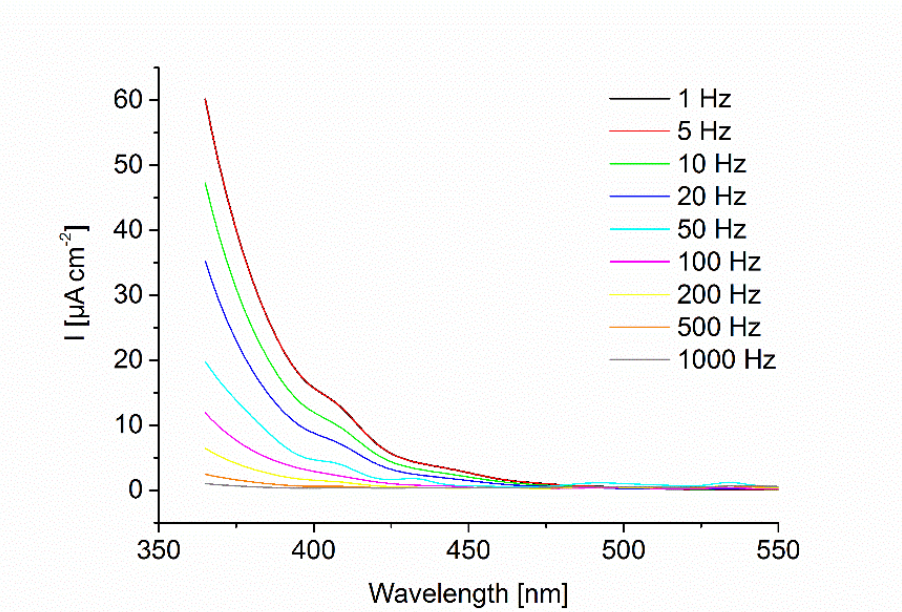

Fig. S1 Wavelength-dependence of the measured photocurrent of an **InGaN/GaN nanowire electrode** depending on the frequency of the modulated light source. (100 mM HEPES pH 7; 5 mW cm^{-2}; 0 mV vs. Ag/AgCl, 1 M KCl)

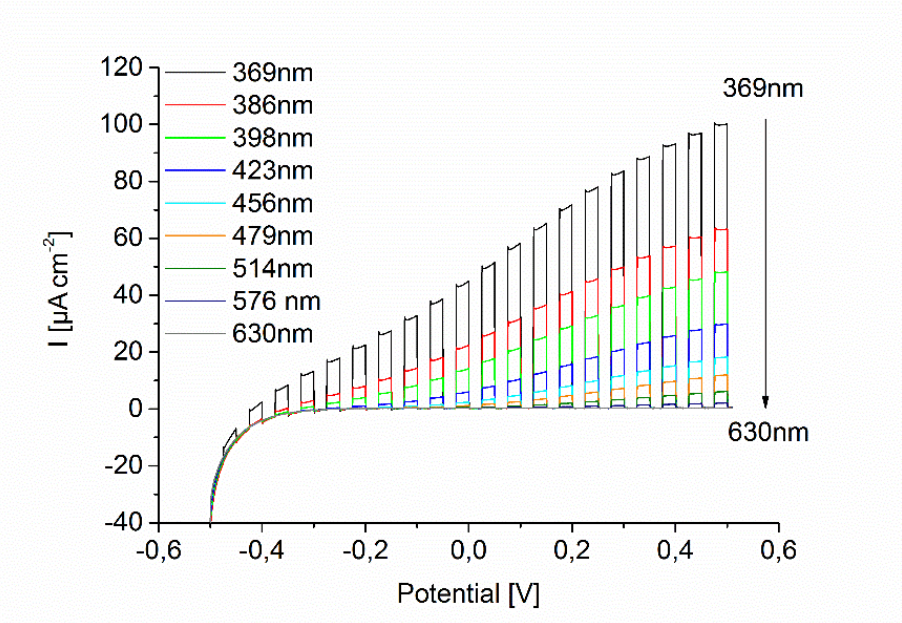

Fig. S2 Chopped light voltammetry of **InGaN/GaN nanowires** grown on Si substrate depending on the wavelength of the illuminated light. (100 mM HEPES pH 7; 5 mW cm^{-2}; light pulses of 5 s; 5 mV s^{-1}; between –500 mV and +500 mV vs. Ag/AgCl, 1 M KCl)

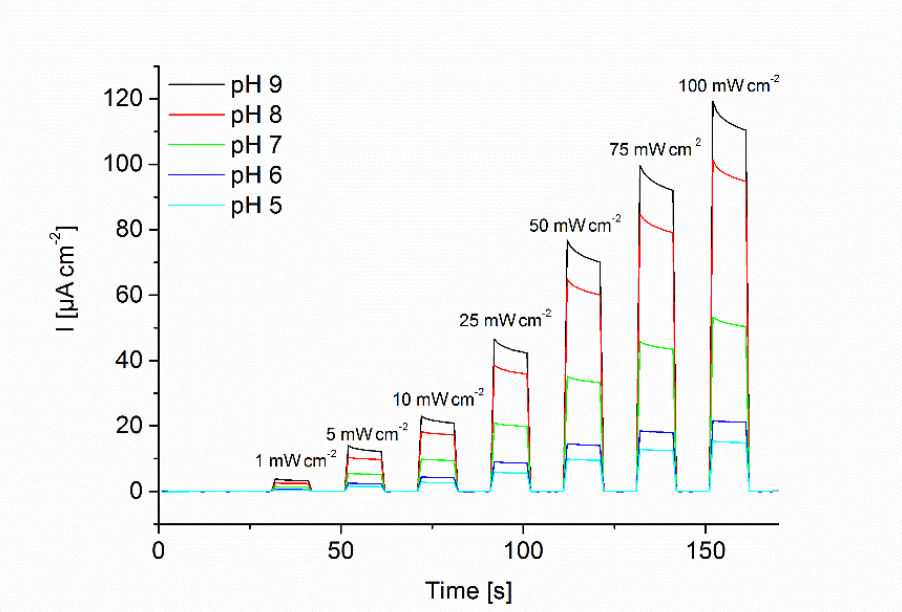

Fig. S3 Photochronoamperometric measurements of an **InGaN/GaN nanowire electrode** at different light intensities and pH. (100 mM HEPES; light source **449 nm +/- 5 nm**; light pulses of 10 s; 0 mV vs. Ag/AgCl, 1 M KCl)

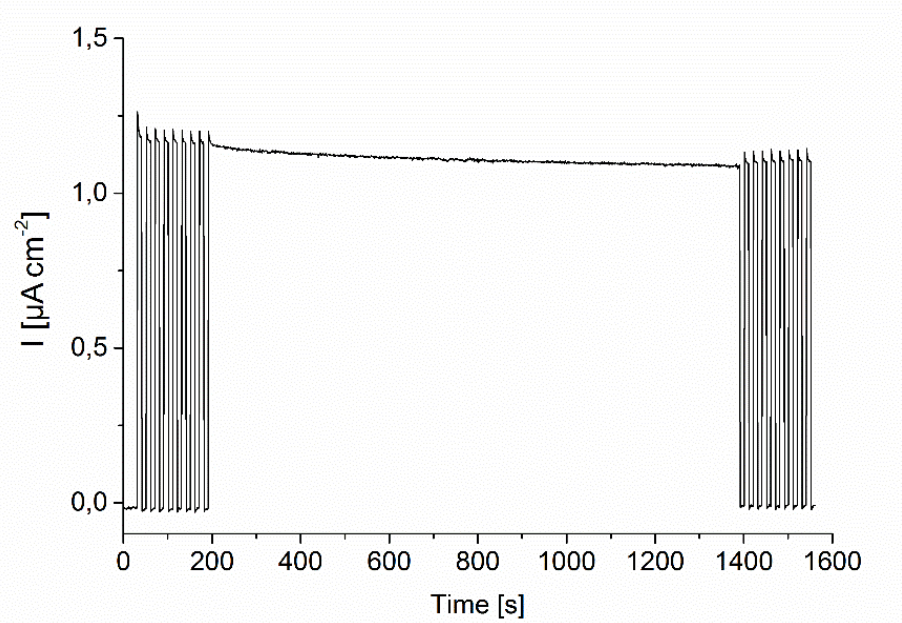

Fig. S4 Photochronoamperometric measurement of an **InGaN/GaN NW electrode** under continuous illumination over 20 min. (100 mM HEPES pH 7; light source **449 nm +/- 5 nm**; 10 mW cm^{-2}; light pulses of 10 s; 0mV vs. Ag/AgCl, 1 M KCl)

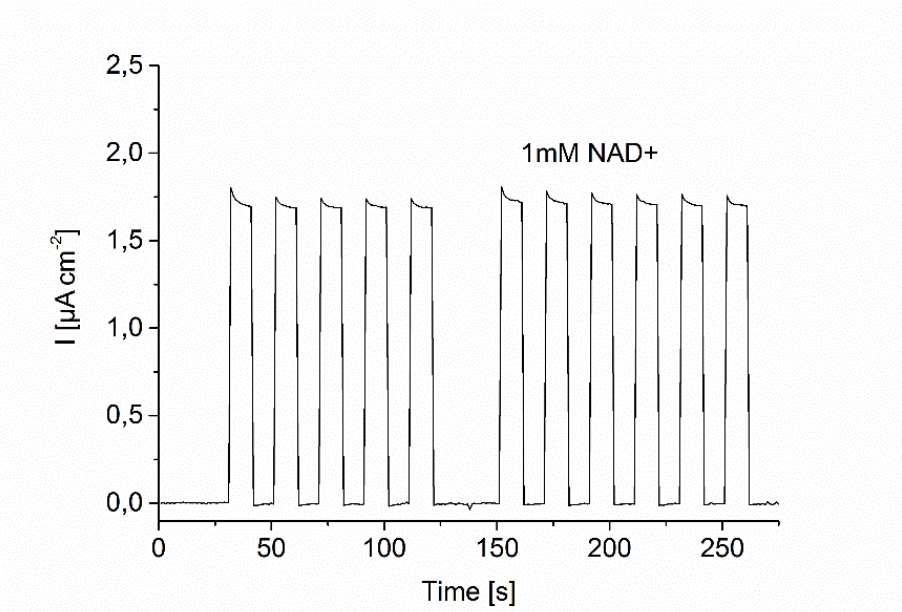

Fig. S5 Photocurrent measurement of an **InGaN/GaN nanowire electrode** before and after addition of 1 mM NAD^+. (100 mM HEPES pH 7; light source **449 nm +/- 5 nm**; 10 mW cm^{-2}; light pulses of 10 s; 500 mV vs. Ag/AgCl, 1 M KCl)

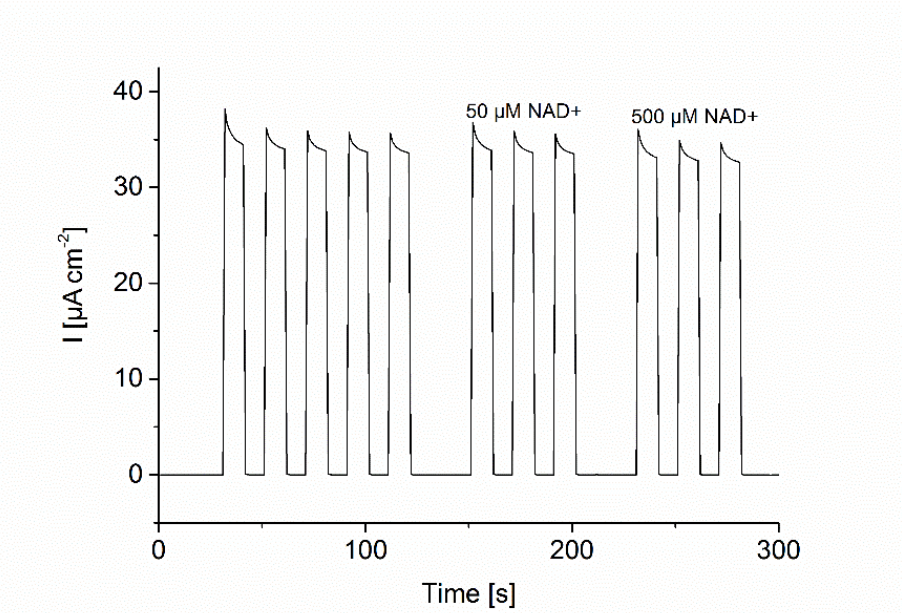

Fig. S6 Photocurrent measurement of an **InGaN/GaN nanowire electrode** before and after addition of 50 µM NAD^+ and 500 µM NAD^+. (100 mM HEPES pH 7; light source **369 nm**; 10 mW cm^{-2}; light pulses of 10 s; 0 mV vs Ag/AgCl, 1 M KCl)

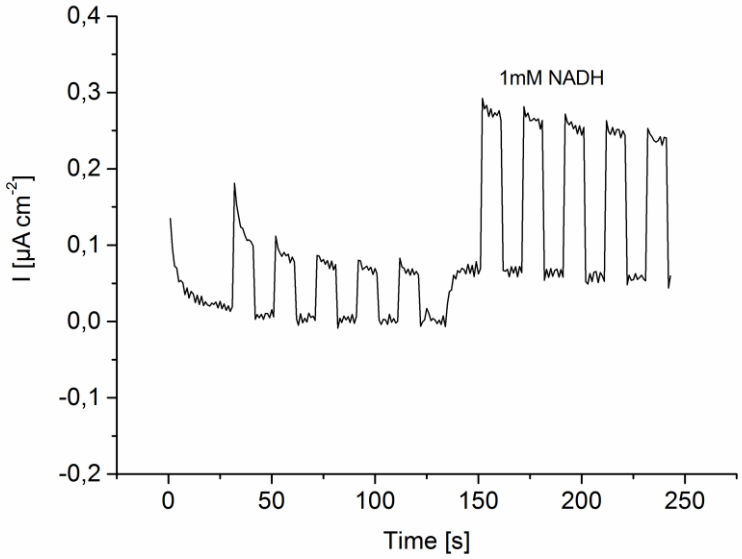

Fig. S7 Photocurrent measurement of a **GaN nanowire electrode** before and after addition of 1mM NADH. (100 mM HEPES pH 7; light source **449 nm +/- 5 nm**; 10 mW cm^{-2}; light pulses of 10 s; 500 mV vs. Ag/AgCl, 1 M KCl)

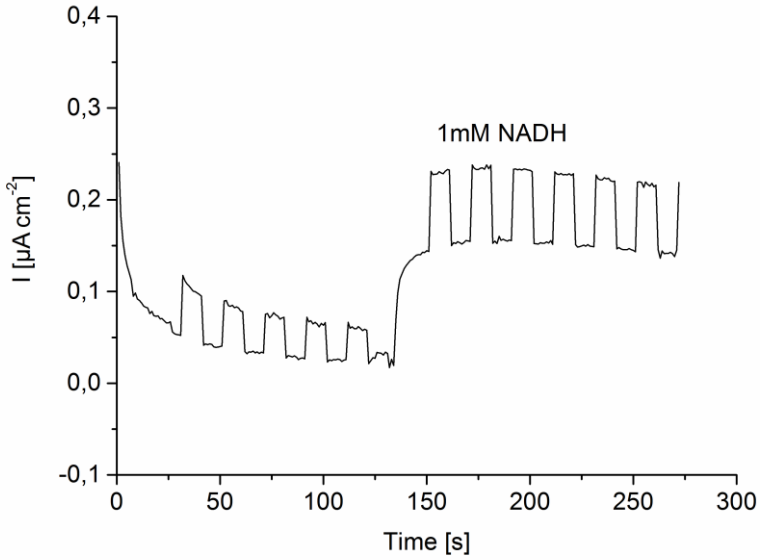

Fig. S8 Photocurrent measurement of a **Si electrode** before and after addition of 1mM NADH. (100 mM HEPES pH 7; light source **449 nm +/- 5 nm**; 10 mW cm^{-2}; light pulses of 10 s; 500 mV vs. Ag/AgCl, 1 M KCl)

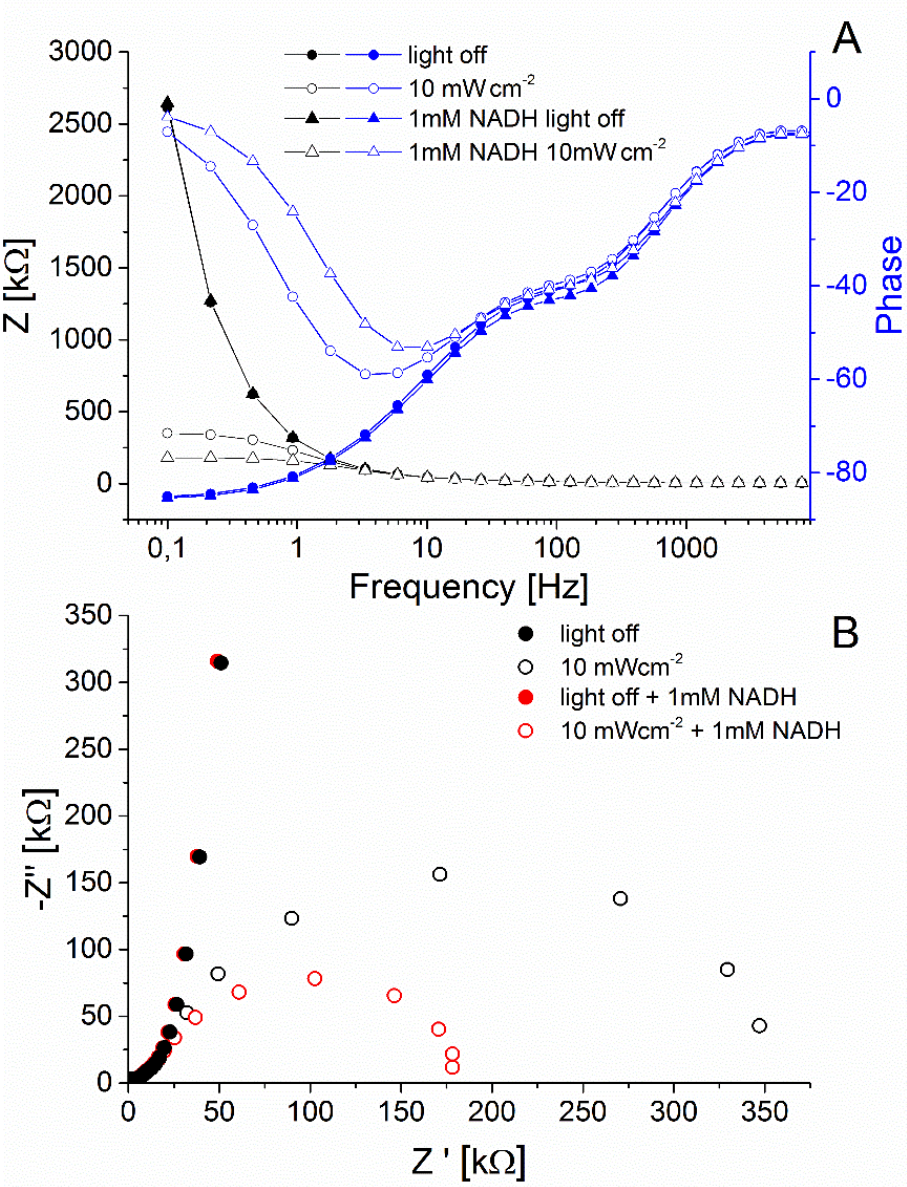

Fig. S9 Bode plot **(A)** and Nyquist plot curves **(B)** of an InGaN/GaN NW electrode in dark or illuminated in the absence and the presence of 1 mM NADH. (100 mM HEPES pH 7; light source **449 nm +/- 5 nm**; 10 mW cm^{-2}; light pulses of 10 s; 0 mV vs. Ag/AgCl, 1 M KCl; AC amplitude 10 mV; frequency range 0.1 Hz – 10 kHz)

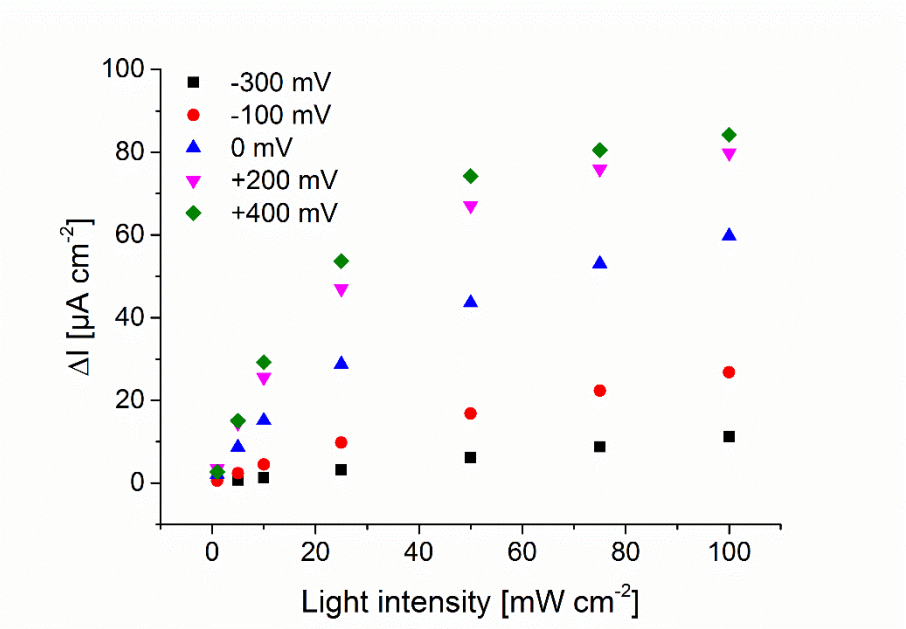

Fig. S10 Photocurrent change ΔI of an **InGaN/GaN nanowire electrode** after addition of 1mM NADH at different light intensities and potentials. (100 mM HEPES pH 7; light source **449 nm +/- 5 nm**; light pulses of 10 s; vs. Ag/AgCl, 1 M KCl)

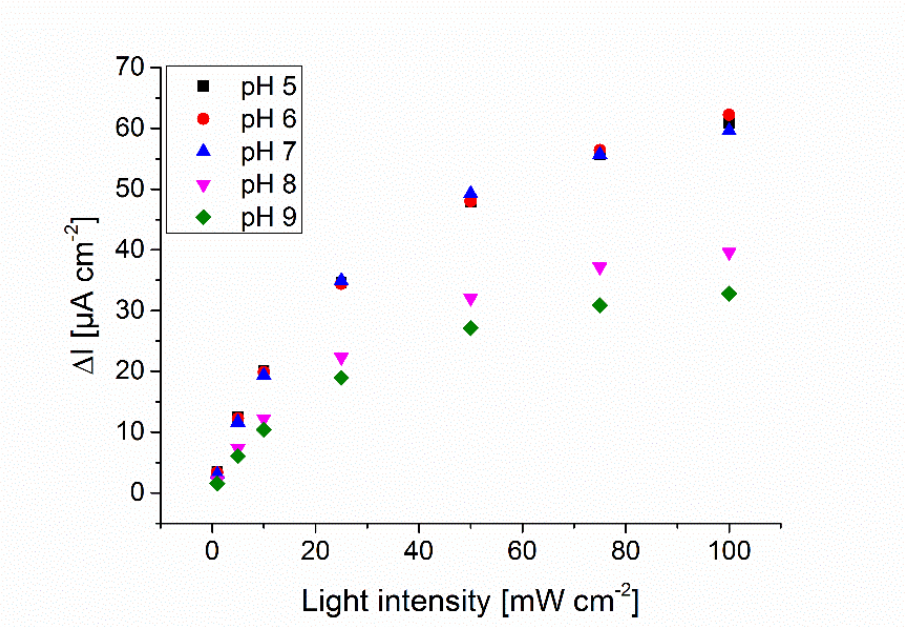

Fig. S11 Photocurrent change ΔI of an **InGaN/GaN nanowire electrode** after addition of 1mM NADH at different light intensities and pH. (100 mM HEPES; light source **449 nm +/- 5 nm**; light pulses of 10 s; 0 mV vs. Ag/AgCl, 1 M KCl)

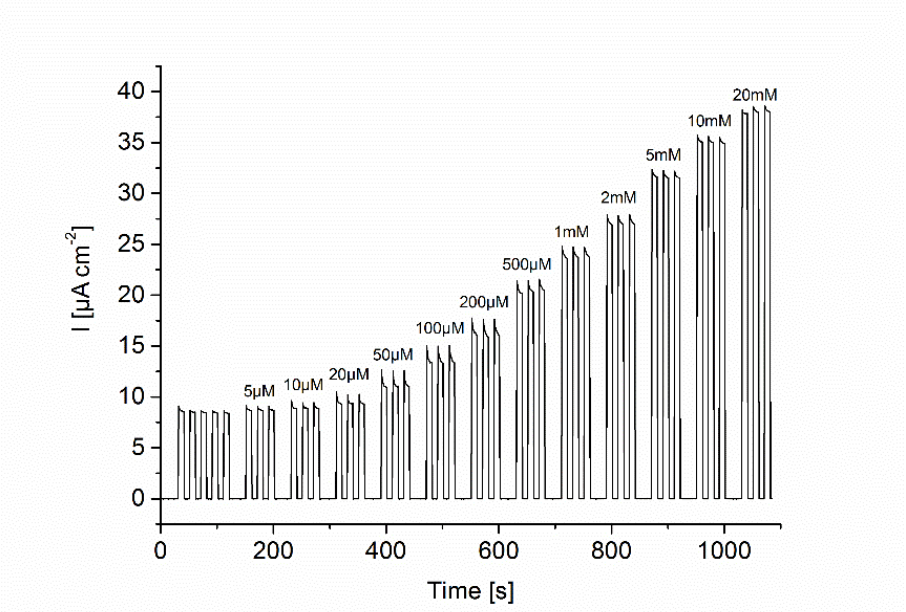

Fig. S12 Photocurrent measurement of an **InGaN/GaN nanowire electrode** and successive addition of NADH. (100 mM HEPES pH 7; light source **449 nm +/- 5 nm**; 10 mW cm^{-2}; light pulses of 10 s; 0 mV vs. Ag/AgCl, 1 M KCl)

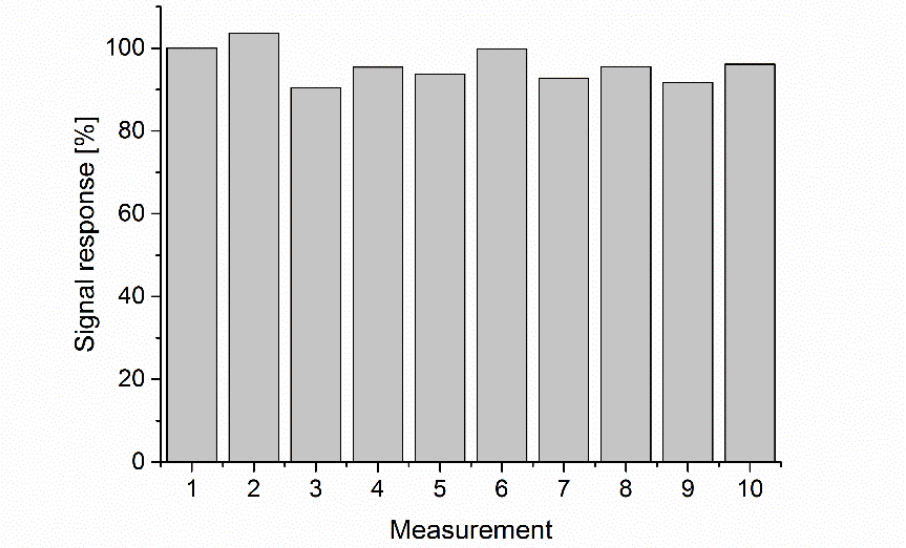

Fig. S13 Normalized photocurrent response of an **InGaN/GaN nanowire electrode** for 10 repetitive measurements of 200 µM NADH. All values are normalized to the signal response obtained for the first measurement. (100 mM HEPES pH 7; light source **449 nm +/- 5 nm**; 10 mW cm^{-2}; light pulses of 10 s; 0 mV vs. Ag/AgCl, 1 M KCl)

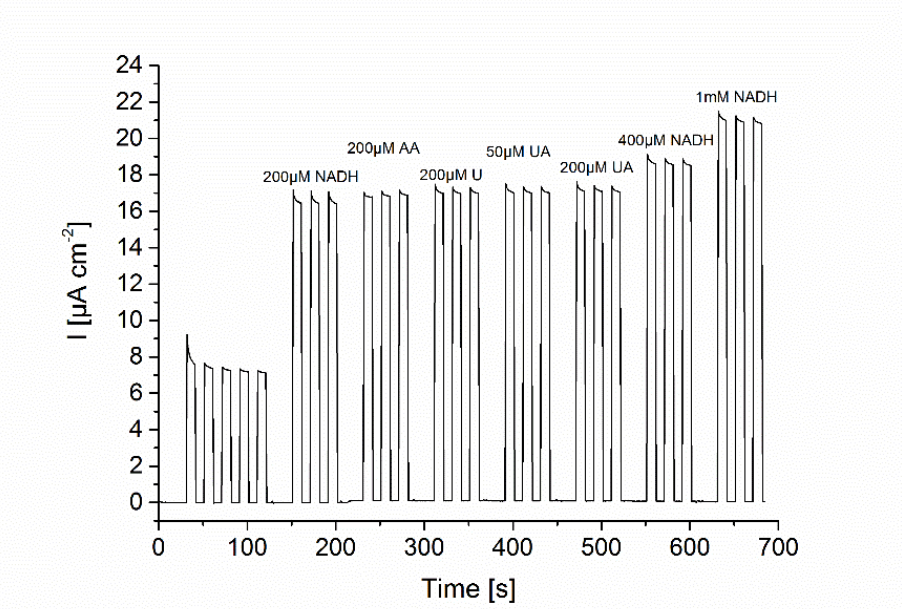

Fig. S14 Photocurrent measurement of an **InGaN/GaN nanowire electrode** after addition of 200 µM NADH and in the presence of potential interfering molecules such as ascorbic acid (AA), urea (U) and uric acid (UA). (100 mM HEPES pH 7; light source **449 nm +/- 5 nm**; 10 mW cm^{-2}; light pulses of 10 s; 0 mV vs. Ag/AgCl, 1 M KCl)

Verification of NAD^+ production during the photoelectrochemical NADH oxidation at the InGaN/GaN NWs

The NAD/NADH-Glo assay from Promega has been used to confirm that NAD^+ is produced during the oxidation of NADH at the illuminated InGaN/GaN NWs. Therefore, photochronoamperometric measurements are carried out in the presence of 100 µM NADH at a potential of 0 mV vs. Ag/AgCl, 1 M KCl under continuous illumination (see Fig. S15A). Samples are removed from the cell during the measurement (5 min, 10 min and 15 min) for the assay. Additionally, a calibration curve with pure NAD^+ solution ranging from 3.125 nM to 100 nM is recorded and control samples (buffer, 100 µM NADH) have been collected. To destroy the excess of NADH acidic thermal treatments of the samples have been performed according to the assay protocol. Afterwards the samples have been analyzed by following the luciferin oxidation (luminescence signal) of the enzymatic assay, which correlates to the concentration of NAD^+ in the sample. As illustrated in Figure S15B raising NAD^+ concentrations have been found with increasing illumination time. In contrast, by continuous illumination of the sample in the absence of the InGaN/GaN NWs no NAD^+ has been detected. This proves that the assay signal can be attributed to the photocatalytic conversion at the illuminated InGaN/GaN NWs.

To check whether the assay correlates with the photoelectrochemical data the NAD^+ concentration has been calculated from the transferred charge during the illumination according to the following equation: $n = Q/(F*z)$; n = amount of substance (mol), Q = transferred charge (As), F = faraday constant (C mol^{-1}), z = transferred electrons per molecule (2 e^-). Here, it has to be mentioned that an accurate calculation of the NADH-dependent charge is difficult, since the basic photocurrent (measured in buffer without

NADH oxidation) cannot be clearly separated from signal based on NADH oxidation. However, for the calculation of Q we assume that the NADH oxidation at the NWs is a cumulative effect; accordingly we have subtracted the basic photocurrent (without NADH) from the signal in the presence of NADH (as schematically depicted by the red line in Figure S15A). The NAD^+ concentration calculated from the charge transfer and from the assay is summarized in Figure S15B. While after 5 min (sample 1) similar results can be obtained for the photoelectrochemical and assay data, after 10 min and 15 min higher NAD^+ concentrations have been determined with the assay. This variation can be attributed to the inaccurate calculated NADH-dependent charge, since a constant basic photocurrent (without NADH) has been assumed for the calcualtion. However, the results show that NAD^+ is the main product of the photoelectrochemical oxidation of NADH at the InGaN/GaN NWs.

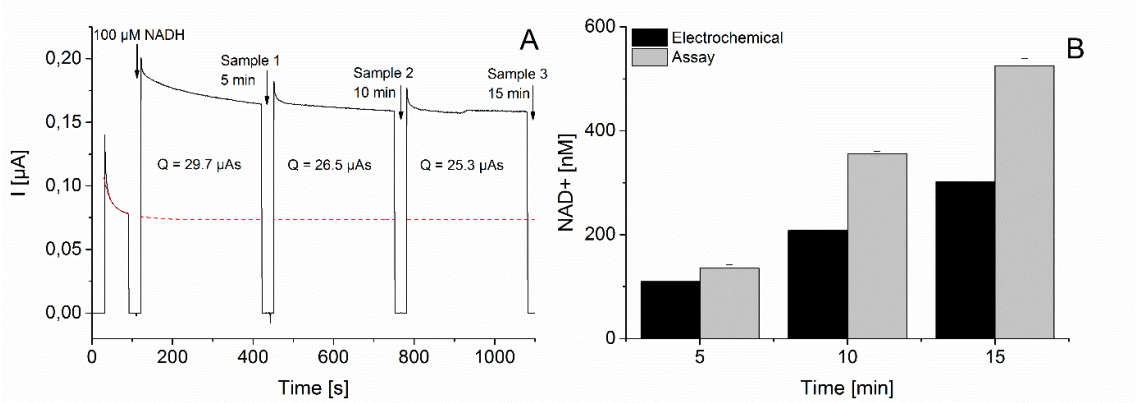

Fig. S15 (A) Photocurrent measurement of an **InGaN/GaN nanowire electrode** before and after addition of 100 µM NADH (100 s). Samples have been removed from the measurement cell for the NAD/NADH-Glo assay from Promega after 5 min, 10 min and 15 min continuous illumination. (100 mM HEPES pH 7; light source **449 nm +/- 5 nm**; 10 mW cm^{-2}; 0 mV vs. Ag/AgCl, 1 M KCl) **(B)** Calculated NAD^+ concentration according to the photoelectrochemical data (charge transfer) and to the NAD/NADH-Glo assay from Promega after 5 min, 10 min and 15 min reaction at the InGaN/GaN NWs under illumination.

Supporting Information: Integration of enzymes in polyaniline-sensitized 3D inverse opal TiO_2 architectures for light-driven biocatalysis and light-to-current conversion

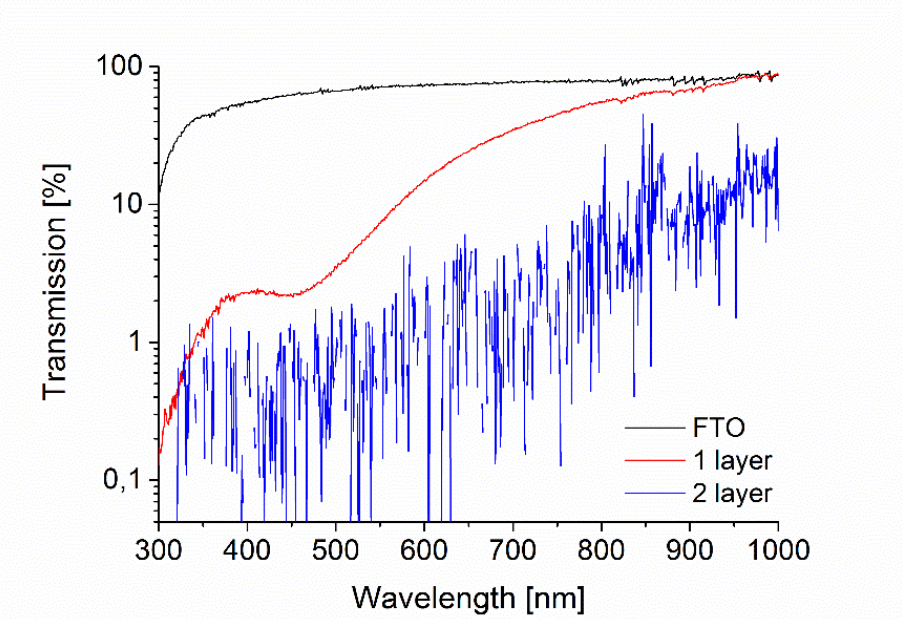

Figure S1 Transmission spectra of FTO electrodes before and after deposition of 1 and 2 sintered layers of IO-TiO_2 structures.

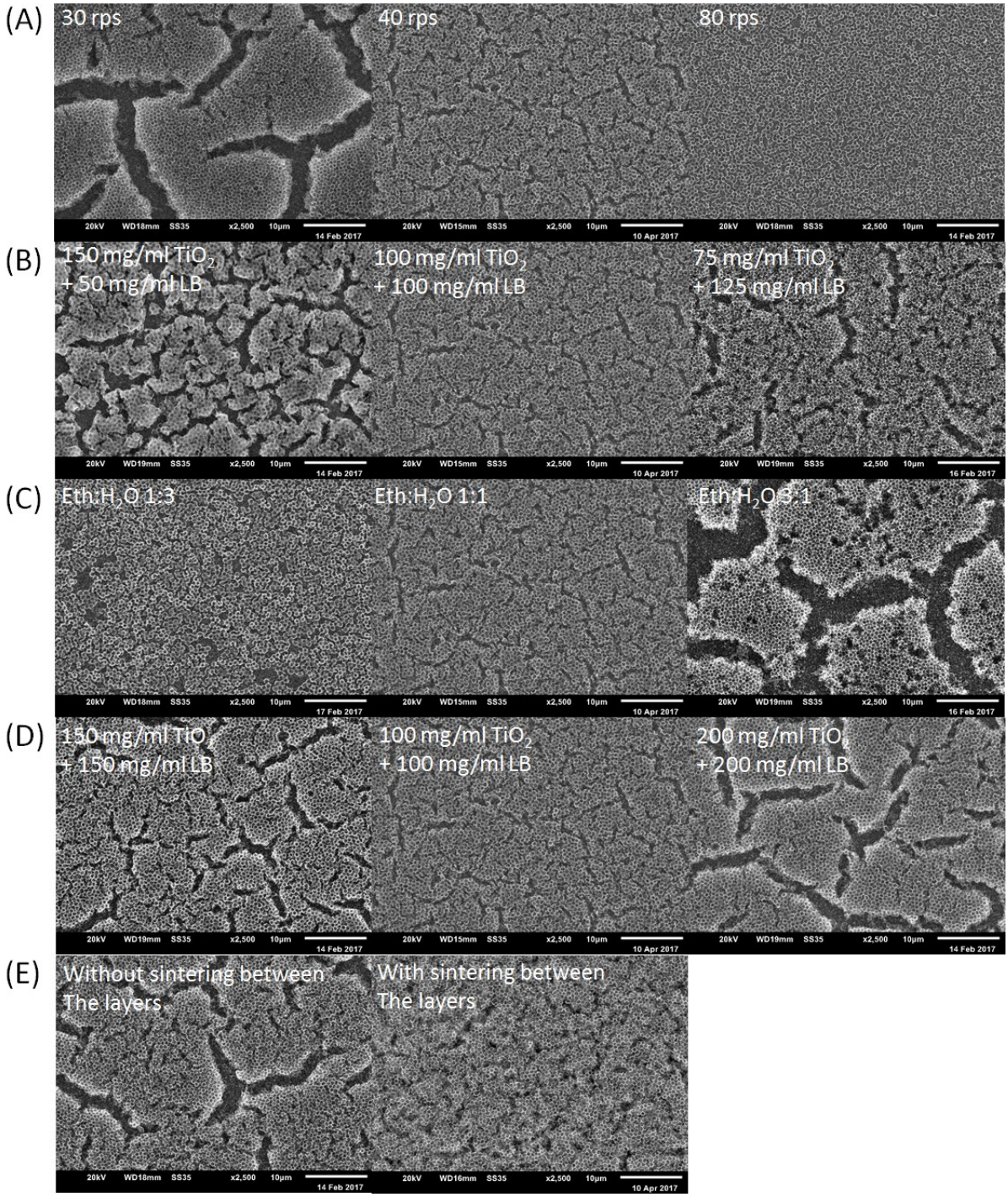

Figure S2 SEM images of differently prepared IO-TiO_2 electrodes. Influence of the rotating speed during spin coating (**A**; 100 mg/ml TiO_2 + 100mg/ml LB; Eth:H_2O 1:1), of the ratio of the TiO_2 nanoparticle/ latex beads mixture (**B**; Eth:H_2O 1:1; 40 rps), the solvent (**C**; 100 mg/ml TiO_2 + 100mg/ml LB; 40 rps), the amount of the TiO_2 nanoparticle/ latex beads mixture (**D**; Eth:H_2O 1:1; 40 rps) for 1 layered IO-TiO_2 electrodes. **(E)** Preparation of 3 layered IO-TiO_2 electrodes with and without a sintering step between the deposited layers (100 mg/ml TiO_2 + 100mg/ml LB; Eth:H_2O 1:1; 40 rps). All experiments have been performed with a 2500x magnification by applying an acceleration voltage of 20 kV.

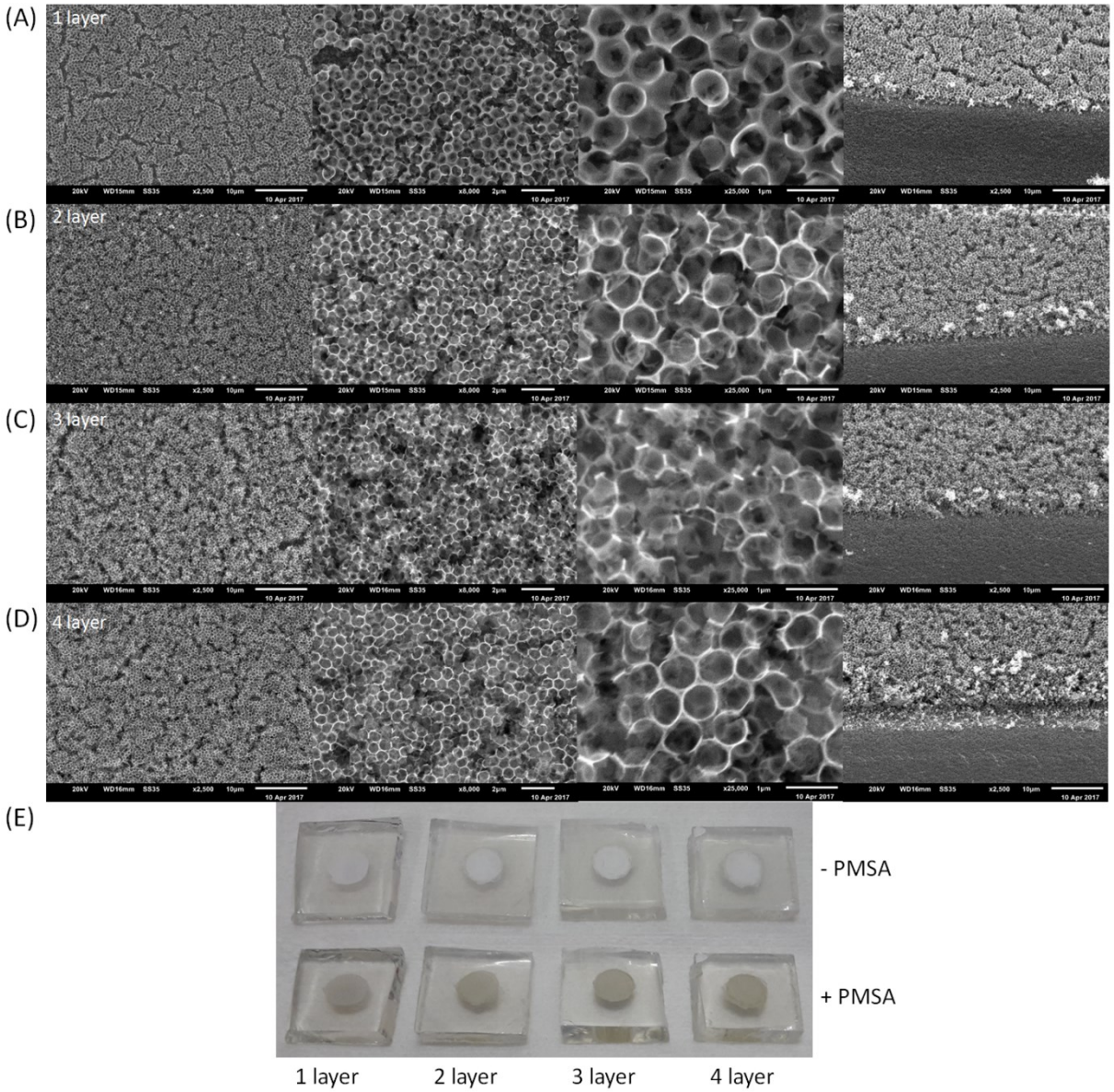

Figure S3 SEM images of 1 layer **(A)**, 2 layer **(B)**, 3 layer **(C)** and 4 layer **(D)** IO-TiO_2 electrodes for 2500x, 8000x and 25000x magnification recorded from the top and under an angle of 45° with a 2500x magnification by applying an acceleration voltage of 20 kV (from left to right). **(E)** Photographic image of the prepared IO-TiO_2 electrodes with different number of layers before and after incubation with 2 mg ml^{-1} PMSA1 in 5 mM MES + 5 mM $CaCl_2$ for 1 h. The successful polymer assembly can be seen by a coloration of the IO-TiO_2 electrodes from white to green.

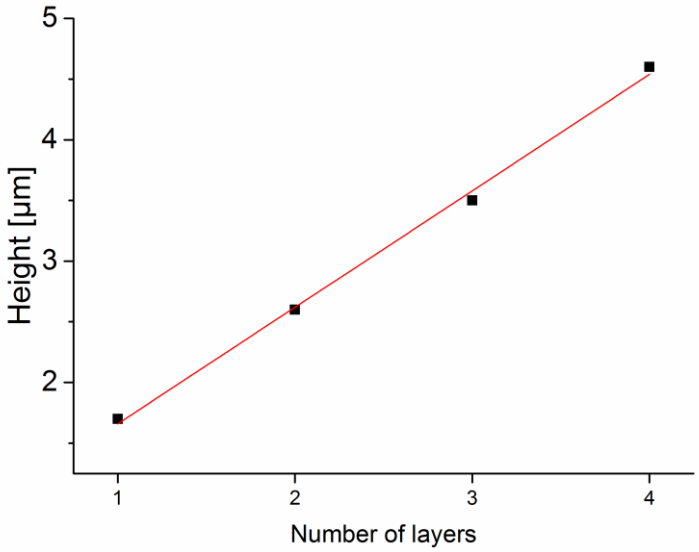

Figure S4 Height of the IO-TiO_2 electrodes with increasing number of layers. The values are obtained from the SEM measurements at an angle of 45°.

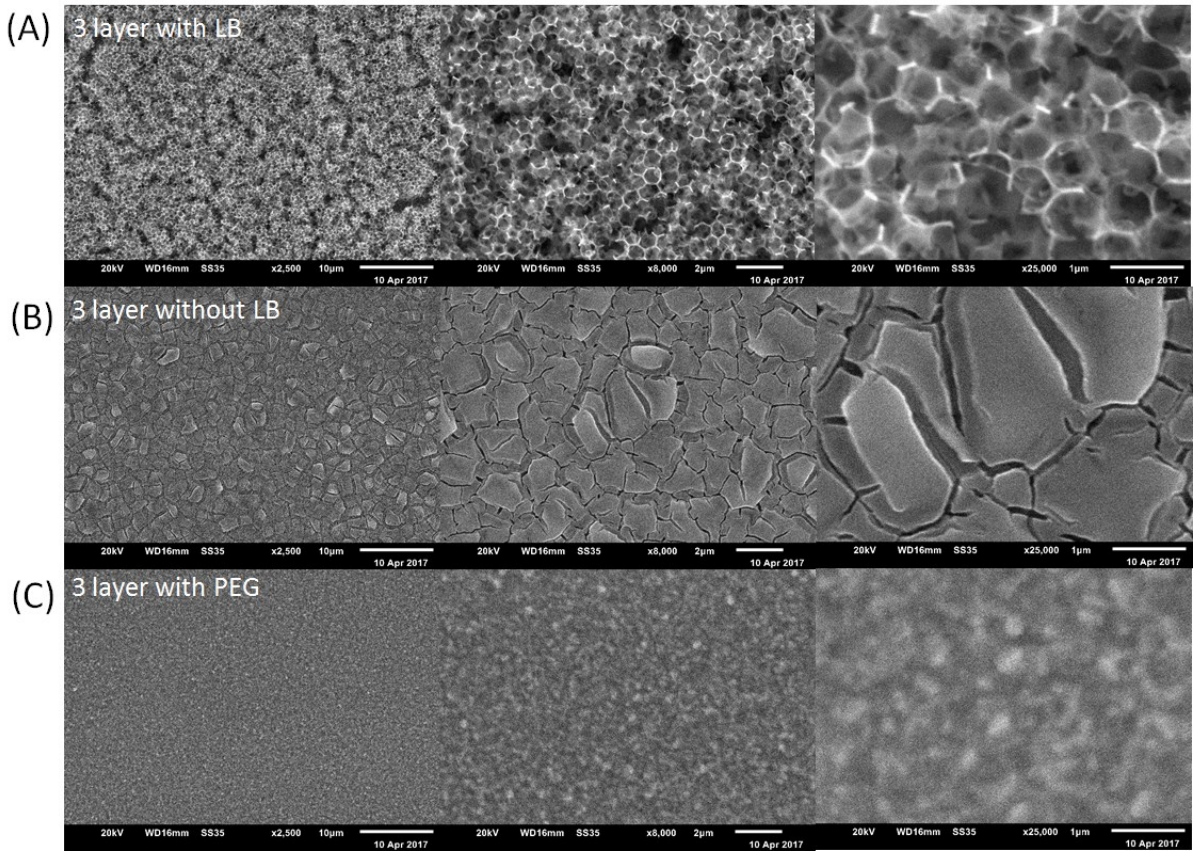

Figure S5 SEM images of 3 layered TiO_2 electrodes prepared with latex beads (LB, **A**), without LB **(B)** and with polyethylene glycol (PEG, **C**) for 2500x, 8000x and 25000x magnification recorded from the top by applying an acceleration voltage of 20 kV (from left to right).

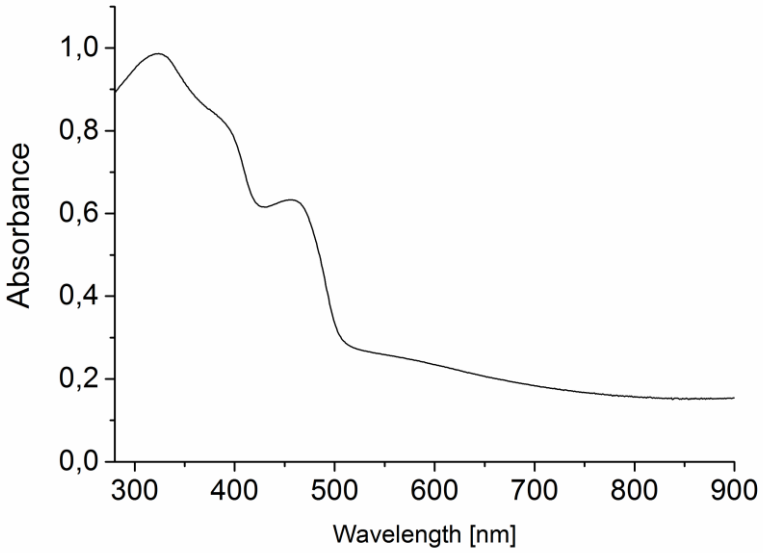

Figure S6 UV/VIS spectra of 50 µg ml^{-1} PMSA1 in 5 mM MES + 5 mM $CaCl_2$ pH 6.5.

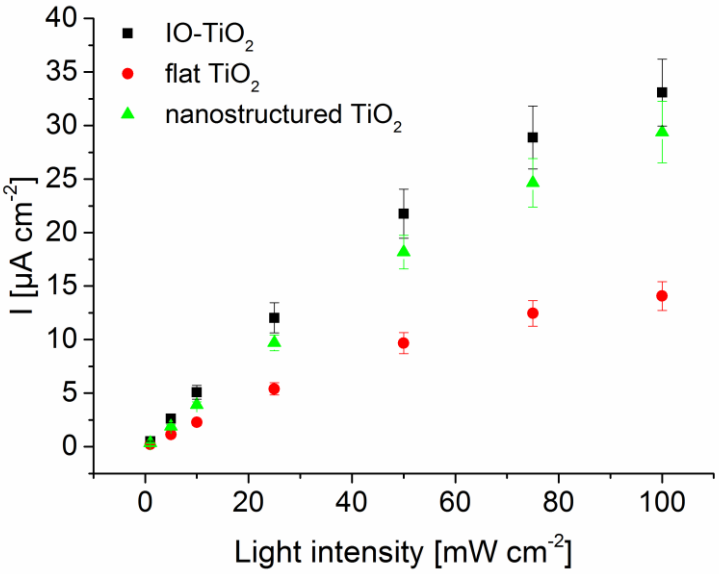

Figure S7 Photocurrent density response of 3 layered PMSA1-sensitized IO-TiO_2, flat TiO_2 (prepared without latex beads) and PEG-TiO_2 electrodes (prepared with PEG instead of LB) at different light intensities in buffer solution (without additional electron donor). (2 mg ml^{-1} PMSA1 in 5mM MES + 5 mM $CaCl_2$ pH 6.5 for 1 h; white light source; 0 mV vs. Ag/AgCl, 1 M KCl; 5 mM MES + 5 mM $CaCl_2$ pH 6.5)

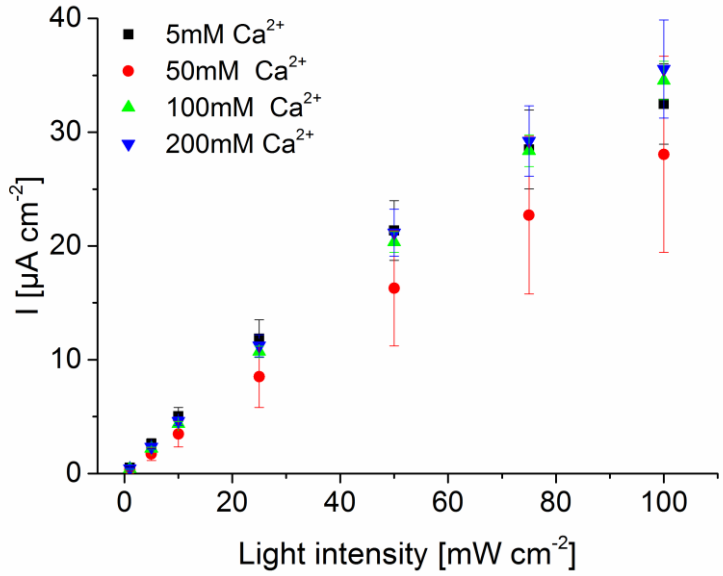

Figure S8 Photocurrent density response of 3 layered IO-TiO_2 after immobilization of 2 mg ml^{-1} PMSA1 under different Ca^{2+} concentrations at different light intensities in buffer solution (without additional electron donor). (2 mg ml^{-1} PMSA1 in 5mM MES + X mM $CaCl_2$ pH 6,5 for 1 h; white light source; 0 mV vs. Ag/AgCl, 1 M KCl; 5 mM MES + 5 mM $CaCl_2$ pH 6.5)

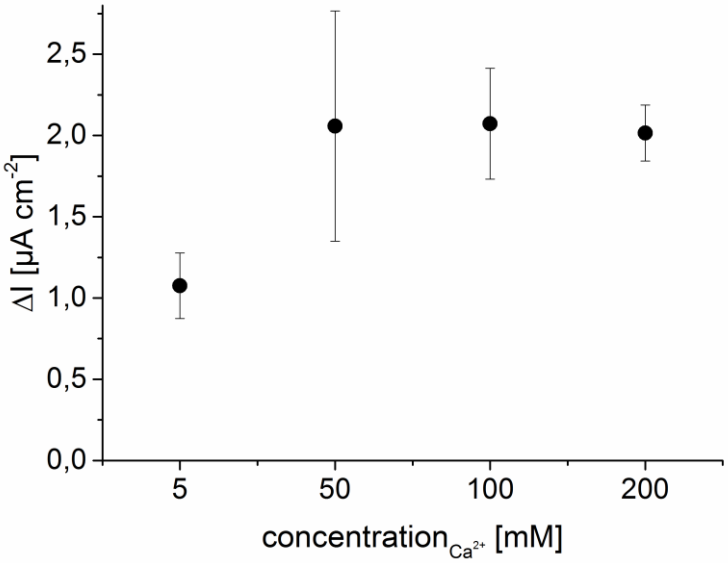

Figure S9 Photocurrent density change ΔI after addition of 10 mM glucose for 3 layered IO-TiO_2|PMSA1|PQQ-GDH electrodes prepared under different Ca^{2+} concentrations. (2 mg ml^{-1} PMSA1 in 5mM MES + X mM $CaCl_2$ pH 6,5 for 1 h; 2 mg ml^{-1} PQQ-GDH in 5 mM MES + 5 mM $CaCl_2$ pH 6.5 for 1 h; white light source; 10 mW cm^{-2}; 0 mV vs. Ag/AgCl, 1 M KCl; 5 mM MES + 5 mM $CaCl_2$ pH 6.5)

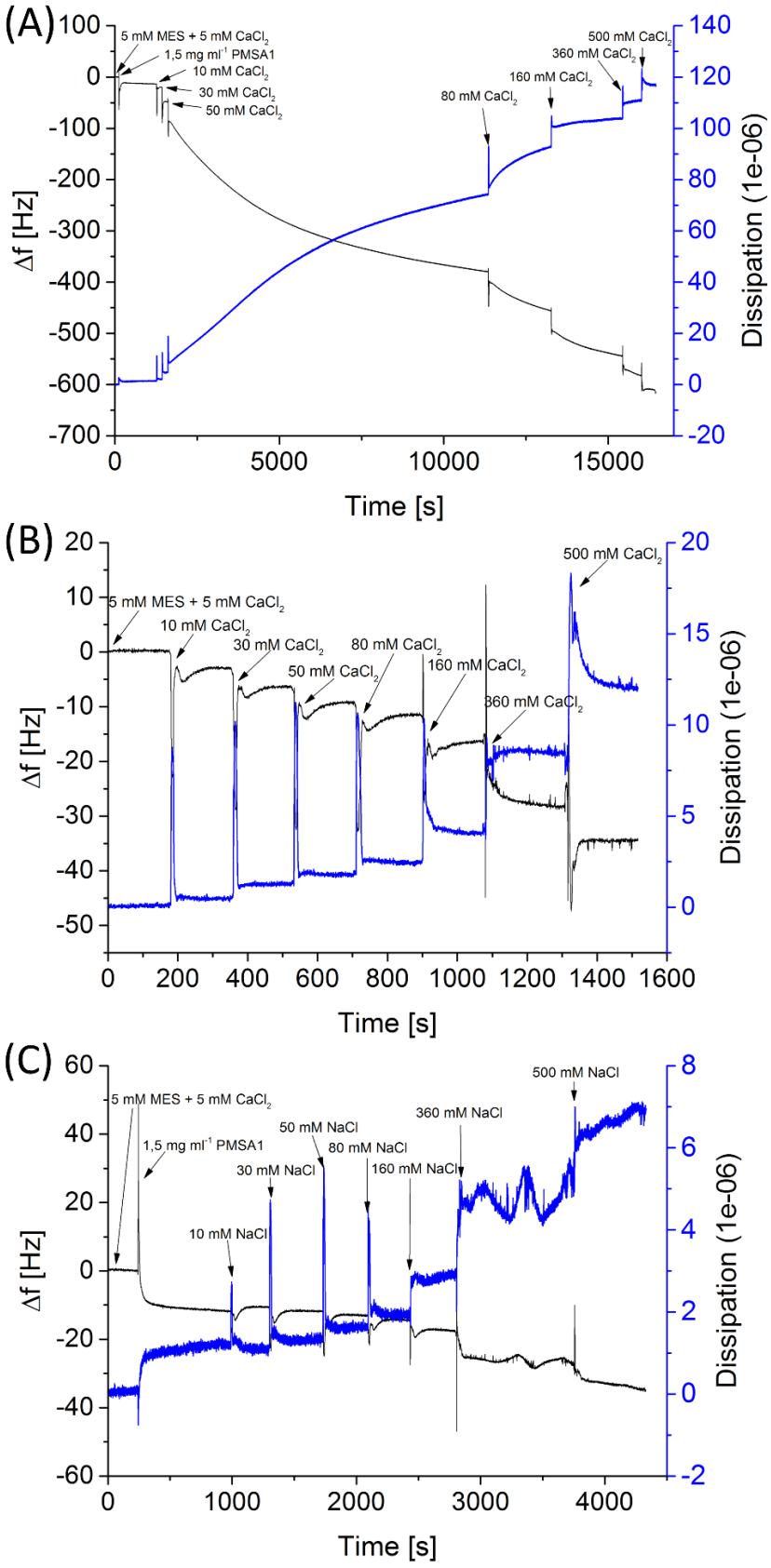

Figure S10 QCM measurement of the PMSA1 assembly on a gold chip in dependence of the cation concentration. All measurements have been performed in 5 mM MES + 5 mM $CaCl_2$ as starting buffer in the presence **(A,C)** and absence of 1.5 mg ml^{-1} PMSA1 **(B)** by successively increasing the $CaCl_2$ **(A, B)** or NaCl **(C)** concentration. The experiments have been performed in a batch cell.

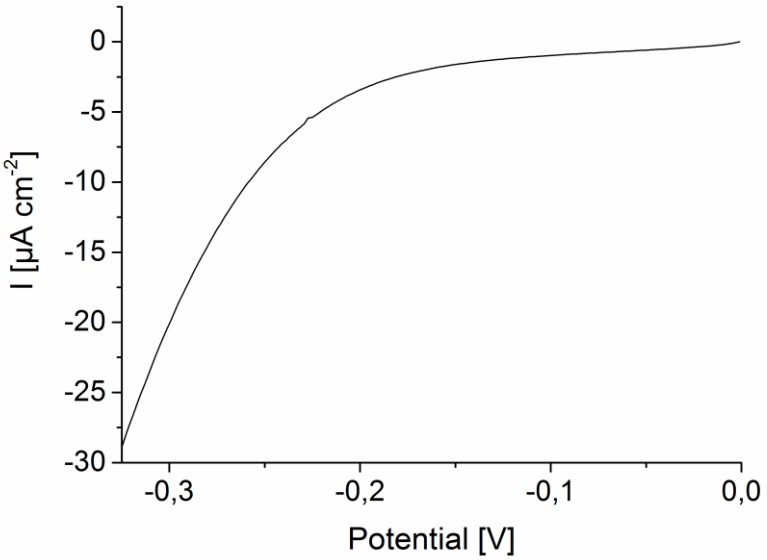

Figure S11 Current density of 3 layered IO-TiO_2|PMSA1|PQQ-GDH electrodes in dependence on the applied potential in the presence of 10 mM glucose and in the dark. (5 mV s^{-1}; potential vs. Ag/AgCl, 1 M KCl; 5 mM MES + 5 mM $CaCl_2$ pH 6.5)

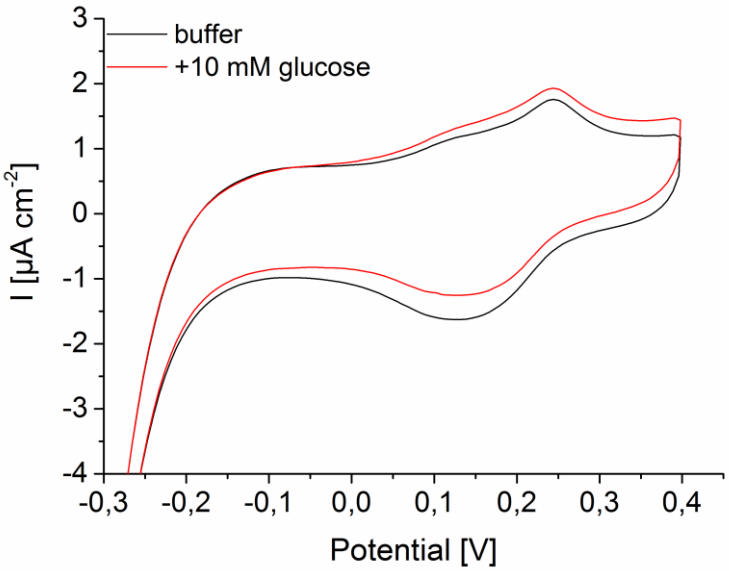

Figure S12 Cyclic voltammetry of a PMSA1 and PQQ-GDH modified FTO electrode in the absence (black curve) and presence of 10 mM glucose (red curve). (2 mg ml^{-1} PMSA1 in 5mM MES + 5 mM $CaCl_2$ pH 6.5 for 1 h; 2 mg ml^{-1} PQQ-GDH in 5mM MES + 5 mM $CaCl_2$ pH 6.5 for 1 h; potential vs. Ag/AgCl, 1 M KCl from -0.3 V to + 0.4 V; 10 mV s^{-1}; 5 mM MES + 5 mM $CaCl_2$ pH 6.5)

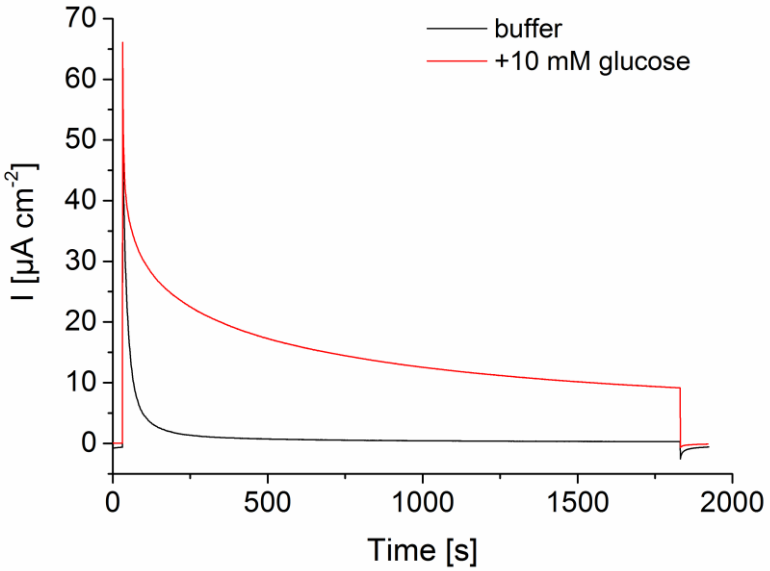

Figure S13 Photochronoamperometric measurement of a 3 layered PMSA1-sensitized IO-TiO_2 electrode with immobilized PQQ-GDH under continuous illumination over 30 min (100 mW cm^{-2}) with and without 10 mM glucose. (2 mg ml^{-1} PMSA1 in 5mM MES + 100 mM $CaCl_2$ pH 6,5 for 1 h; 2 mg ml^{-1} PQQ-GDH in 5mM MES + 5 mM $CaCl_2$ pH 6,5 for 1 h; white light source; 100 mW cm^{-2}; -100 mV vs. Ag/AgCl, 1 M KCl; 5 mM MES + 5 mM $CaCl_2$ pH 6.5)

Photocurrent measurement without glucose conversion (absence of enzyme substrate): After 30 min illumination of the 3 layered PMSA1-sensitized IO-TiO_2 electrode in buffer the photocurrent shows a strong decline, which suggests that the polymer is almost completely oxidized. The transferred charge is about 3.3 mC cm^{-2}, which corresponds to $2.06*10^{16}$ e^- cm^{-2}. The surface concentration of PMSA1 is determined to be around 8 µg cm^{-2}. This corresponds to an aniline surface concentration of 39.34 nmol cm^{-2} by using an average M_w of 203.33 g mol^{-1} per monomer. According to this, the amount of aniline molecules is $2.37*10^{16}$ aniline per cm^{-2}. It is found that this monomer amount correlates to the transferred charge during the photoelectrochemical measurement ($2.06*10^{16}$ e^- cm^{-2}). This may indicate that PMSA1 acts as an electron reservoir for the photoelectrochemical process in the absence of glucose. In the presence of glucose a much higher charge can pass the electrode (27.3 mC cm^{-2}) and the photocurrent is by far not so strongly declining. This underlines the importance of the sugar oxidation process for the supply of electrons for the photoelectrochemical process of the biohybrid system.

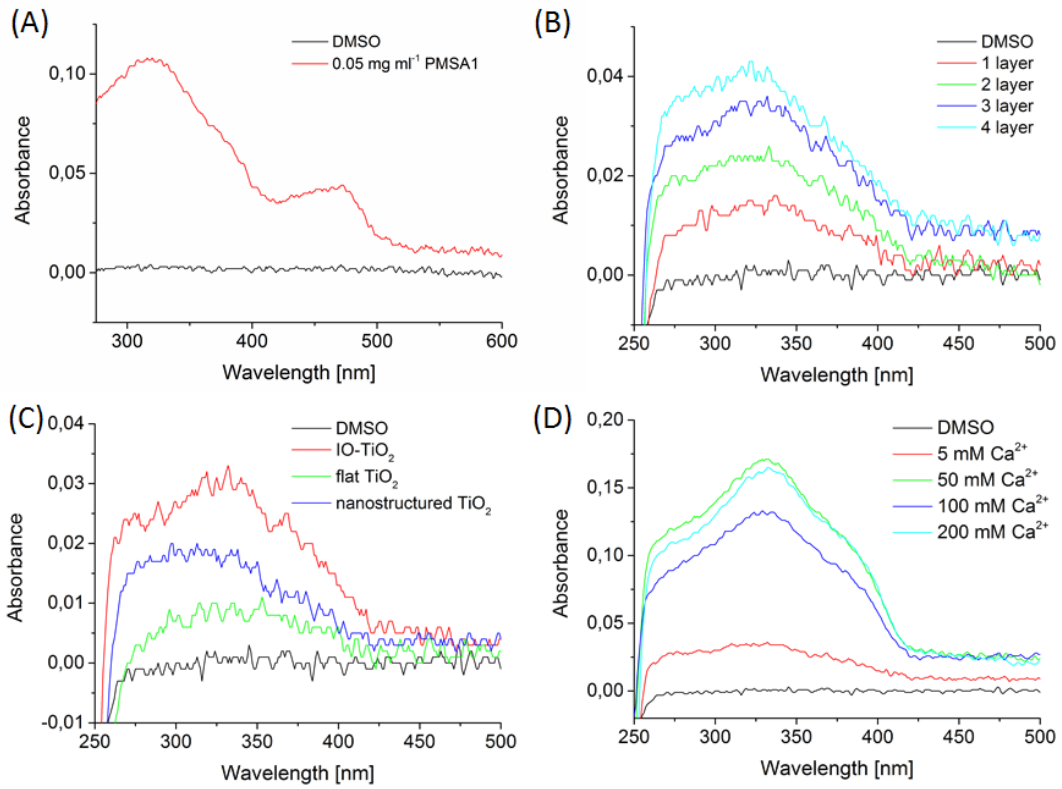

Figure S14 (A) UV/VIS spectra of 0.05mg ml^{-1} PMSA1 dissolved in DMSO. **(B)** UV/VIS spectra of PMSA1 after extraction from IO-TiO_2 electrodes with DMSO for different numbers of layers. For the immobilization of the polymer onto the IO-TiO_2 electrodes a concentration of 2 mg ml^{-1} in 5 mM MES + 5 mM $CaCl_2$ has been used. **(C)** UV/VIS spectra of PMSA1 after extraction from 3 layered IO-TiO_2 electrodes (red curve), 3 layered flat TiO_2 electrodes prepared without latex beads (green curve) and 3 layered TiO_2 electrodes prepared with PEG instead of latex beads (blue curve). For the immobilization of the polymer onto the TiO_2 electrodes a concentration of 2 mg ml^{-1} in 5 mM MES + 5 mM $CaCl_2$ has been used. **(D)** UV/VIS spectra of PMSA1 after extraction from 3 layered IO-TiO_2 electrodes for different Ca^{2+} concentrations used during immobilization of 2mg ml^{-1} PMSA1.

Supporting Information: Light as Trigger for Biocatalysis: Photonic Wiring of Flavin Adenine Dinucleotide-Dependent Glucose Dehydrogenase to Quantum Dot-Sensitized Inverse Opal TiO2 Architectures via Redox Polymers

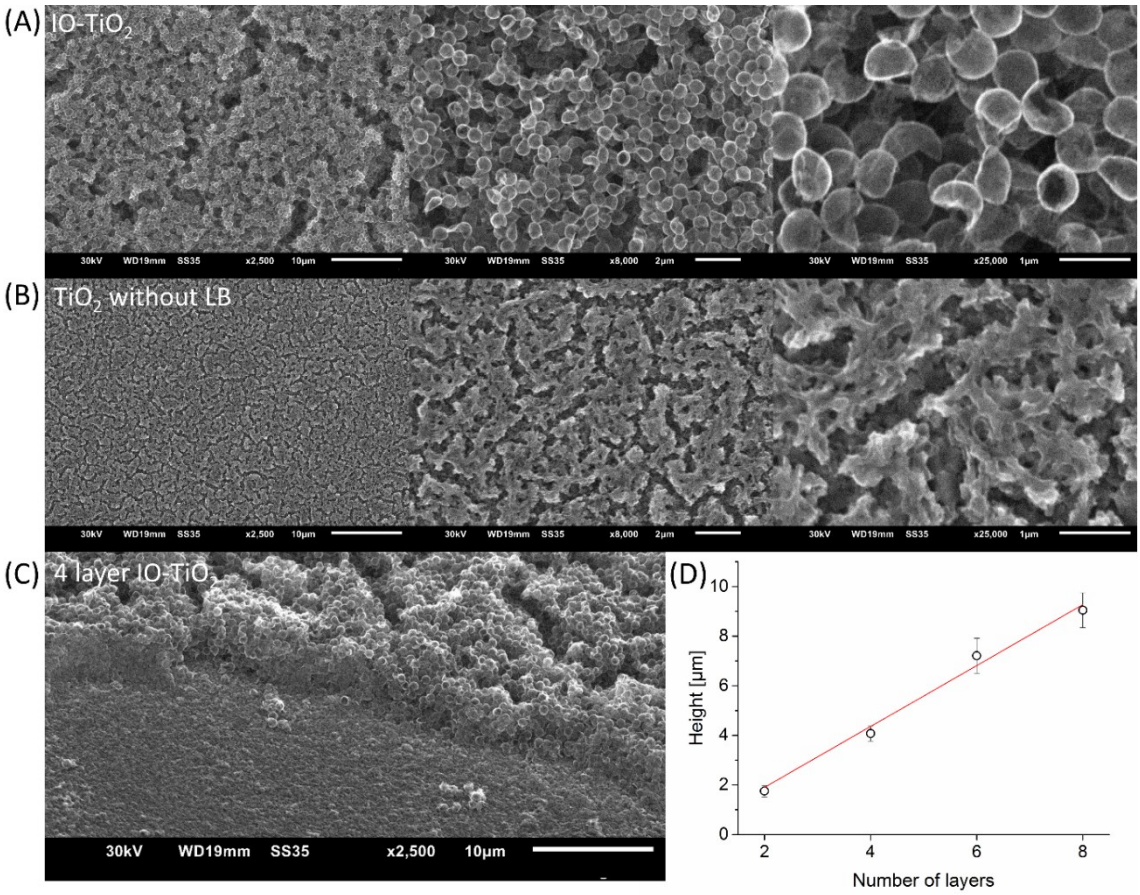

Figure S1 (A) SEM images of 4 layered IO-TiO_2 electrodes and **(B)** 4 layered TiO_2 electrodes prepared without latex beads for 2500-fold, 8000-fold and 25000-fold magnification recorded from the top by applying an acceleration voltage of 30 kV (from left to right). **(C)** SEM images of a 4 layered IO-TiO_2 electrode under an angle of 45° with a 2500-fold magnification by applying an acceleration voltage of 30 kV. **(D)** Height of IO-TiO_2 electrodes for different number of layers. The values are obtained from the SEM experiments at an angle of 45°.

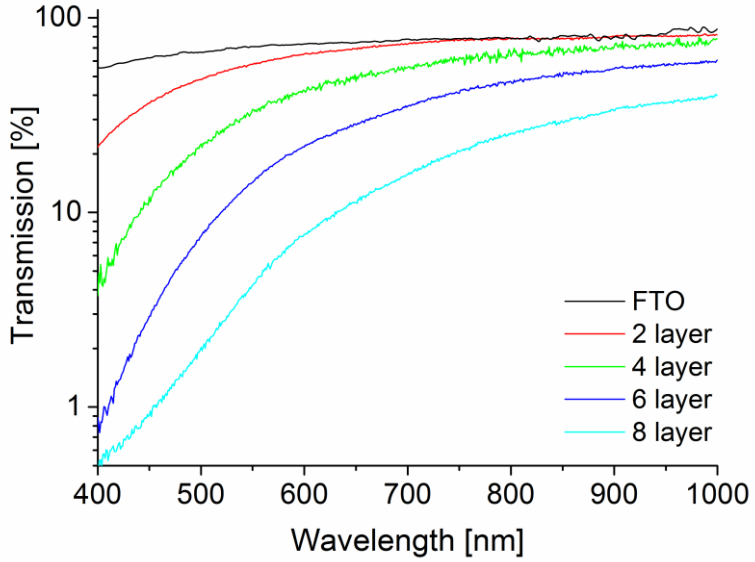

Figure S2 Transmission spectra of FTO electrodes before and after deposition of different number of layers of IO-TiO_2 structures in ethanol.

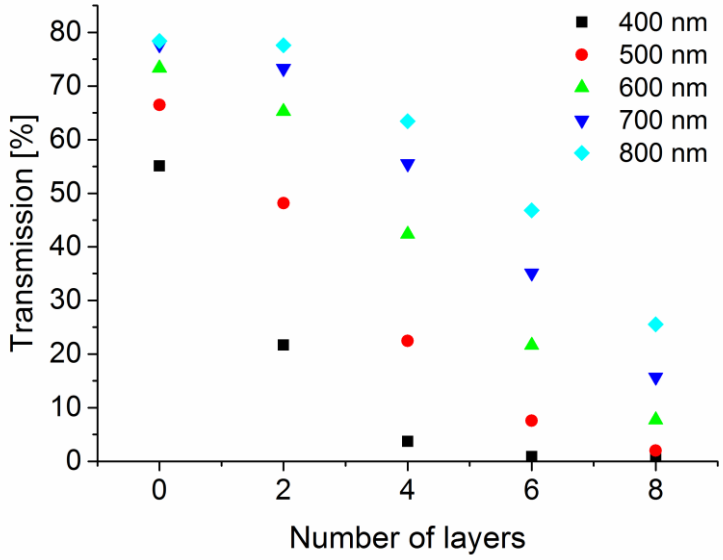

Figure S3 Transmission of FTO electrodes before and after deposition of different number of layers of IO-TiO_2 structures at different wavelengths in ethanol.

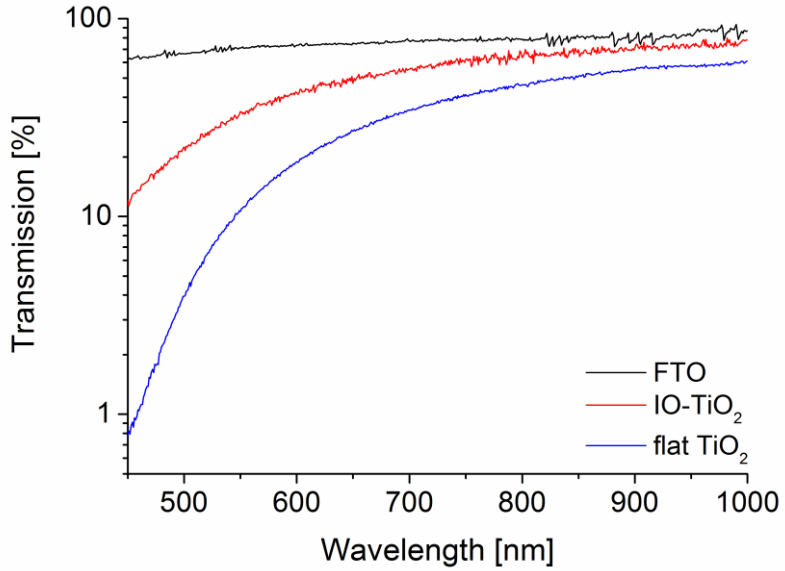

Figure S4 Transmission spectra of 4 layered flat TiO_2 (prepared without latex beads) and IO-TiO_2 structures in ethanol.

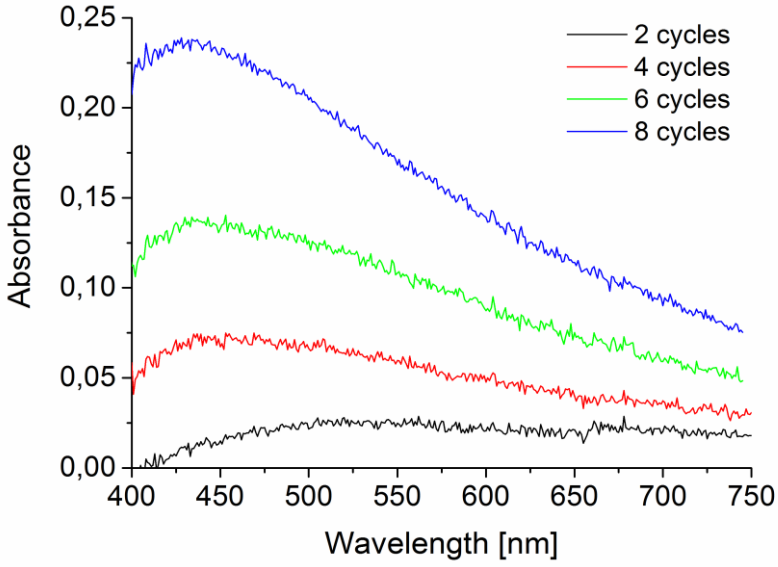

Figure S5 Absorbance spectra of 4 layered IO-TiO_2 structures after deposition of PbS QDs for different number of SILAR cycles in ethanol. The different plotted spectra are obtained by subtracting the UV/VIS absorption spectra of IO-TiO_2 electrodes without QDs from the spectra of electrodes with QDs.

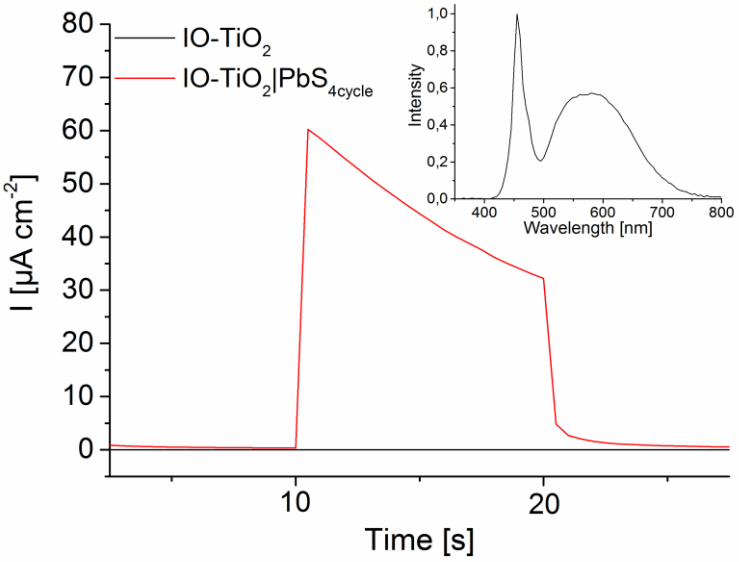

Figure S6 Photochronoamperometric measurement of a 4 layered IO-TiO_2 electrode before (black curve) and after deposition of PbS QDs (4 SILAR cycle, red curve) in the absence of electron donors. The inset displays the light intensity spectrum of the used white light source (which was switched on from 10 s to 20 s), demonstrating that no UV light is used during illumination (white light source; 50 mW cm^{-2}; 0 mV vs. Ag/AgCl, 1 M KCl; 5 mM HEPES pH 7).

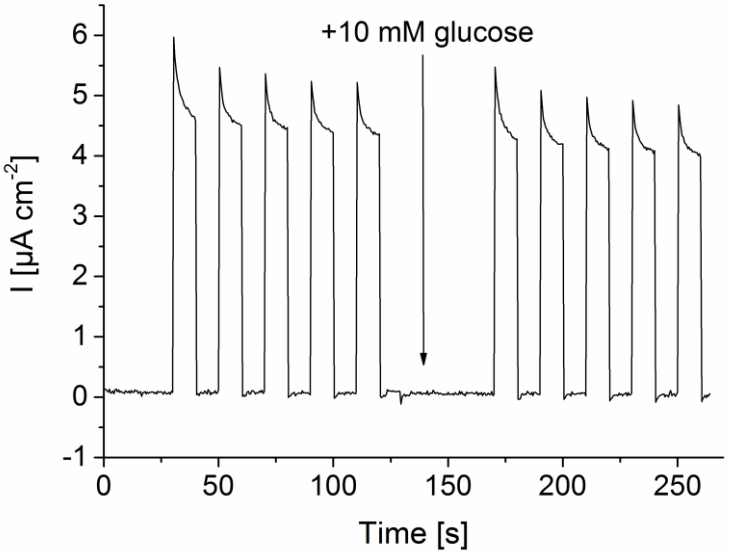

Figure S7 Photochronoamperometric measurement of a 4 layered IO-TiO_2|PbS_{4cycle}|P_{Os} electrode without FAD-GDH before and after addition of 10 mM glucose (chopped white light source; 10 mW cm^{-2}; 0 mV vs. Ag/AgCl, 1 M KCl; 5 mM HEPES pH 7).

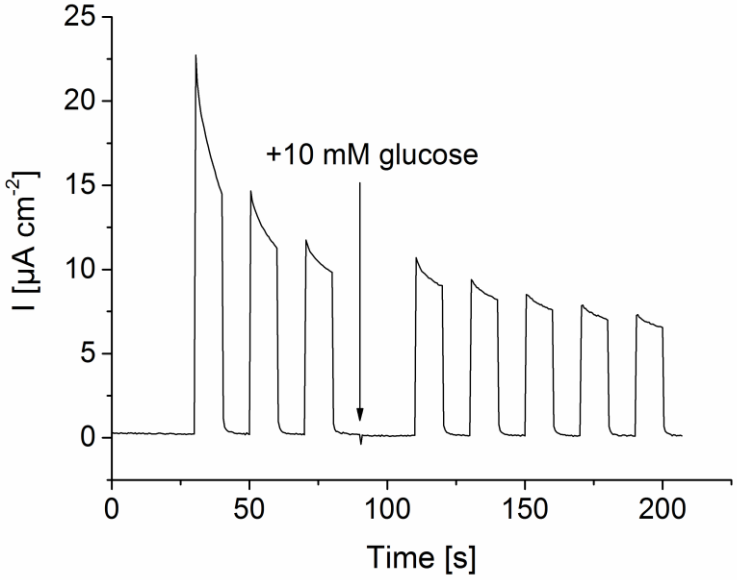

Figure S8 Photochronoamperometric measurement of a 4 layered IO-TiO_2|PbS_{4cycle}|FAD-GDH electrode without P_{Os} before and after addition of 10 mM glucose. Therefore, 4 µl of 5 mg ml^{-1} FAD-GDH in 5 mM HEPES pH 7 has been drop-casted onto the electrode and incubated for 15 min in the dark (chopped white light source; 10 mW cm^{-2}; 0 mV vs. Ag/AgCl, 1 M KCl; 5 mM HEPES pH 7).

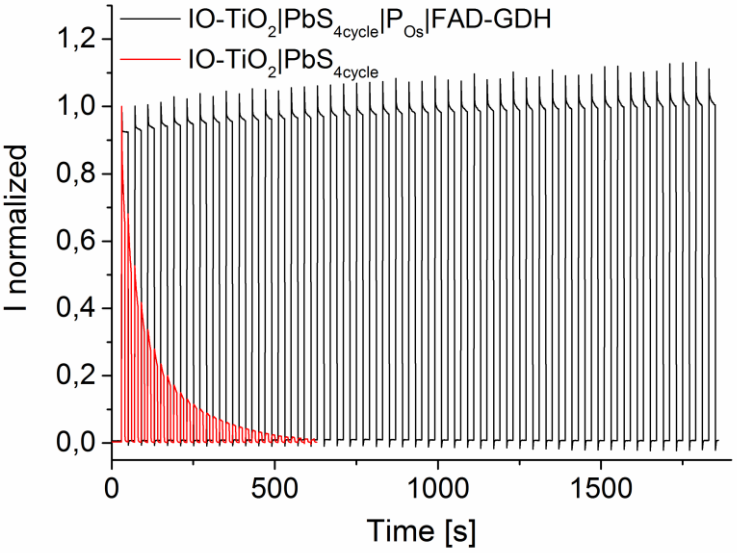

Figure S9 Photochronoamperometric measurement of a 4 layered IO-TiO_2|PbS_{4cycle}|P_{Os}|FAD-GDH electrode and an IO-TiO_2|PbS_{4cycle} electrode under illumination in pulse mode over 30 min in the presence of 10 mM glucose. The photocurrent has been normalized to the first light pulse (chopped white light source; 10 mW cm^{-2}; pulse time 20s; 0 mV vs. Ag/AgCl, 1 M KCl; 5 mM HEPES pH 7).

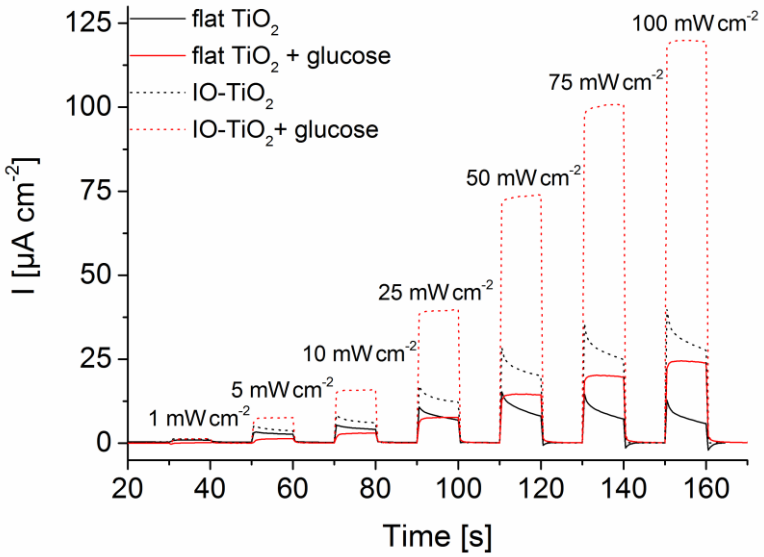

Figure S10 Photochronoamperometric measurement of a 4 layered IO-TiO_2|PbS_{4cycle}|P_{Os}|FAD-GDH and a flat TiO_2|PbS_{4cycle}|P_{Os}|FAD-GDH electrode (prepared without latex beads) at different light intensities in the absence and presence of 10 mM glucose (chopped white light source; 0 mV vs. Ag/AgCl, 1 M KCl; 5 mM HEPES pH 7).

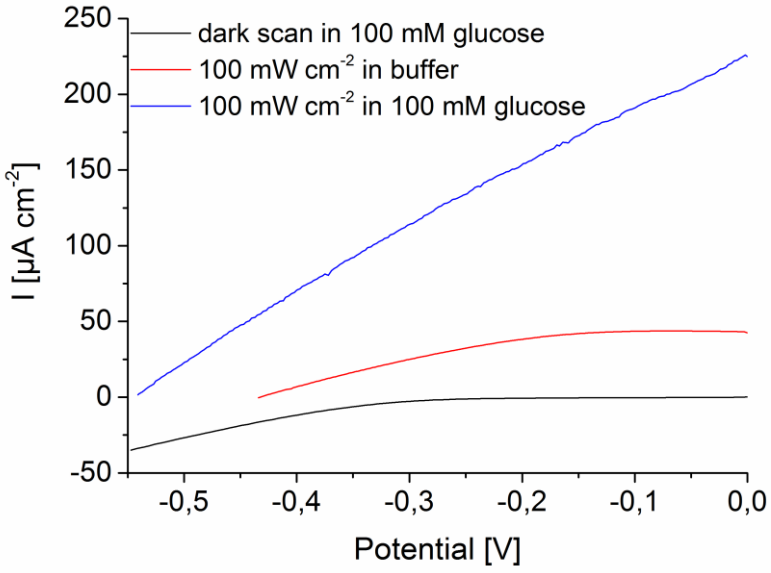

Figure S11 Current density of an 8 layered IO-TiO_2|PbS_{4cycle}|P_{Os}|FAD-GDH electrode in dependence of the applied potential in the dark with 100 mM glucose (black curve) or under continuous illumination with 100 mW cm^{-2} in the absence (red curve) and presence of 100 mM glucose (blue curve) (white light source; 100 mW cm^{-2}; potential vs. Ag/AgCl, 1 M KCl; 5 mM HEPES pH 7).

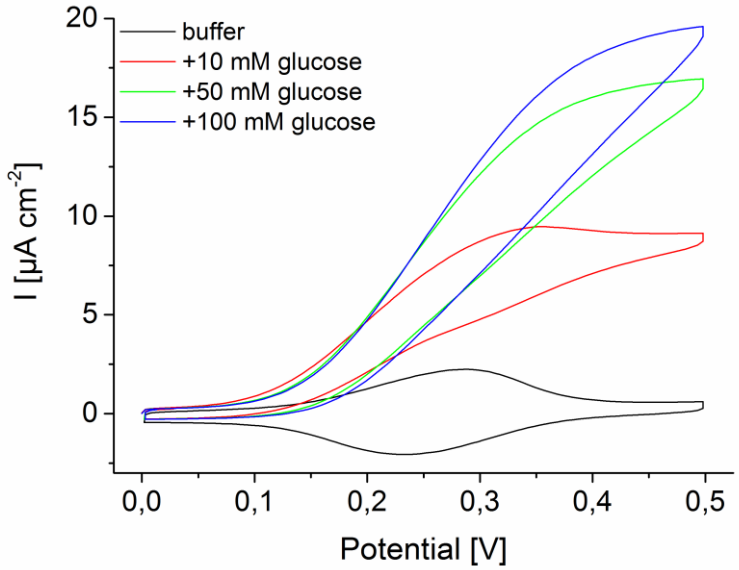

Figure S12 Cyclic voltammetry of a P_{Os} and FAD-GDH modified FTO electrode in the absence and presence of different glucose concentrations in the dark (potential vs. Ag/AgCl, 1 M KCl; from 0 V to +0.5 V; 5 mV s^{-1}; 5 mM HEPES pH 7).

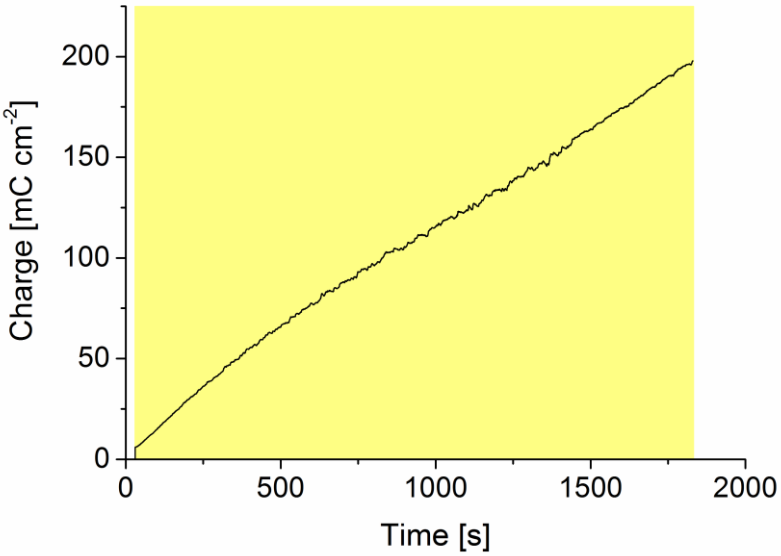

Figure S13 Charge passed through an 8 layered IO-TiO_2|PbS_{4cycle}|P_{Os}|FAD-GDH electrode under illumination over 30 min in the presence of 100 mM glucose (white light source; 100 mW cm^{-2}; 0 mV vs. Ag/AgCl, 1 M KCl; 5 mM HEPES pH 7).

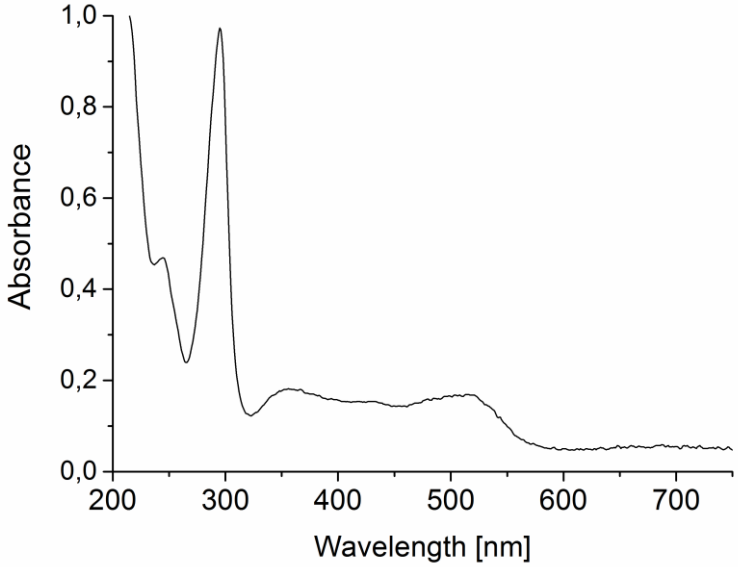

Figure S14 Absorbance spectrum of the redox polymer P_{Os} in 5 mM HEPES pH 7.

Danksagung

Ich möchte an dieser Stelle die Möglichkeit ergreifen, mich bei einigen Personen zu bedanken, welche mich während meiner Doktorarbeit unterstützt haben.

- Prof. Fred Lisdat gilt mein besonderer Dank für die kompetente Unterstützung, die intensive Betreuung, die konstruktiven Diskussionen sowie der Möglichkeit meine Arbeit auf nationalen und internationalen Konferenzen vorstellen zu können und dabei gleichzeitig noch etwas von der Welt zu sehen.
- Prof. Frieder Scheller möchte ich für die Betreuung und Begutachtung meiner Dissertation danken.
- Dr. Till Bachmann danke ich für die unkomplizierte Bereitstellung seiner Zeit für die Begutachtung meiner Arbeit.
- Außerdem danke ich unseren Kooperationspartnern Dr. Nadeem Sabir und Prof. Wolfgang Parak von der Universität Hamburg, Sara Hölzel und Prof. Martin Eickhoff von der Justus-Liebig-Universität Gießen, und Dr. Adrian Ruff und Prof. Wolfgang Schuhmann von der Universität Bochum für die gute Zusammenarbeit und die Bereitstellung der verschieden Materialien.
- Dr. Sven Feifel danke ich für die konstruktiven Fachgespräche, aber vor allem für die lustigen Mittags- und Kaffeepausen, welche meinen Arbeitsalltag bereichert haben. Des Weiteren möchte ich mich für das finale Korrekturlesen meiner Arbeit bedanken.
- Meinen Promotions-Mitstreitern Dr. Kai Stieger und Dimitri Ciornii möchte ich für die Unterstützung im Laboralltag und das freundschaftliche Verhältnis danken. Ihr habt dafür gesorgt, dass auch lange Arbeitstage nicht ganz so langsam vergingen.
- Andreas Kapp, der guten Seele der Arbeitsgruppe, danke ich für die vielen motivierenden Gespräche am „frühen“ morgen im Kaffeeraum sowie die Unterstützung während meiner Promotion.
- Des Weiteren möchte ich der ganzen AG Biosystemtechnik, insbesondere Daniel Schäfer und Gero Göbel, für das gute Arbeitsklima und die stetige Hilfe bei verschiedenen Fragestellungen danken.
- Meinen ehemaligen Bacheloranden und Praktikanten Sophie Melzer, Caroline Ochs, Louis Matuschek, Nelson Matuschek und Fabian Heinrich danke ich für die Mitarbeit an den Projekten.
- Des Weiteren möchte ich mich bei meinen Freunden, insbesondere Brian Liebling und Manuel Grund, für den starken Rückhalt und das Verständnis in stressigen Zeiten bedanken.
- Mein größtmöglicher Dank gilt meiner Familie, insbesondere meiner Mutter Sylvia Riedel und meinen Großeltern Brigitte und Wolfgang Riedel, für das Interesse an meiner Arbeit sowie die liebevolle Unterstützung.

Eidesstattliche Erklärung

Ich erkläre hiermit, dass ich diese Dissertation selbstständig ohne Hilfe Dritter und ohne Benutzung anderer als der angegebenen Quellen und Hilfsmittel verfasst habe. Alle den benutzten Quellen wörtlich oder sinngemäß entnommenen Stellen sind als solche einzeln kenntlich gemacht.

Diese Arbeit ist bislang keiner anderen Prüfungsbehörde vorgelegt worden und auch nicht veröffentlicht worden.

_____

Ort, Datum, Unterschrift